THE HETEROGENEOUS MICROENVIRONMENT OF MALIGNANT PRIMARY AND METASTATIC CENTRAL NERVOUS SYSTEM TUMORS

By

Cymon Nichole Kersch

A DISSERTATION

Presented to the Neuroscience Graduate Program,

Oregon Health and Science University,

And School of Medicine

in partial fulfillment of

the requirements for the degree of

Doctor of Philosophy

May 2019

School of Medicine

Oregon Health & Science University

CERTIFICATE OF APPROVAL

This is to certify that the Ph.D. dissertation of

Cymon N. Kersch

has been approved on

Advisor, Edward A. Neuwelt, M.D.

Co-Advisor, Leslie L. Muldoon, Ph.D.

Member and Chair, Xiaolin Nan, Ph.D.

Member, Philip Stork, M.D.

Member, Jeffery Iliff, Ph.D.

Anthony Paul Barnes, Ph.D.

TABLE OF CONTENTS

LIST OF FIGURES

LIST OF TABLES

ABBREVIATIONS

A2aR	Adenosine A2A Receptor
ABI	Allen Brain Institute
ADC	Apparent Diffusion Coefficient
AKT	Protein Kinase B
ALCAM	Activated Leukocyte Adhesion Molecule
APC	Antigen Presenting Cell
ARG1	Arginase 1
ATRX	α-thalassemia/mental retardation syndrome X-linked
AQP4	Aquaporin 4
BBB	Blood-Brain Barrier
BCL7B	B-cell Lymphoma 7B
BTB	Blood-Tumor Barrier
BTLA	B- and T-lymphocyte attenuator
CA9	Carbonic Anhydrase 9
CAR	Chimeric antigen receptors
CBV	Cerebral Blood Volume
CEL	Contrast Enhancing Lesion
CNS	Central Nervous System
CRT	Chemoradiotherapy
CT	Cellular Tumor
CTC	Circulating Tumor Cell
CTLA4	cytotoxic T-lymphocyte-associated protein 4
DCE	Dynamic Contrast Enhanced
DSC	Dynamic Susceptibility Contrast
DTC	Disseminated Tumor Cell
DTI	Diffusion Tensor Imaging
DWI	Diffusion-Weighted Imaging
ECM	Extracellular Matrix
EGF	Epidermal Growth Factor
EGFR	EGF Receptor
ELISA	Enzyme linked immunoabsorbant assay
EMT	Epithelial-mesenchymal transition
ER	Estrogen Receptor
ERK	Extracellular-signal-related protein
ES	Enrichment Score
ETNK2	Ethanolamine Kinase 2
FAK	Focal Adhesion Kinase
FDA	Food and Drug Administration
FDR	False Discovery Rate
FLAIR	Fluid-attenuated inversion recovery
FPKM	Fragments Per Kilobase of transcript per Million mapped reads
Gal-3	Galectin 3
GBM	Glioblastoma Multiforme
GDF-15	Growth differentiation factor 15
GFAP	Glial fibrillary acidic protein
GFP	Green Fluorescent Protein
GFR	Growth Factor Receptor
GMPS	Guanosine monophosphate synthetase
GO	Gene Ontology
GSEA	Gene Set Enrichment Analysis
GSK3β	Glycogen synthase kinase 3 beta
HB-EGF	Heparin Binding EGF
HBV	Hyperplastic Blood Vessels
HER2	Human Epidermal GFR 2
HR	Hazard Ratio
HRG	Heregulin (see also: NRG1)
Iba1	Ionized calcium binding adaptor molecule 1
IBSP	Integrin binding sialoprotein
ICOS	Inducible T-cell stimulator
IDH1,2	Isocitrate Dehydrogenase 1 & 2
IFN	Interferon
IL	Interleukin
IRB	Institutional review board
IT	Infiltrating tumor
IvyGAP	Ivy Glioblastoma Atlas Project
KPS	Karnofsky performance status
LAG3	Lymphocyte Activating 3
LE	Leading Edge

LOH	Loss of heterozygosity
LPS	Lipopolysaccharide
mAB	Monoclonal antibody
MAPK	Mitogen-activated protein kinase
MGMT	O^6-methylguanine-DNA methyltransferase
MHC	major histocompatibility complex
MIA	Melanoma inhibitory activity
MIB1L	Mindbomb homolog 1
mir	microRNA
MIRB	Molday ion rhodamine B
MM2BH	MD-MB-231-BR-HER2 cell line
MMP	Matrix metalloproteinases
MRI	Magnetic resonance imaging
MRS	Magnetic resonance spectroscopy
MsigDB	Molecular Signatures Database
MVP	Microvascular Proliferation
NCEL	Non contrast-enhancing lesion
NE	Necrosis
NES	Normalized enrichment score
NF1	Neurofibromatosis 1
NK	Natural Killer
NOM	Nominal
NRG1	Neuregulin (See also: HRG)
NVU	Neurovascular Unit
PAN	Pseudopalisading cells around necrosis
PanCK	Pan-cytokeratin
PC	Principle component
PCA	Principle component analysis
PD1	Programmed cell death protein 1
PDGFR	Platelet-derived growth factor receptor
PD-L1	Programmed death-ligand 1
PGAM4	Phosphoglycerate mutase family member 4
PI3K	Phosphoinositide 3-kinase
PLA	Proximity ligation assay
PNZ	Perinecrotic zones
PR	Progesterone Receptor
PTEN	Phosphatase and tensin homolog
PWI	Perfusion-weighted imaging
RB1	Retinoblastoma 1
rCBV	Relative cerebral blood volume
RTK	Receptor tyrosine kinase
S100A4	S100 Calcium Binding Protein A4
SD	Standard deviation
SEM	Standard error mean
STAT3; 5	Signal transducer and activator of transcription 3; 5
SWI	Susceptibility weighted imaging
T1W	T1-weighted
T2W	T2-weighted
TAM	Tumor associated macrophage
TCGA	The Cancer Genome Atlas
TCR	T-cell receptor
TGFβ	transforming growth factor β
TIM3	T-cell immunoglobulin and mucin domain-3
TNFα	Tumor necrosis factor α
TNFRSF4	tumor necrosis factor receptor superfamily member 4
TP53	Tumor protein 53
Treg	Regulatory T cells
TTFields	Tumor treating fields
VEGF	Vascular endothelial growth factor
VEGFR	VEGF receptor
WHO	World Health Organization

DEDICATION

This dissertation is dedicated to my Uncle Steve. Steve was one of a most genuinely kind, supportive, fun-loving, ridiculously intelligent and adventurous people I know, and will be missed dearly. Steve died during the last year of my PhD from melanoma brain metastases, and he will forever be a reminder that each tick mark in the survival curves we study is an uncle, an aunt, a father, a mother, a husband, a wife, and a dear friend. He is a reminder that even with the most promising current therapies, the vast majority of people do not survive after getting a brain tumor. His is a reminder that we need to keep studying what is unique about the tumors that don't respond to treatments, and harness our scientific creatively, knowledge, and enthusiasm to do better. He is a reminder that behind our laboratory experiments, manuscripts, and grants that can feel far removed from the reality of the diseases was are studying, there is a real person who might one day benefit from the work. For all of that and for just being you, thank you.

ABSTRACT

Malignant brain tumors remain incurable and improving outcomes will require personalized treatment strategies. In personalized medicine, therapeutics are tailored to each tumor. To apply personalized medicine to brain tumors, a more thorough understanding of therapeutically actionable tumor features in individuals and patient cohorts is needed. Actionable tumor features include genetic mutations, aberrantly expressed proteins, and tumorigenic microenvironment elements. In brain tumors, applying personalized treatment strategies is complicated by multi-layered heterogeneity, biological complexity, and difficult drug delivery. In this dissertation I investigated factors that currently hinder the use of personalized medicine for malignant brain tumors.

The first chapter of this dissertation reviews the known heterogeneity, brain tumor microenvironment, and current therapeutic approaches for the two most common and deadly brain tumors: glioblastoma multiforme (GBM) and brain metastases, specifically from breast cancer. In GBM, tumor heterogeneity presents one of the most pressing current issues. GBM heterogeneity hinders reliable comparisons and detection of actionable tumor features within and between tumors. Meanwhile, in brain metastases, understanding how infiltrating tumor cells interact with the brain microenvironment remains incompletely characterized, and thus presents a potentially untapped therapeutically targetable feature.

In chapters 2 and 3 I analyzed transcriptomic data from histologic and magnetic resonance imaging (MRI) defined tumor regions of human GBM with the aim of better understanding tumor heterogeneity. Our results showed that intra-tumoral histologic variability influences tumor classification when assessing subtyping and prognostic gene signatures, and

identified the cellular tumor as a GBM structure from which gene signatures can be applied to more accurately stratify patient cohorts. Furthermore, GBM regions with different MRI phenotypes also displayed transcriptional variance, and this variance reflected biological and immunological differences. These results support that developing imaging biomarkers are a viable, non-invasive option for evaluating potentially therapeutically predictive biological processes and key microenvironments in GBM.

The fourth chapter of this dissertation investigates crosstalk between metastatic human epidermal growth factor receptor 2 (HER2) positive breast cancer cells and the brain tumor microenvironment. We found that the cell surface receptors αvβ3-integrin and HER2 physically interact and influence the motile capabilities of human breast cancer cells *in vitro* and *in vivo*. We demonstrated that microglia in the tumor microenvironment express a protein, Galectin-3 (Gal3), which can bind and activate αvβ3-integrin. *In vitro*, microglia secrete Gal3 and increase the migration of breast cancer cells. Inhibiting Gal3 *in vivo*, failed to influence tumor growth, however, it is possible the inhibitor was unable cross the blood brain barrier. These results highlight that microglia and metastatic tumor cells engage in tumorigenic cross-talk, which may provide novel therapeutic targets.

The central theme of this dissertation is to address some of the paramount issues hindering the use of personalized medicine in malignant central nervous system tumors. Future directions from this work include validating our imaging biomarker development findings in a prospective cohort and at the protein level. This method would provide a non-invasive tool to robustly evaluate actionable alternations and therapeutically targetable microenvironments in GBM. Future directions also include evaluating therapeutically actionable points in the crosstalk between infiltrating breast cancer cells and microglia. As such, we present several alterative

growth factors and cytokines that may be important in this interaction. Together, our findings and future directions support developing personalized treatment strategies for malignant brain tumors.

CHAPTER 1: TOWARD PERSONALIZED MEDICINE FOR MALIGNANT BRAIN TUMORS: IMPLICATIONS OF THE HETEROGENEOUS, COMPLEX TUMOR-MICROENVIRONMENT FOR BRAIN TUMOR THERAPY.

Important notes: Text and figures within this chapter's 'Imaging Genomics' section will also be published in the book chapter:

Kersch, CN and Barajas Jr., RF (2019) Imaging Genomics. Glioma Imaging: Physiologic, Metabolic, and Molecular Approaches. Springer International Publishing AG.

Minor discussion on the brain microenvironment and neurovascular unit are also published in:

H. L. McConnell, **C. N. Kersch**, R. L. Woltjer, E. A. Neuwelt, The Translational Significance of the Neurovascular Unit. *J Biol Chem* **292**, 762-770 (2017).

1.1 Personalized care for malignant brain tumors.

Treatments for cancer are moving toward personalized and precision medicine, with the goal of therapeutically targeting tumor characteristics unique to each person. The aim of personalized medicine is to account for unique variances between tumors (such as genetic, epigenetic, and tumor microenvironment features) in tailoring optimal therapeutic strategies to each patient. It is the hope that this therapeutic approach will provide substantial benefit over the more traditional "one size fits all" approaches for biologically heterogeneous and aggressive tumors such as malignant brain tumors. At present, major barrier to applying personalized medicine tactics to brain tumors include: (1) the highly invasive nature of the most malignant cells that form tumors in the central nervous system (CNS), (2) the unique and incompletely characterized microenvironment of brain tumors, (3) the relatively recent appreciation for the role that innate and adaptive immunity play in these tumors, and (4) the impact of the blood-brain barrier (BBB) and blood-tumor barrier (BTB) on drug delivery to the CNS compartment. These factors have limited therapeutic advancements for the most malignant brain tumors: glioblastoma multiforme (GBM) and metastatic brain tumors.

GBM is the most common and malignant primary brain tumor in adults. GBM is uniformly fatal with a median survival of 12-15 months applying standard of care treatment (*1, 2*). Standard treatment consists of maximally safe surgical resection followed by radiation therapy with concurrent and adjuvant temozolomide. An overall survival increase of nearly 5 months was recently reported with the addition of tumor-treating fields (TTFields), but otherwise the prognosis of GBM has changed little over the past 15 years (*3*). The global age-adjusted incidence of GBM is 3.99 and 2.52 cases per 100,000 for males and females, respectively (*4*). The diagnosis of GBM is made by histopathological analysis, with recent subdivisions defined

by the World Health Organization (WHO) based on the mutational status of isocitrate dehydrogenase 1 (IDH1) (*5*). Many other genetic and molecular phenotypes of GBM have been identified, but are not yet classified as official subtypes, and understanding of their role in disease progression and treatment sensitivity is ongoing. Biologically, GBMs are highly heterogeneous, display marked invasiveness, and elicit remarkable local and systemic immunosuppression.

While GBM is the most common primary malignant brain tumor, metastatic brain tumors outnumber GBMs more than 10:1 (*6*). Brain metastasis is a late-stage complication of numerous systemic cancers, occurring most commonly in lung cancer, breast cancer, and melanoma (*7*). Brain metastases are nearly all incurable, with the exception of some metastatic melanomas that have very recently shown long-term durable responses to immunotherapies (*8, 9*). The incidence of brain metastasis is variable, but is as high as 30% in certain breast cancer subtypes (*10, 11*). At the morphological level, brain metastases show less local invasiveness through the brain parenchyma than GBMs and are considered grossly well-circumscribed masses. However, these malignancies are known to be highly invasive in nature, as evidenced by their metastatic capacity. Also dissimilar from GBMs is the immunogenic phenotype of brain metastases. While GBMs are characteristically immunosuppressive, metastatic tumors frequently cause immune stimulation, though this variable between and within metastatic tumor types.

Developing personalized medicine approach for both GBM and metastatic brain tumors has the potential to be hugely beneficial for patient outcomes. To enable the use of personalized medicine for brain tumors a more thorough understanding of actionable tumor features specific to individuals and/or patient cohorts is needed. Actionable features include genetic mutations and altered protein expression of the neoplastic cells (such as overexpressed or mutant growth factor

receptors), as well as specific tumor-microenvironment and tumor-immune interactions (for instance, programmed death-ligand 1, PDL1) that can be pharmacologically targeted. Unfortunately, the vast heterogeneity, biological complexity, and difficult drug delivery greatly complicate this approach in the setting of brain tumors. In this dissertation I evaluated several critical factors that limit the applicability to personalized care to malignant brain tumors.

1.2 Glioblastoma Multiforme (GBM).

1.2.1 GBM overview.

GBMs are primary brain tumors, tumors that initiate within the CNS (*12*). Primary brain tumors include both benign and malignant neoplasms. In adults, gliomas account for 75% of all malignant primary brain tumors (*4*). Gliomas are neuroepithelial tumors derived from glial precursors, include astrocytomas, oligodendrogliomas, and ependymomas, and are categorized as grades I-IV by histopathological and molecular characteristics. WHO grade I gliomas are defined as well circumscribed masses that are benign and frequently curable with complete surgical resection. WHO grades II-IV gliomas are diffusely infiltrative tumors that are stratified by histopathological features including nuclear atypia, mitoses, necrosis, and vascular proliferation and the presence or absence of IDH1 mutation, alpha thalassemia/mental retardation syndrome X-linked (ATRX) mutation, and 1p/19q deletion status. Grade IV gliomas are GBMs; these are the most aggressive gliomas and have a dismal prognosis. GBMs represent more than 50% of all gliomas. Median survival for GBM as 12-15 months with standard treatments, but may be extended to 20 months with the addition of TTFields to the treatment regiment (*1-3*).

GBMs are diagnosed by the histological presence of necrosis and vascular proliferation. As of the 2016 WHO update to CNS tumor classification, GBMs are sub-classified as IDH1-mutant, IDH1-wildtype, and not otherwise specified (NOS; tumors where IDH1 status could not be assigned). IDH1 mutation was first reported in GBM in 2008 (*13*) and is associated with a survival benefit (*14*). IDH1-mutant GBM occurs in approximately 10% of GBM and is typically found in younger patients with a mean age at diagnosis of 45-years-old. Comparatively, the mean age of patients with IDH1 wildtype GBM is 56-59 years of age (*14*).

1.2.2 GBM development and heterogeneity.

GBM natural history.

The tumor initiating events in GBM are an area of active and controversial research. It is probable that a multi-factorial progression of genetic and epigenetic changes in different cell populations and variable microenvironments gives rise to GBMs, and contribute to their characteristic heterogeneity. Advances in lineage tracing experiments applied to developmental neurobiology research have identified two main neurogenic regions in the adult brain: the subventricular and subgranular zones in the lateral ventricles and in the dentate gyrus of the hippocampal formation (*15*). Adult neural stem cells in these regions are multipotent cells with unlimited self-renewal capacity that give rise to proliferative progenitor cells, which in turn can differentiate into mature neurons, astrocytes, and oligodendrocytes (*16, 17*). Experimental evidence from murine glioma models suggests that these progenitor cells as well as adult CNS cells can both develop oncogenic mutations and give rise to tumors (*18-20*). These cell populations can develop one or more mutations driving tumor initiation and growth. Multiple

oncogenes and tumor suppressor genes are commonly present in GBM including tumor protein 53 (TP53), phosphatase and tensin homolog (PTEN), neurofibromatosis type 1 (NF1), epidermal growth factors receptor (EGFR), HER2, retinoblastoma 1 (RB1), phosphoinositide-3-kinase regulatory subunit 1 (PIK3R1), and phosphoinositide-3-kinase catalytic subunit alpha (PIK3CA) (*21, 22*). These mutations arise in different tumor initiating cells, contributing to inter-tumoral diversity. For instance, in mice, the same oncogenic driver mutation in two different cell types (adult neural and oligodendrocyte progenitors) results in the development of molecularly distinct tumors (*19*).

In human GBM, there is a clear delineation of at least two divergent pathways of GBM development. "Primary GBMs" develop through gain of one or multiple genetic and/or epigenetic aberrations including alterations to EGFR, P53, PTEN, O^6-methylguanine-DNA methyltransferase (MGMT), and larger chromosomal losses. These tumors spontaneously develop directly into a GBM with now lower grade tumor prior to diagnosis of the grade IV lesion. "Secondary GBMs" develop from neoplastic precursor cells that have mutant IDH1 and/or IDH2. Secondary GBMs progress from low-grade gliomas to grade IV tumors. Throughout their progression, these tumors can acquire further genetic and epigenetic changes.

GBM heterogeneity.

GBMs are the archetypal heterogeneous tumor (*23*). After the initial oncogenic genetic insult, malignant cells acquire by additional mutations, epigenetic changes, and micro-environmental influences, leading to variations between and within tumors. Inter-tumoral heterogeneity describes the variance observed between different tumors. Clinically, inter-tumoral variances are often categorized based on gene and protein expression differences such as

mutations and/or methylation of IDH1, MGMT, and EGFR. Several of the most common mutations and epigenetic changes in GBM have known functional consequences and are associated with differences in overall survival and treatment sensitivity (Table 1.1).

In addition to single gene inter-tumoral variability, multi-gene panels also describe tumor cohorts (Table 1.1). The most well characterized multi-gene expression-based panel is The Cancer Genome Atlas (TCGA) delineation of molecular subtypes. Philips et al., 2006 described three GBM molecular subtypes termed proneural, proliferative, and mesenchymal, based on dominant biological features in the gene lists that characterized each subclass (*24*). These three subclasses were associated with different prognoses. In 2010, Verhaak et al. refined the gene expression-based subclassification of GBM using gene expression data from 200 newly diagnosed GBM cataloged by TCGA (*25*). Their analyses resulted in an 840-gene expression signature that defined four molecular subtypes: proneural, neural, classical, and mesenchymal. Again, the nomenclature was based on known functions of the signature genes. A recent revision of these subtypes signatures redefined only 3 subtypes (proneural, classical, and mesenchymal) based on expression of a smaller 150-gene panel (*26*).

Several GBM subtypes are correlated with specific gene mutations. Aberrations in EGFR, NF1, and platelet-derived growth factor receptor alpha (PDGFRA)/IDH1 are enriched in the classical, mesenchymal, and proneural subtypes, respectively. These subtypes also show differences in their biology, with the mesenchymal subtype exhibiting a more robust immune response with increased lymphocytic infiltrate and microglial/macrophage activation (*26-32*). Several groups have reported the co-occurrence of multiple subtypes within a single tumor and a shift in subtypes in a single patient over the course of treatment (*26, 33*). Unfortunately, subtype classification has yet to show significant correlations with clinical outcomes.

Table 1.1 Clinically and/or biologically significant molecular aberrations in GBM.

Molecular Characteristic	Biological Function	Clinical Significance	References
EGFR amplification or truncation	A receptor tyrosine kinase involved in multiple cancer signaling pathways. Deletion of exons 2-7 is termed EGFRviii and is constitutively activated. EGFR is amplified in ~50% of GBM and truncated to EGFRviii in 25-33%. EGFR amplification is common in the classical subtype (see below).	EGFRviii is associated with a worse prognosis. Clinical significance of other EGFR mutations and amplifications remains unclear.	Aldape et al., 2004 (*34*). Taylor et al., 2012 (*35*). Yang et al., 2017 (*36*).
PTEN mutation	PTEN mutation occurs more frequently in primary than secondary GBM.	PTEN loss is a negative prognostic marker.	Tohma et al., 1998 (*37*). Han et al., 2016 (*38*) .
MGMT promoter methylation	A DNA repair enzyme that removes alkyl groups from the O^6 position of guanine. In 40% of GBM, promoter methylation inhibits gene expression.	Associated with increased sensitivity to temozolomide and longer survival.	Hegi et al., 2005 (*39*). Weller et al., 2010 (*40*).
IDH1/2 mutation	Oncogenic mutation that causes cells to produce 2-hydroxyglutarate instead of NADPH, and may increase sensitivity to oxidative stress. Mutated in 10% of GBM, predominantly in younger patients (<55 years of age). Associated with secondary GBM. Most frequent mutation is R132H. Common in the proneural subtype.	Associated with significantly longer overall survival. Now defines distinct primary and secondary GBM entities, as defined by the WHO.	Ohgaki 2013 (*14*). Sanson et. al., 2009 (*41*). Cohen et. al., 2013 (*42*).
1p/19q co-deletion or LOH	Co-deletion of the short arm of chromosome 1 and the long arm of chromosome 19; loss of one is termed loss of heterozygosity (LOH). This is uncommon in GBM.	Improved treatment response and longer survival in oligodendrogliomas.	Aldape et al., 2007 (*43*). Zhao et al., 2013 (*44*).
ATRX mutation	Functions to help incorporate histone variant H3.3 into heterochromatin, causing genomic instability. Common in younger patients/secondary GBM with IDH and TP53 mutations.	Associated with increased treatment sensitivity and longer survival.	Schwartzentruber et al., 2012 (*45*). Koschmann et al., 2016 (*46*). Nandakumar et al., 2017 (*47*).
P53 Mutation (gain of function)	Tumor suppressor gene mutated in 25-30% of primary and 60-70% of secondary GBM. May decrease MGMT expression.	Prognostic significance remains controversial.	Wang et al., 2014 (*48*). England et al., 2013 (*49*). Chaurasia et al., 2016(*50*).
Transcriptionally - defined molecular subtypes	4 molecular subtypes: mesenchymal, proneural, neural, and classical are defined based on an 840-gene signature. The mesenchymal subtype is more inflammatory.	Clinical significance is controversial. Proneural may carry a survival benefit.	Phillips et al., 2006 (*24*). Verhaak et al., 2010 (*25*). Wang et al., 2017 (*26*).

In addition to their inter-tumoral variances, GBMs also display intra-tumoral heterogeneity (*23, 51*), whereby one area of a tumor differs from another area of that same tumor or aspects of a single tumor changes over time (*33, 52-55*). Spatial variance within a tumor can be multi-factorial: (1) the genetic or molecular make-up of the malignant cells can vary across a tumor, as demonstrated by single-cell genomic and transcriptomic analyses (*33*), and (2) the tumor microenvironment varies across a tumor, as exemplified by differing histologic structures, areas of necrosis, and regions with extensive angiogenesis (*56*). Several of the single gene aberrations commonly found in GBM, such as EGFR amplification and MGMT promoter methylation, can vary in subclones of a single GBM (*57, 58*). Furthermore, these genetic traits can fluctuate over time, with divergent clonal evolution (*51*). Intra-tumoral heterogeneity has been implicated as a major contributor to therapeutic resistance in GBM and other cancers, with clonal variants in a single GBM tumor displaying different therapeutic sensitivity and resistance (*59, 60*).

Imaging genomics: a non-invasive method to assess GBM heterogeneity.

Robustly evaluating GBM inter- and intra-tumoral heterogeneity presents a significant challenge to the Neuro-Oncology field. Variable tumor features (genomic and proteomic) are commonly assessed using physical tissue samples, and this remains the gold standard. However, collecting tissue specimens in CNS malignancies is more problematic than other tumor types because sampling requires invasive neurological surgery that poses significant cognitive risks to the patient. Furthermore, sampling multiple regions can be complicated by the necessity to preserve tissue in critical function brain regions. These factors make evaluating tissue features nearly impossible across a whole tumor and over time. Thus, analysis of tumor heterogeneity

utilizing tissue samples provides a small snapshot of a tumor at a single point in time. In contrast, clinical imaging obtains a global view of the entire tumor, now with significantly increased resolution for morphological and physiological tumor characteristics, and can be employed to follow these characteristics over time through sequential imaging sessions. However, current imaging techniques and their analytic methods do not directly assess genetic/molecular changes of the tumor.

To overcome the limitations of physical tissue sampling and clinical imaging techniques for tumor analyses, a new field of imaging genomics has developed (Fig. 1.1). Imaging genomics studies the relationship between clinical imaging features and patterns of gene expression, genetic mutations and protein modifications (*61-69*). The central goal of this field is to permit the molecular characterization of tumors across space and time in a non-invasive manner. Imaging genomics is distinguished from 'radiomics' which studies the extraction of quantitative imaging features, and 'radiogenomics' which can be used either synonymously with imaging genomics or alternately refer to the relationship between genomic changes and response to radiation therapy. Imaging genomics has the capacity to improve clinical decision-making and treatment through advanced interpretation of the genetic and biological patterns using non-invasive imaging (*67*).

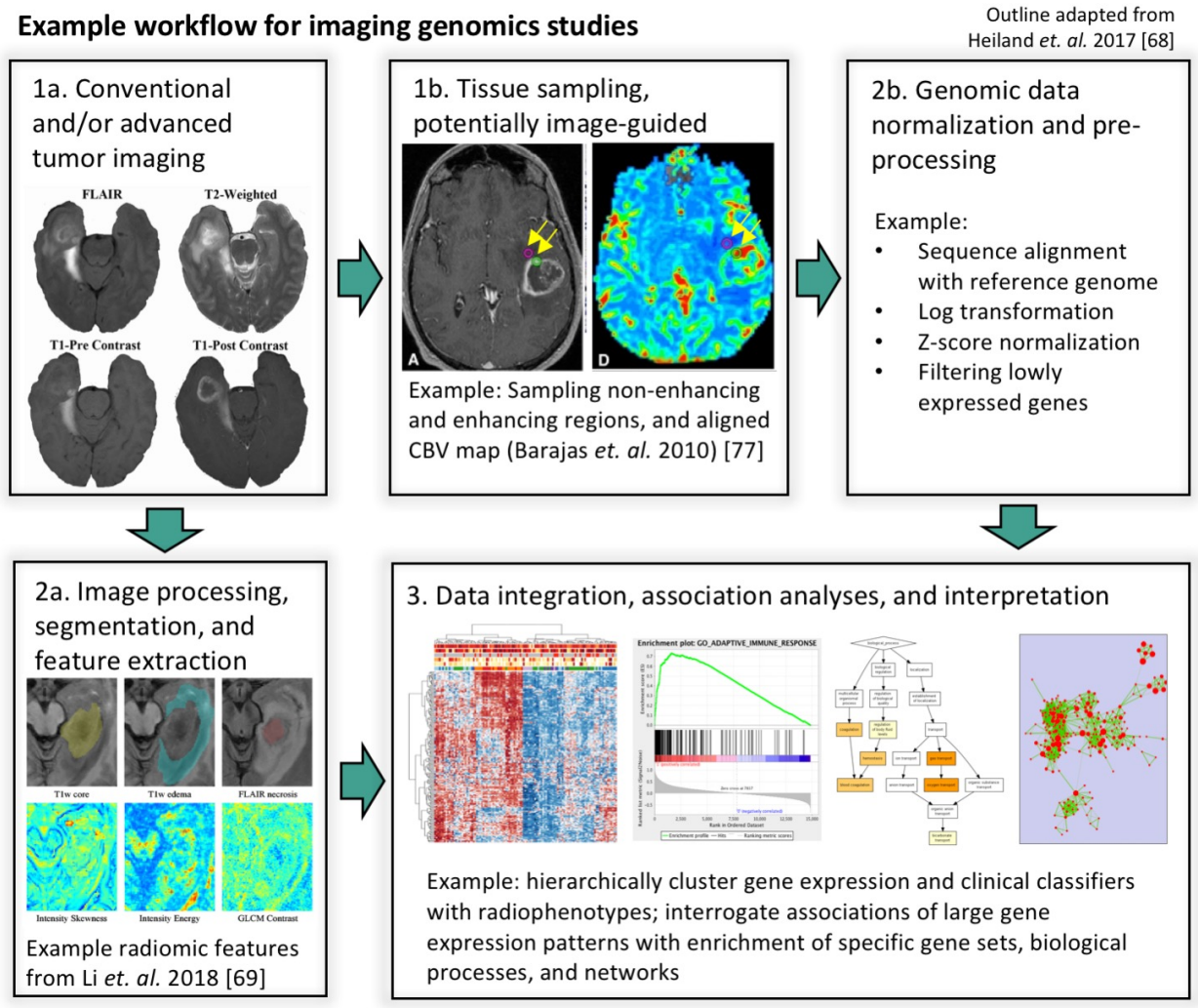

Figure 1.1. Integrating radiophenotypes with molecular features in GBM. Pre-treatment MRI sequences are obtained (**1a**) followed by collection of tumor tissue, sometimes under image-guidance (**1b**). Imaging data undergoes pre-processing (**2a**) while tissue is subjected to genomic, transcriptomic, and/or proteomic analyses. The imaging and molecular data are integrated to evaluate associations between radiophenotypes and molecular features (**3**). These associations are interpreted in the context of the clinical disease and known complex biological processes and pathways.

Table 1.2. MR imaging techniques and their major utility in GBM assessment

Conventional techniques		**Advanced techniques**	
Sequence	Utility	Sequence	Utility
Contrast Enhanced T1-weighted imaging (T1W)	Visualizing tumor mass via qualitative microvascular permeability characteristics	Perfusion-weighted imaging (PWI) [DSC and DCE]	Quantitative measures of vascularity, vascular permeability
T2-weighted imaging (T2W)	Peri-tumoral edema, non-enhancing tumor	Diffusion-weighted imaging (DWI) and apparent diffusion coefficient (ADC)	Cellularity (higher cellularity corresponds to lower ADC)
Fluid attenuated inversion recovery (FLAIR) imaging	Peri-tumoral edema, non-enhancing tumor	Diffusion-tensor imaging (DTI)	Tractography
T2* susceptibility sequence (SWI)	Blood products, calcifications	MR Spectroscopy (MRS)	Metabolic profiles

**Adapted from ElBanan et al. 2015 and Mabray et al. 2015* (*62, 70*)

Imaging genomics has begun to create noninvasive biomarkers of clinically relevant molecular and biological hallmarks of GBMs including MGMT methylation status, IDH1 mutation status, EGFR mutation, molecular subtype, and level of immunoreactivity (*62, 71-76*). Over the first decade of imaging genomics, the field has progressed significantly from binary classification of imaging characteristics with the presence or absence of a molecular feature to complex whole genomic analyses corresponding to computer-identified image spatial textures and advanced imaging elements (Fig 1.2) (*69, 77*). Despite these improvements, imaging genomics remains an area with many unanswered questions and significant potential for future work to influence clinical care by bridging medical imaging with tumor characteristics used to evaluate tumor heterogeneity and plan personalized care.

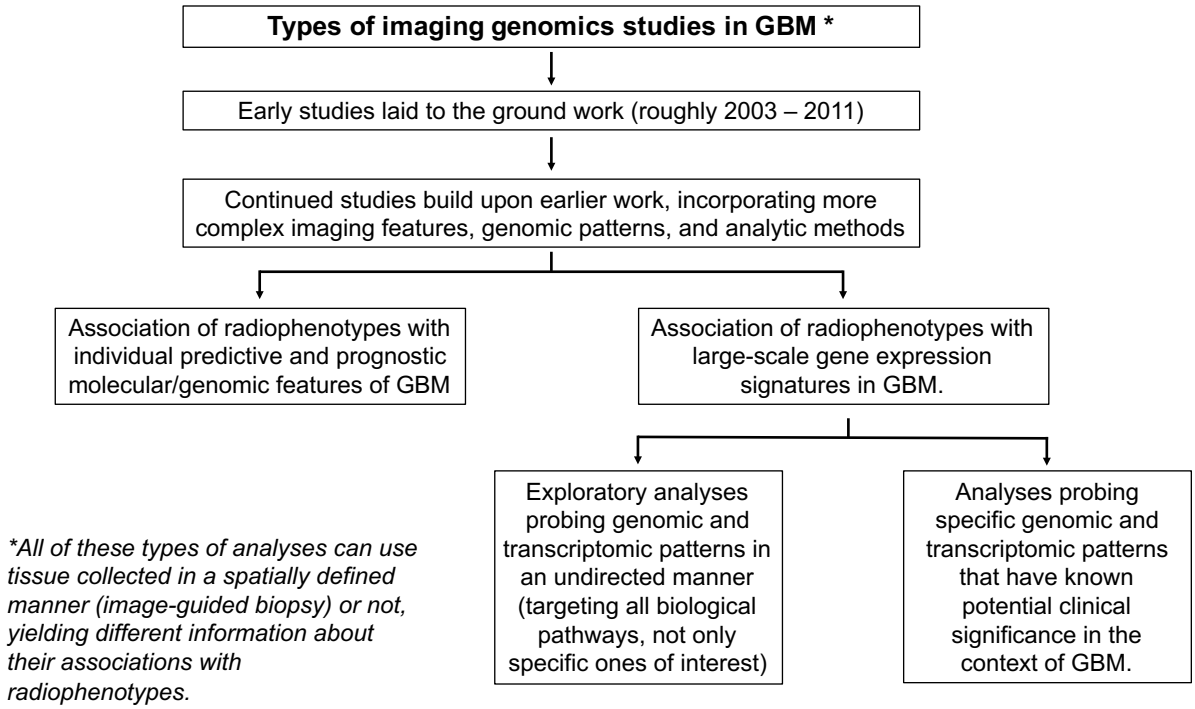

Figure 1.2. Summary of imaging genomics studies in GBM. Following the seminal studies in imaging genomics the field has investigated imaging biomarkers of (1) specific individual molecular traits of the tumor (such as the presence or absence of EGFR amplification or MGMT methylation) or (2) associations with multi-gene signatures. Multi-gene signature studies are either directed, investigating gene sets known to influence GBM biology/classification (i.e. molecular subtypes or signatures of biological processes such as angiogenesis), or undirected (exploring transcriptional patterns without *a priori* knowledge of the gene signature functions being probed). The molecular/genomic features can be assessed from tumor tissue of unknown origin or of known spatial location within the tumor (collected under image-guidance). Analyses of genomic markers from non-selective tissue sampling correlates the presence or presence of the genomic/molecular feature with a general imaging phenotype, while analysis of genomic markers from known spatial locations can be directly related to the imaging feature of that tumor area.

1.2.3 The GBM tumor microenvironment.

Overview of the brain tumor microenvironment.

A critical element of inter- and intra-tumoral heterogeneity in GBM, and a potentially untapped therapeutically actionable tumor feature, is the tumor microenvironment. The tumor microenvironment in GBMs is a complex milieu consisting of malignant cells, an array of resident brain cells (astrocytes, microglia, oligodendrocytes, endothelial cells, pericytes, and neurons), infiltrating immune cells (mostly macrophages and lymphocytes), extracellular matrix (ECM), cerebral vasculature (that is distinguished from vasculature elsewhere in the body by the presence of the BBB), and variable metabolic and stress features (Figure 1.3) (*78*). Many of these elements are also present in the microenvironment of metastatic brain tumors. The tumor microenvironment across a single GBM is variable, with different areas containing extensive necrosis (primarily within the tumor core), elevated mitosis (in the tumor mass), or interactions with local brain elements (at the leading edge and infiltrative tumor). Collectively, all of the elements of the tumor microenvironment influence the growth characteristics and therapeutic sensitivity of GBMs, and present potential therapeutic targets. A thorough understanding of the tumor microenvironment will be essential to personalize therapy for malignant brain tumors.

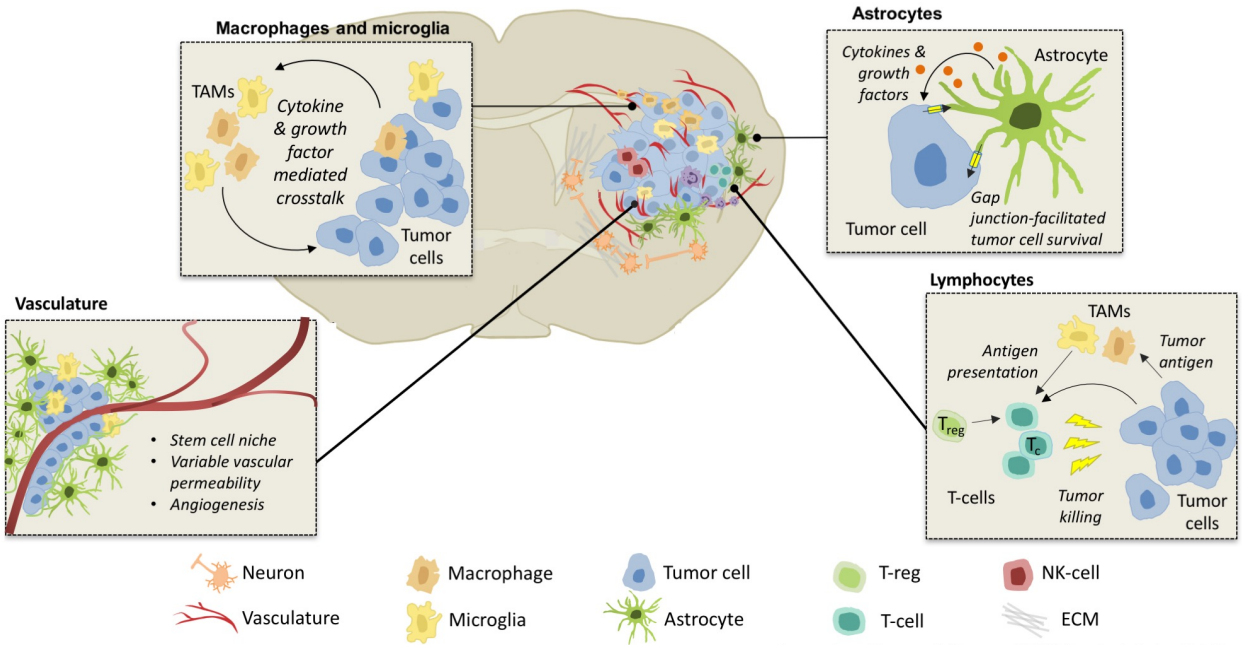

Figure 1.3. The GBM microenvironment. The tumor microenvironment in GBM is composed a variety of resident in infiltrating cell types that interact the malignant tumor cells to influence their survival, growth, and treatment sensitivity. Non-neoplastic cells in the tumor include microglia, macrophages, astrocytes, and infiltrating cells from the peripheral immune system. Non immune cells and acellular microenvironment elements include vasculature, neurons, and extracellular matrix (ECM). Adapted from Quail and Joyce 2017 *(79)*.

Components of the healthy CNS microenvironment.

Under physiologic conditions, local cells and specialized vasculature in the CNS operate synergistically to support cognitive function. Cellular components of the CNS include neurons, support cells (oligodendrocytes, astrocytes and microglia), and vascular cells (endothelial cells and pericytes). Neurons are basic working unit, able to communicate through chemical and electrical signals. The axons of neurons are wrapped in a myelin sheath produced by oligodendrocytes. Astrocytes are a heterogeneous population of star-shaped cells that dynamically support biochemical, physical and metabolic process in the brain, such as modulation of neuronal synapses (*80*). Microglia are amoeboid-shaped, CNS resident macrophages involved in scavenging and immune function (*79*).

The endothelial cells lining cerebral blood vessels are the core anatomic unit of the BBB, which protects the brain from systemic influences (*81*). Cerebrovascular endothelial cells display several unique properties that allow them to function optimally as a barrier. Vascular endothelial cells (1) contain no fenestrae and undergo very low rates of transcytosis, (2) express tight junctions and adherens junctions between endothelial cells that impede paracellular diffusion of solutes, and (3) possess polarized expression of transporters, metabolite-degrading enzymes, receptors, and ion channels on their luminal and abluminal membranes that form a selective transport interface (*82*). These features ensure that essential nutrients are delivered to the brain from the blood, while solutes and metabolic waste products are effluxed to the blood. The specialization of the BBB reflects the requirement of the brain to remain in a truly homeostatic ionic environment free of neuroactive blood-borne solutes. The vascular endothelium is surrounded by a two-layer basement membrane that is composed of a unique array of ECM proteins, compared to vasculature elsewhere in the body (*83*). Pericytes are embedded in the

basement membrane, where they contribute to cerebral vascular formation and function. Meanwhile, astrocytes extend end-foot processes around vasculature, basement membrane, and pericytes to delineate a functional perivascular space. These cellular and acellular components combined with adjacent neuronal processes form the neurovascular unit (NVU) (*81*).

Components of the CNS microenvironment in GBM.

Resident CNS cells, particularly astrocytes and microglia, and cerebral vasculature function aberrantly in GBM. Reactive astrocytes are frequently within and surrounding GBMs. Recent studies employing single cell transcriptomic and flow cytometry protein analytic techniques identified subpopulations of differentially activated astrocytes within murine models of GBM (*84, 85*). Katz et al. found that spatially restricted astrocytes in bulk tumor and in perivascular tumor niches display distinct RNA expression profiles (*84*). Meanwhile, Lin et al. described five astrocytes phenotypes that have variable presence in GBMs dependent on the tumor's molecular subtype (*85*). Through secretion of soluble factors and direct contact, these tumor associated astrocytes exert numerous pro-tumorigenic effects. Astrocytes increase the invasive and proliferative capacity of malignant cells, support GBM initiation, enhance malignant cell migration and invasion, promote drug resistance, and help tumors evade immune attack (*78, 86*). Factors secreted by reactive astrocytes include tumor necrosis factor α (TNFα), transforming growth factor β (TGFβ), interleukin (IL) 6, insulin-like growth factor 1 (IGF-1), and growth/differentiation factor 15 (GDF-15), all of which promote cancer cell proliferation and/or migration (*86*). In vitro co-culture experiments have demonstrated that astrocyte secretion of osteopontin, TGFβ, IL-6, IL-8, and ECM proteins increase in the invasive capabilities of GBM cell lines and GBM stem cells (*87-90*). Soluble factors and exosomes released by

astrocytes also increase the ability of GBM cells to evade apoptosis and to withstand hypoxic conditions and chemotherapy treatments (*91-93*). The roles of microglia and endothelial cells in GBM are discussed in detail in the following sections.

Tumor vasculature and the dysfunctional BBB.

The vascular niche is a significant element of the brain tumor microenvironment. This region serves as a the point of entry for systemic immune cells, its cellular components elicit tumorigenic effects, it is a known GBM stem cell niche, and it influences the bioavailability of intravenously delivered therapeutics (*94-99*). Endothelial cells support tumors by secreting factors including TGFβ, β fibroblast growth factor (β-FGF), and epidermal growth factor (EGF) (*100-103*). Endothelial cells in the tumor may be part of previously established vasculature or may be newly formed neovasculature. In response to local hypoxia and increased metabolic demands in the bulk of the tumor, neoplastic cells and macrophages/microglia secrete soluble factors, including vascular endothelial growth factor (VEGF), that stimulate angiogenesis (*99, 104*). Tumor angiogenesis leads to formation of vessels with abnormal structure and function, which are a hallmark feature of GBM (*105*). Tumor vasculature abnormalities include altered protein expression on the epithelial cell membrane (such as diminished or absent tight junction proteins), inadequate pericyte coverage, and altered basement membrane protein composition. Tumor cells themselves can perform endothelial mimicry, forming functional vessels (*106, 107*). Neoplastic cells can also physically disrupt the NVU by residing between the astrocyte endfeet and abluminal side of endothelial cells, altering vascular tone and decreasing tight junction protein expression (*108*). To account for these differences from the healthy BBB, this barrier in tumors is sometimes referred to as the blood-tumor barrier (BTB).

The abnormality of vasculature in GBMs results in increased, but variable, vascular permeability (*109*). Typically, the bulk tumor region of GBMs have more dysfunctional and leaky vasculature, while vasculature in the tumor periphery resembles more normal cerebral blood vessels (Figure 1.4). These patterns of variable leakiness across a tumor are exemplified by gadolinium contrast enhancement in CNS tumors on MRI (*98*). In much of the bulk tumor, intravenously administered gadolinium is able to leak out of cerebral vasculature and into the extracellular space in the brain parenchyma manifesting as regions of hyperintensity on T1W MRI sequences. Meanwhile, areas of brain surrounding these T1W gadolinium contrast enhancing lesions show more diffuse tumor cell infiltration when assessed by histochemistry and lack contrast leakage (*110*).

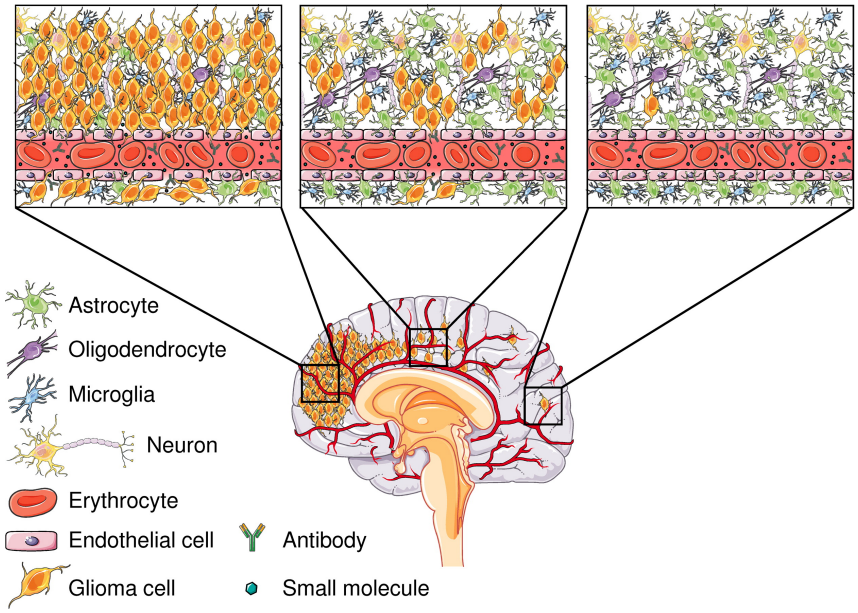

Figure 1.4. The blood-brain barrier (BBB) in GBM. Vasculature is heterogeneous across GBMs, displaying variance in its cellular elements, protein expression, and permeability characteristics. In the bulk tumor, the BBB is typically leaky, while at the tumor periphery the BBB is more intact and prevents most anti-cancer therapeutics from reaching malignant cells in this niche. Reprinted from Van Tellingen et al. 2015 (*98*).

Contribution of immune cells to the GBM microenvironment.

The CNS was previously considered an immune privileged site. Rationale for this dogma included: (1) low expression of adhesion receptors on the BBB that are important for leukocyte extravasation, (2) minimal expression of major histocompatibility complex (MHC) proteins in healthy brain, (3) absence of a brain lymphatic system, and (4) limited antigen presenting cells in the CNS (*111*). It is now known that the brain has a unique lymphatic system that includes perivascular flow pathways and meningeal associated lymphatics (*112, 113*), a functional immune system with a resident macrophage population (microglia), and active surveillance by both the innate and adaptive arms of the systemic immune system (*79*). Immune cell infiltrates in GBMs include macrophages, T-cells, B-cells, and natural killer (NK) cells. Despite the presence of these immune populations, GBMs characteristically result a body-wide immunosuppressive state.

Microglia and macrophages can account for more than 30% of the cells in the bulk tumor mass of GBMs and and influence angiogenesis, tissue remodeling, and tumor progression (Fig. 1.5) (*78, 111, 114*). Microglia and macrophages are differentiated based on their developmental origin. Microglia migrate to the brain from yolk sac progenitor cells early in development and form a self-propagating, tissue resident phagocytic cell population in the CNS (*115*). Macrophages migrate into the brain throughout life from circulating bone marrow derived monocytes. Collectively, microglia and macrophages associated with GBMs are referred to as tumor associated macrophages (TAMs), which are highly plastic, multi-faceted cells. Differentiating the origins of TAMs is challenging as their protein expression changes in pathological states (*114*). Thus, lineage tracing experiments have become the gold standard to differentiate these cells. Recent studies in mouse glioma models suggest that approximately 85%

of TAMs in GBM are macrophages that have infiltrated the tumor from systemic circulation and preferentially locate near tumor vasculature, while the remaining 15% of TAMs are locally activated microglia that are most abundant in the peritumoral region (*116*).

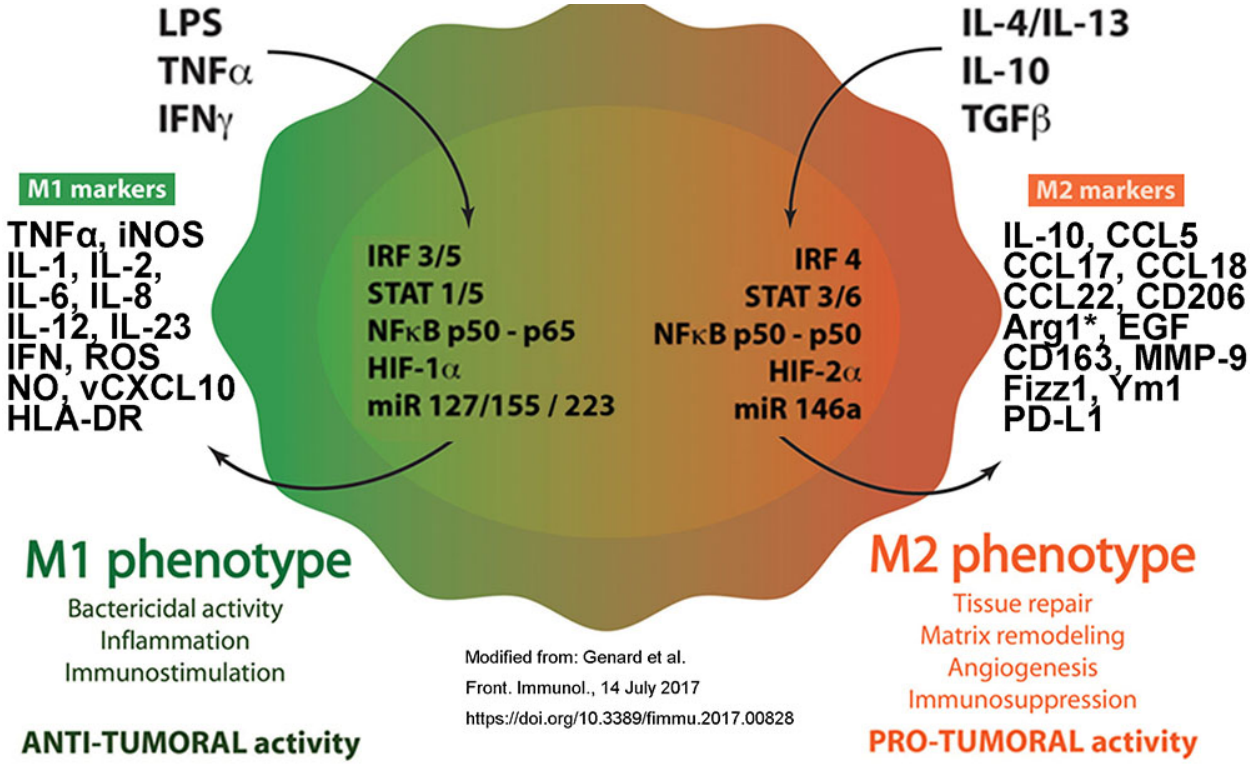

Figure 1.5 TAM activation and divergent phenotypes. Tumor associated macrophages (TAMs) activate along a spectrum of M1 to M2 phenotypes and influence the initiation, survival, growth, and local microenvironment in GBM and metastatic tumors through numerous cellular cross-talk networks. Image adapted from Genard et al. 2017 (*117*) .

TAMs in brain tumors can activate into functional cell phenotypes along a spectrum of pro-inflammatory (M1) to anti-inflammatory (M2) (Fig. 1.5). M1 polarized TAMs are considered anti-tumorigenic and M2 polarized TAMs are pro-tumorigenic. While the

bipolarization M1/M2 model is grossly oversimplified and more realistically operates as ends of a spectrum, it provides a framework to understand the multifunctional roles of TAMs (*118*). Classically activated M1 macrophages typically differentiate in response to pathogen- or damage-associated molecular patterns such as lipopolysaccharide and other toll-like receptor ligands (*119*). M1 macrophages secrete pro-inflammatory cytokines including IL-6, IL-12, IL-23, and TNFα, and express immune stimulatory proteins MHC-II, CD68, CD80, and CD86 (*120*). The functional changes in M1 polarization lead to the propagation of inflammation. As such, this population functions in pathogen and tumor killing, antigen presentation, and activation of a T_H1 cell response (*121*). Alternately activated M2 macrophages differentiate in response to soluble signaling molecules such as IL-4, IL-13, IL-10, and TGFβ, which blunt or terminate inflammation (*114, 122*). Physiologically, cells of the M2 phenotype function to contain and resolve inflammatory reactions. M2 macrophages are highly phagocytic, express characteristic proteins including arginase 1 (ARG1), CD163, CD200R, CD204, CD206, MGL1, and MGL2, and secrete anti-inflammatory cytokines IL-10 and TGFβ, which propagate the anti-inflammatory response (*120, 123*). Several studies in GBM suggest that TAMs predominantly take on an anti-inflammatory phenotype (*124-126*), while others report that TAMS express a combination of M1 and M2 markers (*126*).

TAMs support GBMs in an aggressive feed-forward cycle whereby malignant cells secrete factors that polarize TAMs to in turn produce factors that promote tumor growth and invasion (*123, 127*). Tumor derived factors, such as macrophage colony stimulating factor (M-CSF), drive TAMs toward a M2 phenotype, and blocking this reduces glioma cell invasion (*128, 129*). In response to stimulation by the glioma cells, TAMs secrete multiple soluble factors including stress-inducible protein 1 (STI1), EGF, interleukins, and TGFβ that positively

influence neoplastic cell behaviors and support their aggressive phenotype (*114*). *In vitro* work demonstrates that the presence of microglia triples the motility of GBM cells in co-culture (*130*).

In addition to their direct influence on tumor cells, TAMs help orchestrate the recruitment and activation of systemic immune cells to the tumor. Immune cells found in GBM include CD4+ T helper cells, CD8+ cytotoxic T-cells, CD4+CD25+FoxP3+ regulatory T-cells (Tregs), NK cells, and rare B-cells (*131*). CD4+ T-cells are more numerous than CD8+ T-cells in GBM, but have not been associated with clinical outcomes (*131*). CD8+ T-cell infiltrates in GBM have been associated with prolonged survival in patients. Although CD8+ T-cells are present, they may be inactive as several studies have reported that they the lack CD25 expression (*132-134*). In contrast to CD8+ cells, Tregs have been correlated with a worse prognosis, though their presence in GBMs can be variable ranging from 1-14% of the total intratumoral T-cell population (*135-137*). Tregs function as immune-suppressive T-cells, involved in the resolution of inflammation, and similarly, can repress the anti-tumor immune response in numerous cancers. Overall, T-cell infiltrates are not homogeneously distributed across GBMs, but rather cluster near tumor vasculature, their point of entry (*137*). NK cells can also be found sparsely in GBMs (*131, 138*). Like CD8+ T-cells, NK cells are directly cytotoxic and kill tumor cells.

Immune checkpoints in GBM.

Immune checkpoints are key elements of immune responses in infection, injury, and cancer. Physiologically, immune checkpoints prevent and/or limit the activation of immune responses to self-antigens. Tumors, including GBMs, hijack these mechanisms to prevent immune cells from mounting an inflammatory response against malignant cells (Fig. 1.6).

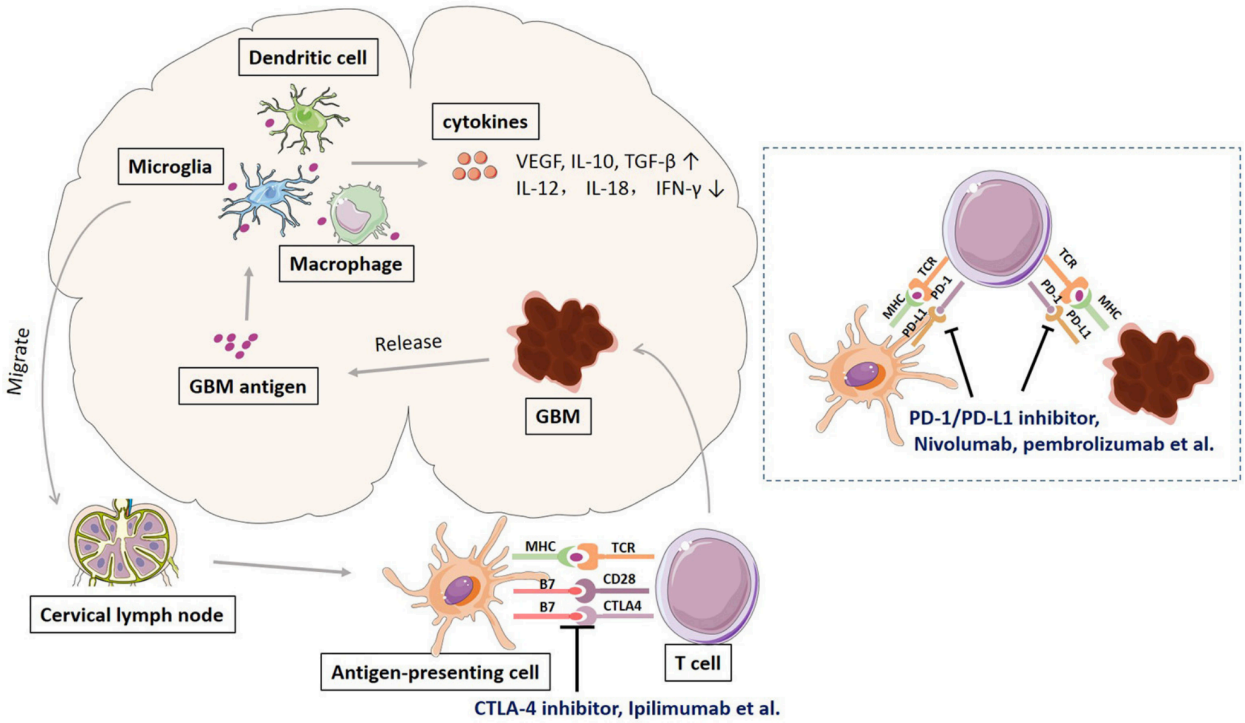

Figure 1.6. Immune checkpoints in GBM. Tumor antigens released from GBM are taken up by TAMs (microglia and macrophages), which present the antigens to local T-cells or can theoretically migrate to cervical lymph nodes and to activate peripheral lymphocytes. Activated lymphocytes, via their T-cell receptor (TCR) can then migrate to the tumor and perform their effector functions. Alternately, GBM antigens may traffic via perivascular flow and meningeal lymphatics to cervical lymph nodes to activate nodal antigen presenting cells (APCs) and lymphocytes. In the tumor, the malignant cells, TAMs, and activated lymphocytes all secrete cytokines that propagate pro- and anti-inflammatory events. These cytokines recruit and activate other immune cells, such as NK cells, which contribute to neoplastic cell death. Immune checkpoints commonly targeted thus far in the setting of GBM are PDL1, programmed cell death protein 1 (PD1) and cytotoxic T-lymphocyte-associated protein 4 (CTLA4), which function locally in the tumor and in the draining lymph nodes. Schematic reprinted from Huang et al. 2017 (*139*).

In the absence of immune checkpoint activation, the immune system has the capacity to inhibit cancer growth through a series of steps (*140, 141*). First, tumor cells produce tumor-specific antigens that are either expressed on the cell surface, secreted, or released upon cell death. Tumor-specific antigens can be proteins that are greatly overexpressed, aberrantly expressed, mutated, or uniquely post translationally modified. Antigen presenting cells (APCs) display these antigens on MHC I and II molecules to CD8+ and CD4+ T-cells. These interactions occur in both the tumor microenvironment and in lymph nodes that drain the tumor tissue. Activated T-cells then migrate to the tumor tissue, where CD8+ cells elicit cytotoxic functions resulting in tumor cell killing. During tumor cell death, more antigens are released triggering this cycle to repeat. Immune checkpoints function throughout this process during points of cell-cell contact that activate TAMs and T-cells. These checkpoints are secondary protein-protein interactions that serves as co-stimulatory or co-inhibitory signals to either confirm or inhibit immune cell activation in response to tumor-antigen presentation. If a co-inhibitory signal is present or a co-stimulatory signal is absent simultaneously with presentation of the tumor antigen, then the immune cell activation will not occur and the immune cell may enter an exhausted, anergic state where it cannot be activated in the future. Activation of both NK cells and cytotoxic T-cells can be inhibited by immune checkpoints in tumors.

T-cell and NK cell activation are major points of immune response control, and present therapeutic targets. As noted above, two signals are required for T-cell activation: (1) antigens presented on MHC molecules bind antigen-specific T-cell receptors (TCRs), and (2) co-stimulatory and/or co-inhibitory signals, which are immune checkpoints. Co-stimulatory signaling proteins include CD28, CD80, CD86, CD40L, CD137, OX40 (also termed tumor necrosis factor receptor superfamily member 4, TNFRSF4), CD58, CD28, and inducible T-cell

costimulator (ICOS) (Fig. 1.7) (*140, 141*). Co-inhibitory proteins include PD1, CTLA4, lymphocyte activation gene 3 (LAG3), T-cell immunoglobulin and mucin domain-3 (TIM3), B- and T-lymphocyte attenuator (BTLA), and adenosine A2A receptor (A2aR) (Fig. 1.7) (*140, 141*). Decreased expression of co-stimulatory proteins or overexpression of co-inhibitory proteins are mechanisms tumor cells use to evade immune attack. Immunotherapies that increase activation of the co-stimulatory molecules or inhibit activation of co-inhibitory proteins are in multiple clinical trials. Commonly modulated targets in GBM are CTLA4, PD1, and PD-L1.

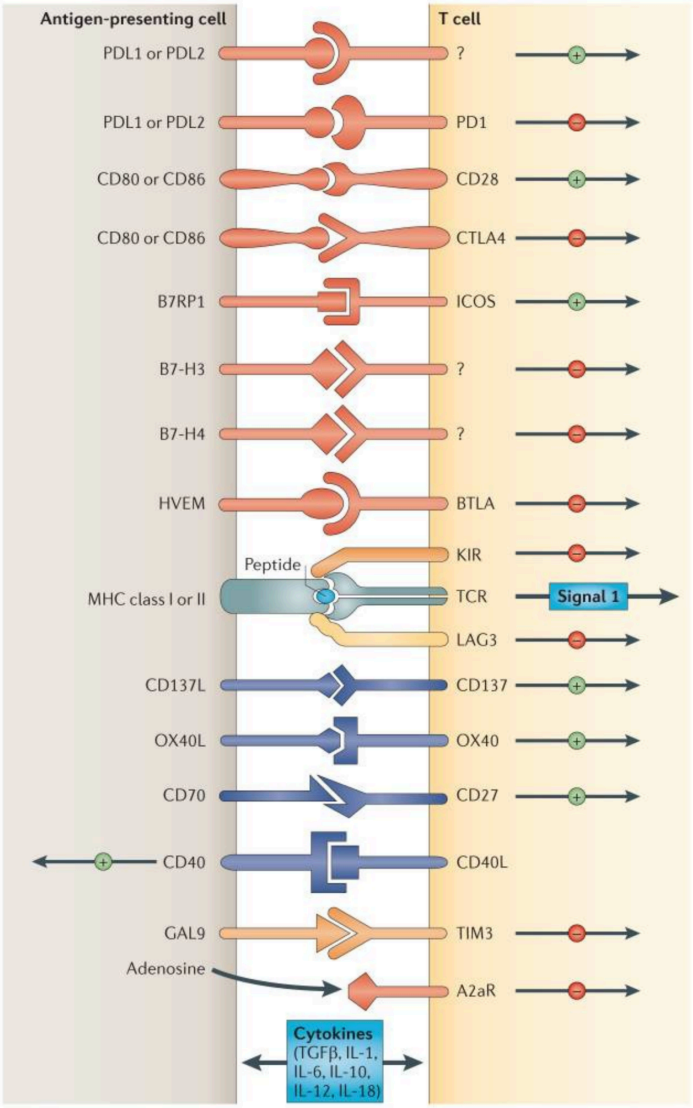

Figure 1.7. Key immune checkpoint proteins. Ligand-receptor interactions that mediate immune activation include co-stimulatory (green + arrows) and co-inhibitory (red – arrows) signals. Therapeutically targeting the PDL-1/PD1 and CD80 or CD86/CTLA4 interactions have been the most extensively investigated and are in clinical trials for GBM. Reprinted from Pardoll et al. 2012 (*140*).

The consequence of immune checkpoints extend beyond their functions in T-cells (adaptive immunity), and also influence innate immunity-mediated anti-tumor responses (*142*). Several immune checkpoints are also expressed and utilized in the activation of NK cells and TAMs, and recent studies shows that NK cells respond to PD1 and PDL-1 inhibition (*142, 143*). PD1/PD-L1 signaling mediates NK cell activation and cytotoxicity in certain tumors and can independently eradicate advanced tumors in the absence of CD8+ T-cells. Tumor–infiltrating NK cells acquire high levels of PD-L1 expression, resulting in impaired dendritic cell maturation and reduced tumor-specific CD8+ T-cell priming, and are associated with NK cell exhaustion (*144, 145*). TAMs also express PD-L1 and blocking the PD1/PD-L1 axis may enhance their independent antitumor activity (*146*). Thus, while significantly less is known immune checkpoints in innate immunity, recent evidence suggests these cell populations may be therapeutically mobilized to increase immune-mediated tumor cell death, similar to T-cells, thorugh immune checkpoint modulation.

In GBM, tumor cells and TAMs express ligands for immune checkpoint receptors and secrete immunosuppressive proteins (i.e. anti-inflammatory cytokines such as prostaglandin E2 [PGE2], TGFβ, indoleamine 2,3-dioxygenase [IDO], and IL-10). Prominent expression of PD-L1 (the ligand for PD1) has been found in 88% of patients with newly diagnosed GBM and in 72% of recurrent GBM tissue (*147*). These values are higher than in many other cancers (*141*). Variability of PD-L1 expression in GBM has been partially attributed to molecular subtypes, with the mesenchymal subtype demonstrating the highest expression of PD-L1 (*148*). Expression of PD-L1 has been found in the neoplastic GBM cells, circulating monocytes in GBM patients, and in TAMs (*149-152*). PD-L1/PD1 mediated immunosuppression appears to not be exclusive to GBM tumors, but is active in multiple CNS malignancies (*147, 153, 154*).

1.2.4 The current state of treatments for GBM.

An increased understanding of GBM heterogeneity and its microenvironment are already impacting therapy development for GBM. Targeted therapies are being assessed to harness tumor-specific antigens for selective cell death and to mediate responses in specific tumor niches, such as vascular proliferation. Meanwhile, immunotherapies are being actively investigated as new modalities to alter the tumor-immune interaction towards an anti-tumor response. Most recently, the possibility of therapeutically targeting TAMs as an anti-tumor mechanism has gained traction. Together, a combination of these tactics applied to the unique state of each person's tumor, will allow for personalized medicine in GBM.

One prominent category of anti-cancer treatment targets drugs directly at genetic, epigenetic and protein aberrations in malignant cells. Examples include small molecular weight receptor tyrosine kinase (RTK) inhibitors and monoclonal antibodies (mAbs) targeting EGFR and EGFRviii, such as erlotinib and cetuximab (*155*). While several agents in this category have shown anti-tumor effects in preclinical GBM models, they failed prolong survival in clinical trials. Signaling pathways activated by EGFR have also been tested as druggable vulnerabilities in GBM. These pathways include the phosphoinositide-3 kinase (PI3K)/ protein kinase B (AKT) pathway and the Ras/RAF/Mitogen-Activated Protein Kinase Kinase (MAPKK)/Mitogen-Activated Protein Kinase (MAPK) pathway. Again, inhibition of these pathways with agents including temsirolimus and everolimus showed promise in rodent GBM models, but had disappointing results when tested for clinical efficacy (*155*). Agents targeting MGMT to enhance temozolomide chemotherapy sensitivity have similarly not been clinically useful, but new antisense oligonucelide approaches may make MGMT a viable target in the future (*156, 157*).

As researchers are recognizing the GBM microenvironment as a strong regulator of tumor growth, therapeutically targeting specific elements of the tumor microenvironment has become another treatment strategy. Of the tumor microenvironment components, the vascular niche has received significant interest (*105, 158, 159*). Strategies to prevent angiogenesis include inhibition of VEGF, downstream signaling of VEGFR, and certain integrin receptors implicated in vascular development. The only current U.S. Food and Drug Administration (FDA) approved drug that directly influences tumor vasculature in GBM in bevacizumab, a humanized mAb that binds VEGF-A. In preclinical models, bevacizumab inhibits GBM growth. Early clinical trials with bevacizumab showed a significant decreased in the enhancing volume on MR imaging, leading to its rapid FDA approval. Unfortunately, two large phase 3 clinical trials have since demonstrated no survival benefit in patients with GBM following the addition of bevacizumab to standard of care therapy (*160, 161*). Pharmacological agents such as cediranib and enzastaurin that inhibit downstream signaling in the VEGF cascade also did not show improved efficacy over standard of care in phase 3 clincal trials (*162, 163*). Integrins are another family of cell surface proteins that are involved in vascular development and remodeling. Integrin inhibitors decreased tumor growth in preclinical GBM models, but showed no survival benefit in clinical trials (*164*). Thus, while the vascular niche is still considered a key microenvironment in GBM, therapeutically targeting it without patient stratification, and perhaps with suboptimal combinations of other therapies, has thus far failed.

Modulating the tumor-immune interaction is a current topic of interest in GBM treatment. Immunotherapies aim to harness the body's natural immune system to destroy tumor cells. Several types of immunotherapies exists including checkpoint inhibitors, immunogenic vaccines, and chimeric antigen receptor (CAR) T-cells (*139-141*). Immune checkpoint modulation is

typically achieved using mAbs to target key ligands and receptors (Fig. 1.6). In contrast, CAR T-cell therapies, employ exogenously generated host derived T-cells that express receptors engineered to selectively bind antigens on that patient's tumor. Lastly, in the cancer vaccine strategy, a patient is immunized with an antigen that is specific to their tumor. These approaches have demonstrated robust, durable responses in a broad spectrum in cancers and are approved by the FDA as therapeutic options in specific clinical scenarios.

In the setting of GBM, numerous immunotherapy trials have been completed or are ongoing (*111, 165*). Trials that have reached interim analyses or their end points have unfortunately shown little to no overall survival benefit in the entire test cohort. For example, the CheckMate-143 study showed promise in its early phase, but eventually failed to meet its endpoints, at least in part due to faulty response assessment (*165-167*). However, a durable response occurred in a small subset of the patients enrolled in the trial. Given the inter-tumoral heterogeneity characteristic of GBM, post hoc sub group analyses have been proposed and may shed light on subsets of GBM patients that will benefit from these therapies.

Recently, TAMs have been proposed as a potential therapeutic target in GBM (*114*). TAMs influence the entire immune response within the tumor microenvironment and impact the sensitivity of neoplastic cells to chemotherapies and radiation therapy (*79*). Thus, targeting TAMs can have a two-fold benefit: directly inhibit tumor growth and/or modify the tumor microenvironment in such a way that it becomes sensitized to other therapies. Techniques to modulate TAMs can alter their recruitment, survival, and activation state. Modulation of TAMs as therapeutic targets in numerous malignancies have been recently been reviewed (*120, 123, 168*). In glioma, inhibition of the CSF-1 receptor on TAMs decreased tumor volume and prolonged survival in a mouse GBM model (*129, 169*). Disrupting periostin signaling is another

avenue of TAM modulation that has shown potential therapeutic benefit preclinically. In mouse GBM models, periostin inhibition decreased the M2 polarized, pro-tumorigenic macrophage population (*170, 171*). Interestingly, several agents that are classically used as antibiotics, Amphotericin B and minocycline, have both shown benefits in GBM models by altering microglial activation and interaction with GBM stem cells (*172, 173*). As trials are ongoing, the clinical efficacy of modulating of TAMs remains unknown.

Despite these exciting new avenues of GBM therapy, efforts to advance care are hampered by a still incomplete understanding of the complexity of GBM: the tumor antigens, microenvironments within a tumor, immune-tumor interactions, and differences between tumors. A more thorough understanding of these elements is essential to develop novel therapeutic targets, understand how to most effectively utilize currently available therapies, and craft treatment strategies that will have the best efficacy for each individual patient.

1.3 Breast cancer brain metastases.

1.3.1 Brain metastasis overview.

While decades of research have begun to unravel the multifaceted biology of GBM, less is known about the complex landscape of metastatic tumors in the brain, which are 10 times more common than all primary malignant brain tumors combined. Brain metastases are almost uniformly fatal and occur in more than 20% of all cancers (*174*). However, this incidence rate may grossly underestimate the incidence of brain metastases as autopsy studies have shown the presence of metastatic brain lesions in up to 40% of subjects (*7*). Brain metastases occur most commonly in breast cancer, lung cancer, and melanoma. Within breast cancer brain metastasis,

the specific breast cancer subtype influences brain metastasis incidence, with HER2 positive and triple negative subtypes having the highest incidence rates and negatively impacting patient prognosis (*10, 175-178*).

The propensity of specific cancer types to selectively seed and colonize brain tissue highlights the organotropic nature of metastasis, and the fact that this is not a random process (*179*). The theory of organ specific metastasis by different types of malignancies is commonly explained by the "seed and soil" principle, which was first described by Stephen Paget in 1889. In this theory, the seed (a metastatic cancer cell) can only survival and grow in certain soils (tissue microenvironments), explaining the propensity of specific tumor cells for successful interactions with select organ microenvironments (*180*). This phenomenon highlights that cancer-stromal interactions play a key role in the process of metastasis.

1.3.2 Breast cancer heterogeneity and development of brain metastases.

Breast cancer heterogeneity.

Breast cancer is the most common cancer in women worldwide (*181*). Breast cancer is an umbrella term describing a heterogeneous collection of malignancies that share a tissue of origin, but vary in their clinical behavior, histological features, and molecular and genetic characteristics. Developing a unifying taxonomy for breast cancers continues to be a challenge (*182*).

Multiple classification systems based on these different features have been implemented over the past decade that have led to a current multidisciplinary classification approach (*183*). Conventionally, morphological and histological features defined by the WHO differentiated at

least 17 histological subtypes including infiltrating ductal and lobular carcinoma, tubular carcinoma, mucinous carcinoma, medullary carcinoma, invasive papillary carcinoma, and others (*184, 185*). Analyzing gene expression patterns subtyped breast cancers into 6 molecularly defined classes: basal-like, HER2 positive, normal breast-like, luminal A, luminal B, and luminal C. This subtyping method intrigued the scientific and clinical oncology communities as the resulting subtypes were associated with variable clinical outcomes and had implications for differing therapeutic sensitivities (*186*). As one of the primary rationales for subtyping cancers is to identify patient cohorts that have specific therapeutic sensitivities, breast cancers can also be classified based on the presence of absence of key actionable targets, such as tumor-specific receptors. Under this classification scheme, breast cancers are subdivided as triple negative (lacking expression of the estrogen receptor (ER), progesterone receptor (PR), and HER2), HER2 positive, luminal B, and luminal A. Of these subtypes, triple negative tumors have the worst prognosis and are typically treated with chemotherapies, HER2+ tumors have mixed prognoses and can be treated with targeted therapies such as trastuzumab, and the luminal B and A subtypes have the best prognoses and may be sensitive to endocrine-targeted therapeutic approaches as they are often ER and/or androgen receptor positive (*182*). The distinction of basal-like and luminal-like are also used in discussing breast cancer heterogeneity, and are categorized based on expression of cytokeratins present in basal cells and absent in luminal cells of the mammary duct tissue (*187*). While these do not perfectly line up with other classifications, basal-like tumors typically overlap with triple negative malignancies and share their poor prognosis, while luminal-like tumors overlap with the luminal molecular classes. Based on mixed expression of several specific cytokeratins, a basoluminal class has also been identified, of which many are HER2 positive (*188*). Recent advances in 'omic' technologies have further

complicated the sub classification of breast cancers. Numerous genetic mutation, transcriptomic, and epigenetic modification based classifications have been proposed (*189-191*). While these multiple methods complicate the sub classification of breast cancer, they have made breast cancer the optimal target for personalized medicine as therapies can more easily be targeted to multiple distinct characteristics of each tumor (*192*).

Of these classification systems, the receptor expression model has been primary assessed in the propensity of breast cancers to metastasize to the brain. The triple negative and HER2 positive subtypes most commonly result in metastatic brain lesions (*10, 11, 176-178, 193-195*). A recent population-based study on the incidence of brain metastases in newly diagnosed breast cancer found that of patients with metastasis at the initial time of breast cancer diagnosis, 11.5% of those with hormone receptor negative and 11.4% of patients with HER2 positive tumors had already established metastatic brain tumors (*175*).

Heterogeneity of metastatic tumors is further complicated by variances in molecular differences between the primary and metastatic tumors. Several groups have classified differences between metastatic brain tumors and their primary tumor counterparts (*196, 197*). These studies reveal that expression of cell surface receptors, such as EGFR and its ligand heparin-binding EGF (HB-EGF), likely contribute to the cells metastatic potential.

Breast cancer metastasis to the brain: the metastatic cascade.

The process of successful metastatic tumor formation follows a series of pathological steps known as the metastatic cascade (Fig. 1.8). The metastatic cascade consists of a series of sequential, interrelated steps that result in neoplastic cells from a primary tumor to seed, survive, and grow in a foreign tissue microenvironment (*7, 198*). The first stage of the metastatic cascade

occurs before tumor cells leave the primary tumor and is termed the "pre-colonization" phase of metastasis. During this phase changes occur in both the primary tumor cells and in distant tissue where future metastatic lesions can grow. In breast cancer, a pre metastatic change critical to tumor invasion and dissemination is the epithelial-mesenchymal transition (EMT) program in primary tumor cells. Physiologically, EMT is a developmental and wound healing process that can be hijacked by neoplastic cells (*199*). In malignant cells, EMT increases their invasiveness, motility, and ability to degrade stromal elements such as the ECM. EMT involves a loss of traditional epithelial cell properties, such as polarized expression of cell-cell adhesion and structural proteins (e.g. e-cadherin and certain cytokeratins), and acquisition of mesenchymal properties, such as a spindle-shaped morphology and increased expression of n-cadherin, vimentin, and the EMT promoting transcription factors Snail, Slug, Twist, and Zeb1 (*199, 200*). Similar to the evolving understanding of M1/M2 phenotype as a spectrum of macrophage polarization rather than clearly delineated cell types, the classification of neoplastic cells as epithelial or mesenchymal also operates along a continuum and malignant cells can identify as intermediate EMT states (*201*).

Concurrent with the genetic and epigenetic changes occurring in the cancer cells, future metastasis niches are conditioned and primed by soluble factors, including cytokines and exosomes, and infiltrating immune cells (*202, 203*) (*204*). Preclinical studies of breast cancer brain metastasis suggest that prior to seeding of malignant breast cancer cells in the brain there is increased infiltration of myeloid-derived cells mediated by elevated S100 calcium-binding protein (S100)-A9 (*204*). This generates a more hospitable environment for incoming breast cancer cells. Preclinical studies have also shown that malignant cells release growth factors, cytokines and extracellular vesicles that contain biologically activate microRNAs (mir), which

can alter endothelial cell properties in the BBB, enhancing the binding and brain transmigration of future intravascular metastatic cells (*205-207*).

The EMT properties acquired by breast cancer cells increase the release of stromal modifying factors, such as matrix metalloproteinases (MMPs), which enable cells to leave the primary tumor tissue and enter systemic vasculature (*208*). Tumor cells escape the primary tumor as single cells, small clusters of cells, or as a growing edge of the large bulk tumor, and then intravasate, entering the systemic circulatory system. Once in the blood stream, metastasizing cells, now termed circulating tumor cells (CTCs), are subject to extreme stressors such as shear forces, lack of adhesion, and different nutrients (*199*). CTCs can physically and functionally associate with platelets and monocytes to facilitate their survival and entry into distant tissues (*198, 199, 209-211*). Mechanical entrapment of CTC in small capillaries, which have a diameter of only 8μm, serves as the main mechanism by which CTC begin their invasion of foreign organs. Intravascularly arrested CTCs can actively extravasate between endothelial cells (transendothelial migration) or cause vessel rupture, leading to seeding of distal organs as single cells or emboli, respectively. The high proportion of total blood flow to the brain increases the exposure of CTCs to brain capillary beds (*7, 199, 212*).

In the brain, malignant cells must cross the BBB and components of the NVU to reach the brain parenchyma. Several signaling molecules including the sialyltransferase enzyme ST6GALNAC5, cathepsin S, mir-105, and mir-181c have been found to mediate the ability of metastatic cells to breach the BBB by increasing adhesion to or destruction of the endothelium (*196, 207, 213, 214*). Metastatic cells can also increase intracellular signaling pathways, such as Src signaling, which stimulate the production and release of factors that break down the BBB and its basement membrane components (*215-217*). Gene expression and proteomic studies of

breast cancer cells destined for the brain show increased expression of multiple genes and proteins that improve their ability to traverse the BBB (*196*, *213*).

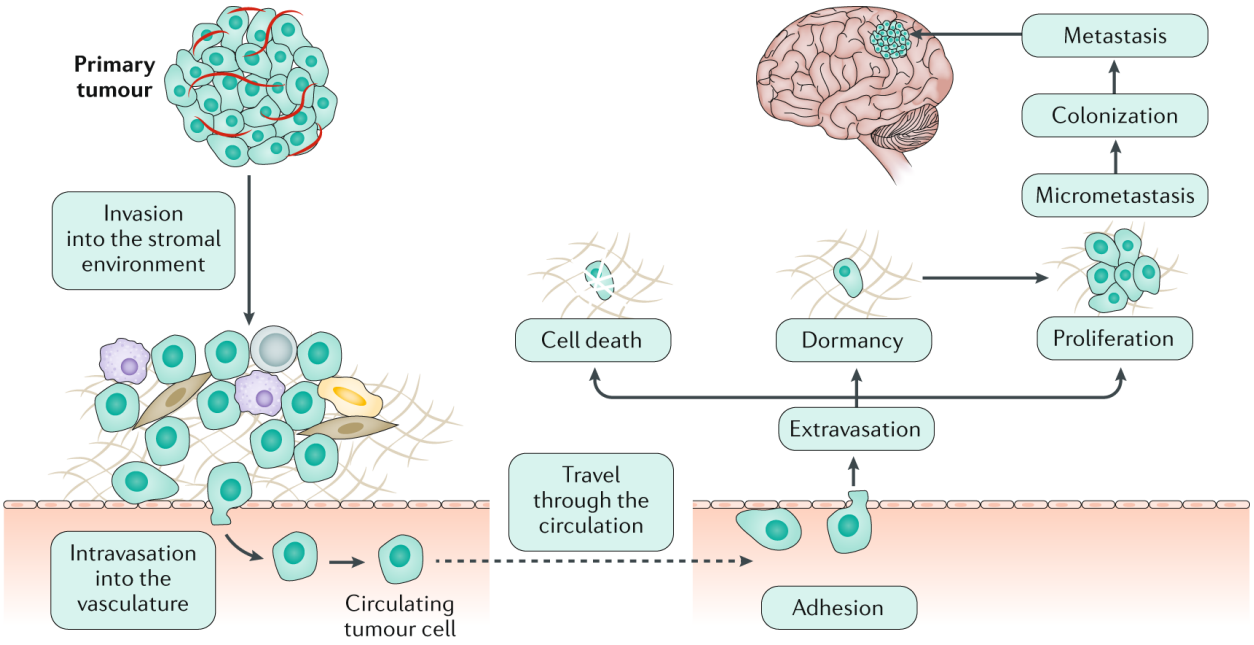

Figure 1.8 The metastatic cascade leading to successful formation of brain tumors. Breast cancer metastasis to the brain follows a series of steps known as the metastatic cascade. These steps include changes within the primary tumor to the neoplastic cells and their microenvironment, priming of the pre-metastatic niche, dissemination of primary tumor cells, seeding of distant organs, and growth of metastasized tumor cells in the brain. Reprinted from Achrol et al 2019 (*7*).

Once metastatic cells have seeded a distant organ they are termed disseminated tumor cells (DTCs). Upon initial entry of DTCs into new tissue microenvironments, the malignant cells must survive a new set of pressure and stressors; the vast majority of metastasizing cells perish at this point. Rodent models of the metastatic cascade suggest that more than 90% of tumor cells

that enter the brain disappear within 1 week (*218, 219*). As previously described herein, the CNS is known to have an active immune system. It has been proposed that immune surveillance significantly contributes to the high attrition rate of metastasizing cells in the brain. Local CNS cells, including microglia and astrocytes, have also been shown to interact with metastatic cells upon brain entry in both pro- and anti-tumorigenic fashions. Valiente et al. 2014 demonstrated that astrocytes secrete serine protease plasminogen activator, which ultimately functions to initiate apoptosis in infiltrating cancer cells. However, the invading metastatic cancer cells, similar to GBM cells, can secrete immune inhibiting factors that alter their new microenvironment to a more hospitable niche to overcome local anti-tumor reseponses (*220, 221*). For example, tumor cells can stimulate the production and release of MMPs from astrocytes and proteinase cathepsin S from macrophages, both of which alter the brain microenvironment to become a more favorable niche for breast cancer survival and growth (*213, 221*).

Once DTCs set up a favorable pro-tumorigenic environment, they are able to survive dormant in the brain for years to decades and grow into overt, clinically significant metastases. Established metastatic tumors continue to release self-survival signals, modify the activation state of local and immune cells, and develop resistance pathways to therapeutic insults. Metastatic breast cancer can reside as single cells or small clusters within the perivascular niche in a state of dormancy in the brain for long periods of time, even years (*218, 219, 222*). It has been proposed that perivascular-specific microenvironmental factors such as thrombospondin 1 may actively signal infiltrating cells to survive in a dormant state in this location (*219*). Recent reports suggest that pharmacologically targeting metastatic cells in the perivascular niche can increase their sensitivity to chemotherapy (*223*). In other metastatic tumor sites, modulation of

immune cell reactions to cancer cells contributes to maintenance of dormant metastatic cell populations, however this has not yet been assessed in the context of brain metastasis (*199*). Clinically, understanding the dormant niche is critical as it may be a critical cellular reservoir responsible for delayed relapse in patients with no other evidence of clinical disease following treatment for their primary tumors. The specific signals that activate dormant metastatic breast cancer cells in the brain remain unclear.

Actively growing metastatic tumors in the brain contain diverse intra-tumoral regions, analogous to the intra-tumoral heterogeneity in GBM. Metastatic tumors have a more defined leading edge than GBMs, as exemplified by their clear delineation on MR imaging. At this tumor/brain interface, the malignant cells are in close proximity to resident brain cells including astrocytes, microglia, and neurons. Meanwhile, in the bulk tumor, malignant cells encounter regions of increased angiogenesis, hypoxia, and necrosis.

Understanding the cellular signaling pathways that control metastatic cell (1) survival in the brain, (2) dormancy, (3) and overt outgrowth into the brain parenchyma will aid in developing therapeutic options for tumors at different stages of metastasis. In this dissertation I focus on factors contributing to outgrowth of established tumors, as the majority of clinical cases present at this stage.

1.3.3 The microenvironment of breast cancer brain metastases.

Overview of the metastatic brain tumor microenvironment.

Similar to GBM, the microenvironment of metastatic brain tumors influence the tumor's survival, local invasiveness, and therapeutic sensitivity/resistance. The interactions between the

tumor and its microenvironment are bidirectional, with the malignant cells impacting the non-malignant CNS cells, and vice versa. As in GBM, the malignant cells primarily interact with astrocytes, microglia, endothelial cells, pericytes, neurons, infiltrating immune cells and ECM (*224*). Developing a more thorough understanding of the heterogeneous microenvironment interactions in brain metastases will aid in the development of personalized treatment approaches for these tumors.

Components of the CNS microenvironment in breast cancer brain metastases.

Astrocytes have multiple pro- and anti-tumorigenic effects on breast cancer brain metastasis. In nearly all brain metastases there is significant astrogliosis in the peritumoral brain and moderate, but more variable, astrogliosis within the bulk tumor (*225*). Reactive astrocytes interact with the breast cancer cells through secreted factors and direct physical contact (*226-229*). Factors secreted by astrocytes that activate oncogenic signaling pathways in carcinoma cells and/or degrade ECM to permit cell invasion include IL6, TGFβ, interferon α (IFNα), TNF, MMP2, MMP9, and growth factors (*226, 228-230*). In murine models of brain metastasis, inhibiting several of these factors, such as IL-6, that can initiate the production and release of additional cytokines that in turn elicit anti-tumor effects (*230, 231*). Murine models have also been used to assess physical contact between astrocytes and breast cancer cells that promote tumor survival and growth. These studies have shown that functional gap junctions composed of Connexin-43 exisit between astrocytes and breast cancer cells in the brain and allow passage of tumor promoting metabolites directly between the cytoplasm of the two cells (*229*). Inhibiting these gap junctions with meclofenamate and tonabersat decreased the formation of breast cancer brain metastases and shrank established metastatic lesions. The direct and indirect interactions of

astrocytes and breast cancer cells increase the expression of survival genes, including signal transducer and activator of transcription 5 (STAT5), B-cell lymphoma 2 (BCL2)-L1, and twist-related protein 1 (TWIST1), and contribute to therapeutic resistance (*232, 233*). Subsets of astrocyte populations secrete cytokines that upregulates EGFR signaling in cancer cells in response to estrogen, ultimately leading to increased S100A4 that in turn promotes tissue invasive cellular behaviors (*234*). Astrocytes also exhibit anti-tumor responses. For example, astrocytes can release exosomes containing miRNAs that inhibit tumor growth (*235*). The multifaceted roles of astrocytes in the setting of breast cancer brain metastasis remain incompletely understood, but pre-clinical evidence collected to date demonstrates that they are significant contributors to tumor growth and therapeutic sensitivity.

Microglia and macrophages are important elements of the metastatic brain tumor microenvironment and cluster around metastatic brain tumors in murine models and human tumors (*221, 225, 236, 237*). Less is known about the role of TAMs than astrocytes in metastatic brain tumors. Lineage tracing experiments, with corroboration of cell-specific protein expression in human brain metastasis samples, have shown that both local microglia and bone marrow derived macrophages infiltrate metastatic brain tumors (*238*). Potential differing roles of these cells in metastatic tumors are areas of active investigation. In the metastatic brain tumor microenvironment, TAMs are activated by several extracellular factors, including relaxins, chondroitin sulfate, proteoglycans and neurotropin 3, produced by the tumor cells (*239-242*). Numerous reports suggest that TAMs preferentially develop an M2 polarization phenotype, which impairs further anti-tumor immune responses (*242-245*). However, recent experimental evidence suggests that both M1 and M2 TAM populations are present in metastatic tumors, and that selectively eliminating the M2 TAM population in a murine models elicits anti-tumor effects

(*246*). One mechanism by which TAMs promote brain colonization is by increasing Wnt signaling in malignant cells (*242*). Opposingly, increased production of MMPs and angiostatin by TAMs in response to tumor produced granulocyte-macrophage colony-stimulating factor (GM-CSF) suppressed tumor growth (*247*). TAMs have also been found to influence BBB and phagocytose fragments of damaged vasculature (*248, 249*). Similar to vascular mimicry by neoplastic cells in GBMs, TAMs appear to have a vascular mimicry capacity within metastatic lesions. Increased expression of E-cadherin allows TAMs to transiently form functional vessels in tumors (*249*). Despite these advances and ongoing studies, the mechanisms that dictate TAM phenotype in brain metastases and the ability of TAMs to alter tumor growth remain largely uncharacterized.

Very little is known about the interactions of metastatic cells with neurons. One report found that breast cancer cells in the CNS mimic neuronal properties, such as expression of gamma-aminobutyric acid receptors, which increases malignant cell proliferation (*250*). Metastatic cells have also been found to cause neuronal cell death, but experimental models show neuronal function can be maintain by modulating the cytokine pigment epithelium–derived factor (*251*).

Interactions between invading malignant cells and tumor vasculature has been more thoroughly studies than interactions with resident brain cells, as the tumor-vasculature relationship is critically involved in metastatic cell seeding and tumor growth. Early in metastatic tumor development, invading cancer cells reside in the perivascular niche where they adhere to and travel/grow along the abluminal side of vasculature (*218, 221, 252*). Here, tumor cells bind vascular basement membrane components via cell surface receptors, such as β1-integrin, which impact cell survival during the brain colonization phase of tumor development (*252*). As the

protein composition of both the vascular basement membrane and endothelial cell itself differs in CNS and breast tissues, malignant cells likely utilize a different set of cell surface receptors for optimal interactions as they invade the brain (*83*). Furthermore, experimental models suggest that protein composition in the brain's vascular niche change throughout metastatic tumor progression and that this variable protein expression can be targeted to inhibit tumor growth. For instance, the expression of proteins including E-selectin, vascular cell adhesion protein (VCAM)-1, activated leukocyte cell adhesion molecular (ALCAM), intracellular adhesion molecule (ICAM)-1, very late antigen (VLA)-4, and β4 integrin were markedly increased on endothelial cells early in tumor seeding, and inhibiting ALCAM and VLA-4 decreased the number of metastatic tumors in murine models (*253*). The vascular co-option displayed by metastatic tumor cells is also mediated by serpins, which influences the expression of L1 cell adhesion molecule (L1CAM), and present another potential point for therapeutic intervention (*220*). Pericytes are another important cell in cerebral vasculature that influence the vascularization of metastatic tumors, integrity of the BBB in these tumors, and tumor dormancy (*219, 254*). The intricate interactions of invading tumor cells with existing vasculature and neovasculature elements within the tumor alters BBB properties. As in GBM, the permeability of brain metastases is inconsistent and can vary between tumors and within a single tumor, which can be seen by multiple imaging modalities (*109, 255-257*). Different subtypes of breast cancer have different effects on BBB integrity. Metastatic brain tumors of the HER2 positive breast cancer subtype have a more intact BBB than tumors of the triple negative breast cancer subtype (*258*). The variable BBB permeability in metastatic tumors have been proposed as a cause of therapeutic failures in brain metastases (*259*). Key differences between a healthy BBB and the BBB/BTB in metastatic brain tumors include: increased VEGF, swollen endothelial cells, altered

expression of junctional proteins, cytokine receptors, and transporters by endothelial cells, varied basement membrane composition, presence of reactive microglia and astrocytes, altered expression of aquaporin 4 on astrocyte endfeet, and altered pericyte phenotypes (*7, 254*).

Infiltration of systemic immune cells into metastatic brain tumors is variable and remains incompletely characterized in metastatic breast cancer. Rare CD8+ cytotoxic T-lymphocytes, CD4+ T-cells, and B-cells can be present (*153, 236*). Comparing brain metastases with their matched primary breast tumors, T-cell infiltration is significantly lower in the metastatic tumors than in primary tumors (*260*). Within metastatic brain tumors, those with higher numbers of T-lymphocyte infiltration had longer overall survival. While analyses of immune checkpoints expression have been limited, expression of PD1/PD-L1 appears to be common in brain metastases, irrespective of tumor subtype (*153*).

Breast cancer cell surface receptor exploited in CNS microenvironment interactions.

Metastatic cancer cells interact with cellular and extracellular brain microenvironment components through cell surface receptors. Understanding the specific roles of key surface receptors on malignant cells in the metastatic niche is essential as they provide therapeutic targets. Two key families of cell surface receptors involved metastatic cancer progression are integrins and growth factor receptors. Integrins are cell membrane proteins that classically bind ECM, and have been implicated in nearly every step of cancer progression and metastasis (*261-263*). Similarly, growth factor receptor signaling is altered in many malignancies and their metastatic complications. Growth factor receptors, as their name implies, respond to growth factors in the tumor microenvironment, activating numerous intracellular signaling pathways that regulate cell fate, proliferation, and motility.

Integrins are heterodimeric transmembrane receptors that consist of an α and β subunit (*264*). At present, 18α and 8β subunits have been identified that can form 24 functional heterodimers. These heterodimeric integrins facilitate bi-directional signaling between extra- and intracellular environments that are capable of inside-out and outside-in signal transmission across the cell membrane (*261, 262*). Several integrins bind only one ECM ligand, but most integrin heterodimers can bind multiple ECM proteins that contain similar motifs within the protein structure. For example, αvβ3-integrin binds vitronectin, fibronection, thrombospondin and others. Integrins are grouped into classes based on their ligand preferences. The four classes of integrins are receptors that recognize Arg-Gly-Asp (RGD) peptide motifs (that are present in several ECM components), laminin receptors, collagen receptors, and integrins that are expressed solely in leukocytes (*264*). Upon ligand binding or activation through intracellular signals, integrins form clusters on the cell membrane. These clusters can function as signaling platforms, which recruit modulators of variable downstream signaling cascades that control cellular behaviors including survival, motility, invasiveness, and cell division. The dynamics of integrin recycling between the cell membrane and intracellular compartments, and localized expression of integrins on specific cell membrane features contribute to the diverse signaling cascades they activate (*265, 266*).

In cancer, integrins are associated with nearly all phases of disease progression and metastasis including metastatic niche priming, therapeutic resistance/sensitivity, and malignant cell migration, invasion, survival, stemness, dormancy, extravasation in foreign tissue, and outgrowth (Fig. 1.9) (*261, 263*). In particular, the αv subunit and the αvβ3 heterodimer are associated with breast cancer brain metastasis. The αv-integrins are frequently overexpressed in metastases (*267-270*), and influence cancer cell survival, proliferation, migration and invasion

(*271-273*). Activation of αvβ3-integrin promotes tumor angiogenesis and metastatic growth in mouse brain (*274*), while transcriptional silencing of this integrin with MYC decreases migration and invasion of breast cancer cells *in vitro* and *in vivo* (*275*). Integrin-αvβ3 has several known ECM ligands that are expressed around cerebral vasculature (*83*), giving this receptor the potential to coordinate interactions with the brain perivascular microenvironment. Non-ECM soluble factors, such as Gal3, which has been identified in the brain microenvironment, can also cause clustering and activation of αvβ3-integrin (*276-281*). In preclinical models, targeting αv with the monoclonal antibody intetumumab or αvβ3- and αvβ5-integrins with the cyclic peptide cilengitide have shown anti-tumor effects as well as metastasis prevention activity (*282-284*). However, in clinical trials, intetumumab and cilengitide have demonstrated minimal therapeutic efficacy inducing tumor cell death in metastases (*285-287*). The inadequacies of current therapy emphasize the need to precisely understand the tumor-specific biology and signaling within the brain niche so that suitable biomarkers and therapeutic strategies can be developed.

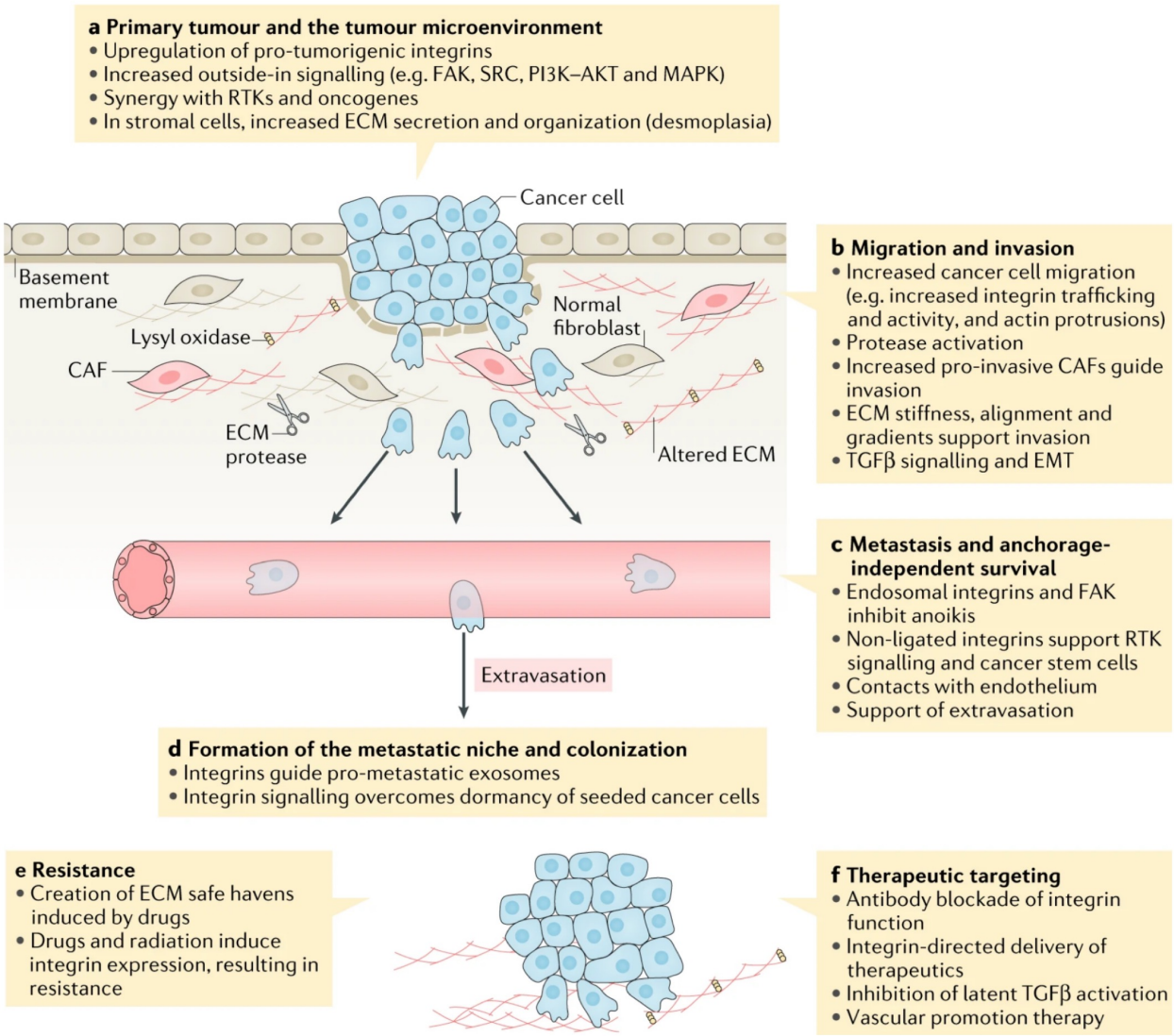

Figure 1.9. The multi-faceted roles of integrins in cancer metastasis. Integrins are involved in tumor-microenvironment interactions, migration/invasion, metastasis, and therapeutic sensitivity. Reprinted from Hamidi & Ivaska 2018 (*261*).

Growth factor receptors are another family of cell surface proteins expressed by metastatic cells that regulate important tumorigenic interactions between the malignant cells and their microenvironment. Numerous growth factor receptors including EGFR, HER2, PDGFR, insulin like growth factor 1 receptor (IGF1R), and insulin like growth factor 2 receptor (IGF2R)

have been implicated in metastatic progression. In the setting of breast cancer brain metastasis, the role of the growth factor receptor HER2 in tumor establishment and growth is particularly intriguing given the high proficiency of HER2 positive breast cancers to metastasize to the brain; up to 30% of patients with HER2 positive breast cancers develop brain metastases.

HER2, a member of the EGFR RTK family (ERBB1-4, also termed EGFR, HER2, HER3, and HER4), is an orphan RTK overexpressed in some breast cancers. Activation of most RTKs is initiated by binding their respective growth factor ligand(s). HER2 is the exception, as it has no known ligand. Receptor activation leads to oligomerization with adjacent growth factor receptor monomers, trans-autophosphorylation of their intracellular domains, and induction of variable intracellular signaling cascades. Specific ligand binding selectivity is dictated by the homo- and heterodimer receptor composition (Fig. 1.10).

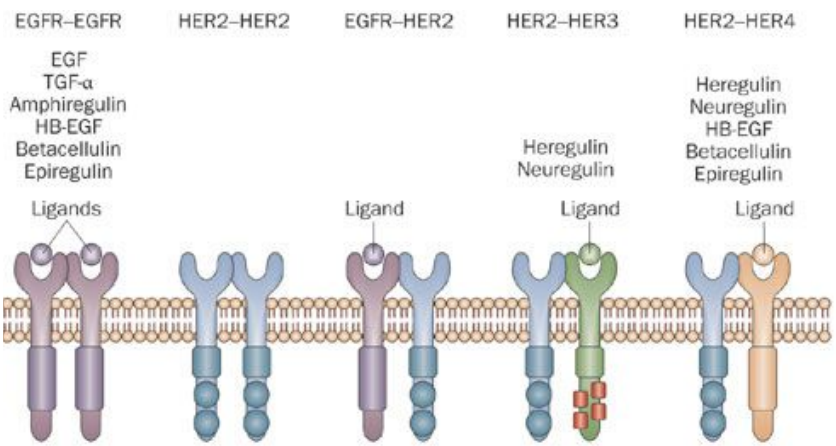

Figure 1.10. Ligand - receptor interactions in the EGFR family. Homo-and hetero-dimers have differential ligand bindings capacities (*288*). Reprinted from Linardou et al. 2009.

In the setting of breast cancer brain metastasis all members of the EGFR family have been implicated in some fashion (*289*). Similar to correlative studies showing increased brain metastasis in HER2 positive breast cancer, primary breast cancers that express EGFR have also

been found to have increased incidence of brain metastasis (*11, 290*). Analysis of clinical breast cancer brain metastasis samples have shown that 39% of the tumors express EGFR, and that compared to primary breast tumors, EGFR expression is increased in brain metastases (*291, 292*). Expression of HER3 is also significantly higher in brain metastases than in primary breast tumors (*293*). A possible contributing factor to this selection the high expression of neuregulin (NRG1) in the brain, which is the ligand for HER3. Ligands for EGFR are present in the brain and in the brain tumor microenvironment, including EGF and HB-EGF. Differential gene expression analyses have implicated HB-EGF in specifically mediating breast cancer metastasis to the brain, compared to metastasis to other organs (*196*). In contrast to the other members of the EGFR family, HER4 expression is down regulated in breast cancer brain metastases compared to primary breast tumors (*197*).

RTKs have been shown to physically and functionally interact with in cancer cells, and in doing so promote metastatic cellular behaviors and drug resistance (*294*). Interactions of integrins with growth factor receptors including PDGFR, EGFR, hepatocyte growth factor receptor (HGFR), and VEGF receptor (VEGFR) can induce growth factor receptor activation even in the absence of growth factor bindings (*215, 294-298*). Further exploring the relationship between cell surface receptors known to be upregulated in brain metastasis and able to mediated microenvironment interactions has the potential to open up new therapeutic avenues.

1.3.4. Advancing treatments for breast cancer brain metastases.

Current treatments for breast cancer brain metastases are similar to those employed in treatment of GBM including cytotoxic chemotherapy and radiation therapy, with stereotactic

radiosurgery used in well-defined lesions (*7*). Surgical resection is used if there are three or fewer metastatic lesions, but patients often have a large number of dispersed lesions (*299*). Unfortunately, outcomes remain dismal for brain metastases, with the overall survival after initial diagnosis of brain metastasis from HER2 positive breast cancer being 16.5 months (*300*). Several factors have hampered improving effective therapies for breast cancer brain metastases including: poor penetrance of therapeutics across the BBB, differing actionable mutations across patients, molecular heterogeneity within the tumor, and protective effects of the tumor microenvironment.

Therapies for breast cancer brain metastasis falls into two broad categories: preventing the formation of metastases in high-risk patients with systemic disease and shrinking established brain lesions (*301*). Prevention strategies can target nearly every step of the metastatic cascade, including disrupting CTCs, blocking CTC binding to brain vasculature, inhibiting CTC translocation into the brain parenchyma, and maintaining the DTCs in a dormant state. Specific targets include proteins with upregulated expression in metastatic tumors compared to their primary tumor counterparts and/or proteins known to confer an increased risk of neurotropic metastasis. Treatment of micrometastases and clinically overt metastases could target mutations that alter key cellular signaling pathways and cell viability, functional interactions between the malignant cells and their brain microenvironment, and soluble factors and exosomes that mediate perivascular tumor dissemination and interaction with the CNS niche. Recent advances in genomic techniques have allowed improved characterization of metastatic tumors, revealing that 53% of brain metastases harbor pharmacologically actionable mutations not present in their matched primary tumors (*302*).

Targeted therapeutics, such as inhibitors of HER2, are effective in systemic breast cancer, but these have limited efficacy in brain metastases (*303-306*). Anti-HER2 drugs include low molecular weight RTK inhibitors such as lapatinib and neratinib, mAbs such as trastuzumab (Herceptin), and antibody-drug conjugates such as azo-trastuzumab emtansine (*307*). To date, anti-tumor effects from these drugs on metastatic lesions have been modest at best. Trastuzumab is unable to cross the intact BBB and has poor penetrance across the BTB (*303-306*). Slightly improved trastuzumab CNS penetrance can be achieved following BBB disruption with radiation therapy, increasing CSF to plasma levels from 1:420 to 1:76 (*305*). Intrathecal administration of trastuzumab in combination with pertuzumab has also been tested as a method to circumvent the BBB, and results are pending (NCT02598427). Both lapatinib and neratinib are able to cross the BBB. Results of clinical trials with lapatinib have been mixed and ongoing trails are evaluating the efficacy of neratinib in combination with chemotherapy treat treatment of metastatic brain tumors (*308*).

Integrins present druggable targets in brain metastases. Integrin $\alpha v\beta 3$ can be inhibited with the small molecular inhibitor cilengitide. Cilengitide was original evaluated in CNS malignancies for treatment of gliomas, where it failed to show efficacy in phase III trials (*164*). Despite this failure, preclinical work suggests that cilengitide may be efficacious in preventing the spread of metastatic tumors in the brain, administered alone and/or in combination with other agents including radioimmunotherapy (*282, 287, 309*).

Interrupting pro-tumorigenic interactions between the malignant cells and the brain tumor microenvironment may block processes that are indispensable for tumor survival and growth. Druggable aspects of this complex milieu include angiogenesis, the dysfunctional BBB/BTB, and direct and indirect bidirectional communication between malignant cells and reactive

microglia and astrocytes, neurons, endothelial cells, and infiltrating leukocytes (Fig. 1.11) (*7, 301*). Modulators of several of these interactions have entered clinical trials (*7*). While immunotherapies have been studied in melanoma and non-small cell lung cancer (NSCLC) brain metastases, less is known about the influence of immunotherapies in breast cancer metastases.

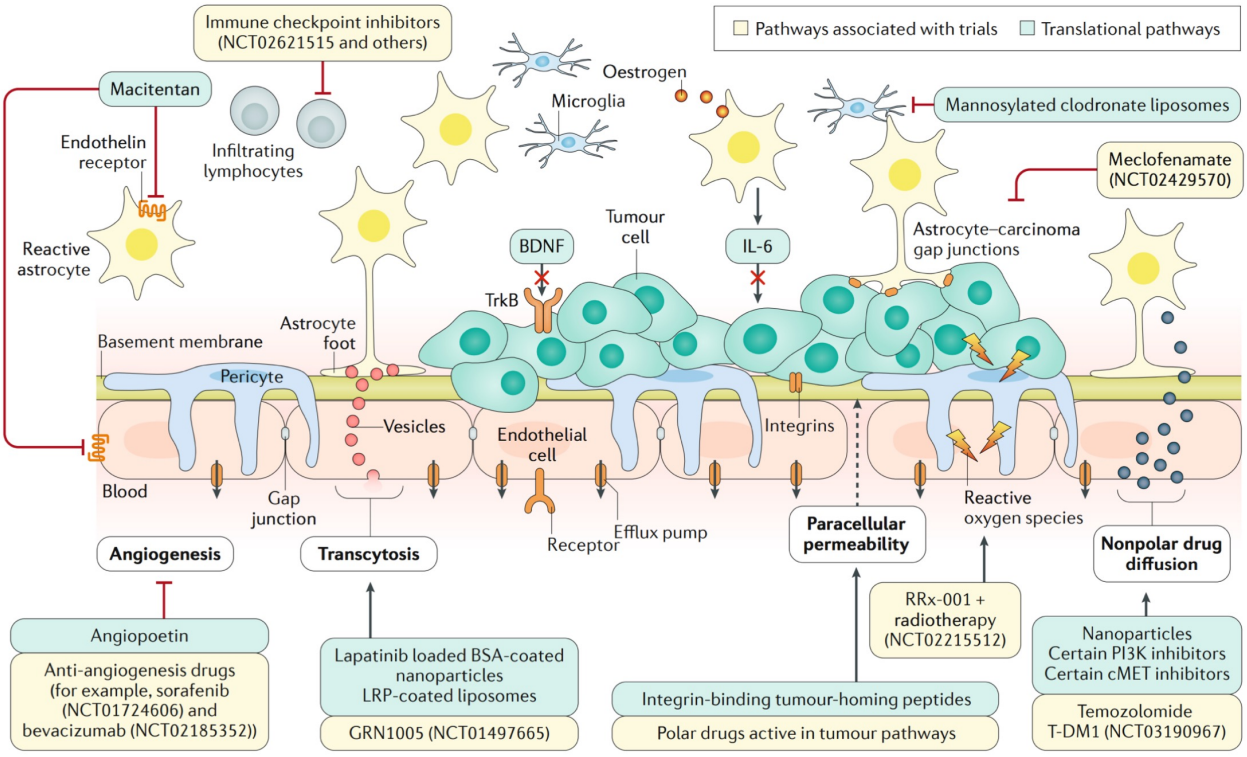

Figure 1.11. Targeting the tumor microenvironment in brain metastasis. Therapeutic strategies to control brain tumors through modulation of the brain tumor microenvironment and microenvironment molecular interactions with malignant cells are in various phases of preclinical and clinical development. Yellow boxes: agents being investigated for efficacy preclinically. Green boxes: inhibitors currently in clinical trials. Reprinted from Achrol et al. 2019 (*7*).

1.4 Remaining challenges in developing personalized treatment for CNS tumors.

While significant work has been done to begin characterizing malignant brain tumors and their microenvironment, several barriers remain and prevent the translation of novel findings to improved patient care. In GBM, the influence of intra-tumoral heterogeneity on tumor assessment hinders our ability to reliably characterize tumors. Furthermore, evaluating this variability currently require invasive techniques that do not permit assessment of the whole tumor across space and time. In breast cancer brain metastases, interactions between the tumor cells and their microenvironment are emerging as significant drivers of tumor progression, yet remain incompletely characterized. Furthermore, the potential interactions between proteins overexpressed in neurotropic breast cancer and the brain microenvironment have been minimally explored, and these molecular interactions may provide biological explanations for the success of certain cancers to colonize the brain and present novel therapeutic targets.

In this dissertation I address these remaining problems in CNS malignancies. Chapters two and three aim to identify new methods to assess the heterogeneity of GBM and develop non-invasive techniques to evaluate tumor characteristics including the immune microenvironment. Chapter four investigates how expression of cell surface receptors on metastatic breast cancer cells promotes pro-tumorigenic interactions with the brain microenvironment. Together, these findings will aid in the continued development of personalized medicine approaches for GBM and metastatic brain tumors by providing improved tools for tumor assessment and increased knowledge of the complex biological interactions critical for tumor progression.

CHAPTER 2: INTRA-TUMORAL HETEROGENEITY IN GLIOBLASTOMA IMPACTS THE UTILITY OF PREDICTIVE AND PROGNOSTIC GENE SIGNATURES.

Authors: **Cymon N. Kersch[1]**†, Cheryl J. Claunch[2]†, Prakash Ambady[1], Elmar Bucher[2], Daniel L. Schwartz[3], Tyler Risom[4]‡, Ramon F. Barajas Jr.[5], Jeffrey J. Iliff[6], Laura Heiser[2], Leslie L. Muldoon[1], James E. Korkola[2], Joe W. Gray[2], Edward A. Neuwelt[1,7,8]

Affiliations:

[1]Department of Neurology, Blood-Brain Barrier Program, Oregon Health and Sciences University, Portland, OR 97239, USA.

[2] Department of Biomedical Engineering, Knight Cancer Institute, OHSU Center for Spatial Systems Biomedicine, Oregon Health and Sciences University, Portland, OR 97239, USA.

[3] Advanced Imaging Research Center, Oregon Health and Sciences University, Portland, OR 97239, USA.

[4] Department of Molecular and Medical Genetics, Oregon Health and Sciences University, Portland, OR 97239, USA.

[5] Department of Radiology, Oregon Health and Sciences University, Portland, OR 97239, USA.

[6] Department of Anesthesiology, Oregon Health and Sciences University, Portland, OR 97239, USA.

[7] Department of Neurosurgery, Oregon Health and Sciences University, Portland, OR 97239, USA.

[8] Office of Research and Development, Department of Veterans Affairs Medical Center, Portland, OR 97239, USA.

†These authors contributed equally to this work.

‡ Current address: Department of Pathology, Stanford University, Stanford, CA 94305, USA.

Manuscript in preparation.

Important notes: Text and data within this chapter will also appear in the dissertation of Cheryl Claunch, PhD due to the collaborative nature of the project and the significant, equal contributions in project creation, hypothesis generation, analysis design, results interpretation, and manuscript writing and editing.

2.1. Abstract

Glioblastoma multiforme (GBM) are rapidly fatal, extremely diverse tumors that exhibit both intra- and inter-tumoral heterogeneity. To improve outcomes, personalized treatment strategies are needed. Personalized treatment of GBM will require tumor stratification into subtypes that differ in therapeutic vulnerability and outcome. To date, GBM stratification has been hampered by immense intra-tumoral heterogeneity, limiting our ability to compare tumors in a consistent manner. In the present study we used open-source transcriptional profiles of predefined histological structures from human GBM to develop methods that mitigate the impact of intra-tumoral heterogeneity on transcriptomic-based patient stratification. We show that intra-tumoral histologic architecture influences tumor classification when assessing established gene signatures for subtyping and prognostic marker development, and that using mixed structure samples, which are classically used for these types of studies, can give misleading results. We identify the cellular tumor as a GBM structure from which transcriptional subtyping and prognostic strategies can be applied to more accurately stratify patient cohorts. We analyzed this specific architecture to create an improved risk stratification tool. Our results highlight that biomarker performance for diagnostics, prognostics, and prediction of therapeutic response can be improved by analyzing transcriptional profiles in pure cellular tumor, which is a critical step toward developing personalized treatment for GBM.

2.2. Introduction

GBM, grade IV gliomas, are the most common and aggressive malignant primary brain tumor, with a median survival of only 18.1 months (*1*). Efforts to improve survival are hindered

by the current inability to stratify GBMs into groups with differential sensitivity to therapy (chemoradiotherapy [CRT], immunotherapies, and targeted therapies), and to identify patients with the highest risk of rapid disease progression. Being able to identify patient cohorts with similar GBM tumors would improve clinical decision-making, design of clinical trials, preclinical therapeutic development, and ultimately patient outcomes.

Stratification of GBM is particularly challenging because these tumors display complex multilayered inter- and intra-tumoral heterogeneity, as their name "multiforme" implies(*23, 310*). Current clinical stratification methods include: extent of resection, Karnofsky Performance Score (KPS), age, O^6-methylguanine-DNA methyltransferase (MGMT) promoter methylation, and isocitrate dehydrogenase 1 (IDH1) mutation, none of which capture the intricate molecular and heterogeneous landscape of GBM (*13, 39, 311-314*). However, modern 'omic' technologies, such as high-throughput genomic, transcriptomic, and proteomic profiling enable new approaches for tumor subset identification. Omic analyses of GBM samples from The Cancer Genome Atlas (TCGA) defined four molecular subtypes: classical, neural, proneural, and mesenchymal(*25*). However, these subtypes and subsequent prognostic gene signatures have not found clinical utility.

We explore the hypothesis that GBM's intra-tumoral heterogeneity has impeded the development of robust molecular tools for patient stratification in this tumor type due to sampling regions that differ in histological structure composition. Nearly all omic studies investigating GBM have used samples collected with little regard for histological structure other than necrosis (*22*). This methodology captures non-uniform, varying amounts of histologically diverse tissue architecture composed of cancer cells, stromal cells, vasculature, immune infiltration, and some necrosis. Samples that contain a mixture of these elements may obscure

detection of key tumorigenic processes enriched or depleted in specific tumor microenvironments. This histologic heterogeneity likely interferes with inter-patient comparisons when biopsies are composed of inconsistent tissue architecture.

In the present study we show that characterizing transcriptional patterns in intra-tumoral heterogeneity enables identification of a consistent histologic region that can be assayed to improve inter-patient comparisons. Specifically, we demonstrate that (1) histologic structures within a tumor are molecularly distinct and that variations in histology confound results of established gene signatures created from mixed structure samples, and (2) focusing specifically on the dense cellular tumor histological structure improves both GBM subtyping into biologically distinct cohorts and patient risk stratification that are more strongly associated with clinical outcome. These advances will guide the future development of personalized medicine approaches for GBM and enhance prognostics to identify patients with the highest risk of rapid progression.

2.3. Methods

Data sets. The analyses described herein were performed on either the Ivy Glioblastoma Atlas Project (IvyGAP) or The Cancer Genome Atlas (TCGA) dataset with described processing steps.

IvyGAP. We mined RNA-sequencing data from the open-source Ivy Glioblastoma Atlas Project (Allen Brain Institute) and Swedish IvyGAP Database for clinical data. A detailed explanation of the methods used to generate these data are available (http://glioblastoma.alleninstitute.org). Briefly, tissue blocks were obtained at tumor resection, subdivided, and rapidly frozen. Tissues were later sectioned and subjected to H&E staining (Fig.

2.1). Pre-defined histologic structures including IT, LE, MVP, HBV, PNZ, PAN, and CT were outlined on one section and then laser microdissected on adjacent sections (Table 2.1). Dissected structures then underwent RNA sequencing; results were normalized as fragments per kilobase of exon per million reads (FPKM) mapped reads. The total number of patients enrolled was 42; 36 patients (18 male; 18 female) had usable samples with intact RNA, and of these each subject had variable numbers of samples obtained for each region. Not all patients have data from all structures and recurrent tumors (2) were excluded.

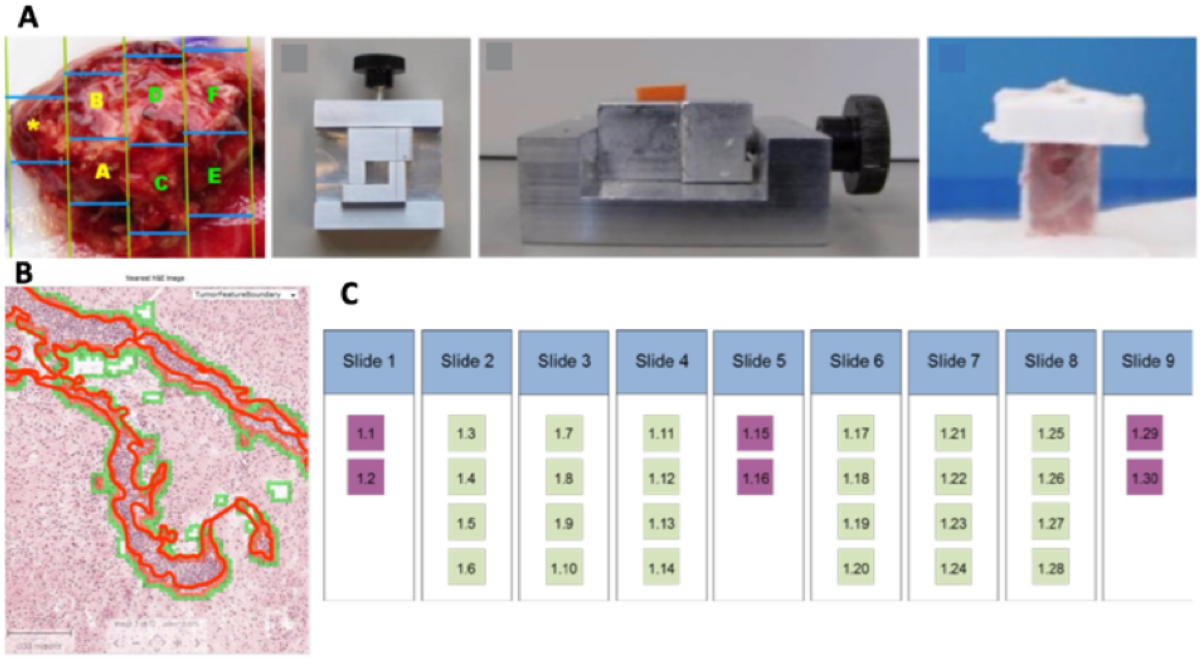

Fig. 2.1. Tissue collection and processing. (**A**) Tissue collection, sub-sectioning, and freezing done by the Allen Brain Institute (ABI). (**B**) Example of histologic structure identification done by the ABI. (**C**) Slide layout for serial sections for structure alignment, completed by the ABI. Images: ABI, technical white paper.

Table 2.1. Tumor structure definitions. Adapted from IvyGAP Technical White Paper Fig. 2-9

Structure	Example Images	Definition
Leading Edge (LE)	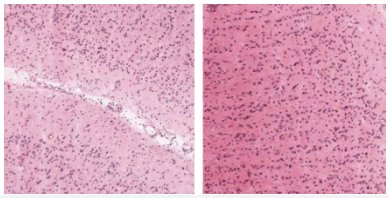	"Leading Edge is the outermost boundary of the tumor, where the ratio of tumor to normal cells is about 1-3/100. Layers of the cortex are often observed."
Infiltrating Tumor (IT)	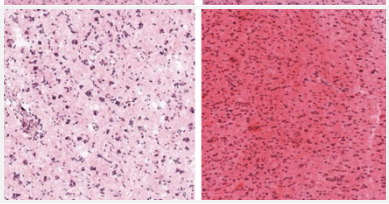	"Infiltrating tumor is the intermediate zone between the Leading Edge (LE) and Cellular Tumor (CT), where the ratio of tumor cells is about 10-20/100. Neuronal cell bodies as well as glial cell aggregating on neurons, are often observed."
Cellular Tumor (CT)	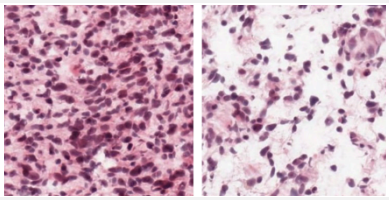	"Cellular tumor constitutes the major part of core, where the ratio of tumor cells to normal cells is about 100/1 to 500/1. Tumor densities often exceed typical levels of cells (left panel), but can also have low cell mass due to edema or early necrosis (right panel)."
Microvascular Proliferation (MVP)	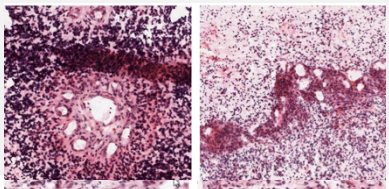	"…generally found in the core of tumors, and is marked by two or more blood vessels sharing a common vessel wall of endothelial and smooth muscle cells (e.g. 100 μm diameter). They can appear as glomerulus (left panel, 100 μm diameter), or as a "garland" of multiple interconnected blood vessels (right panel, 50 μm diameter x 1-6 mm)."
Hyperplastic Blood Vessels (HBV)	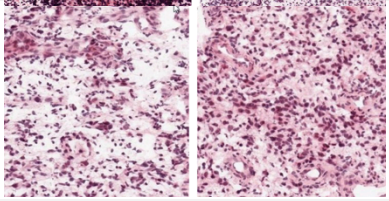	Hyperplastic blood vessels are found throughout tumors, and exhibit many sizes and shapes (left panel). The features are marked by increased density of blood vessels that appear to have thickened walls (endothelial cell proliferation) (right panel).
Pseudo-palisading Cells around Necrosis (PAN)	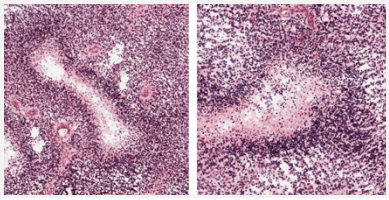	Pseudopalisading cells around necrosis is generally found in the core of tumors. Tumor cells aggregate or line up in rows 10-30 nuclei wide at higher density than the surrounding CT to form pseudopalisading cells, which may appear to point toward a common center in necrosis. Necrosis is required for PAN."
Perinecrotic Zone (PNZ)	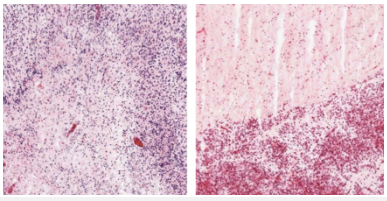	"Perinecrotic zone is generally found in the core of tumors, and refers to a boundary of tumor cells typically 10-30 nuclei wide along the edge of necrosis that lacks a clear demarcation of PAN."
Necrosis (NE)*	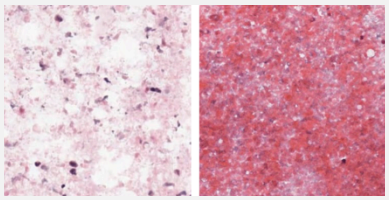	"Perinecrotic zone is generally found in the core of tumors, and refers to a boundary of tumor cells typically 10-30 nuclei wide along the edge of necrosis that lacks a clear demarcation of PAN." **No RNAseq data for this structure*

TCGA. The gene expression data (174 cases, Workflow Type: HTSeq-FPKM) and corresponding clinical information were downloaded from the Genomic Data Commons Data Portal for the Glioblastoma Multiforme projects (TCGA-GBM; https://portal.gdc.cancer.gov). Methylation data was downloaded from https://tcga-data.nci.nih.gov/docs/publications/gbm_2013/. Recurrent tumors and normal brain samples were excluded yielding a total of 156 cases.

Data pre-processing. To obtain a log-transformed, normal distributed data set, we excluded genes with very low expression across all samples by applying the following filtering method to IvyGAP and TCGA data sets: 1) Take expression values for all genes and all samples, remove zero's and find quartiles to be used as filtering value. 2) Calculate mean of each gene across samples and exclude genes with a mean less than the lower quartile filtering value. A combination of raw FPKM values, log2-transformed data, and z-score normalized values, where every transcript had mean value of 0 and standard deviation of 1, were used for all analyses.

Variation in gene expression is primarily explained by histologic structure. To assess the interrelationships between all samples in the IvyGAP data set, we used principal component analysis (PCA) and transcript-to-transcript correlation network analysis. To determine the optimal number of clusters within the dataset, we applied the gap statistic method, followed by k-means clustering and hierarchical clustering to identify the constituents of the optimally numbered clusters.

PCA. We performed PCA using the 1000 most variable genes in the IvyGAP data set to assess the variance among sample transcriptomes on the log2-transformed and z-score

normalized data matrix (PCA() function in [FactoMineR *R* package] and [factoextra package in *R*]) (*315*).

Correlation network analysis. Regional differences were also assessed in BioLayout Express3D by plotting a sample-to-sample correlation graph with the Pearson correlation threshold, r = 0.92, for visualization. Nodes represent individual samples, and edge length depicts the degree of correlation between samples with Pearson correlation coefficients above the selected threshold.

Gap statistic analysis. To identify the optimal number of clusters for subsequent partitioning methods in the IvyGAP dataset, we determined the gap statistic on the top 1000 most variable genes, which compares the total intra-cluster variation for k = 1-10 with expected values under null distribution of the data. The optimal number of clusters is the value that maximizes the gap statistic, meaning that the clustering structure is far from random uniform distribution (fviz_nbclust() function [factoextra R package]) (*315*).

K-means clustering. To identify which of the seven histologic structures collapse together for subsequent analysis, we performed k-means clustering on the 1000 most variable genes in the IvyGAP data set using k=4, the optimal number of clusters determined by the gap statistic analysis. The clusters were visualized by principal components (kmeans() function [stats *R* package]; fviz_cluster() function [factoextra *R* package]) (*315*).

Dendrogram. To identify which of the seven histologic structures collapse together for subsequent analysis, we also computed a distance matrix on the 1000 most variable genes in the IvyGAP dataset using Euclidean distance measure and performed hierarchical cluster analysis using Ward's method. The dendrogram was constructed using k=4 groups, as determined by gap

statistic analysis (distance matrix and clustering was computed using dist() and hclust() functions in [stats *R* package]; fviz_dend() function in [factoextra *R* package]) (*315*).

Structure-based lasso logistic regression classifier. We aimed to create a method for discriminating between GBM histologic structures using transcriptomic features with the goal of applying this method to mixed GBM samples to identify the predominant CT region for further analysis.

The IvyGAP data set was first balanced between structures and evenly split into train and test sets based on structure using Stratified K-Folds cross-validator (n_splits=5). Next, using train sets, a lasso regularized multinomial logistic regression classifier was built to predict GBM structure in independent data sets (penalty='L1'; solver='saga'; C='1/8', multi-class= 'multinomial', fit intercept=True,). The 5-fold cross validation average accuracy for the logistic regression classifier on test sets is 98.45%. Lastly, the classifier was used to predict the structure classification of all GBM-TCGA samples (class sklearn.linear_model.StratifiedKFolds and .LogisticRegression; Python3.6) (*316*).

Gene Set Enrichment Analysis (GSEA) to assess for enriched biological processes and perform GBM subtype analysis. Gene set enrichment analysis was performed using GSEA software with FPKM gene expression data (*317*). Defaults were used for GSEA analysis, including Signal2Noise ranking metrics. Gene sets were excluded that were smaller than 15 genes and greater than 500 genes, and enrichment p-values were estimated by 1,000 permutations and corrected for multiple testing using the Benjamini-Hochberg method. Analyzed

gene sets were from the molecular signature database (MsigDB), Gene Ontology (C5), Hallmark (H), or Positional (C1) collections, at www.broadinstitute.org/gsea/msigdb/collections.jsp.

For structurally enriched biological processes, GSEA results were visualized using the Enrichment Map plugin for Cytoscape (V2.8, www.cytoscape.org) (*318*). For visualization purposes, clusters of functionally related enriched GO terms were manually circled and labeled, and significance thresholds were set to be highly conservative for the LE/IT and HBV/MVP structures (p-value cutoff 0.005; FDR q-value cutoff 0.001), conservative for PNZ/PAN (p-value cutoff 0.005; FDR q-value cutoff 0.1), and loose for CT (p-value cutoff 0.1; FDR q-value cutoff 0.4).

Survival prediction using an established prognostic gene signature and metagene score. To determine if expression of an established multigene predictor of GBM outcome has structural specificity, we calculated a metagene score for each sample in the IvyGAP dataset (z-scored using all samples) following methods from Colman and colleagues(*319*).Kaplan-Meier survival analysis was performed using the metagene score to separate all IvyGAP samples into high (metagene score > 0) and low risk (metagene score < 0) groups.

To test if assessing the gene signature within a specific structure could accurately stratify subjects in terms of overall survival, we z-scored samples within each structure independently, and re-calculated a metagene score for each sample followed by Kaplan-Meier analysis as before.

Cox proportional hazards model for survival analysis. We aimed to create a method for discriminating between high risk (short overall survival) versus low risk (long overall survival) patients using transcriptomic features in the CT and clinical characteristics to calculate an individual's risk score. This risk score method was then applied to CT predicted GBM samples for validation.

Univariate Analysis. To determine whether the clinical covariates age, gender, MGMT methylation status, IDH1 mutation status, 1p19q deletion status and KPS score were significantly associated with overall survival in the IvyGAP CT samples, univariate Cox proportional hazards regression was performed (coxph() function in [survival package in *R*]).

Multivariate Analysis. To determine whether genes were significantly associated with overall survival and independent of clinical covariates, multivariate Cox proportional hazards regression using the clinical covariates MGMT methylation status, IDH1 mutation status and age was performed. Each gene was assigned a hazard ratio (HR), Wald statistic, and a corresponding p-value using Cox regression analysis. Genes were selected as candidates significantly associated with survival if the p-value was < 0.05, which also coincides with the confidence interval for the combined HR for a given gene not crossing the baseline risk (HR = 1). The HR for a given gene >1, was defined as a potential risk gene, <1, it was defined as a potential protective gene (coxph() function in [survival package in *R*]).

Stepwise selection. The gene candidates from multivariate analysis were applied to the process of forward stepwise selection, which is designed to add genes to the base model with clinical covariates that increase the model's ability to discriminate between long versus short-term survivors. First, 10 random seeds were generated and for each seed the IvyGAP CT samples were split into train and test sets using 5-fold cross validation. Next, using train sets, HR's, log-

rank test scores and associated p-values are computed for the base model, iteratively fit with each candidate gene. An updated model is created adding only the candidate gene with the highest log-rank test score (and the lowest log-rank test p-value) to the base model. Then, the process is repeated to determine which of the remaining candidate genes will lead to the greatest improvement if added to the model. This process is continued until the concordance for the model reaches 1, signifying that the discriminatory power of the model is perfect, or 10 genes have been added, whichever occurs first (createFolds() function in [caret *R* package]; coxph() function in [survival package in *R*]).

Internal validation. The model for each train set that underwent stepwise selection was used to predict the HR of the corresponding test set and the concordance and log-rank test p-value was computed. Models were excluded that, upon prediction on the test set, had concordance < 0.5 or log-rank test p-value > 0.05. To avoid overfitting, the model that was selected for subsequent analyses was the model with concordance nearest the mean (0.75) of all remaining models (predict() function in [stats package in *R*]).

Finalized survival model. Since we want to ensure generalizability and that each feature of the model is an independent predictor, to finalize the model, it was applied to the entire IvyGAP CT data set and features were excluded that had a Wald statistic p-value >0.05. The resulting finalized model was trained on the IvyGAP CT data and used to predict the HR's for each sample in the IvyGAP CT set alone as well as the entire IvyGAP data set (coxph() function in [survival *R* package]; predict() function in [stats *R* package]).

External validation. The GBM-TCGA samples that were predicted to be predominantly CT by the structure-based lasso logistic regression classifier were used for external validation of the finalized survival model. The model was trained on the IvyGAP CT data and used to predict

the HR's for the GBM-TCGA CT samples alone as well as the entire GBM-TCGA data set (predict() function in [stats package in *R*]).

Survival analysis. Under different circumstances, an HR of 1 (high risk: HR > 1; low risk: HR < 1) was taken as the cut-off point for group classification, or tertiles of HR values were used to classify into two (high risk: HR > quantile($^2/_3$); low risk: HR < quantile($^2/_3$)) or three groups (high risk: HR > quantile($^2/_3$); medium-risk: quantile($^1/_3$) < HR < quantile($^2/_3$); low risk: HR < quantile($^1/_3$)). The Kaplan-Meier method was used to generate survival curves based on the different cut-offs and the difference between survival curves was evaluated using the log-rank test. All tests were two-tailed, and p-values less than 0.05 were considered to be significant (survfit() function in [survival package in R]; ggsurvplot() function in [survminer *R* package]).

Heatmaps. For all heatmap visualizations, if clustering was performed, transcripts and samples were organized by unsupervised hierarchical clustering using Ward's method with the Euclidean distance metric. Heatmap visualization and hierarchical clustering were performed on log2-transformed and *z*-score-normalized data (pheatmap() function [pheatmap *R* package]).

2.4. Results

Histologic structures in GBM tumors are molecularly distinct, explaining in part intra-tumoral heterogeneity

We analyzed RNA-sequencing and corresponding clinical data from the Ivy Glioblastoma Atlas Project (IvyGAP) to compare the transcription profiles of different histological structures (*56*). The IvyGAP dataset is comprised of two companion databases: (1) RNAseq and In Situ Hybridization data from histologically identified tumor structures and (2) clinical information including patient demographics, pathology, and survival. Briefly, this database was generated by analyzing RNA in GBM tissue blocks that were obtained at tumor resection (Fig. 2.1 A). Pre-defined histologic structures including: infiltrative tumor (IT), leading edge (LE), cellular tumor (CT), perinecrotic zones (PNZ), pseudopalisading cells around necrosis (PAN), areas of hyperplastic blood vessels (HBV), and areas of microvascular proliferation (MVP), were outlined on H&E stained tumor sections and microdissected on adjacent sections at the Allen Brain Institute (Fig. 2.2 A; Fig. S2.1 B-C; Table 2.1). The number of different structures sampled varied between patients. Dissected structures underwent RNA sequencing and results were archived as Fragments Per Kilobase of transcript per Million (FPKM) mapped reads. We used the FPKM data from 34 newly diagnosed GBM in the present analyses.

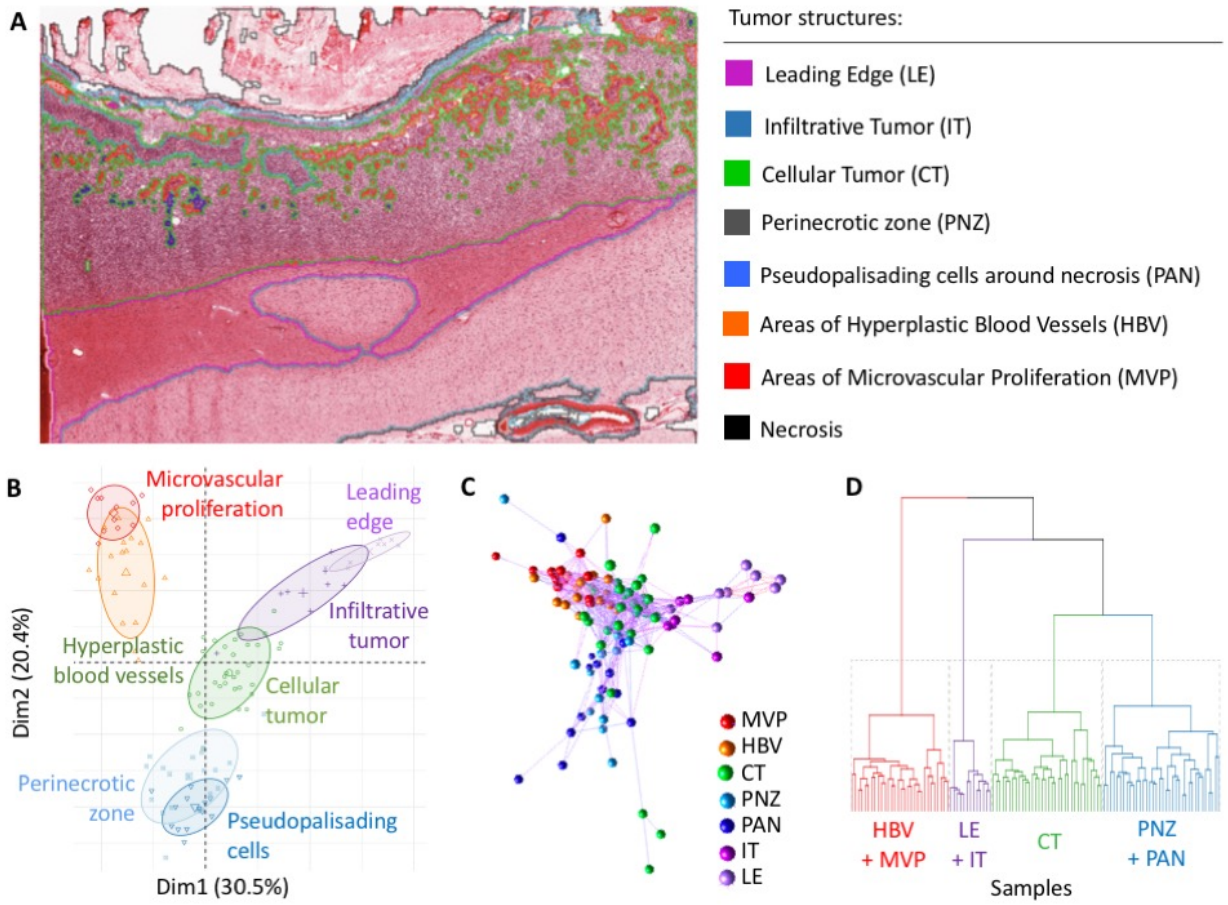

Fig. 2.2. Variation in GBM sample gene expression is primarily explained by histologic structure. (**A**) Representative image demonstrating the histologic structures identified by the Allen Brain Institute (ABI), outlined by different colors. The ABI microdissected these structures, performed RNAseq on the dissected structures, and then archived the FPKM level data in the Ivy Glioblastoma Atlas Project (IvyGAP) database. See Fig. S1 for higher magnification structure images and definitions. (**B-D**) Analysis of the 1000 most variable genes in the IvyGAP data set. (**B**) Principle component analysis (PCA) of dimensions 1 (Dim1) and 2 (Dim2) demonstrate that most variation in the data is explained by the histologic structure from which the RNA was extracted. Each sample is represented as a symbol, and colored by the structure the sample is from; ellipses are drawn around samples from the same structure (ellipse

level=0.66). (**C**) Correlation network analysis shows samples from a histologic structure are clustered. Nodes represent samples, color represents the structure samples came from, and edge length depicts the degree of correlation between samples. (**D**) Dendrogram of hierarchically clustered (k = 4) samples demonstrating structures with the most similarity.

We analyzed histological structure specific transcriptional profiles from the IvyGAP database using principal component analysis (PCA) and correlation network analysis (*315, 320, 321*). The first two principal components in the PCA explained 50.9% of the variance in the 1000 most variable genes in the dataset and separated samples by structure, but not by other clinical features associated with GBM such as KPS, age, MGMT promoter methylation, and IDH1 mutation (Fig. 2.2 B; Fig. 2.3 A-G). This finding suggests that sample variance was driven by histologic structure and not by other patient characteristics. Transcript-to-transcript correlation network analysis corroborated PCA results, confirming that samples within a region were more highly correlated to one another than to samples from different regions, even in cases where samples were from the same patient (Fig. 2.2 C) (*320, 321*).

Samples from several of the 7 histologically-defined structures had overlapping clusters in PCA and network analyses, indicating that their transcription profiles were similar. Applying the gap statistic method, k-means clustering, and hierarchical clustering showed that the original 7 histologic structures could be collapsed to 4 molecularly distinct structures having high tumor cellularity (CT), tumor invasion (LE/IT), vascular involvement (HBV/MVP) and necrosis (PAN/PNZ) (Fig. 2.2 D; Fig. 2.3 H-I). The analyses that follow focus on these four structures.

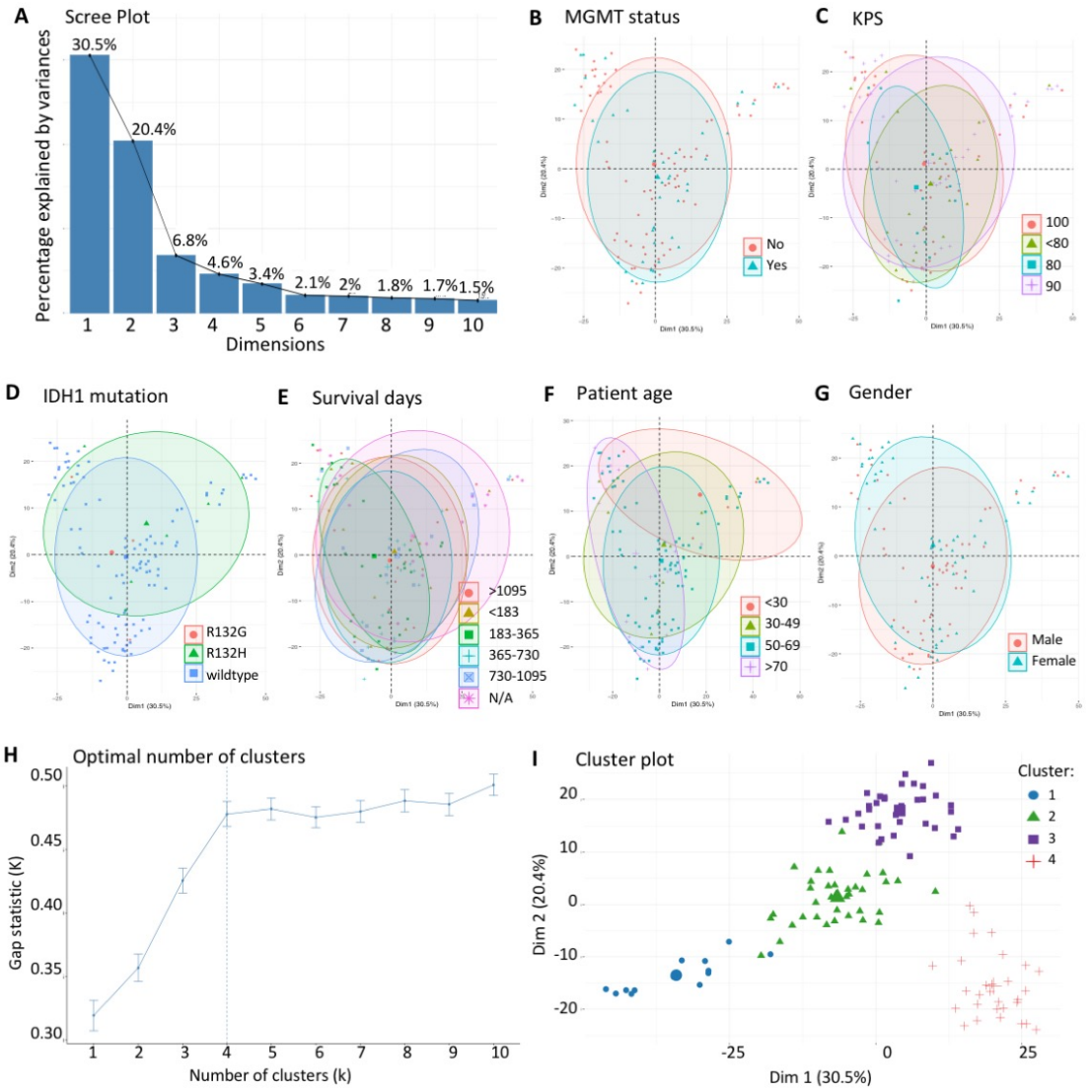

Fig. 2.3. Additional PCA and clustering analyses. (**A**) Scree plot showing percent of variance described by each principle component (dimension) in analysis of the top 1000 most variable transcripts. PCA labeling clinical patient stratifiers (**B**) MGMT methylation status, (**C**) Karnofsky Performance Score (KPS), (**D**) IDH1 mutation status, (**E**) overall survival days, (**F**) patient age at time of diagnosis, and (**G**) gender of the samples (each symbol represents and individual sample). No alternative labeling explains variance in the data set as well or better than histologic structure seen in figure 1. (**H**) Gap statistic method identifying optimal number of clusters for k=1-10. (**I**) K-means clustering using k=4 and visualization of clusters using PCA.

Distinct biological processes are enriched in tumor structures

We analyzed whole transcriptome measurements of each of the four transcriptionally distinct structures using Gene Set Enrichment Analysis (GSEA) of gene ontology (GO) to identify biological processes enriched in each structure relative to the rest of the tumor (Fig. 2.4)(*317, 318, 322-324*). The LE/IT structure, where the ratio of tumor cells to central nervous system (CNS) cells is low, had enrichment of normal CNS processes such as neuron development, synaptic signaling, and regulation of ion and neurotransmitter homeostasis. Thus, transcriptomic analysis of the bulk tumor edge captures CNS processes, rather than cancer specific biology. The vascular architecture (HBV/MVP), as expected, was associated with angiogenesis, regulation of blood pressure, vascular permeability, cell junction assembly, and extracellular structure organization. This region also was enriched in immune processes including regulation of phagocytosis, leukocyte migration and activation, and cytokine production, suggesting this is an inflammatory microenvironment in GBM. The PNZ/PAN architecture also was associated with enhanced immune processes, such as monocyte and lymphocyte differentiation, and leukocyte migration and chemotaxis. Additionally, the PNZ/PAN region was characterized by biological networks associated with necrosis, cellular starvation, hypoxia, and oxidative stress.

The CT structure has the highest density of neoplastic cells and the transcription profiles of this structure varied between patients, suggesting that analysis of transcription profiles from CT might enable more precise identification of biologically distinct GBM cohorts. The variation between patients decreased our ability to identify biological processes associated with the overall CT structures. However, there was a trend toward enhancement of traditional cancer processes including DNA replication and repair, chromatin remodeling, and stem cell proliferation.

The diversity of biological networks interacting in spatially distinct histological structures highlights the complexity of GBM tissue. These studies suggest that efforts to compare tumors using samples containing unknown quantities of these structures may be compromised by variance in the tumor architecture. Instead, comparing tumors using gene expression profiles measured for a consistent structure across patients, particularly the CT, may be an effective inter-tumoral comparison method.

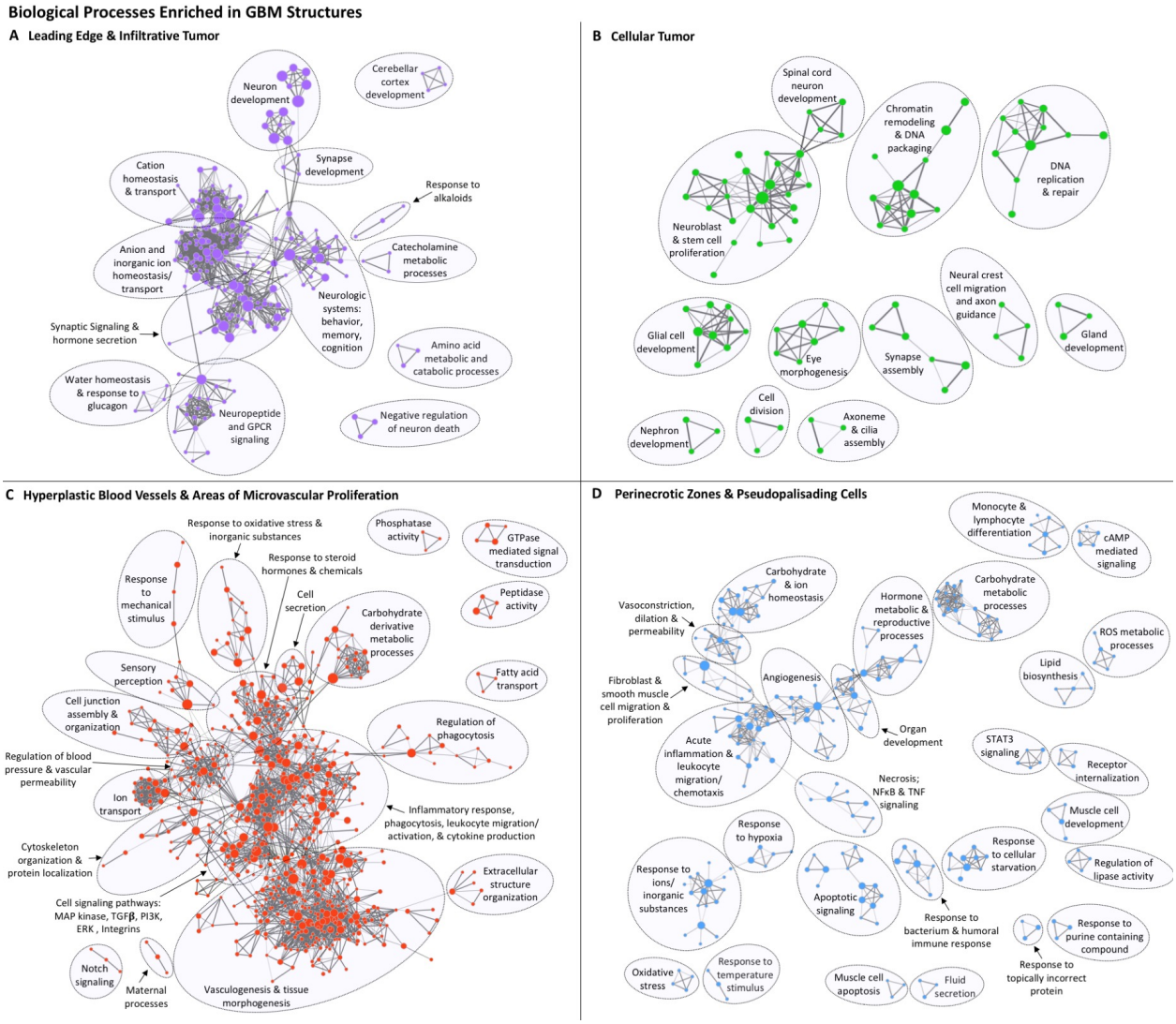

Fig. 2.4. Biological processes enriched in tumor structures. Gene Set Enrichment Analysis (GSEA) followed by enrichment map visualization shows gene ontology (GO) biological processes enriched in (**A**) leading edge (LE) and infiltrating tumor (IT), (**B**) cellular tumor (CT), (**C**) hyperplastic blood vessels (HBV) and microvascular proliferation (MVP), as well as (**D**) perinecrotic zones (PNZ) and pseudopalisading cells around necrosis (PAN) relative to the rest of the tumor. Nodes represent GO terms. Clusters of functionally related enriched GO terms were manually circled and labeled. Node color represents the structure enriched (Purple: LE/IT; Green: CT; Dark orange: HBV/MVP; Blue: PNZ/PAN). Node size within each structure quadrant is proportional to the number of genes within each GO term. Edge thickness signifies the overlap between GO terms (number of genes shared between two gene sets); thicker edges depict connections between nodes that share more genes than thinner edges. For visualization purposes, significance thresholds were set highly conservative for the LE/IT and HBV/MVP structures (p-value cutoff 0.005, false discovery rate (FDR) q-value cutoff 0.001), conservative for PNZ/PAN (p-value cutoff 0.005, FDR q-value cutoff 0.1), and very loose for CT (p-value cutoff 0.1, FDR q-value cutoff 0.4).

Molecular subtype classification depends on structure, with CT best able to distinguish subtypes

Existing GBM molecular subtypes (mesenchymal, classical, neural, and proneural) defined by expression of an 840-gene classifier, are not strongly associated with clinical endpoints (*25*). Thus, this gene classifier has not translated clinically. Additionally, several analyses have reported classification of a single tumor into multiple subtypes (*33, 51, 325*). We reasoned that both of these issues might be related to histological heterogeneity within and between tumors.

Our analyses of subtype gene expression profiles showed that histological architecture significantly influenced subtype classification of samples, using previously defined subtype criteria (*25*) (Fig. 2.5 A; Fig. 2.6 A). Neural and proneural subtype-defining genes were strongly expressed in LE and IT samples, while mesenchymal subtype genes were highly expressed in HBV and MVP samples. This suggests that a biopsy taken from the tumor edge might be classified as neural or proneural, while a biopsy from the same tumor taken from a highly vascular region might be classified as mesenchymal. To test this, we subtyped all samples from each structure, using single-sample GSEA. We found that, in many cases, a single patient would be classified as every subtype depending on the structure analyzed. To avoid this problem, we focused on using solely the CT since this structure showed the most variability in subtype gene expression. Our analyses demonstrated that all four subtypes could be distinguished in CT (Fig. 2.5 B-C; Fig. 2.6 B). Furthermore, these results suggested three main subtypes exist: proneural, classical, and mesenchymal (Fig. 2.4 C). This result supports the idea that the original neural subtype may have been an artifact (*26*).

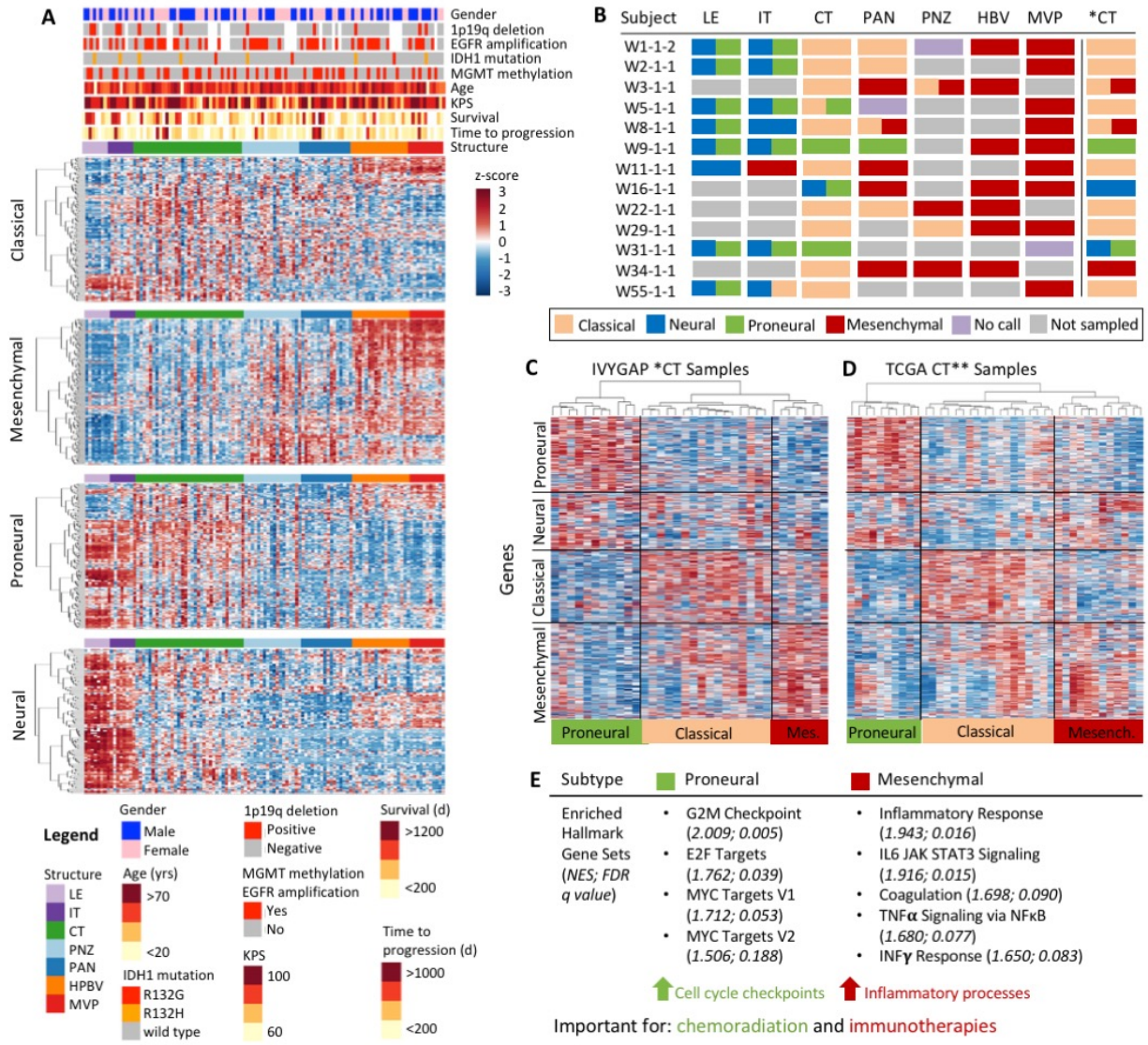

Fig. 2.5. Molecular subtype classification depends on the structure sampled, with cellular tumor (CT) able to distinguish biologically distinct subtypes. (**A**) Expression of subtype gene set (y-axis) in IvyGAP samples from each region (x-axis) show that sample structure is a main contributor to expression of subtype gene signatures. Genes corresponding to each subtype were organized independently by unsupervised hierarchical clustering. (**B**) Subtype classification for samples corresponding to subjects with ≥4 samples from different regions. All sample calls are shown in Fig. S3b. CT* represents subtype analysis using only CT (z-scored data across CT samples only). (**C**) Unsupervised hierarchical clustering of IvyGAP CT samples (z-scored data

across CT samples only) showing 3 main clusters with signatures of proneural, classical, and mesenchymal GBM subtypes. (**D**) Unsupervised hierarchical clustering of TCGA samples predicted to be composed predominantly of CT, also showing 3 main clusters with signatures of proneural, classical, and mesenchymal subtypes. (**E**) Enrichment of hallmark gene sets in the GBM subtypes (stratified based on the CT sample analysis) showing statistically significantly enriched processes in proneural and mesenchymal tumors (none were statistically significant in classical or neural). Proneural and mesenchymal tumors have enrichment of cell cycle checkpoints and immune processes, respectively. NES: normalized enrichment score; FDR: false discovery rate.

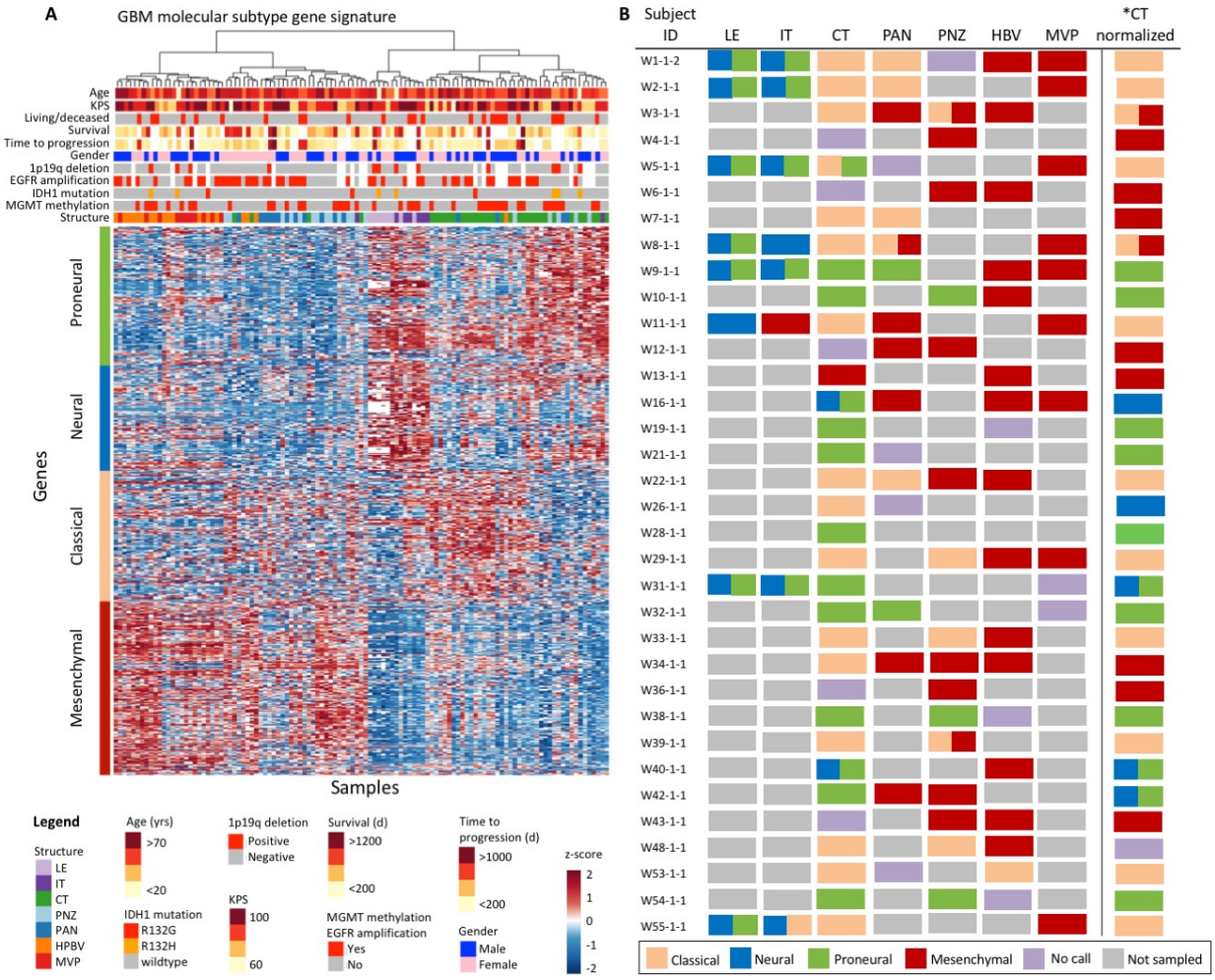

Fig. 2.6. IvyGAP molecular subtyping. (**A**) Expression of subtype gene set (y-axis) in the IvyGAP samples from each region (x-axis) showing sample structure is a main contributor to expression of subtype gene signatures. Samples were organized by unsupervised hierarchical clustering using Ward's method and the Euclidean distance metric. (**B**) Subtype classification calls for structures from all samples. CT* represents subtype calls using CT z-scored data across only the CT samples.

The finding that analyses limited to CT structures could stratify molecular subtypes needed to be validated in an independent dataset. Doing so was complicated since all other GBM gene expression databases, to our knowledge, have been created from mixed-structure samples. Therefore, we created a novel gene expression classifier, using lasso logistic regression on each of the 4 transcriptionally distinct tumor structures in the IvyGAP database, to identify expression profiles that distinguish the 4 structures (Fig. 2.7 A-B) (*316*). Applying this new gene classifier to tissue composed of mixed structures identifies the predominant structure in a sample. We applied this structure classifier to GBM samples from TCGA and identified 40 samples predicted to be composed of predominantly CT (Fig. 2.7 C) (*21*). Clustering these 40 predicted CT samples revealed proneural, classical, and mesenchymal cohorts, similar in pattern to the IvyGAP CT samples (Fig. 2.5D).

Molecular subtype classification using CT distinguishes tumors with unique biology

We applied GSEA to the proneural, classical, and mesenchymal cohorts identified in the CT samples from the IvyGAP database to identify enriched hallmark gene sets in each subtype (*317, 326*). The proneural and mesenchymal, but not classical and neural, cohorts had significantly enriched gene sets (Fig. 2.5 E; Fig. 2.8). Cell cycle checkpoints (G2M and E2F hallmark gene sets) and MYC signaling (MYC targets hallmark gene set) were enriched in proneural tumors, while the mesenchymal tumors were highly inflammatory (enriched inflammatory response, IL6/JAK/STAT3 signaling, coagulation, and IFNγ response gene sets). These patterns were corroborated in the CT-predicted TCGA samples (Fig. 2.8).

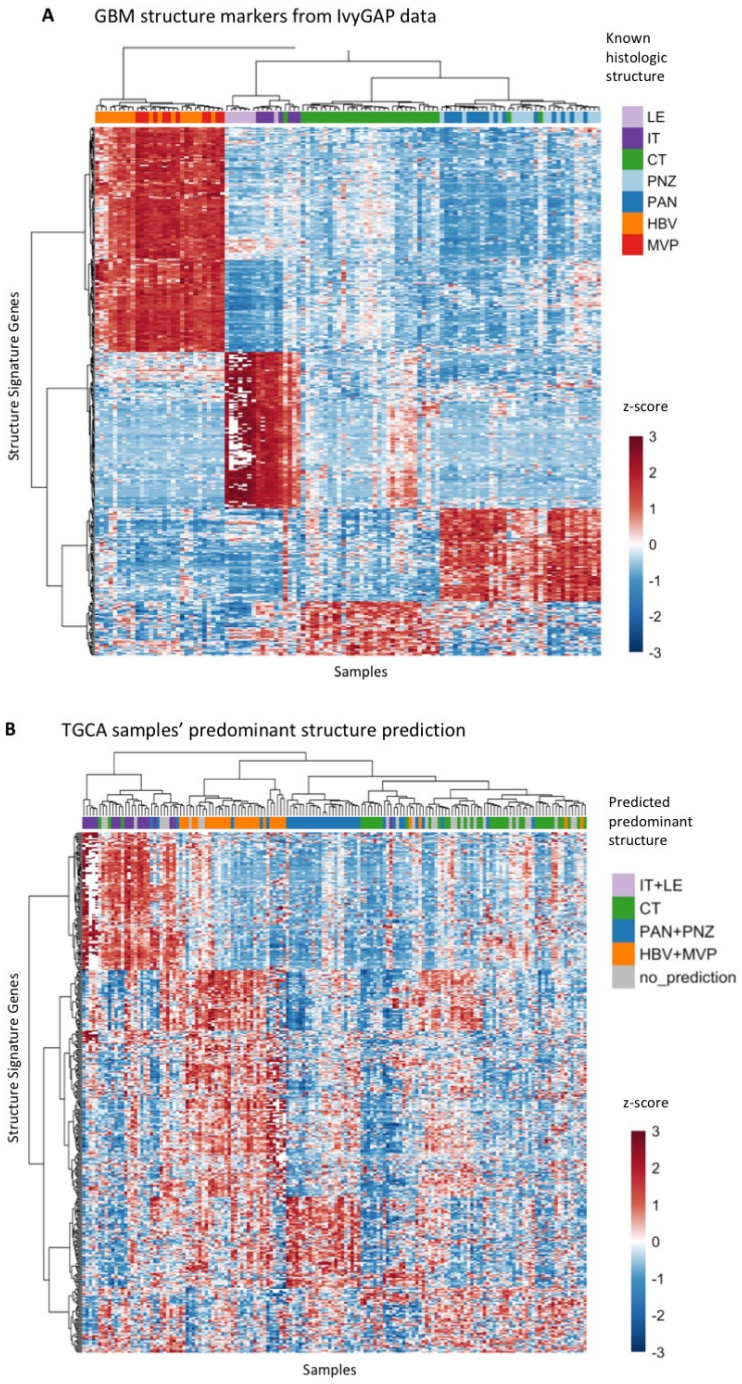

Fig. 2.7. Structure-based gene signature. (**A**) Heatmap displaying z-score normalized expression of the structure-based genes signature, which was created by logistic regression modeling on the IvyGAP data with known tumor structures. (**B**) Heatmap of the structure-based signature genes in the TCGA GBM data. The predominant structure was predicted by applying the model learned by logistic regression from the IVGAP data to the TCGA GBM data. (**A**,**B**) Samples and genes were organized by unsupervised hierarchical clustering, which results in a nearly perfect separation of the structure (A). Genes are on the y-axis, samples on the x-axis.

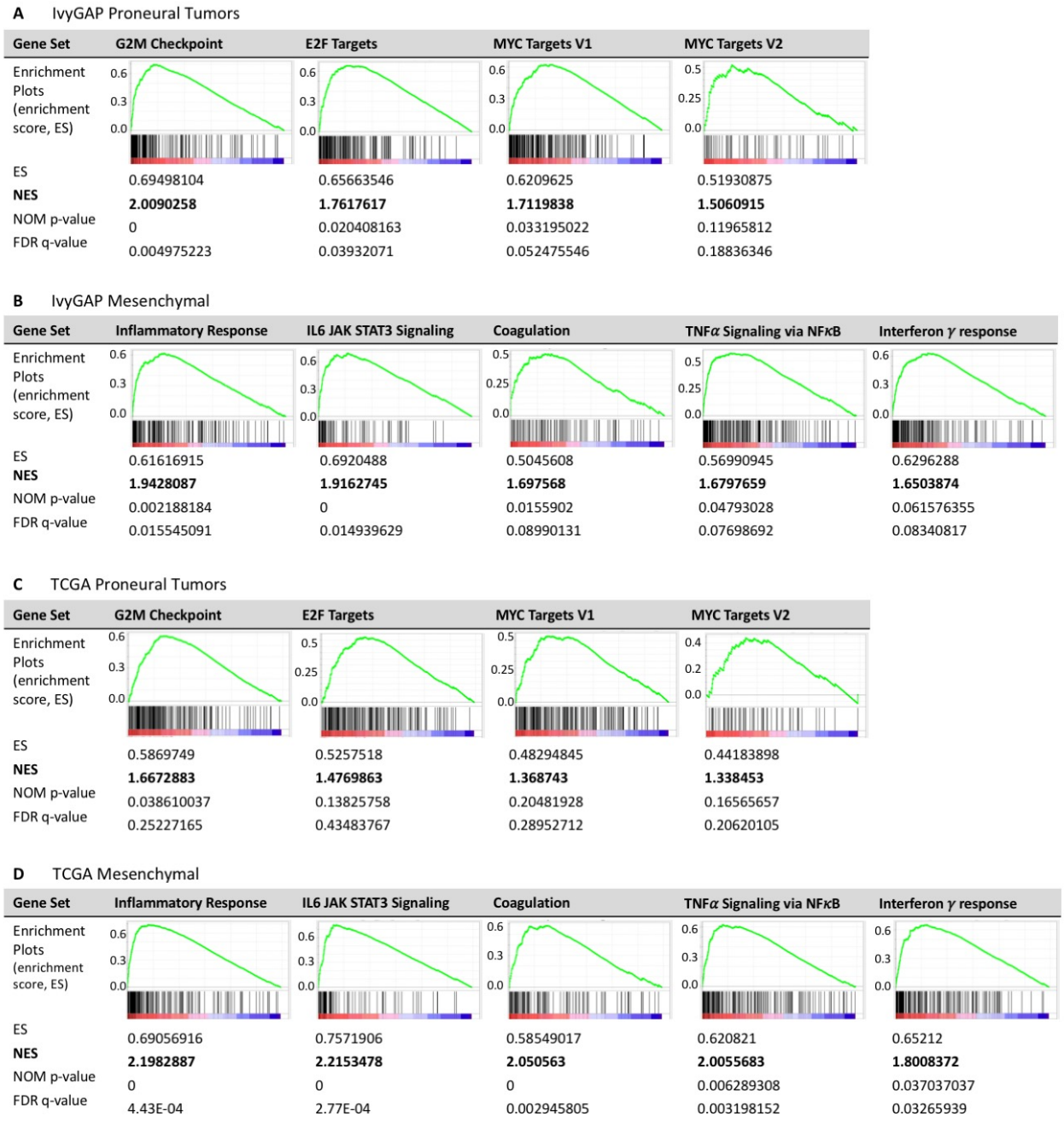

Fig. 2.8. GSEA hallmark gene set enrichment in CT stratified molecular subtypes.

Enrichment plots of top enriched hallmark gene sets in IvyGAP CT samples from (**A**) Proneural versus REST (all samples not classified as proneural), and (**B**) Mesenchymal versus REST (all samples not classified as mesenchymal) analyses. The top enriched hallmark gene sets in IvyGAP CT samples were also enriched in TCGA CT-predicted samples as shown by

enrichment plots of (**C**) Proneural versus REST, and (**D**) Mesenchymal versus REST analyses. No results were statistically significant in Classical or Neural versus REST in both IvyGAP and TCGA analyses. Molecular subtyping was determined after z-score normalizing within only the IvyGAP CT and TCGA CT-predicted samples. ES: Enrichment score; NES: Normalized enrichment score; NOM: Nominal; FDR: False discovery rate.

Survival prediction using an established prognostic gene signature is driven by tumor structure

We applied an established multigene predictor of GBM outcome to transcriptomic profiles from structurally distinct samples and observed that predicted outcome was confounded by structure (Fig. 2.9 A; Fig. 2.10 A) (*319*). This analysis predicted that samples rich in LE and/or IT would have good prognoses, while samples rich in PNZ, PAN, HBV, and/or MVP have poor prognoses, independent of patient origin. In other words, an individual could be assigned either a good or poor prognosis based on the histological structure analyzed (Fig. 2.9 B; Fig. 2.10 B) (*319*). Using the metagene score to separate all IvyGAP samples into high versus low-risk groups showed no survival difference in Kaplan-Meier analysis. This result was observed due a single endpoint being associated with multiple samples with opposite outcomes.

We performed independent Kaplan-Meier analyses on samples within each structure to test whether applying the survival prediction gene signature to a specific structure could accurately stratify patients. CT showed a minor trend in correctly stratifying patients, but only analysis of HBV samples was statistically significant ($p<0.05$). However, analysis of HBV samples inverted the survival curve, alarmingly predicting opposite outcomes; patients predicted to have a poor prognosis had longer overall survival.

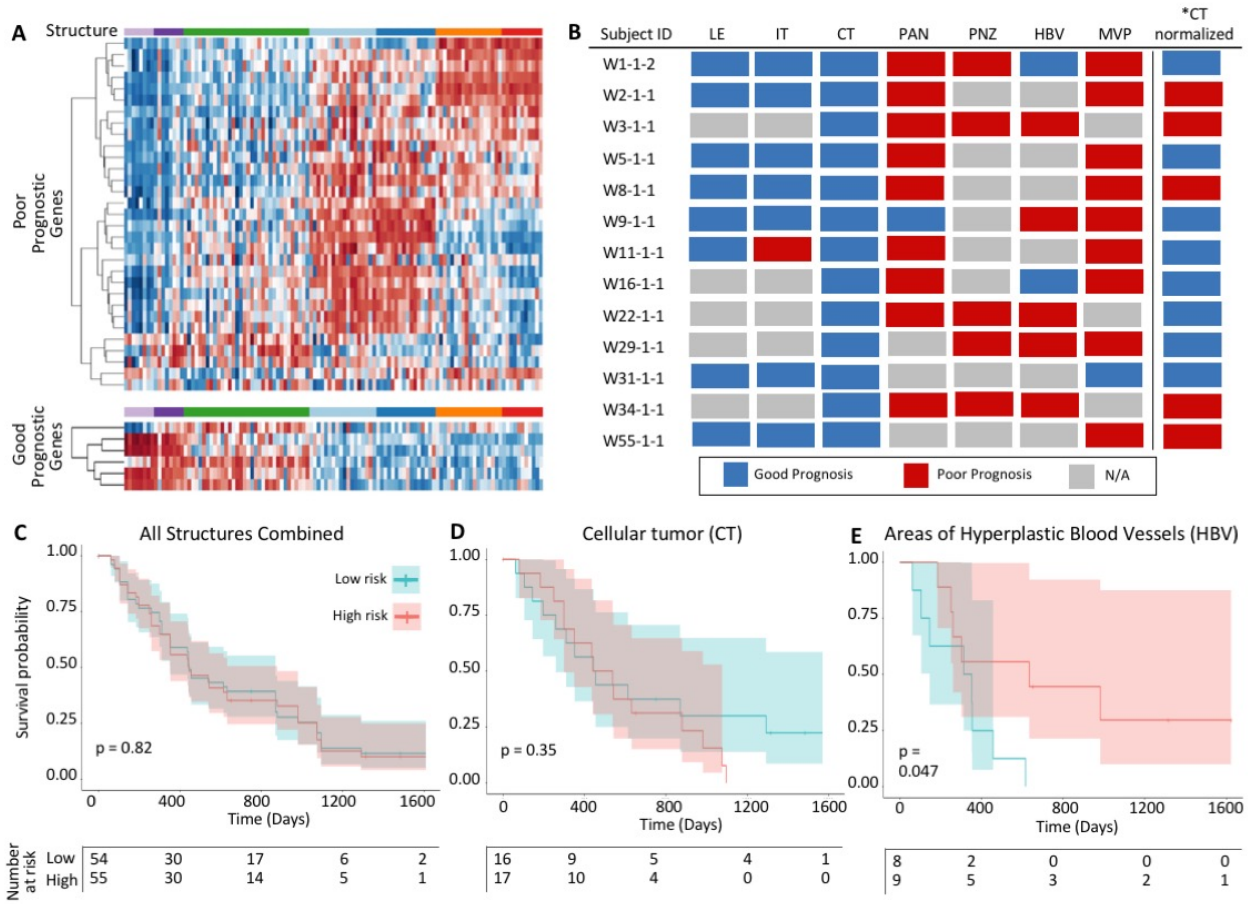

Fig. 2.9. Established prognostic gene signature expression is driven by tumor structure. (**A**) A survival prediction gene set, composed of genes associated with poor or good prognosis, shows differential expression based on tumor structure, with opposite expression in the IT/LE compared to the PAN/PNZ/HBV/MVP. The prognostic gene sets were organized independently by unsupervised hierarchical clustering. (**B**) Prognostic prediction for samples from subjects with ≥4 samples from different structures, with prognosis determined based on sample metagene score. A single patient (subject) can be predicted to be either high or low risk depending on which structure in their tumor is analyzed. All sample calls are shown in Fig. S6b. (**C**) Kaplan-Meier survival analysis of all IvyGAP samples. (**D**) Analysis of survival prediction using a metagene score based on only CT samples. Results in a Kaplan-Meier curve show a minor, but

correct trend in survival stratification. (**E**) Analysis of survival prediction using a metagene score based on only HBV samples results in a statistically significant Kaplan-Meier curve that incorrectly, and oppositely, stratified long versus short survivors. For survival analysis, metagene scores were used to risk stratify (poor prognosis: metagene score > 0; good prognosis: metagene score < 0). Differences between survival curves was evaluated using the log-rank test. All tests were two-tailed; p-values < 0.05 were considered significant.

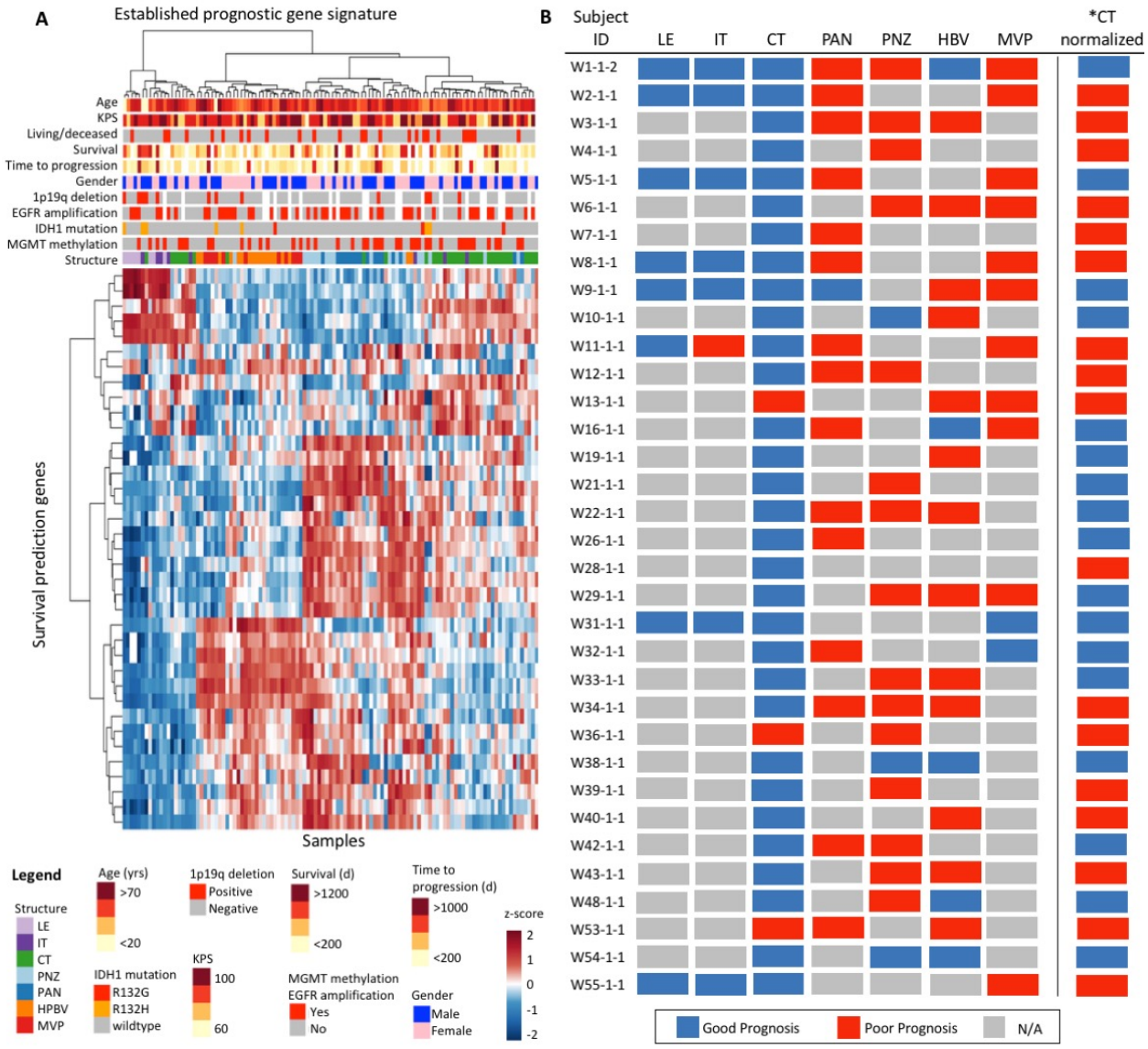

Fig. 2.10. Analysis of established prognostic gene signature expression with all samples. (**A**) A survival prediction gene set, composed of genes associated with poor and good prognosis, shows differential expression based on tumor structure, with opposite expression in IT/LE compared to PAN/PNZ/HBV/MVP. Samples and genes were both organized by unsupervised hierarchical clustering. (**B**) Survival prediction for each sample, with prognosis determined based on sample metagene score (poor prognosis: metagene score > 0; good prognosis: metagene score < 0).

Our analyses suggest that applying this existing gene signature to a mixed structure sample could assign a prognosis based on the structure composition of the sample more than aggressiveness of the neoplastic cells, with highly vascular and necrotic tumors having a worse prognosis. Guided by this, we next asked whether patients could be better stratified according to outcome using gene expression profiles measured for the cancer cell rich CT structure.

A novel prognostic gene signature, created utilizing CT transcriptomics, identifies highest-risk GBM patients

We performed stepwise multivariate Cox proportional hazards regression on IvyGAP CT samples to create a novel prognostic model and risk score equation for GBM (Fig. 2.11 A; Table 2.2). We included known prognostic factors including age, MGMT status, and IDH1 mutation in the model. The final risk score calculation included MGMT status, age, and expression of 6 genes: phosphoglycerate mutase family member 4 (PGAM4), ethanolamine kinase 2 (ETNK2), melanoma inhibitory activity (MIA), guanine monophosphate synthase (GMPS), B-cell lymphoma 7B (BCL7B), and integrin binding sialoprotein (IBSP).

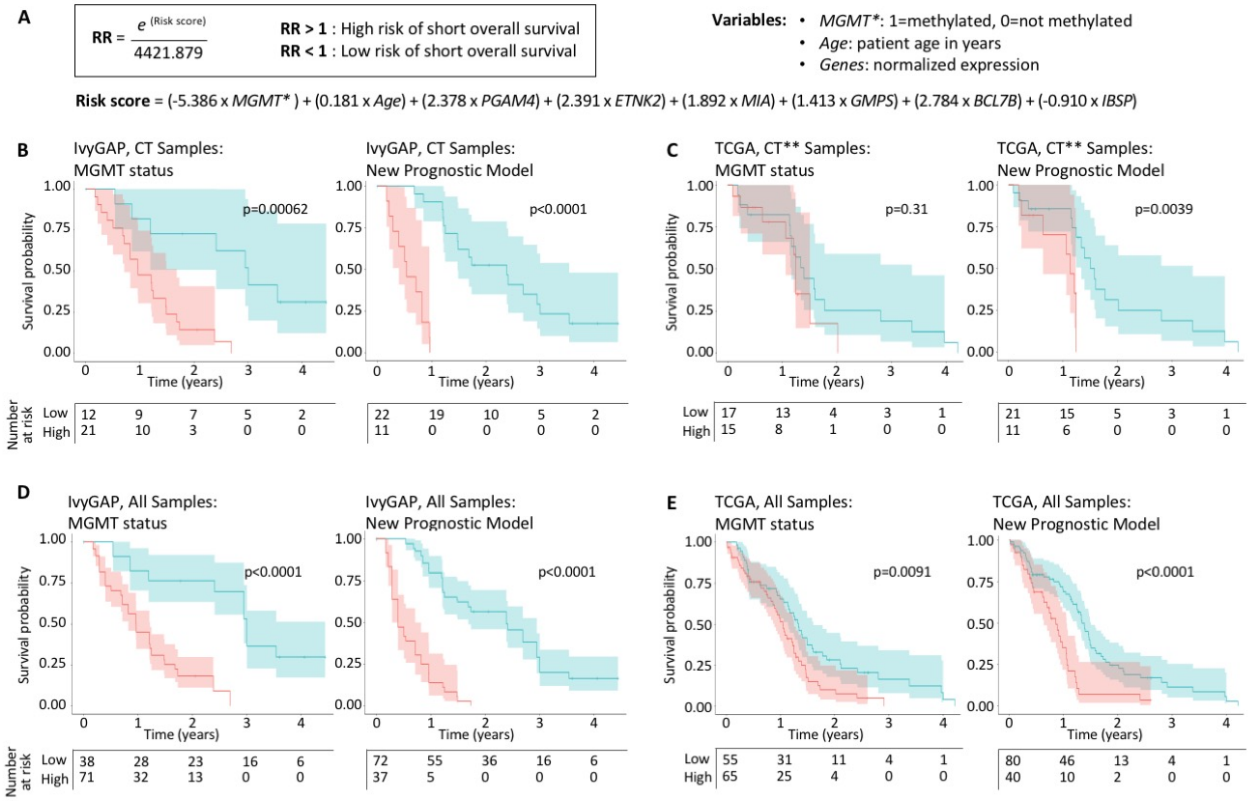

Fig. 2.11. Novel prognostic gene signature created utilizing solely cellular tumor (CT) sample gene expression data. (**A**) Risk score and hazard ratio (HR) prediction equation created using a novel prognostic model for GBM. The risk score is calculated as the sum of the product of the defined weighting factors with the corresponding predictors, MGMT promoter methylation status (0: not methylated; 1: methylated), patient age (in years), and normalized expression values of 6 genes: PGAM4, ETNK2, MIA, GMPS, BCL7B, and IBSP. Kaplan-Meier survival analysis of (**B**) IvyGAP CT samples, (**C**) CT-predicted TCGA samples, (**D**) all IvyGAP samples, and (**E**) all TCGA samples dichotomized into high and low risk groups based on MGMT promoter methylation status (left) and predicted HR (right). For MGMT promoter methylation status, survival was evaluated by separating samples into methylated (low risk) or unmethylated (high risk) groups. For assessing survival using the new prognostic model, tertiles of HR values were used to risk stratify (high risk: HR > quantile($^2/_3$); low risk: HR <

quantile($^2/_3$). Differences between survival curves was evaluated using the log-rank test. All tests were two-tailed; p-values < 0.05 were considered significant. Shading on survival lines correspond to 95% confidence intervals. *MGMT promoter methylation status. ** Samples predicted to be predominantly CT as classified using the structure-based lasso logistic regression classifier.

Table 2.2. New prognostic marker gene signature components.

	Beta	HR	Std error	Wald statistic	Significance p-value	95% confidence interval for β Lower bound	Upper bound
Methylated MGMT	-5.386419	0.004578	1.29504	-4.159	3.19E-05	0.0003617	0.05795
Age	0.180779	1.198151	0.040497	4.464	8.04E-06	1.106726	1.29713
PGAM4 (441531)	2.378263	10.786156	0.632315	3.761	0.000169	3.1234858	37.24722
ETNK2 (55224)	2.390812	10.92236	0.665472	3.593	0.000327	2.9639155	40.25012
MIA (8190)	1.891907	6.632006	0.536646	3.525	0.000423	2.3165995	18.98623
GMPS (8833)	1.412626	4.106727	0.412839	3.422	0.000622	1.8284657	9.22369
BCL7B (9275)	2.784148	16.186019	0.656765	4.239	2.24E-05	4.4678673	58.63809
IBSP (3381)	-0.910068	0.402497	0.368536	-2.469	0.013534	0.1954627	0.82882

We assessed hazard ratios in samples from IvyGAP and validated these using the CT samples in the TCGA dataset in order to determine whether our prognostic signature improved survival prediction over MGMT methylation status alone. In both datasets, stratification of patients into moderate versus highest-risk groups was statistically significant and better than MGMT expression alone (Fig. 2.11 B-C). When we applied the gene signature to all samples from IvyGAP and TCGA (not only CT samples), the model correctly stratified patients, again improving stratification over MGMT expression alone (Fig. 2.11 D-E). These results suggest that our survival prediction model, created based on CT gene expression, can be applied to samples containing either pure CT or mixed structures. The model also effectively identified medium and low risk groups (Fig. 2.12).

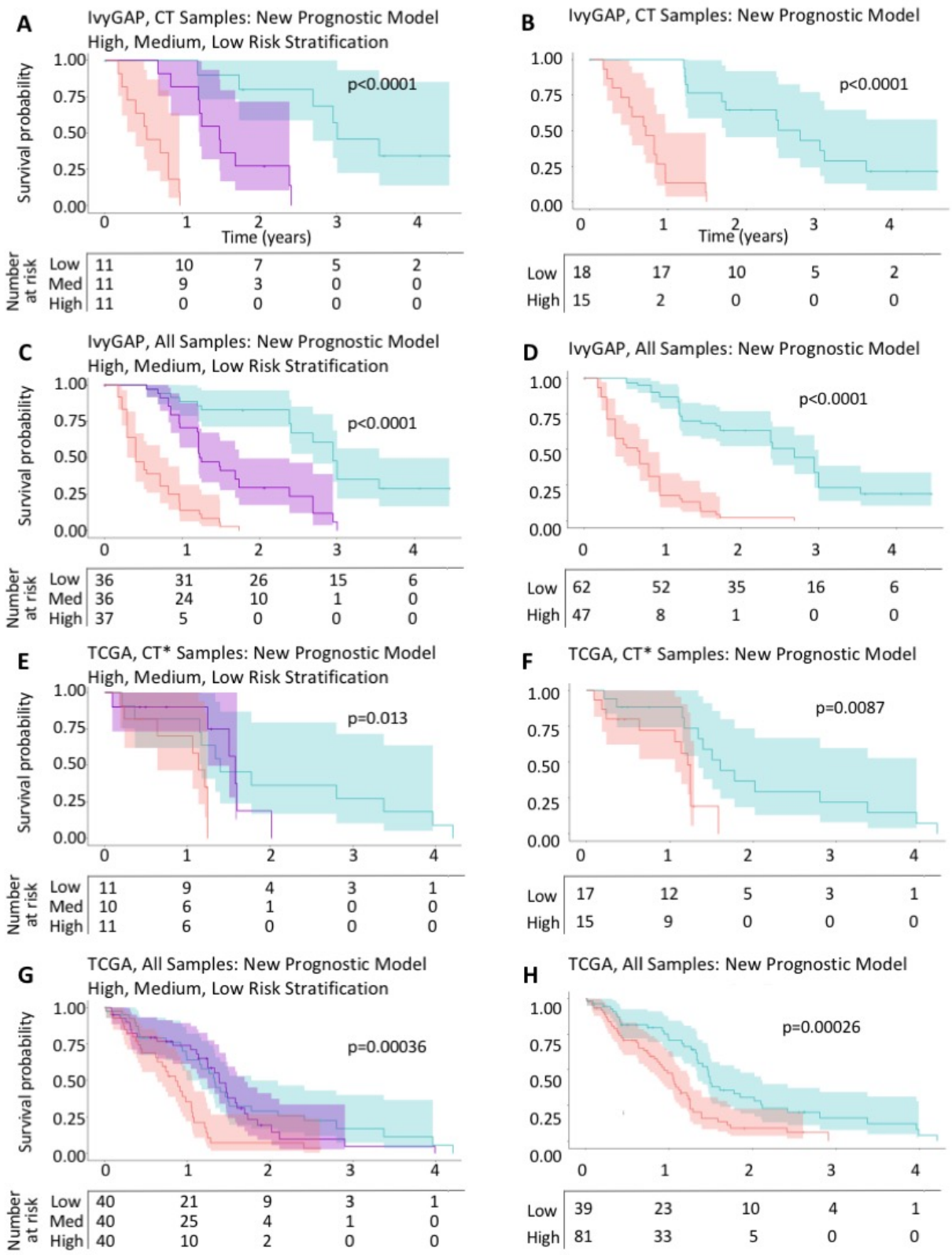
A
IvyGAP, CT Samples: New Prognostic Model
High, Medium, Low Risk Stratification
Survival probability
1.00
0.75
0.50
0.25
0.00
p<0.0001
0
1
2
3
4
Time (years)
Number at risk
Low 11 10 7 5 2
Med 11 9 3 0 0
High 11 0 0 0 0
B
IvyGAP, CT Samples: New Prognostic Model
p<0.0001
Time (years)
Low 18 17 10 5 2
High 15 2 0 0 0
C
IvyGAP, All Samples: New Prognostic Model
High, Medium, Low Risk Stratification
p<0.0001
Low 36 31 26 15 6
Med 36 24 10 1 0
High 37 5 0 0 0
D
IvyGAP, All Samples: New Prognostic Model
p<0.0001
Low 62 52 35 16 6
High 47 8 1 0 0
E
TCGA, CT* Samples: New Prognostic Model
High, Medium, Low Risk Stratification
p=0.013
Low 11 9 4 3 1
Med 10 6 1 0 0
High 11 6 0 0 0
F
TCGA, CT* Samples: New Prognostic Model
p=0.0087
Low 17 12 5 3 1
High 15 9 0 0 0
G
TCGA, All Samples: New Prognostic Model
High, Medium, Low Risk Stratification
p=0.00036
Low 40 21 9 3 1
Med 40 25 4 1 0
High 40 10 2 0 0
H
TCGA, All Samples: New Prognostic Model
p=0.00026
Low 39 23 10 4 1
High 81 33 5 0 0

Fig. 2.12. Survival analysis using the new survival prediction gene signature. Kaplan-Meier survival analysis of (**A**,**B**) IvyGAP CT samples, (**C**,**D**) all IvyGAP samples, (**E,F**) CT-predicted TCGA samples, and (**G,H**) all TCGA samples. Based on predicted HR, samples were separated into high, medium, and low risk groups (**A**,**C**,**E**,**G;** high risk: HR > quantile($^2/_3$); medium risk: quantile($^1/_3$) < HR < quantile($^2/_3$); low risk: HR < quantile($^1/_3$)), or high and low risk (**B**,**D**,**F**,**H**; high risk: HR > 1; low risk: HR < 1). Differences between survival curves was evaluated using the log-rank test. All tests were two-tailed, and p-values less than 0.05 were considered to be significant. Shading on survival lines correspond to 95% confidence intervals. *Predicted to be predominantly CT as classified using the structure-based lasso logistic regression classifier.

We next asked whether genes associated with high-risk had enriched biological patterns that could highlight key tumorigenic processes. To test this, we ranked the entire transcriptome in order of the Wald statistic calculated during multivariate Cox regression analysis. We then used GSEA to probe this ranked list for established gene signatures enriched in transcripts with the greatest Wald statistic. Hallmark pathways, including oxidative phosphorylation, MYC targets, MTORC1 signaling, Glycolysis and DNA repair, were associated with high-risk genes (Fig. 2.13 A). Furthermore, enrichment of genes at chromosomal locations Chr13q12, ChrXp11, Chr16p12, Chr3q22, and Chr3q25 were associated with high-risk status (Fig. 2.13 B).

A Hallmark gene sets enriched in genes associated with increased risk

NAME	SIZE	ES	NES	NOM p-value	FDR q-value
HALLMARK_OXIDATIVE_PHOSPHORYLATION	200	0.48250204	2.3438652	0	0
HALLMARK_MYC_TARGETS_V1	199	0.4811729	2.3402896	0	0
HALLMARK_MTORC1_SIGNALING	198	0.4453736	2.1591268	0	0
HALLMARK_GLYCOLYSIS	174	0.4292439	2.0522869	0	0
HALLMARK_DNA_REPAIR	143	0.4340285	2.048816	0	0
HALLMARK_ADIPOGENESIS	184	0.39027727	1.8796716	0	7.95E-04
HALLMARK_PROTEIN_SECRETION	95	0.41465107	1.8330313	0	0.001475098
HALLMARK_UNFOLDED_PROTEIN_RESPONSE	111	0.4068424	1.7815337	0	0.003368181
HALLMARK_MYC_TARGETS_V2	56	0.4356806	1.7215402	0	0.005289557
HALLMARK_HYPOXIA	183	0.35446128	1.6935923	0	0.006379128
HALLMARK_E2F_TARGETS	193	0.34097087	1.6559026	0.00152439	0.009363162
HALLMARK_FATTY_ACID_METABOLISM	132	0.3566749	1.6433091	0.001545595	0.009962969
HALLMARK_PEROXISOME	86	0.35787502	1.5513692	0.006688963	0.021522515
HALLMARK_HEME_METABOLISM	166	0.32647696	1.5462751	0.001547988	0.021377744

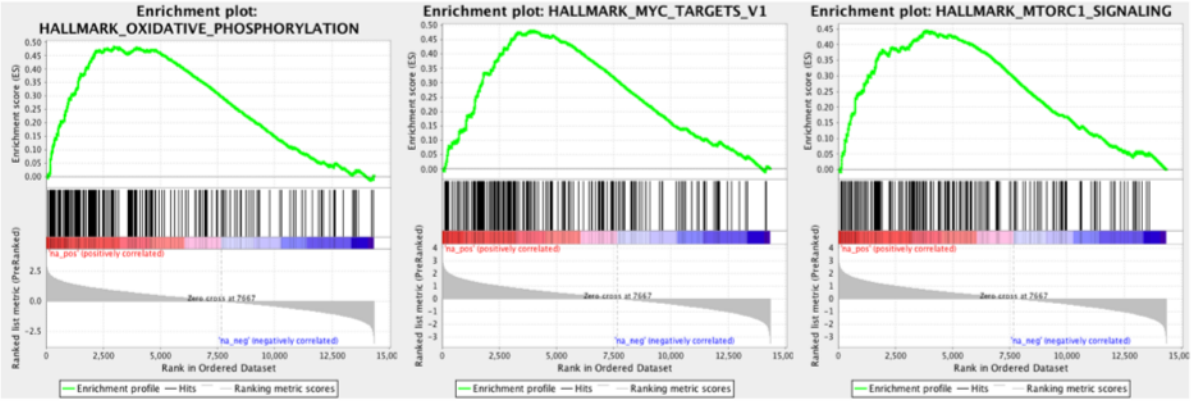

B Chromosome location gene sets enriched in genes associated with increased risk

NAME	SIZE	ES	NES	NOM p-value	FDR q-value
CHR13Q12	54	0.58430266	2.3514516	0	0
CHRXP11	101	0.5114061	2.2415895	0	0
CHR16P12	56	0.5525256	2.172779	0	3.84E-04
CHR3Q22	26	0.6217498	2.0837045	0	0.001436358
CHR3Q25	39	0.540593	1.9820813	0	0.00526297
CHR17Q12	40	0.53095615	1.9600989	0	0.005811802
CHR11Q14	32	0.5403765	1.8738503	0	0.013258558
CHR15Q23	19	0.5982987	1.837828	0.001795332	0.016123157
CHR8P22	29	0.5085268	1.7315481	0.003571429	0.040951725
CHR16Q23	23	0.526617	1.7146358	0.008741259	0.041767307
CHR11P14	18	0.5191604	1.5899329	0.02259887	0.08823041
CHRXQ24	19	0.52990526	1.5853989	0.02877698	0.08869763
CHR21Q21	15	0.5295314	1.5300134	0.047368422	0.11551796

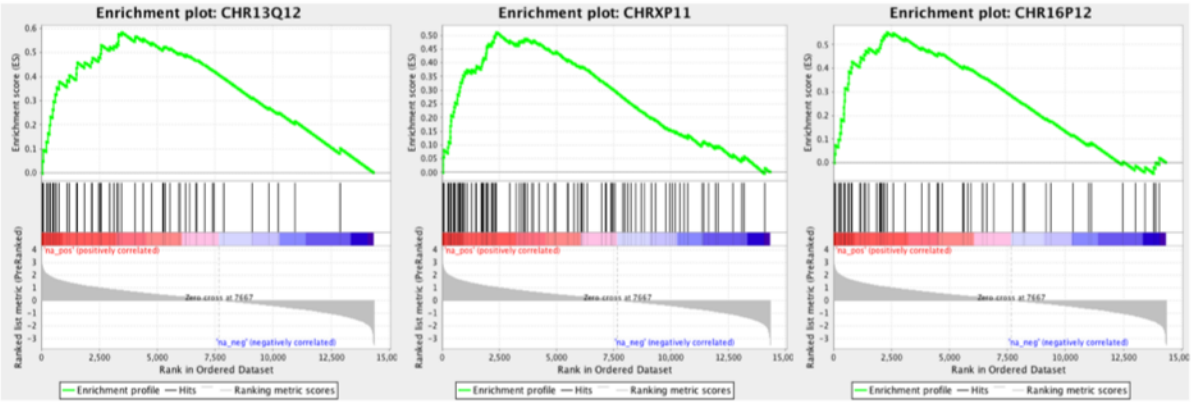

Fig. 2.13. Enriched gene sets in IvyGAP CT genes associated with increased risk. (**A**) Hallmark and (**B**) chromosome location gene sets enriched in genes associated with high risk of short overall survival with enrichment plots of the top 3 gene sets for each. ES: Enrichment score; NES: Normalized enrichment score; NOM: Nominal; FDR: False discovery rate.

2.5. Discussion

Improving outcomes for GBM is hindered by our inability to stratify patients into cohorts that have biologically distinct tumors requiring different clinical care. Patient-to-patient tumor comparisons are problematic in GBM due to intra-tumoral heterogeneity. We demonstrated that histologic structures account for part of this heterogeneity, and propose that assessing gene expression in CT will improve inter-tumoral comparisons. Our results highlight that using mixed-structure samples or samples rich in non-CT regions to determine GBM subtype could produce invalid results, while classifying subtypes using CT identifies distinct cohorts with unique biology. Additionally, utilizing exclusively CT, we created a prognostic model to identify the highest-risk patients. The biological patterns uncovered in the subtypes and risk-stratified groups have important implications for guiding precision medicine and steering future studies investigating malignant pathways in GBM.

The enriched biological processes we identified in GBM subtypes have the potential to guide therapeutic intervention. Proneural tumors showed enrichment of genes expressed during cell cycle checkpoints, stages of cell replication when DNA integrity is assessed. Current standard-of-care treatment for GBM is CRT, which functions through eliciting DNA damage (*1*). Having elevated expression of cell cycle checkpoints makes it plausible that proneural tumors

have different sensitivity to CRT than other subtypes, as CRT is known to have increased efficacy on highly proliferative cells. Accordingly, purely proneural tumors have been reported to have longer survival than other GBMs, while mesenchymal differentiation has been associated with therapeutic resistance and decreased survival (*24, 27, 33*). In contrast, mesenchymal tumors had enriched immune processes - the target of immunotherapies. This is consistent with previous reports showing that mesenchymal GBM has elevated immune activation and leukocyte infiltration (*30, 31, 141*). This distinction is essential to consider in the context of immunotherapies, as highly immunogenic tumors are more responsive to immunotherapy than tumors with a weak endogenous immune response (*140*). Thus, mesenchymal GBM may be exceptional candidates for single-agent immunotherapy, whereas proneural tumors may require an immunogenic vaccine prior to immunotherapy (*141, 327, 328*). Future studies should investigate the influence of pretreatment levels of cell cycle checkpoint transcripts and immune phenotype on GBM susceptibility to CRT and immunotherapies. Additionally, stratifying patients based on CT-characterized subtype in analysis of retrospective and prospective treatment efficacy trials may identify cohorts sensitive or resistant to specific therapies.

Our analyses of the established prognostic gene signature suggest that structure composition contributes to its prognostic prediction. Colman and colleagues noted that worse prognosis in their gene set was associated with a mesenchymal-angiogenic phenotype (*319*). This observation is supported by our findings that vascular and necrotic tissue have a poor prognostic signature and that vascular regions have a strong mesenchymal phenotype. While GBM is differentiated from grade III gliomas by the presence of vascular proliferation and necrosis (*5*), much less is known about how the extent of vascular proliferation and necrosis within GBM relate to the rate of tumor progression. It is plausible that the relative amount of these regions

within GBM may be prognostic themselves, perhaps secondary to rapid tumor proliferation. Other groups have noted that angiogenic, necrotic and highly proliferative GBMs may be more aggressive (*24, 329, 330*). As immunohistochemistry and magnetic resonance imaging (MRI) can detect these elements (*331, 332*), investigating the relationship between the level of vascularity and necrosis in GBM with survival merits further evaluation.

Using CT to create a novel prognostic gene signature allowed us to identify the highest-risk patients and probe the underlying biology of this cohort. Among the pathways we identified in the high-risk genes, MYC targets are attractive because MYC has multiple pro-tumorigenic functions in GBM (*333, 334*). Unfortunately, there are currently no clinically viable MYC inhibitors (*335*). Work developing these inhibitors is critical as they may have utility in treating the most aggressive GBMs. Additionally, multiple metabolic pathways were associated with high risk of rapid progression (Fig. 2.13A). Previous work has demonstrated a link between differential metabolic signatures with GBM subtypes (proneural-like and mesenchymal-like GBM stem cell lines) and outcomes (*336*). Taken together with our findings, this highlights the importance of GBM subtypes as possibly harboring distinct biology, bioenergetics, proliferative capacity, immune interaction, and disease progression, all of which are appreciable when accounting for structural variability in tumor analysis. Expression of genes from specific chromosomal locations were also enriched in the high-risk group. As MGMT promoter methylation is strongly correlated with survival outcomes in GBM (*39*), it is probable that unappreciated epigenetic modifications that drive rapid tumor progression exist. Epigenetic modifications are aberrant in many cancers, and are intriguing as they provide modifiable targets (*337*). While studies have investigated global methylation in GBM (*338*), we propose that specifically analyzing these patterns in CT may expose novel drivers of GBM malignancy.

As we have shown, CT-based transcriptomics permit inter-patient comparisons. This method can now be applied to developing a host of predictive gene signatures for clinical utility in GBM, and may be considered in developing transcriptomic-based predictions in other heterogeneous cancers. Specifically, the next steps include (1) creating predictive signatures for tumor sensitivity and response to different treatments, and (2) identifying methods to collect CT without microdissection. To create predictive signatures for treatment sensitivity that can be used for personalized medicine, studies should correlate gene expression in newly diagnosed GBM with outcomes following CRT, targeted therapies, and immunotherapies. This may be done in conjunction with standard treatment and during future clinical trials. Unfortunately, using CT for clinical purposes will be hindered by the labor-intensive microdissection that was used in development of the IvyGAP database, and work is needed to identify clinically feasible methods to collect CT. Image-guided biopsy is one potential method to obtain predominantly CT tissue. Previous investigations demonstrated that diffusion weighted MRI and amino acid positron tomography can localize GBM regions with elevated tumor cellularity and mitotic indices prior to resection (*339, 340*). These imaging modalities are already being integrated into the operating room via neuro-navigational image-guided tissue sampling and would allow for selective CT localization and biopsy (*341*). Alternatively, macro-dissection may be sufficient to collect cellular tumor with minimal contamination of other structures, and a study comparing the utility of this method versus microdissection is needed.

We have shown that analysis of transcriptomics in CT can stratify patients into distinct cohorts, and that using mixed structure samples can give misleading information. Ultimately, we believe the present study is a critical step in generating a novel set of transcriptomic-based clinical tools utilized to plan and execute optimal care for GBM patients.

Acknowledgements

The results described here are utilize data generated by the Allen Institute of Brain Science in collaboration with Swedish Medical Center and the Ben and Catherine Ivy Foundation and The Cancer Genome Atlas project and we thank them for all of the time and hard work dedicated to developing and maintaining these databases. We also sincerely thank Randall L. Woltjer, Paul Spellman, Rochelle Fu, and Guillaume Thibault for meaningful discussions throughout phases of conducting research and manuscript writing.

Data and materials availability All computer code used in this work will be free and open-source software available at https://github.com/gbm-dx (see below). IvyGAP data were acquired from http://glioblastoma.alleninstitute.org. TCGA data were acquired from https://portal.gdc.cancer.gov and https://tcga-data.nci.nih.gov/docs/publications/gbm_2013/.

Compiled code: This text provides the code used for all data analyses herein. These files are uploaded to GitHub and will be made public and freely available upon acceptance of the manuscript. The files include: (1) Creating the IvyGAP heatmaps in R; (2) Creating the TCGA heatmaps in R; (3) Performing IvyGAP data transformations in R; (4) Performing TCGA data transformations in R; (5) Identifying the top 1000 most variable genes in R; (6) Performing PCA in R; (7) Collapsing structures in R; (8) Analysis of previously established prognostic gene set in R; (9) Coxph survival univariate and multivariate analysis in R; (10) Stepwise CV coxph analysis in R; (11) Coxph survival model validation KM in R; (12) Logistic regression analysis in Python; (13) Balanced structures in Python.

CHAPTER 3: NON-INVASIVE ADVANCED IMAGING METRICS PROVIDE POTENTIAL BIOMARKERS FOR GBM BIOLOGICAL HETEROGENEITY AND IMMUNE LANDSCAPE VARIANCE.

Authors: **Cymon N. Kersch**[1], Leslie L. Muldoon[1], Rochelle Fu[2], Cheryl J. Claunch[3], Edward A. Neuwelt[1,4,5], and Ramon F. Barajas Jr.[6,7]

Affiliations:

[1]Department of Neurology, Blood-Brain Barrier Program, Oregon Health and Sciences University, Portland, OR 97239, USA.

[2] OHSU-PSU School of Public Health, Oregon Health and Sciences University, Portland, OR 97239, USA.

[3]Department of Biomedical Engineering, Knight Cancer Institute, OHSU Center for Spatial Systems Biomedicine, Oregon Health and Sciences University, Portland, OR 97239, USA.

[4] Department of Neurosurgery, Oregon Health and Sciences University, Portland, OR 97239, USA.

[5] Office of Research and Development, Department of Veterans Affairs Medical Center, Portland, OR 97239, USA.

[6] Advanced Imaging Research Center, Oregon Health and Sciences University, Portland, OR 97239, USA.

[7] Department of Radiology, Oregon Health and Sciences University, Portland, OR 97239, USA.

Manuscript in preparation.

Important notes: The analyses herein use data generated at the University of California San Francisco and documented in:

R. F. Barajas, Jr. *et al.*, Glioblastoma multiforme regional genetic and cellular expression patterns: influence on anatomic and physiologic MR imaging. *Radiology* **254**, 564-576 (2010).

3.1. Abstract

Background: Glioblastoma multiforme (GBM) is the most common and aggressive primary malignant brain tumor. Personalized treatment strategies for this tumor type is needed, but will require patient stratification, which is complicated by extensive tumor heterogeneity. We previously found that accounting for intra-tumor histological variability improved GBM genetic subtyping and tumor stratification. Unfortunately, analysis of transcriptional variance in histologically-defined tumor regions requires invasive tissue sampling, labor-intensive laser microdissection, and only provides a small snapshot of a single part of a tumor at one point in time. We hypothesize that neuroimaging measures correlate with genetic signatures, providing an alternative method for stratification.

Methods: We correlated gene expression patterns with magnetic resonance imaging (MRI) and histological features in newly diagnosed human GBM, using previously collected transcriptional profiles of GBM tissue obtained from image-guided biopsies. Gadolinium contrast enhancing lesion (CEL) and non-enhancing lesion (NCEL) regions within GBMs were subdivided based on physiologic imaging parameters (relative cerebral blood volume [rCBV] and apparent diffusion coefficient [ADC]) and histopathological features. Gene expression networks were probed using Gene Set Enrichment Analysis, while key immunologic genes were individually examined.

Results: GBM regions with different MRI and histopathological phenotypes displayed extensive transcriptional variance. This variance reflected biological networks, including multiple immune pathways. Comparing CEL and NCEL tumor revealed that CEL areas were more immunologic than NCEL, while NCEL regions showed stronger immune signatures than gliotic non-tumor brain. Subdividing CEL and NCEL based on rCBV, ADC, and histological phenotypes identified

sample clusters with different immune responses and expression of immune checkpoints. Mesenchymal subtype samples had the greatest immune response in all subgroup analyses. Conclusion and implications: MRI features identify tumor regions with discrete immunologic phenotypes. In the era of immunotherapies, understanding intra- and inter-tumoral immunologic variability is critical. Imaging biomarkers are a viable option for localizing GBM biological processes and tumor immune microenvironments across space and time.

3.2. Introduction

Glioblastoma multiforme (GBM) is the most common and aggressive primary malignant brain tumor, with a median survival of 18.1 months with standard of care surgical resection followed by chemoradiation (*1, 2*). Improved therapeutic protocols are desperately needed, but given the extensive inter-tumoral heterogeneity of GBM will necessitate stratifying patients based on different tumor biology and predicted therapeutic sensitivity (*23, 51*). Unfortunately, it is particularly challenging to stratify GBMs because this tumor also displays extensive intra-tumoral heterogeneity. The intra-tumoral heterogeneity of GBMs likely impacts therapeutic efficacy across a single tumor due to variable malignant cell phenotypes (such as The Cancer Genome Atlas (TCGA) molecular subtypes) and unique immune microenvironments in different spatial regions (*342*).

Previous work by our group demonstrated that GBM stratification techniques are improved by accounting for tissue histological variance (See Chapter 2). However, histological microanalysis relies on assessing gene signatures from laser microdissected tumor tissue, which is costly, labor-intensive, and unlikely to be clinically feasible. Furthermore, assessment of gene

expression from physical tissue samples requires invasive tumor sampling, which for patients with brain tumors can be accompanied by risks of cognitive deficits that have high morbidity (*343*). Tumor tissue sampling also captures only a small region of the tumor at a single point in time, and thus presents a small snapshot of the whole tumor and does not take into account therapeutically induced changes in the tumor over time. To overcome these significant clinical limitations, methods to assess clinically relevant molecular-level tumor biology using non-invasive imaging or simple tissue histochemistry biomarkers are needed.

Imaging genomics is a relatively new field within cancer biology and examines the relationship of imaging features with genomic and/or molecular tumor traits (*67*). It is the analytic marriage of new "omic" data with advanced non-invasive imaging phenotypes. Imaging features can be derived from multiple modalities including magnetic resonance imaging (MRI), computed tomography, and positron emission tomography (PET). The genomic and/or molecular tumor traits associated with imaging features can be (1) single gene or protein expression patterns or (2) multi-gene/protein networks. Most work in the field has focused on using imaging features as biomarkers to predict the phenotype of tumor related to a single prognostically significant gene. For instance, a large non-enhancing frontal lobe GBM lesion has been associated with isocitrate dehydrogenase 1 (IDH1) mutation, and rim enhancement in GBM is correlated with unmethylated O^6-methylguanine–DNA methyltransferase (MGMT) promoter status (*73, 74*). In this approach, the presence or absence of a radiographic feature from an entire MRI scan is correlated with the presence or absence of a molecular or genetic tissue characteristic that is assumed to be homogenous across a tumor; i.e. MGMT would be methylated in all tumor regions and thus the location of the tissue sample within the tumor is irrelevant. As such, the majority of imaging genomics studies have used samples from

unspecified locations within the tumor. Recently, imaging genomics studies have begun using image guidance to collect tissue from areas with defined imaging features (*68, 77, 344*). Common features sampled are gadolinium contrast-enhanced lesion (CEL) and non-contrast-enhanced lesion (NCEL). These image guided tissue samples with known imaging phenotypes enable identification of genetic/molecular signatures that vary across a tumor and are correlated with specific localized changes in gross tumor imaging. As this is a relatively new field, many molecular-imaging associations remain untested leaving important potential imaging biomarkers undiscovered.

Previous work by Barajas *et. al.,* 2010, one of the first publications linking spatially unique gene expression patterns to advanced imaging phenotypes, found that genetic and cellular expression patterns influence both anatomic and physiologic imaging of GBMs (*77*). The authors collected tissue under stereotactic image-guidance during initial tumor resection, targeting regions with pre-defined imaging characteristics including gadolinium CEL verses NCEL, and further defined areas of high verses low relative cerebral blood volumes (rCBV) and high verses low relative apparent diffusion coefficients (rADC) across their samples. rCBV, a measure of tumor angiogenesis, is obtained using dynamic susceptibility-weighted contrast-enhanced MRI. rADC, obtained using diffusion-weighted imaging, provides a measure of water diffusion within tissue. They performed RNA microarray analysis of the tissue samples and identified individual genes differentially expressed in samples with contrasting imaging regions. Additionally, the authors performed correlation analyses between histological patterns (tissue vascularity, hypoxia, and cellularity) with the imaging metrics. This seminal paper provided a foundation for the field, while also creating a data resource for further exploration of associations between tissue genetic characteristic with standard and advanced imaging phenotypes.

We questioned if the imaging and tissue expression patterns collected in Barajas *et al* could be used to develop biomarkers that identifying clinically important, unique biological and immunological networks in GBM. Previous analysis of this data investigated associations between standard immunohistochemical patterns and individual gene expression with imaging phenotypes, but did not probe larger biological networks. Now with current big data analysis tools, having whole transcriptome data allows for analysis of multi-gene signatures, which can provide robust associations between biological networks and sample variables (*317*). In the era of immunotherapies, we focused particularly on investigating gene signatures that inform on the immune landscape of GBMs and their relationship with imaging features that could provide non-invasive biomarkers for variable immune microenvironments. We tested the hypothesis that advanced imaging features can provide biomarkers for clinically important molecular phenotypes, including the tumor immune microenvironment.

In the present study we had three aims: (1) investigate the contribution of imaging metrics, histochemical features, and molecular attributes to heterogeneity in gene expression across all tumor samples, (2) explore tissue heterogeneity in the CEL, specifically probing for correlations between physiologic MRI and histopathological phenotypes with biological and immunology networks, and (3) examine tissue heterogeneity in the NCEL, again exploring correlations between physiologic MRI and histopathological phenotypes with biological and immunology networks. These analyses will help understand GBM inter- and intra-tumoral heterogeneity, aid in the development of non-invasive biomarkers to GBM tissue biological variances, and better understand biologic tissue features that underlie MRI features.

3.3. Methods

The data set and gene expression pre-processing. The analyses described herein were performed on previously described data (*77*). We mined imaging characteristics, histologically graded quantification, and microarray dataset. A detailed explanation of the data and methods used to generate these data are available, see Barajas et al 2010. Briefly, adult patients seen by the Neurological Surgery Department of the University of California, San Francisco were enrolled prospectively in a Health Insurance Portability and Accountability Act and Institutional Review Board compliant study. The total number of patients included in the final study was 13 (age 57.5±11 mean±SD; 8 male; 5 female). All tumors were newly diagnosed, treatment naïve primary GBM. Preoperatively, each subject underwent MR imaging on a 1.5 T Sigma Horizon MR imager (GE Medical systems, Milwaukee, WI). Diffusion weighted (DW) and dynamic susceptibility weighted contrast enhanced (DSC) MR imaging sequences were previously described (*77*). T2* DSC perfusion weighted (PW) images and DW images were used to produce cerebral blood volume (CBV) and apparent diffusion coefficient (ADC) maps, respectively. rCBV and rADC were calculated by standardizing the PW and DW measurements to a normal appearing white matter region on the contralateral hemisphere. MR images were processed by a blinded author on the original study and scored for tumor location, presence/absence of contrast enhancement, and area(s) of central necrosis. These regions were used for selection of biopsy site; up to six CEL and peritumoral NCEL regions were selected per subject prior to surgery.

Tissue specimens were collected with image-guided stereotactic biopsy. Each subject had variable numbers of samples obtained for each imaging region. Not all patients have data from

both regions. Half of each biopsy sample was used for histopathological assessment and half for RNA microarray analysis. For histopathology the following features were quantified: tumor cellular density, proliferation index, hypoxia, and microvascular expression and morphology (Table 3.1). Microarray analysis was performed using standard techniques by the UCSF Sandler Asthma Basic Research Center Functional Genomics Core Facility and staff (*345, 346*). Microarray RNA expression patterns from six gliotic, non-neoplastic human brain specimens were included for comparison. The RNA expression data was quantile normalized using the Linear Models for Microarray Data (LIMMA) R package (Bioconductor, Cambridge, England). These values were used for all analysis herein. For heatmap visualizations, the expression values were z-score normalized by gene across either all samples, CEL only samples, or NCEL only samples as indicated, where every transcript had mean value of 0 and standard deviation of 1.

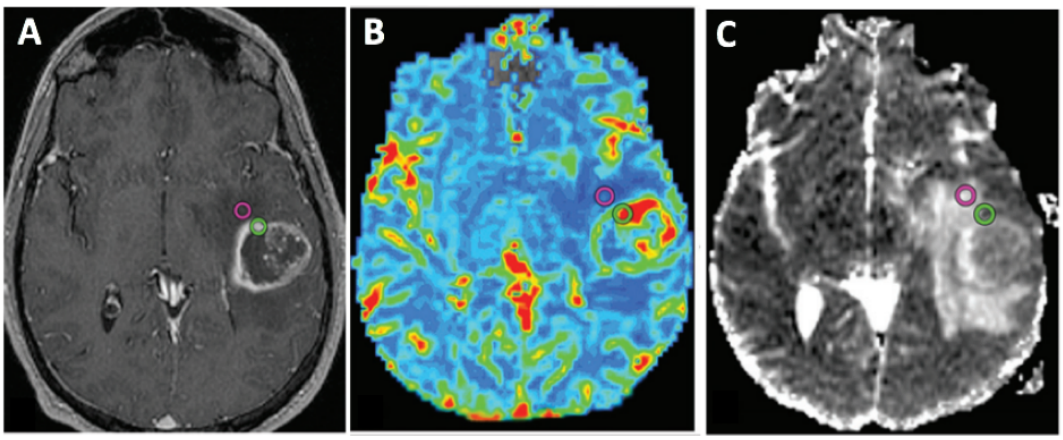

Fig. 3.1. Image-guided tumor tissue collection for gene expression analysis. MR imaging of a 51-year-old male with a left temporal GBM showing (**A**) T1-weighted contrast enhanced image, (**B**) aligned CBV map, and **(C)** aligned ADC map. Pink circles represent peritumoral contrast non-enhancing lesion (NCEL) tissue. Green circles represent contrast-enhancing lesion tissue (CEL). Green and pink circles show examples of biopsy location selection. Figure adapted from Barajas et al. 2010 (*77*).

Table 3.1. GBM MR imaging and histopathological phenotypes definitions; definitions adapted from Barajas et al. 2010 (*77*).

Tissue phenotype	Description
Contrast Enhancing Lesion (CEL)	Post-gadolinium signal enhancements on anatomic (T1- and T2-weighted) MR imaging.
Non-Contrast Enhancing Lesion (NCEL)	Post-gadolinium regions of non-enhancing tissue on anatomic (T1- and T2-weighted) MR imaging that surrounds enhancing material ('peritumoral').
ADC	Diffusion weighed (DW) images were processed to obtain the apparent diffusion coefficient (ADC). DW measurements were standardized to a normal appearing white matter region on the contralateral hemisphere to generate the relative ADC (rADC).
rCBV	T2* dynamic susceptibility weighted contrast-enhanced (DSC) perfusion weighed (PW) images were processed to calculate the cerebral blood volume (CBV). PW measurements were standardized to a normal appearing white matter region on the contralateral hemisphere to generate the relative CBV (rCBV).
CEL- or NCEL- CBV mean	Diffusion weighed (DW) images were processed to obtain the apparent diffusion coefficient (ADC). The mean of ADC measurements from the CEL or NCEL were then calculated.
Ca9 level*	Carbonic anhydrase IX (Ca9) monoclonal antibody immunohistochemical staining for tissue hypoxia on tissue sections were quantified on a four-tier scale: 0 = no immunoreactivity; 3 = intense immunoreactivity) in three 20x magnification fields.
Vascular Expression (Factor VIII morphology)*	Factor VIII monoclonal antibody immunohistochemical staining for vascular endothelium on tissue sections were quantified on a four-tier scale: 0 = no immunoreactivity; 3 = intense immunoreactivity) in three 20x magnification fields. Vascular morphology was graded as either: 1. Delicate: resembling normal vasculature. 2. Simple: hyperplastic vessels with a definitive lumen. 3. Complex: glomeruloid hyperplastic vessels.
MIB1L*	Mindbomb homolog 1 (MIB1L; AKA, Ki-67) monoclonal antibody immunohistochemical staining on tissue sections were quantified on a standard proliferation index (ref 40-45 in original pub).
Cell Count*	The total number of cells in 3 high power (20x magnification) fields were manually quantified and averaged.

**All assessment of histochemical tissue staining was performed by a blinded neuropathologist at UCSF.*

Heatmap Visualizations. Transcripts and samples were organized by unsupervised hierarchical clustering using Ward's method with the Euclidean distance metric; for molecular subtype heatmap displays rows were not clustered to maintain pre-determined gene order in relation to subtype signatures. Heatmap visualizations and hierarchical clustering were performed on *z*-score normalized data in R (pheatmap() function [pheatmap *R* package]) (Supplementary code S2, section 2.2). Gene lists for immune phenotypes were manually curated based on extensive literature search.

Principal Component Analysis (PCA). To assess variance among all sample transcriptomes in the data set, we performed PCA using the 1000 most variable genes (PCA() function in [FactoMineR *R* package] and [factoextra package in *R*])(*315*). Plots were made displaying principle component (PC) 1 vs PC2, PC3 vs PC4, and PC5 vs PC6. Samples on plots were colored by imaging metrics (contrast enhancement, rCBV, rADC mean, or CEL or NCEL ADC mean), histological score (overall vascular expression, Factor VIII expression with the morphological traits of delicate, simple, and complex vascular architecture, Ca9 expression, MIB1L expression, and total cell count), and TCGA molecular phenotype (original and revised molecular subtype gene expression signatures for proneural, neural, classical, and mesenchymal GBM subtypes) (*25, 26*) (Supplementary code S2, section 2.3).

Gene Set Enrichment Analysis (GSEA) to assess for correlated biological and immune processes and perform GBM subtype analysis. Gene set enrichment analysis was performed using GSEA software on quantile normalized expression values to compare CEL, NCEL and non-neoplastic gliotic tissue samples groups, and on pre-ranked lists of (1) z score normalized expression data of

CEL samples for subtyping analyses and (2) correlation coefficients from CEL and NCEL samples (described below) for association of biological and immunological processes with imaging and histopathological phenotype (*317, 322, 326, 347, 348*). Defaults were used for GSEA analysis, including Signal2Noise ranking metrics. Gene sets were excluded that were smaller than 15 genes and greater than 500 genes, and enrichment p-values were estimated by 1,000 permutations and corrected for multiple testing using the Benjamini-Hochberg method. Analyzed gene sets were from the curated molecular signature database (MsigDB): Gene Ontology (C5), Hallmark (H), or Immune (C7) collections, available at www.broadinstitute.org/gsea/msigdb/collections.jsp (*326, 347, 348*).

To test the correlation between gene expression networks and continuous (not dichotomized) imaging and histopathological metrics, a multi-step analysis pipeline was developed. The following was performed for CEL and NCEL samples separately. Spearman correlation analysis between every gene in the array dataset and each macroscopic and microscopic imaging phenotype variable (rCBV, rADC mean, CEL or NCEL ADC mean, MIB1L, Ca9, Cell Count, Vascular Expression, and Factor VIII simple, delicate and complex scores) were calculated (df.corr() function in R) (Supplementary code S2, section 2.4). Results including the gene name, statistic, and rho value were bound to a results table and exported. For each macroscopic and microscopic imaging phenotype variable, genes were ranked by their rho value. The ranked lists were converted to .rnk files and uploaded to GSEA software for interrogation of established gene sets for network analyses. Each ranked list was run for enrichment of Hallmark (n = 50) and Gene Ontology biological processes (n = 4436) gene sets. Ranked correlation lists describing the relationship between advanced physiologic MRI imaging parameters and gene expression were additionally probed for expression of Immunologic (n =

4872) gene signatures (C7) (*326, 347, 348*). Conservative Normalized Enrichment Score (NES) and false discovery rate (FDR) q values of 2.0 and 0.05, respectively, were selected as cut offs to define significantly enriched gene signatures. Compiled lists of all significantly enriched results are provided (Supplementary file S3). Functionally related enriched gene sets were manually interpreted and summarized herein. 'NA' in the summarized results tables indicates tests where no gene sets reached our thresholds for significance, with the exception of 'NA' in the NCEL correlation Ca9 and Factor VIII – Complex rows indicating comparisons that were not possible because the histopathological phenotypes did not exist in that tumor region.

For biological processes correlated with imaging features, GSEA results were visualized using the Enrichment Map plugin for Cytoscape (V2.8, www.cytoscape.org) (*318*). For visualization purposes, clusters of functionally related enriched GO terms were manually circled and labeled, and significance thresholds were set at a p-value cutoff 0.005 and an FDR q-value cutoff of 0.1.

Single gene expression assessment. Quantile normalized expression values for individually selected genes were plotted using GraphPad Prism version 6.0. Significant for differences between groups was tested applying a student's t-test with Bonferroni corrections to account for multiple comparisons. A p-value threshold of 0.05 was used to determine significance.

Ivy Glioblastoma Atlas Project (IvyGAP) database and analysis. Data from the IvyGAP, as described in detail in Chapter 2, was downloaded and used to assess expression of immune checkpoint genes and immune cell markers genes across GBM histological structures (*56*). Fold

change of individual gene expression was calculated from FPKM values. Significance was determined using a student's t-test, applying the Bonferroni method to correct for multiple comparisons. A p-value threshold of 0.05 was used to determine significance.

3.4. Results

3.4.1. MRI features, histopathological patterns, and molecular subtypes contribute to gene expression variability between and within GBMs.

Gadolinium contrast enhancement stratifies GBM samples with unique transcriptional characteristics.

We retrospectively analyzed microarray and corresponding imaging and histopathological data that were previously collected at the University of California, San Francisco (UCSF) (*77*). This dataset is comprised of microarray data from CEL and NCEL treatment naïve primary GBM tissue (Fig. 3.1). Advanced physiological imaging features (rCBV and ADC mean) were derived by a trained clinical neuroradiologist, and immunohistochemistry was performed on corresponding tissue blocks to assess vascularity (Factor VIII), hypoxia (Ca9), proliferation index (MIB1L), and cellularity (H&E) at UCSF (Table 3.1). In the present analyses we used quantile normalized microarray gene expression data from 13 subjects.

We analyzed the transcriptional profiles of CEL, NCEL, and non-tumor gliotic brain samples using principle component analysis (PCA) and gene set enrichment analysis (GSEA) (Fig. 3.2) (*315, 317, 326*). The first two principle components in the PCA explained 57.9% of the variance in the 1000 most variable genes in the dataset (Figure 3.2B). Samples separated along

the first principle component by enhancement characteristic (CEL vs NCEL) (Fig. 3.2 C). GSEA comparing CEL to NCEL and CEL or NCEL to gliotic non-neoplastic brain showed enrichment of cell division and immune processes, with cellular stress processes elevated in the CEL samples.

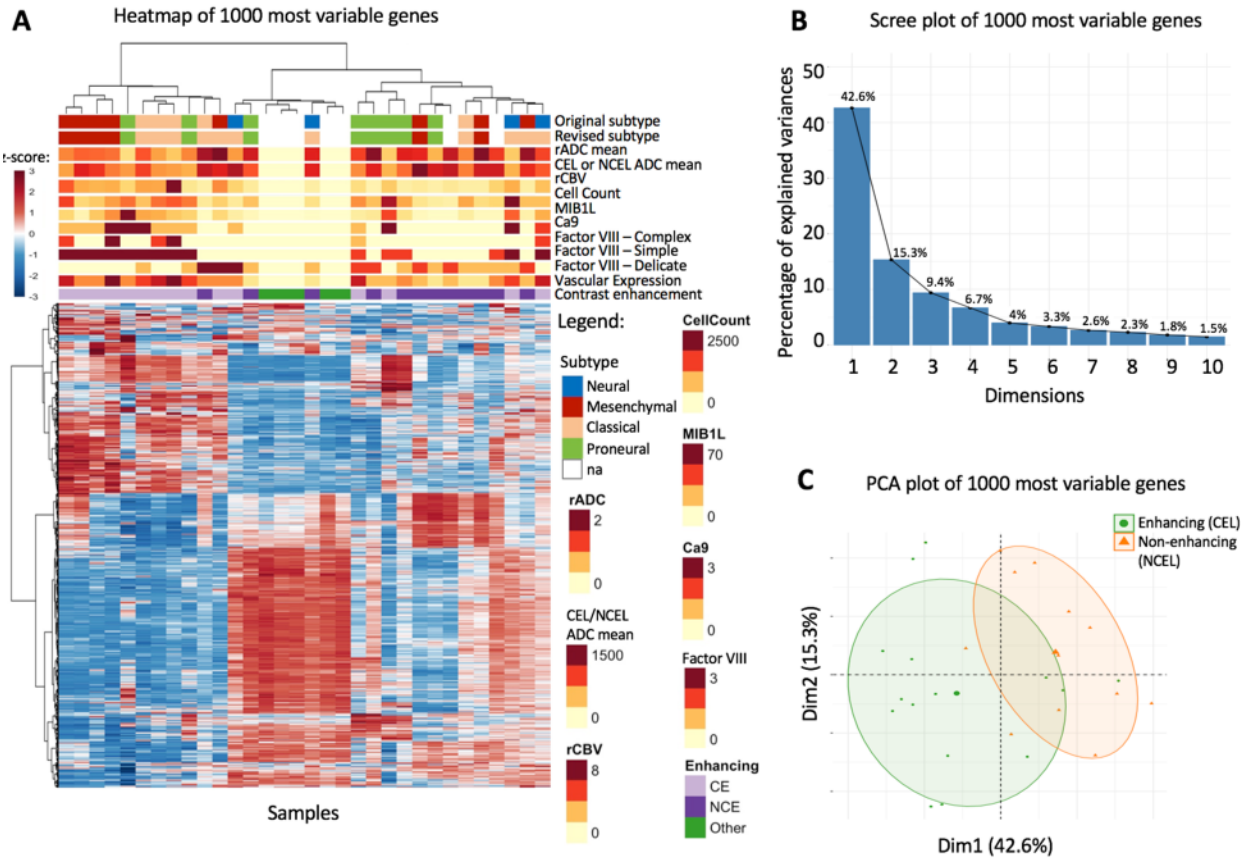

D Hallmark gene sets significantly enriched in:

CEL vs NCEL	CEL vs Non-neoplastic tissue	NCEL vs Non-neoplastic tissue
EPITHELIAL MESENCHYMAL TRANSITION	E2F TARGETS	G2M CHECKPOINT
E2F TARGETS	G2M CHECKPOINT	E2F TARGETS
G2M CHECKPOINT	EPITHELIAL MESENCHYMAL TRANSITION	INTERFERON ALPHA RESPONSE
TNFA SIGNALING VIA NFKB	INTERFERON GAMMA RESPONSE	INTERFERON GAMMA RESPONSE
INFLAMMATORY RESPONSE	ALLOGRAFT REJECTION	MITOTIC SPINDLE
IL6 JAK STAT3 SIGNALING	IL6 JAK STAT3 SIGNALING	ALLOGRAFT REJECTION
ALLOGRAFT REJECTION	INTERFERON ALPHA RESPONSE	
INTERFERON GAMMA RESPONSE	COAGULATION	
HYPOXIA	INFLAMMATORY RESPONSE	
ANGIOGENESIS	APOPTOSIS	
MYC TARGETS V1	ANGIOGENESIS	
COMPLEMENT		

Figure 3.2. MRI, histological, and molecular subtype features contribute to patterns of variation in GBM sample gene expression. (A) Heatmap displaying z-score normalized expression of the 1000 most variable genes (rows) in the dataset across all samples (columns; CEL, NCEL, and non-tumor controls). Samples and genes were organized by unsupervised hierarchical clustering, which results in a nearly perfect separation of the samples by enhancement region and of controls. Slight patterns of separation of samples by advanced imaging, histological, and molecular subtype features are also apparent. **(B)** Scree plot showing percent of variance described by each principle component (dimension) in analysis of the top 1000 most variable transcripts. **(C)** Principle component analysis (PCA) of dimensions 1 (Dim1) and 2 (Dim2) demonstrate that most variation in the data is explained by presence or absence of contrast enhancement in the tumor region from which the RNA was extracted. Each sample is represented as a symbol, and colored by the region (contrast enhancing, CEL, or peritumoral non-enhancing, NCEL) the sample was from; ellipses are drawn around samples from the same enhancement region (ellipse level=0.66). **(D)** Results from GSEA comparing samples showing major subdivisions in (A). Hallmark gene sets were tested, significance was defined as having a normalized enrichment score (NES) > 2.0 and false discovery rate (FDR) q value < 0.05.

Physiologic MRI, simple histological, and previously establish molecular features contribute to variance in GBM gene expression.

To determine if physiologic MRI, histopathological, and/or molecular features contribute to GBM gene expression heterogeneity we investigated if these characteristic contribute to any of the data point spread in the first six dimensions of the PCA, which together account for 81.3% of variance in the 1000 most variable genes. Our analyses revealed that while imaging and histopathologic features other than contrast enhancement contributed a lesser degree to variance in the 1000 most variable genes than contrast enhancement alone, they did show trends of impacting heterogeneous gene expression patterns (Fig. 3.3-3.5). Specifically, there were slight separations of samples along (1) the first and second principle component by rCBV, rADC mean, CEL ADC mean, Factor VIII expression classified morphologically, and Ca9 expression, (2) the third and fourth principle component by Factor VIII expression with complex morphology, and (3) the fifth and sixth principle component by MIB1L expression and cell count.

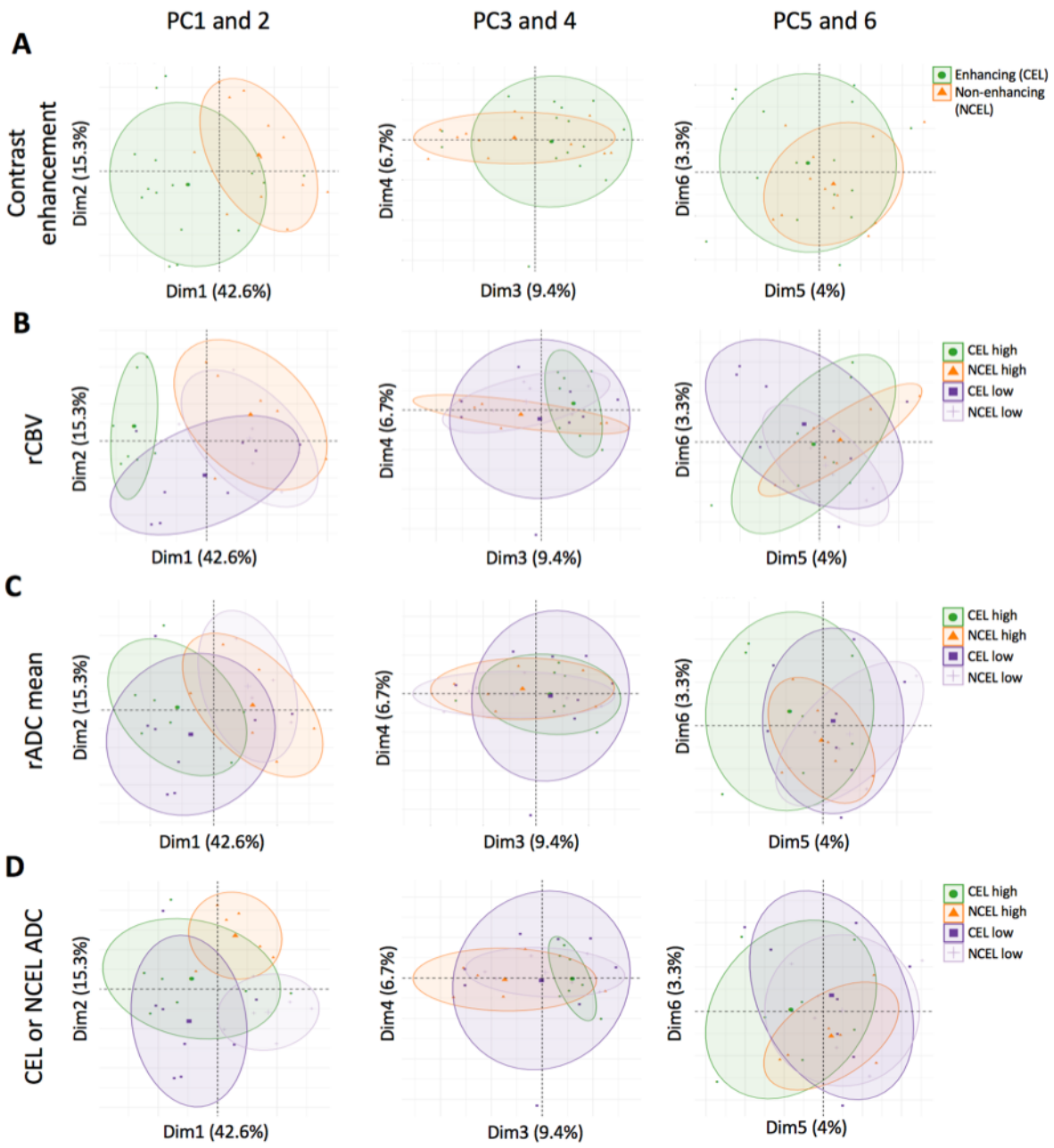

Figure 3.3. PCA labeling MRI features. Labeling samples from regions of **(A)** CEL and NCEL, **(B)** high rCBV (greater than the median rCBV in CEL [median = 3.79] and NCEL [median = 1.105]) and low rCBV in CEL and NCEL samples, **(C)** high rADC mean (greater than the median rADC mean in CEL [median = 1.09] and NCEL [median = 1.635] and low rADC mean in CEL and NCEL samples, and **(D)** high CEL or NCEL ADC mean (greater than the

median not adjusted ADC mean in CEL [median = 914] and NCEL [median = 1413.5] and low CEL or NCEL ADC mean on CEL and NCEL samples. Left column displays PC1 and PC2, middle column displays PC3 and PC4, and right column shows PC5 and PC6. Each symbol represents an individual sample. Ellipses are drawn around samples from the same imaging feature region (ellipse level = 0.66).

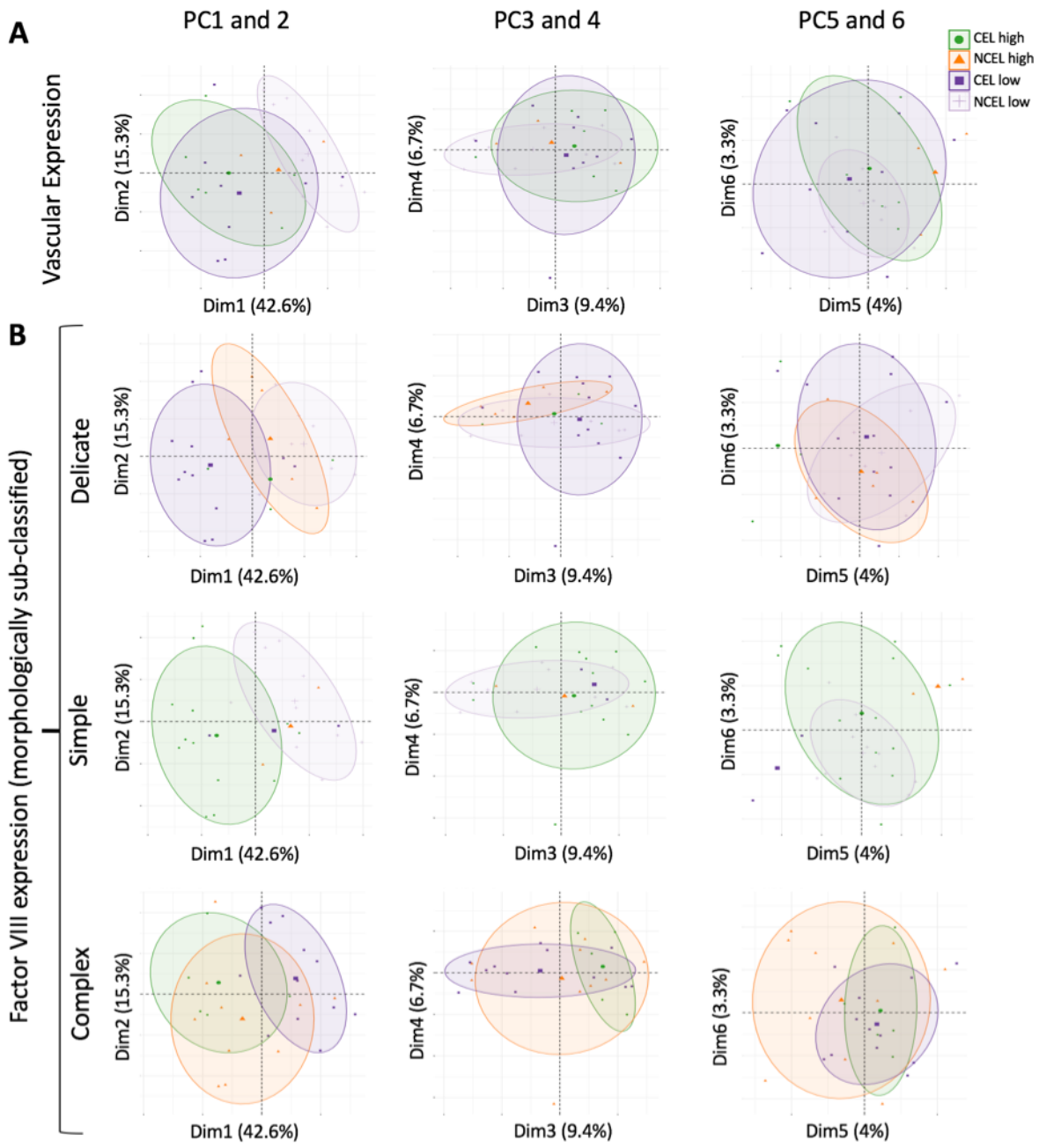

Figure 3.4. PCA labeling histologically defined vascular features. Labeling samples from regions of **(A)** high overall factor VIII expression (expression score ≥ 5 or 3 for CEL or NCEL, respectively) and low factor VIII expression (score < 5 or 3) in CEL and NCEL samples and **(B)** high and low factor VIII expression subdivided into complex, simple, and delicate vascular morphology (high expression score ≥ 2 for CEL and NCEL; low <2) in CEL and NCEL samples.

Left column displays PC1 and PC2, middle column displays PC3 and PC4, and right column shows PC5 and PC6. Each symbol represents an individual sample. Ellipses are drawn around samples from the same histological feature category (ellipse level = 0.66).

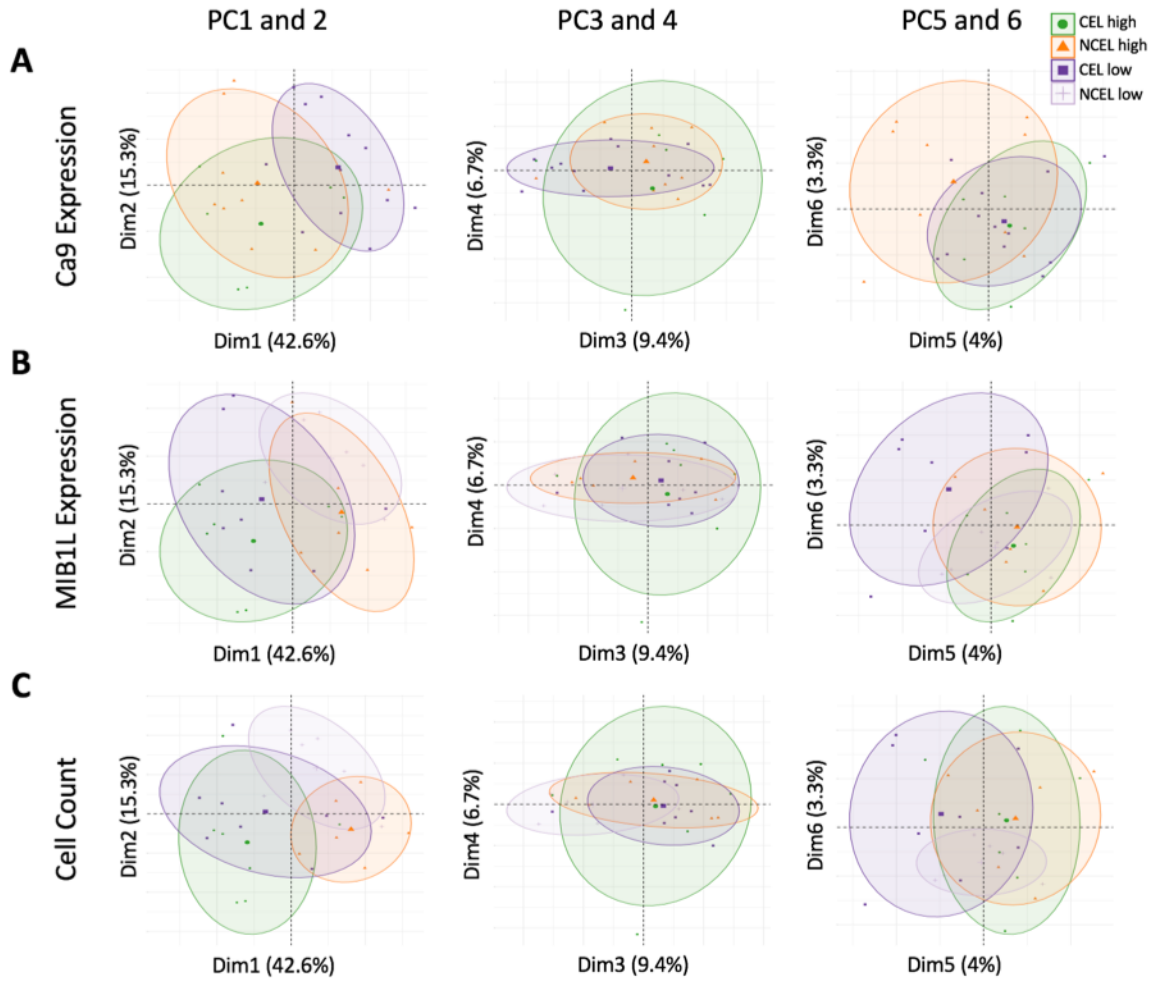

Figure 3.5. PCA labeling histologically defined tumor features. Labeling samples from regions of **(A)** high and low Ca9 (high expression score ≥ 2 for CEL and NCEL; low <2) in CEL and NCEL samples, **(B)** high MIB-1L.I% (greater than the median MIB-1L.I% in CEL [median = 22.1] and NCEL [median = 3.5]) and low MIB-1L.I% in CEL and NCEL samples, and **(C)** high total cell count (greater than the median cell in CEL [median = 1259] and NCEL [median = 617]) and low cell count in CEL and NCEL samples. Left column displays PC1 and PC2, middle column displays PC3 and PC4, and right column shows PC5 and PC6. Each symbol represents an individual sample. Ellipses are drawn around samples from the same histological feature category (ellipse level = 0.66).

Molecular gene expression panels have previously been shown to contribute to variance in GBM gene expression (*349*). Existing GBM molecular subtypes (proneural, neural, classical, and mesenchymal) were originally defined by expression of an 840-gene signature (*25*). Recently, this classification system was revised to three subtypes (proneural, classical, and mesenchymal) based on a 150-gene profiler (*26*). Previously, we showed that subtype signatures are more robust when classified based on gene expression in the cellular tumor histological structure (Chapter 2). As the contrast enhancing regions of GBM have the highest density of neoplastic cells, while peritumoral non enhancing tumor regions have lower cellularity (*77*), we reasoned that classification of subjects based on gene expression from CEL samples would be superior to classification calls derived from gene expression in NCEL samples. We therefore assigned the molecular subtypes of subjects in the current dataset based on gene expression in the CEL samples, and labeled samples from the NCEL the same subtype as their matched (same subject) CEL sample. Two NCEL samples did not have a matched CEL sample, and thus do not have a molecular subtype call. Molecular subtypes were determined using the single-sample GSEA subtyping method with pre-ranked gene expression lists (*26, 350*). Two molecular subtype calls were made for each subject applying the original and revised molecular subtype signatures. Other than the neural samples from the original subtype gene set calls, only two samples were reclassified as a different subtype using the revised molecular subtype gene signature. All samples labeled neural applying the original gene signature were re-classified as classical when the revised gene panel was used.

Similar to the imaging and histological features, molecular subtype classification contributes to variance in the gene expression dataset (Fig. 3.6). Heatmap visualization of the original and revised molecular subtype genes in all samples (CEL, NCEL, and non-tumor

controls) shows excellent separation of subtypes (Fig. 3.6 A,B). Furthermore, applying the original molecular subtype gene signatures showed that all of the control samples clustered together with high expression of the neural subtype genes. Neural has been proposed to be an artifact of the original gene signature that represent typical central nervous system tissue. It also appears that rCBV may be slightly elevated in the mesenchymal samples relative to other subtypes. Probing the top six principle components, subtype classification contributed to sample spread in multiple dimensions (Fig. 3.6 C,D).

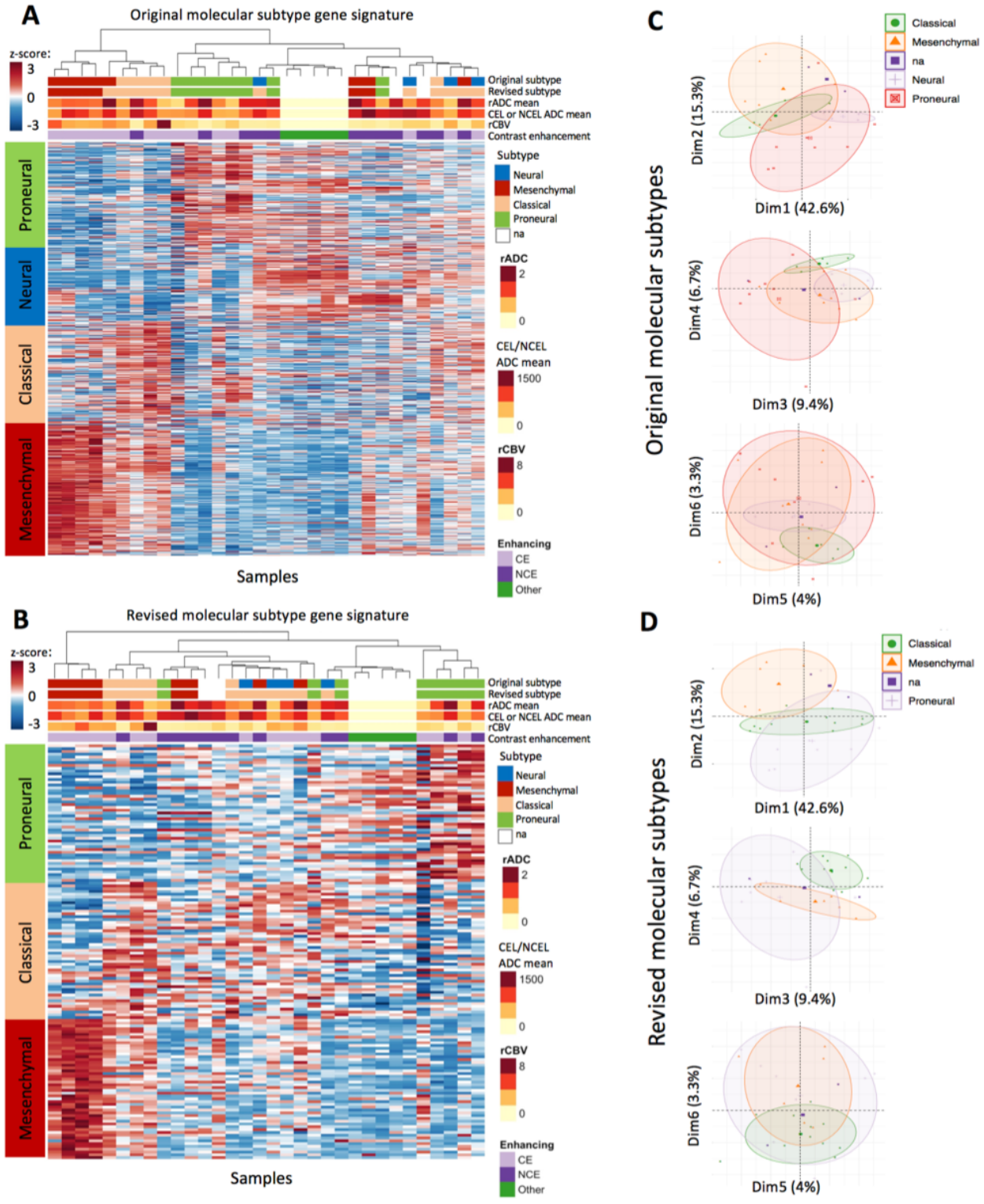

Figure 3.6. Molecular subtype classification contributes to variance in the dataset. (A, B)

Heatmap visualizations of the gene signatures for (**A**) the original GBM molecular subtype

classification scheme and (**B**) revised molecular subtypes gene signature in all samples. Unsupervised hierarchical clustering of samples (with individual gene expression z-score across all samples) showing clustering of samples based one subtype with minor patterns of sub-clustering relating to imaging features. **(C, D)** PCA plots labeling samples by molecular subtype as defined by (**C**) the original gene signature and (**D**) the revised gene signature. Left column displays PC1 and PC2, middle column displays PC3 and PC4, and right column shows PC5 and PC6. Each symbol represents an individual sample. Ellipses are drawn around samples from the same subtype (ellipse level = 0.66).

3.4.2. MRI features, histopathological patterns, and molecular expression signatures distinguish biological and immunological microenvironments within the CEL.

Biologically unique molecular subtypes can be distinguished within the CEL.

As discussed in Chapter 2, existing molecular subtypes of GBM (proneural, neural, classical, and mesenchymal) do not yet aid in clinical decision-making. We previously found that subtype gene expression varies across histological structures of GBMs, with gene expression in the cellular tumor best able to distinguish the subtypes. We reasoned that assessing subtype gene expression in the CEL of GBMs could provide a method to subtype tumors by targeting a region of high cellularity, but without having to microscopically dissect out cellular tumor. Our present analysis of subtype gene expression in CEL GBM samples showed that strong molecular subtype gene signatures are indeed present in the CEL, using both the original GBM molecular subtype gene signature and the revised gene signature (Fig. 3.7 A,B). Subtle patterns of potential

associations between subtype-specific gene expression and imaging and histopathological features were present. While we were unable to perform statistical comparisons due to the limited sample size for each subtype, these observational patterns provide hypothesis-generating information for future work. The mesenchymal subtype samples compared to the proneural subtype may be associated with elevated ADC, rCBV, and simple vasculature, and with decreased cell count, proliferation, and hypoxia. Meanwhile, the proneural subtype may have the highest cell count, proliferation index, and hypoxia of all the subtypes and the lowest rCBV and CEL ADC mean. Classical subtype samples appeared to fall between mesenchymal and proneural on the spectra of MRI features and histological tumor cellularity, proliferation and hypoxia. All samples that were classified as neural using the original subtype gene signature were re-classified as classical subtype with the updated signature. Performing unsupervised hierarchical clustering based on expression of only the revised gene set produced a near perfect split of the classical subtype samples that had been classified as classical in using both gene signature from those samples that were classified as neural using the original gene signature and then classical with the revised version (Fig. 3.7 B).

Using the revised subtype classification to define the molecular subtype of each CEL sample we tested the underlying biological differences between the subtypes. Our enrichment analysis testing hallmark gene sets differently expressed between the subtypes showed results that were remarkably similar to the those seen for the proneural and mesenchymal subtypes from both the IvyGAP and TCGA sample cohorts analyzed in Chapter two (Fig. 3.7 C,D). Proneural tumors had enrichment of cell cycle checkpoints (G1S and G2M) as well as elevated MYC targets. Mesenchymal tumors had enrichment of immunological processes including the IL-6, JAK, STAT3 signaling pathway, IFNγ response, and TNFα signaling via NFκB (Fig 3.7 D).

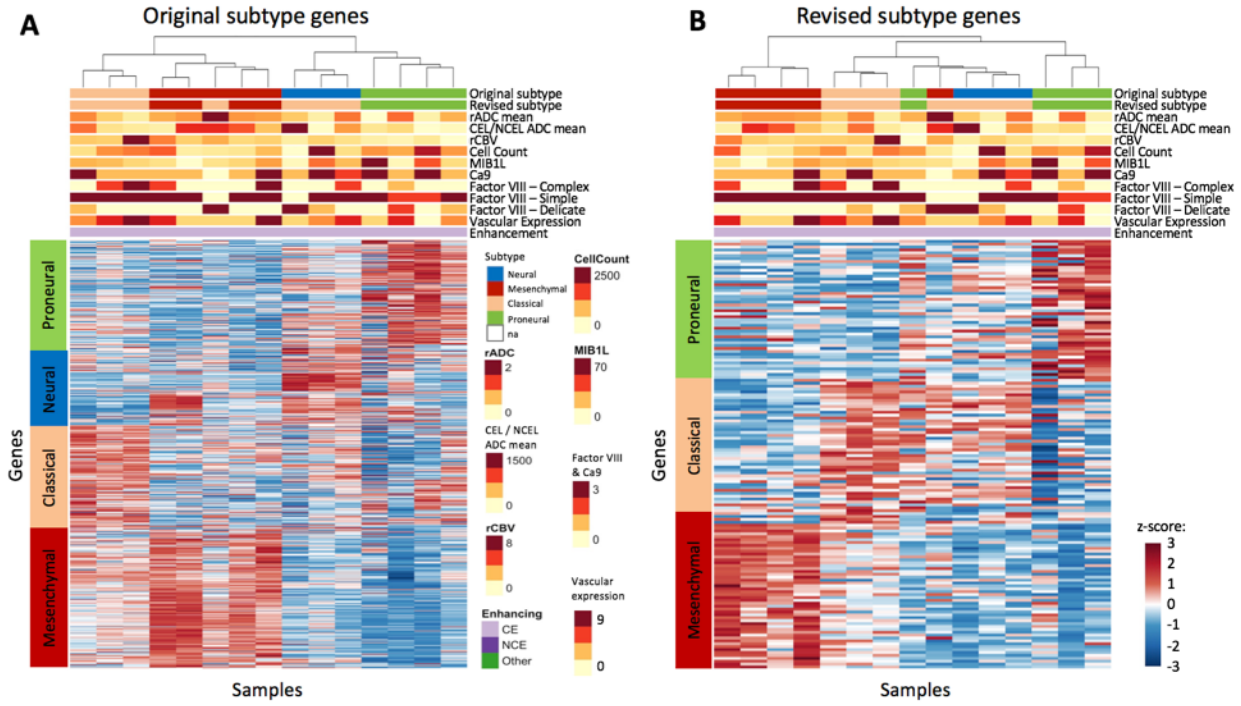

C Proneural Tumors (revised gene signatures)

Gene Set	G2M Checkpoint	E2F Targets	MYC Targets V1	MYC Targets V2
Enrichment Plots (enrichment score, ES)	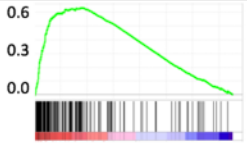	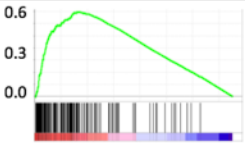	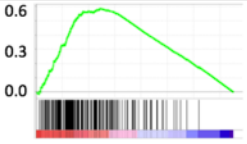	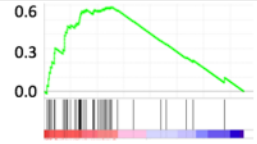
ES	0.635	0.697	0.585	0.588
NES	**2.789**	**3.042**	**2.506**	**2.077**
NOM p-value	0	0	0	0
FDR q-value	0	0	0	0

D Mesenchymal Tumors (revised gene signatures)

Gene Set	Inflammatory Response	IL6 JAK STAT3 Signaling	Interferon γ response	TNFα Signaling via NFκB
Enrichment Plots (enrichment score, ES)	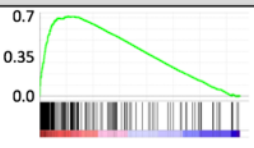	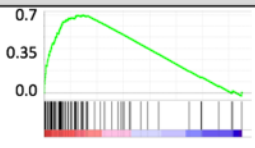	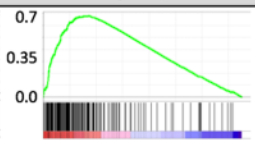	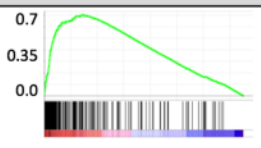
ES	0.711	0.697	0.679	0.702
NES	**2.729**	**2.411**	**2.604**	**2.676**
NOM p-value	0	0	0	0
FDR q-value	0	0	0	0

Figure 3.7. Molecular subtype classification of samples from the CEL are biologically distinct. (A) Heatmap displaying expression of the original GBM molecular subtype genes applying unsupervised hierarchical clustering of CEL samples (z-scored data across CEL

samples only) shows 4 main clusters with signatures of classical, mesenchymal, neural, and proneural GBM subtypes. **(B)** Heatmap displaying expression of the revised GBM molecular subtype genes applying unsupervised hierarchical clustering of CEL samples (z-scored data across CEL samples only) shows 3 main clusters with signatures of classical, mesenchymal, and proneural GBM subtypes. **(C-D)** Enrichment plots of hallmark gene sets in CEL samples from (C) Proneural versus REST (all samples not classified as proneural), and (**D**) Mesenchymal versus REST (all samples not classified as mesenchymal) analyses. Molecular subtyping was determined after z-score normalizing within only CEL samples and applying the revised GBM subtyping gene signature. ES: Enrichment score; NES: Normalized enrichment score; NOM: Nominal; FDR: False discovery rate.

Radiophenotypes are correlated with immunologic and tumor proliferation networks in the CEL.

We next investigated correlations between imaging features (radiophenotypes) and enriched hallmark and gene ontology biological processes in the CEL tumor samples. Our results showed that primarily immunologic, angiogenic, and tumor proliferation networks are significantly correlated with rCBV, rADC, and CEL ADC mean (Tables 3.2-3.3; Fig. 3.8, 3.9). Increasing rCBV is associated with elevated immunological networks including aspects of both the innate and adaptive immune system, type I and II interferon signaling, cytokine regulation and production (IL-1, 2, 4, 6, and 8), and macrophage activation with increased phagocytosis. Increasing rADC and CEL ADC mean were both positively correlated with a potentially less robust immune response, but still including interferon signaling, regulation of interleukins, production of TNF, and regulation of lymphocyte and macrophage activity. Alternately,

increases in rADC and CEL ADC mean were negatively correlated with cell proliferation networks such as cell cycle checkpoints and DNA replication, recombination, and repair.

Table 3.2 Hallmark networks associated with radiophenotypes in CEL.

	Positive correlation	Negative correlation
rCBV	**Strong immune response** (IFNγ and IFNα responses, TNF signaling via NFκB, and IL6/JAK/STAT3 and IL2/STAT5 signaling), **Epithelial-mesenchymal transition**, **Hypoxia, Angiogenesis, KRAS** signaling	NA
rADC	**Mild immune response** (IFNγ and IFNα responses, IL2/STAT5 signaling)	**Cell cycle/proliferation** (E2F targets and G2M checkpoint), **MYC targets expressed**
CEL ADC mean	**Mild immune response** (IFNα and IFNγ responses)	**Cell cycle/proliferation** (E2F targets and G2M checkpoint), **MYC targets expressed**

Table 3.3 Biological process networks associated with radiophenotypes in CEL.

	Positive correlation	Negative correlation
rCBV	**Immune response** (response to type I and II IFN, Leukocyte migration and activation, IL6 and IL8 production, regulation of IL1, IL2, and IL4, TLR signaling, innate and adaptive immune response, T and B cell migration and activation, macrophage activation and increased phagocytosis), **Angiogenesis**	**Normal neuronal biological processes** (synaptic signaling, regulation of calcium homeostasis, neurotransmitter transport and release), **RNA processing**
rADC	**Immune response** (response to type I and II IFN, negative regulation of a defense response and inflammation, B cell differentiation, Regulation of Th1 immune response, cytokine mediated signaling, regulation of IL1 and IL17 production, regulation of leukocyte activation and migration)	**Cell proliferation** (DNA transcription, replication, repair, and packaging, sister chromatid separation, cell cycle phase transition, histone methylation, cell division, microtubule organization, RNA processing)
CEL ADC mean	**Immune response** (innate & adaptive, positive & negative regulation of inflammation, regulation of IL1, IL6, IL4, IL10, and IL13 production, IL1 secretion, positive regulation of TNF superfamily production, T cell activation/differentiation, regulation of Th1 response, regulation of phagocytosis and respiratory burst)	**Cell proliferation** (DNA replication, recombination, repair, and packaging, sister chromatid separation, chromosome segregation, cell cycle phase transition, histone methylation, cell division, RNA processing)

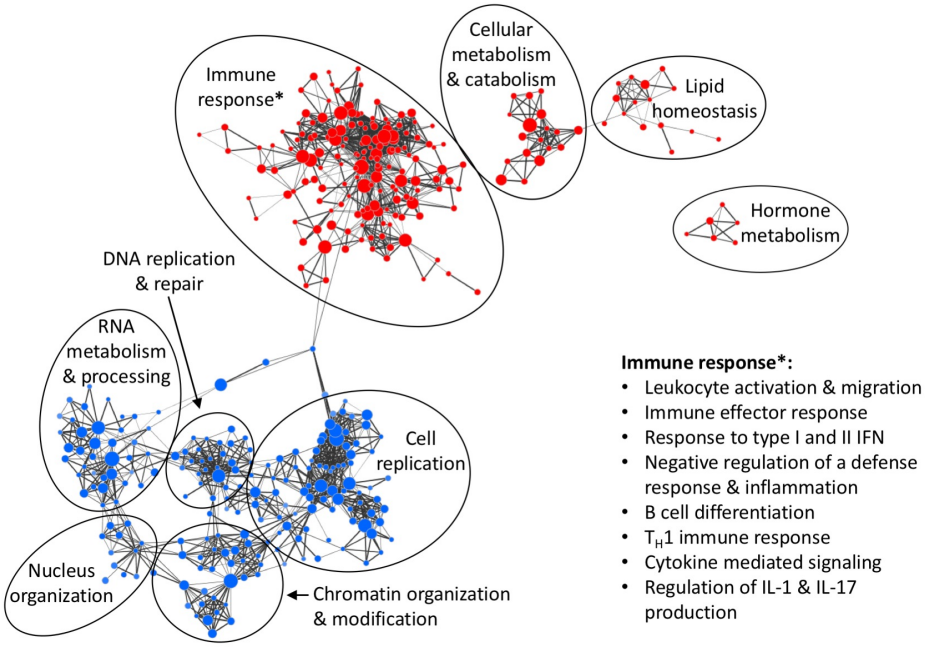

Figure 3.8. Biological networks correlated with ADC in CEL. Gene Set Enrichment Analysis (GSEA) followed by enrichment map visualization shows gene ontology (GO) biological processes that are positively (red nodes) and negatively (blue nodes) correlated with increasing ADC in CEL samples. Nodes represent GO terms. Clusters of functionally related enriched GO terms were manually circled and labeled. Node color represents a positive (red) or negative (blue) correlation. Node size is proportional to the number of genes within each GO term. Edge thickness signifies the overlap between GO terms (number of genes shared between two gene sets); thicker edges depict connections between nodes that share more genes than thinner edges. P-value cutoff = 0.005, FDR q-value cutoff = 0.1.

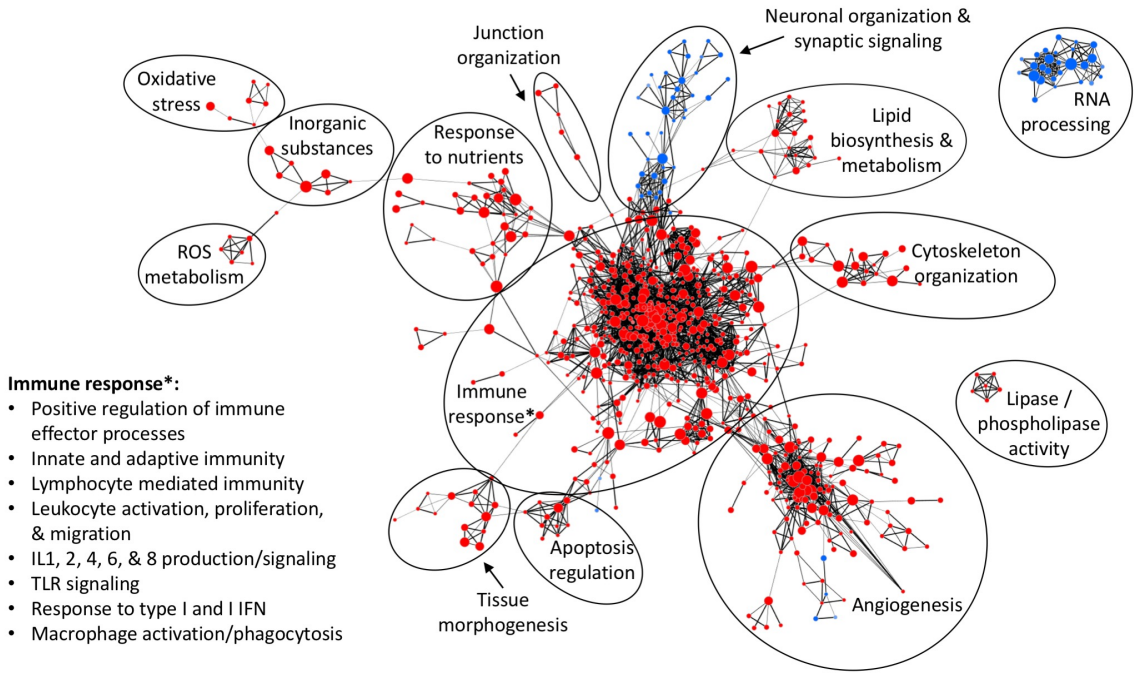

Figure 3.9. Biological networks correlated with rCBV in CEL. Gene Set Enrichment Analysis (GSEA) followed by enrichment map visualization shows gene ontology (GO) biological processes that are positively (red nodes) and negatively (blue nodes) correlated with increasing rCBV in CEL samples. Nodes represent GO terms. Clusters of functionally related enriched GO terms were manually circled and labeled. Node color represents a positive (red) or negative (blue) correlation. Node size is proportional to the number of genes within each GO term. Edge thickness signifies the overlap between GO terms (number of genes shared between two gene sets); thicker edges depict connections between nodes that share more genes than thinner edges. P-value cutoff = 0.005, FDR q-value cutoff = 0.1.

Histopathological phenotypes are correlated with immunologic, tumor proliferation, angiogenesis, cellular stress, and cellular metabolism networks in the CEL.

We tested correlations between histopathological phenotypes (immunohistochemistry markers of hypoxia, vascular expression and morphology, cell proliferation, and total cellularity) with enrichment of hallmark and biological processes in a similar manner to the imaging correlations addressed above. Our results showed that the underlying gene expression of tissues matched their histopathological phenotypes, which increased our confidence in the validity of the gene expression data and analysis pipeline used herein. For instance, enrichment of angiogenesis networks were significantly correlated with increasing expression of vascular markers and enrichment of cell division networks was significantly correlated with markers of cell proliferation and tumor cellularity. Our results also showed that increased expression of Ca9 is correlated with a robust and complex immune response, which likely includes counteracting arms of the immune system that both positively and negative regulate the immune response (Table 3.5). Vascular morphology patterns were shown to be differentially associated with molecular networks. Increased levels of simple and complex vasculature were positively correlated with angiogenesis, cellular metabolic processes, and cellular stress/hypoxia, while delicate vasculature was negatively correlated with cellular metabolic processes and vascular development. Increases in MIB1L (a marker of cell proliferation index) and total cellularity were negatively correlated with immunological networks including cytokine signaling, lymphocyte and monocyte chemotaxis, and positive and negative regulation of innate and adaptive immune elements (Table 3.4).

Table 3.4 Hallmark networks associated with histopathological phenotypes in CEL.

	Positive correlation	Negative correlation
Ca9	**Cell cycle/proliferation** (E2F targets and G2M checkpoint), **MYC targets** expressed, **MTORC1** signaling, and **cell stress** (unfolded protein response)	**Immune response** (IFNγ and IFNα responses and complement)
Vascular Expression	**Immune response** (IFNγ and IFNα responses, TNFα signaling via NFκB, and TGFβ, IL6/JAK/STAT3, and IL2/STAT5 signaling), **Epithelial-mesenchymal transition, hypoxia, and apoptosis**	NA
FVIII Delicate	NA	**Epithelial-mesenchymal transition, cell cycle/proliferation** (E2F targets, G2M checkpoint, and mitotic spindle), **MTORC1** and **MYC signaling, hypoxia, glycolysis, cytokine signaling** (TNFα signaling via NFκB), **coagulation,** and **cell stress** (unfolded protein response)
FVIII Simple	**Epithelial-mesenchymal transition**, **immune response** (IFNγ & IFNα responses, TNFα signaling via NFκB, and IL6/JAK/STAT3 and IL2/STAT5 signaling), **hypoxia, glycolysis, angiogenesis, cellular stress** (apoptosis, unfolded protein response, and UV response), **cholesterol homeostasis, coagulation, and PI3K/AKT/MTOR** & **MTORC1** signaling	NA
FVIII Complex	**Epithelial-mesenchymal transition, immune response** (IFNγ & IFNα responses, TNFα signaling via NFκB, and IL6/JAK/STAT3), **hypoxia, apoptosis, and coagulation**	NA
MIB1L	**Cell cycle/proliferation** (E2F targets, G2M checkpoint, and mitotic spindle), **MYC targets** expressed, and **MTORC1** signaling	**Immune response** (IFNγ and IFNα responses)
Cell Count	**Cell cycle/proliferation** (E2F targets, G2M checkpoint, and mitotic spindle) and **MYC targets** expressed	NA

Table 3.5 Biological process networks associated with histopathological phenotypes in CEL.

	Positive correlation	Negative correlation
Ca9	**Cell division** (DNA replication, repair, and packaging, sister chromatid segregation, cell cycle phase transition, membrane disassembly, mitotic nuclear division, chromatin modification, and histone methylation), **RNA processing**	**Positive & negative regulation of an** immune response (innate & adaptive, response to IFNγ, myeloid leukocyte activation, regulation of IL1, IL4, IL6, & TNF production, macrophage activation, monocyte chemotaxis, Th1 response, positive regulation of: lymphocyte differentiation, B & T cell proliferation, and phagocytosis, and negative regulation of: IL1 production, coagulation, and cell killing.
Vascular Expression	**Immune response** (IFNγ mediated signaling, antigen processing and presentation, response to type I IFN), and **tissue morphogenesis** (extracellular structure organization, cell matric adhesion, morphogenesis of epithelial sheet, blood vessel development, branching morphogenesis of an epithelial tube, establishment of planar polarity)	**Mixed cellular metabolic processes** (RNA catabolic process, protein localization to the ER, translation initiation), and **cholinergic synaptic transmission**
FVIII Delicate	**Normal neuronal processes** (neurotransmitter transport, synaptic signaling, calcium ion homeostasis, and dendritic spine development)	**Mixed cellular metabolic processes** (ER nucleus signaling, response to ER stress, ATP generation from ADP, telomere maintenance, monosaccharide biosynthesis, and response to topically incorrect protein), **vascular development** (blood vessel morphogenesis and extracellular structure organization), and **DNA packaging and repair**
FVIII Simple	**Angiogenesis** (blood vessel & branching structure morphogenesis, extracellular structure organization, smooth muscle cell migration), **immune response** (positive regulation of innate response, antigen processing/presentation via MHC I, response to type I and II IFN, and TLR4 signaling), **cell metabolic processes** (ER-nucleus signaling, ER stress, macromolecular metabolism, ATP generation from ADP), and **cellular stress** (glucose & amino acid starvation, extrinsic apoptotic signaling, membrane protein proteolysis, cytochrome c release from mitochondria, IRE1 mediated unfolded protein response, response to γ radiation)	**Mixed cellular metabolic processes** (RNA catabolic process, protein localization to the ER and cell membrane, translation initiation, and cytoplasmic translation) and **neurotransmitter regulation** (neurotransmitter transport, regulation of neurotransmitter levels, dopamine secretion, and neurotransmitter uptake)

FVIII Complex	**Angiogenesis** (extracellular organization, morphogenesis of vasculature, VEGF production, and regulation of endothelial cell apoptosis), **mixed cellular metabolic processes** (ER-nucleus signaling and macromolecular & nitrogen species metabolic processes), **cellular senescence**, **immune response** (IFNγ mediated signaling, leukocyte apoptosis, and antigen processing/presentation via MHC I), **cellular stress** (membrane protein proteolysis and response to: ER stress, topically incorrect proteins, & heat)	NA
MIB1L	**Cell division** (sister chromatid segregation, DNA replication, recombination, repair, & packaging, cell cycle transitions/checkpoints, chromatin modifications, telomere organization, mitotic spindle organization) and **RNA processing** (tRNA transport, mRNA and ncRNA processing, and RNA splicing)	Positive and negative regulation of innate and adaptive **immune responses** (cellular defense response, myeloid leukocyte activation, response to type I and II IFN, monocyte chemotaxis, Th1 response, Positive regulation of: IL1 secretion, T cell differentiation & proliferation, leukocyte proliferation, lymphocyte migration, and Negative regulation of: cell killing, leukocyte mediated immunity, IL1 production, lymphocyte mediated immunity, and leukocyte apoptosis
Cell Count	**Cell division** (sister chromatid segregation, DNA replication, mitotic nuclear division, recombination, repair, & packaging, cell cycle transitions/checkpoints, chromatin modifications, telomere organization, mitotic spindle organization), **RNA processing** (tRNA transport, mRNA and ncRNA processing, RNA splicing), and **positive regulation of cytokines**	**Immune response** (chemokine mediated signaling, lymphocyte & monocyte chemotaxis, regulation of IL6 production, and detoxification)

The CEL has a heterogeneous immune microenvironment, including variable expression of immune checkpoint genes.

Detection of immunologic networks were some of the most variable biological patterns observed in the CEL samples in the correlation analysis, leading us to investigate specifics of the immune response in enhancing regions of GBM. In the era of immunotherapies, establishing a detailed understanding the heterogeneity of cells crucial for tumor-immune interaction and expression of immune checkpoints is imperative. Furthermore, developing simple histopathological or even non-invasive imaging biomarkers for these tumor-immune interaction patterns will aid in the continued development and personalized use of immune modulating therapies. We probed the expression of immune checkpoint genes and individual genes known to mark immune cell types critical to the tumor-immune response (T cells, NK cells, and macrophages/microglia). Mesenchymal tumors had CEL regions with strong expression of both immune checkpoint and immune cell specific genes (Figure 3.10 A,B). As TAMs can activate to pro-inflammatory (anti-tumorigenic) or anti-inflammatory (pro-tumorigenic), also referred to as M1 and M2 phenotypes respectively, we questioned if there was heterogeneity in the polarization of TAMs across the CEL of GBMs. We found that genes associated with both M1 and M2 phenotypes were upregulated in the mesenchymal subtype CEL samples, while both were down regulated in proneural tumors, and displayed moderate expression in classical tumors (Fig. 3.10 C,D).

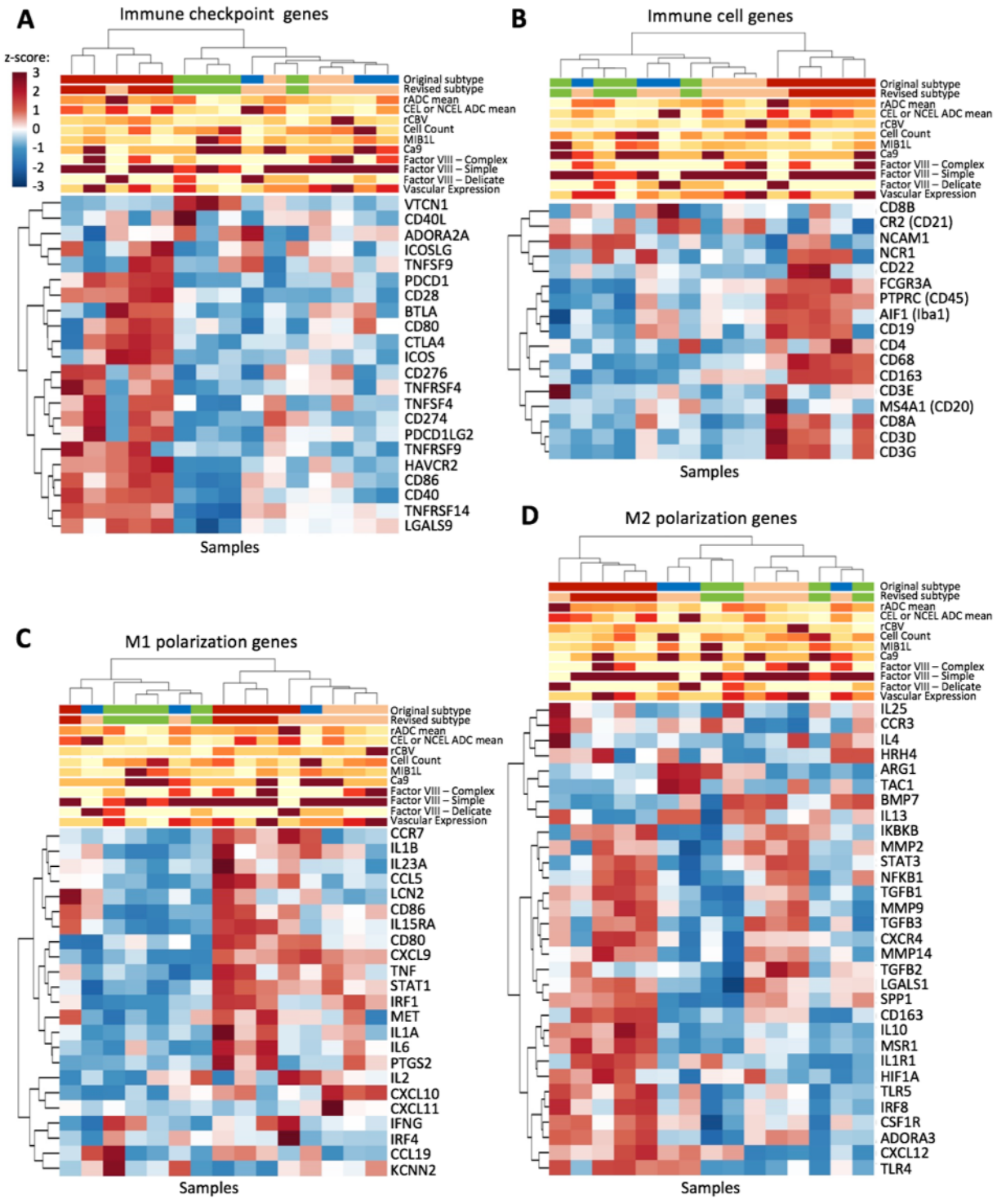

Figure 3.10. Immune gene expression in CEL samples. Heatmaps showing unsupervised hierarchical clustering of **(A)** immune checkpoint genes, **(B)** immune cell marker genes, and **(C, D)** M1 and M2 polarization gene panels. All genes were z-score normalized across CEL samples.

Cellular tumor samples from mesenchymal GBMs in the IvyGAP database display up regulated immune checkpoint and immune cell genes, corroborating the immune patterns of the CEL.

Contrast enhancing regions of GBM have generally higher tumor cellularity, thus it is plausible that gene expression in the cellular tumor of samples in the IvyGAP dataset may contain similar gene expression patterns to those of the image-guided CEL samples. We assessed if the expression of immune microenvironment and immune checkpoint genes differed between molecular subtypes in the cellular tumor using the IvyGAP database. Our results showed the same patterns that we observed in the CEL samples: mesenchymal tumors showed elevated expression of immune cell genes and immune checkpoint genes in the cellular part of the tumor compared to other subtypes, while proneural tumors had the lowest expression of these features (Figure 3.11).

A Checkpoint genes expressed in cancer and antigen-presenting cells

		PDL1 CD274_29126	B7H3 CD276_80381	CD86 CD86_942	CD40 CD40_958	CD70 CD70_970	B7RP1 ICOSLG_23308	GAL9 LGALS9_3965	PDL2 PDCD1LG2_80380	HVEM TNFRSF14_8764	OX40L TNFSF4_7292
PRO	Mean (SD)	0.640 (0.644)	5.129 (2.330)	4.394 (2.362)	1.618 (1.099)	3.078 (3.048)	0.403 (0.235)	3.706 (1.910)	1.146 (1.041)	1.254 (1.031)	0.456 (0.159)
REST	Mean (SD)	1.660 (1.481)	8.130 (2.607)	7.754 (4.991)	3.180 (3.497)	1.020 (1.366)	0.841 (0.488)	9.023 (4.827)	3.080 (2.499)	3.025 (1.945)	1.008 (1.205)
⬇	Fold change	0.386†	0.631†	0.567†	0.509	3.018	0.479†	0.411*	0.372†	0.414†	0.452
MES	Mean (SD)	1.920 (1.915)	8.783 (2.666)	10.771 (5.873)	4.619 (4.675)	1.278 (1.588)	1.023 (0.466)	11.228 (5.362)	4.033 (3.330)	3.916 (2.409)	1.555 (1.597)
REST	Mean (SD)	1.092 (0.948)	6.513 (2.691)	4.851 (2.101)	1.822 (1.214)	1.963 (2.584)	0.571 (0.409)	5.657 (3.370)	1.784 (1.193)	1.829 (1.134)	0.506 (0.306)
⬆	Fold change	1.758	1.349†	2.221*	2.536†	0.651	1.792†	1.985*	2.261†	2.141*	3.071†
CLA	Mean (SD)	1.919 (1.661)	7.853 (1.999)	6.182 (3.403)	2.058 (1.259)	0.471 (0.698)	0.744 (0.462)	7.751 (3.558)	2.768 (1.514)	2.823 (1.519)	0.980 (1.515)
REST	Mean (SD)	0.968 (0.979)	6.823 (3.309)	7.175 (5.352)	3.268 (3.905)	2.379 (2.457)	0.706 (0.494)	7.255 (5.627)	2.332 (2.795)	2.281 (2.131)	0.752 (0.538)
	Fold change	1.983	1.151	0.862	0.630	0.198†	1.054	1.068	1.187	1.238	1.304
NEU	Mean (SD)	1.072 (0.734)	7.302 (3.240)	6.446 (2.509)	2.338 (1.319)	0.944 (1.011)	0.616 (0.358)	7.691 (3.916)	2.240 (1.752)	1.958 (0.966)	0.734 (0.520)
REST	Mean (SD)	1.517 (1.604)	7.217 (2.701)	6.941 (5.484)	2.992 (3.771)	1.903 (2.423)	0.783 (0.527)	7.333 (5.339)	2.659 (2.625)	2.802 (2.214)	0.907 (1.245)
	Fold change	0.707	1.012	0.929	0.782	0.496	0.786	1.049	0.842	0.699	0.810

B Checkpoint genes expressed in T cells

C T cell and macrophage/microglia genes

		TIM3 HAVCR2_84868	A2aR ADORA2A_135	CD3 CD3D_915	CD3 CD3G_917	CD4 CD4_920	CD8 CD8A_925	IBA1 AIF1_199	CD68 CD68_968	CD163 CD163_9332
PRO	Mean (SD)	5.260 (2.918)	0.551 (0.392)	3.695 (6.718)	1.489 (1.419)	3.343 (1.548)	1.236 (2.359)	119.904 (71.056)	15.719 (9.310)	9.406 (6.534)
REST	Mean (SD)	9.715 (5.255)	0.421 (0.301)	2.324 (2.487)	1.355 (1.247)	8.112 (6.497)	0.514 (0.505)	246.348 (148.245)	31.047 (16.800)	21.117 (22.364)
⬇	Fold change	0.541†	1.309	1.590	1.099	0.412†	2.404	0.487†	0.506†	0.445
MES	Mean (SD)	12.168 (5.419)	0.481 (0.333)	3.029 (3.343)	1.906 (1.660)	10.205 (7.448)	0.724 (0.673)	343.068 (139.083)	38.757 (17.881)	32.578 (27.515)
REST	Mean (SD)	6.605 (3.860)	0.447 (0.332)	2.543 (4.449)	1.150 (1.005)	4.856 (3.978)	0.728 (1.582)	146.261 (90.770)	20.695 (12.258)	10.544 (8.719)
⬆	Fold change	1.842*	1.076	1.191	1.656	2.101†	0.995	2.346*	1.873*	3.090*
CLA	Mean (SD)	7.637 (3.998)	0.400 (0.258)	1.729 (1.348)	1.043 (0.584)	6.537 (4.119)	0.327 (0.201)	182.134 (111.737)	22.871 (10.371)	12.587 (12.501)
REST	Mean (SD)	8.942 (5.758)	0.503 (0.374)	3.381 (5.091)	1.641 (1.567)	6.621 (6.864)	1.006 (1.706)	233.769 (161.023)	29.106 (19.483)	21.232 (23.180)
	Fold change	0.854	0.795	0.511	0.636	0.987	0.325	0.779	0.786	0.593
NEU	Mean (SD)	9.463 (5.661)	0.500 (0.285)	1.276 (0.687)	0.940 (0.495)	6.956 (5.072)	0.450 (0.265)	219.540 (123.326)	32.778 (20.940)	20.805 (21.393)
REST	Mean (SD)	7.827 (4.774)	0.432 (0.355)	3.570 (4.945)	1.643 (1.504)	6.385 (6.288)	0.877 (1.654)	207.477 (155.256)	23.136 (12.696)	15.964 (19.074)
	Fold change	1.209	1.157	0.357†	0.572†	1.089	0.513	1.058	1.417	1.303

Red = corrected p < 0.05*
Green † = p < 0.05 before multiple comparison correction

Figure 3.11. Immune checkpoint distribution in the cellular tumor of different GBM molecular subtypes from the IvyGAP database. Mean gene expression and standard deviation for proneural (PRO), mesenchymal (MES), classical (CLA), and neural (NEU) samples for **(A)** immune checkpoint genes expressed by tumor and antigen presenting cells, **(B)** immune checkpoint genes expressed by T cells, and **(C)** T cell and macrophage/microglia marker genes. Fold changes was calculated for each by dividing the average gene expression for subtype by the average gene expression of all other subtypes. P values were corrected for multiple comparisons using the Bonferroni method. Fold changes highlighted in red with * have p-values < 0.05 after correcting for multiple comparisons, while fold change values in green with † had p-values <

0.05 before adjusting for multiple comparisons, but not after. Red arrows: overall trend of differential gene expression in that row.

Radiophenotypes in the CEL may provide biomarkers for specific immune network expression.

Immune networks were among the top enriched processes in the hallmark and biological networks in the CEL samples. As developing an imaging biomarker for variable immune phenotypes would be clinically beneficial, we investigated deeper into complex immune processes correlated with radiophenotypes. We evaluated correlations between physiologic imaging phenotypes in the CEL with a large database of immunologic gene signatures (*348*).

Our analysis of the immune microenvironment in the CEL revealed that rCBV, rADC, and CEL ADC mean are all correlated with unique immune phenotypes (Table 3.6). Increasing rCBV was positively correlated with a high prevalence of mixed phenotypic macrophages/ microglia with evidence for M2 polarization, T cell populations (CD4+ and CD8+) that may be immunosuppressive, a minor population of unstimulated B cells, and a unique subset of polyfunctional NK cells that are potentially more prevalent than other cytotoxic cells. Increasing rADC was positively correlated with weakly stimulated macrophages, pro-inflammatory activated lymphocytes, the presence of polyfunctional NK cells, and possible mast cell infiltration. Lower rADC was correlated with IL-4 stimulated and resting macrophages, effector CD8+ cytotoxic T cells, unstimulated B cells, and IL-15 stimulated NK cells (IL-15 has been shown to cause exhaustion in NK cells) (*351*). Patterns of immunologic networks that were correlated with rADC and CEL ADC mean were highly similar. Results also suggested that increasing CEL ADC mean correlated with increased neutrophils.

Table 3.6 Immunological networks associated with radiophenotypes in CEL.

		Positive correlation	Negative correlation
rCBV	Macrophage & Microglia	Mixed phenotypes: Possible IFNγ stimulated microglia and M2 polarization, untreated>TGFβ or IFNγ stimulated macrophages, pro-inflammatory monocytes	NA
	T cell	Possibly CD4+>CD8+, effector>memory and memory>unstimulated CD8+, CD8+ are BTLA+, CD161high, and CXCR1-, Tregs present, possible Th2 and Th23 CD4+	NA
	B cell	Naïve/unstimulated > plasmablasts, IgM, or IgG stimulated cells, less B than T cells	NA
	NK cell	Polyfunctional subset present (CD56dim CD62L+), NK > NKT and CD8+ T cells	NA
	Other	Macrophages > other immune cell types; possible neutrophil & basophil presence	NA
rADC	Macrophage & Microglia	Weakly stimulated macrophages and monocytes, more macrophages than other immune cells	IL4 stimulated and resting macrophages (vs steroid treated and M2 cells)
	T cell	Th1>Th17, IL4>control & untreated>IL2 or IL21 stimulated	Effector CD8+, Unstimulated CD4+, Induced Treg presence
	B cell	B2 (adaptive) > B1 (innate phenotype)	Unstimulated>IgM stimulated
	NK cell	Polyfunctional subset present (CD56dim CD62L+)	IL15 stimulated
	Other	Possible mast cell presence	NA
CEL ADC mean	Macrophage & Microglia	Weakly stimulated macrophages and monocytes, more macrophages than other immune cells	IL4 stimulated and resting macrophages (vs steroid treated and M2 cells)
	T cell	IL4>control & untreated>IL2 stimulated, possible Tregs & memory CD8+	Effector CD8+, Unstimulated CD4+, Induced Treg presence
	B cell	NA	Unstimulated>IgM stimulated; likely more B than NK cells
	NK cell	Polyfunctional subset present (CD56dim CD62L+)	IL15 stimulated
	Other	Possible neutrophil presence	NA

3.4.3. MRI features, histopathological patterns, and molecular expression signatures distinguish biological and immunological microenvironments within the NCEL.

Molecular subtype defining genes are expressed irregularly in the NCEL.

Expression of genes defining the original and revised GBM molecular subtypes show only minor expression patterns in the NCEL (Fig. 3.12 A,B). We previously found that GBM samples from the infiltrative and leading edge of the tumor contain variable amounts of non-tumor brain tissue that skews genotyping toward the neural and proneural subtypes, independent of gene expression within the malignant cells. Therefore, we did not subtype the NCEL samples; all molecular subtype assignments were determined based on gene expression in the matched CEL sample. Subjects that had only a NCEL sample with no CEL sample do not have a subtype call. Clustering of samples followed subtype calls from the matched CEL samples, as demonstrated by the clustering of subtype calls at the top of each heatmap (Fig. 3.12 A,B). Again, samples that were classified as neural applying the original subtype signature and classical utilizing the revised gene set, separated from all other classical samples. Samples classified as mesenchymal show a minor trend in having increased NCEL ADC mean, while classical subtype NCEL samples show low rCBV values. We were unable to test differences in hallmark gene expression of NCEL samples of varying subtypes due to the small sample size within each subtype cohort.

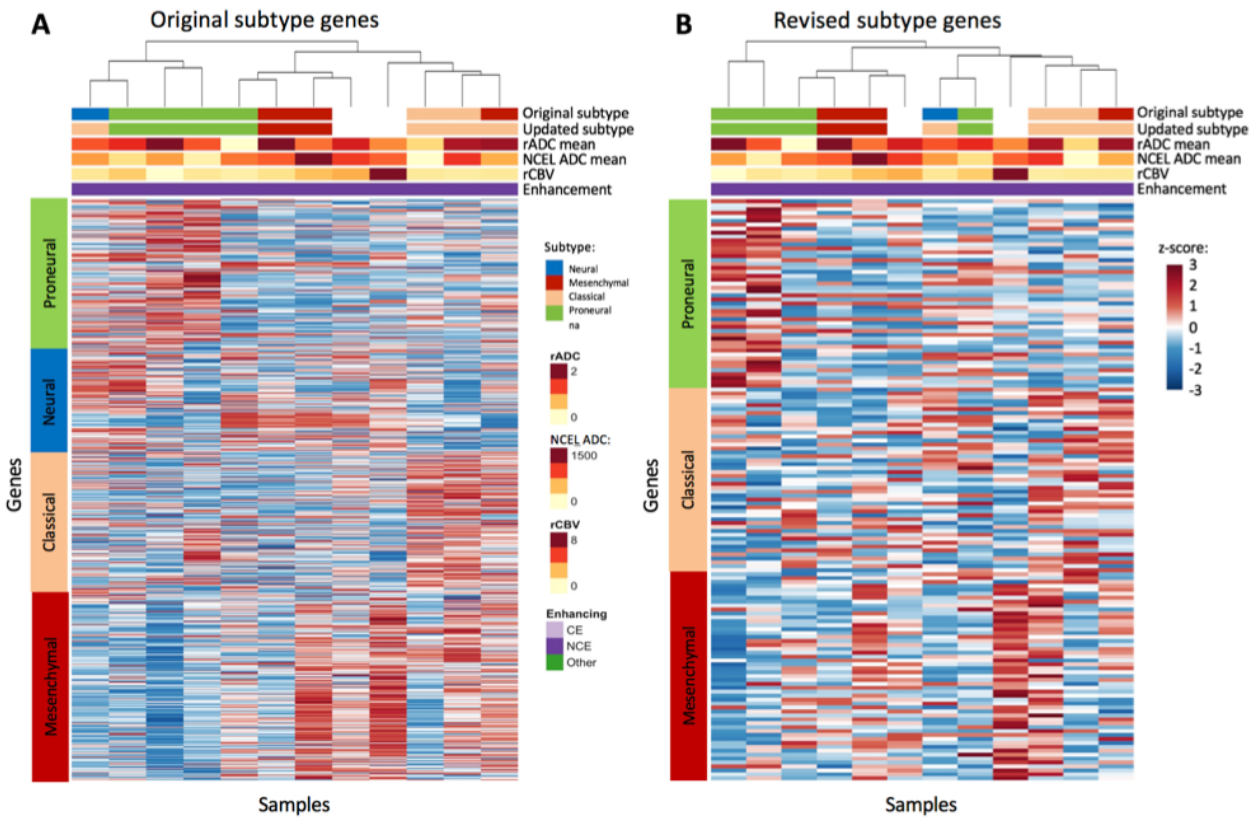

Figure 3.12. Expression of molecular subtype defining genes in samples from the NCEL. **(A)** Heatmap displaying expression of the original GBM molecular subtype genes applying unsupervised hierarchical clustering of NCEL samples (z-scored data across NCEL samples only) shows 3 weak clusters with signatures of classical, mesenchymal, and proneural GBM subtypes. **(B)** Heatmap displaying expression of the revised GBM molecular subtype genes applying unsupervised hierarchical clustering of NCEL samples (z-scored data across NCEL samples only) shows weak sample clustering. Subtypes calls in the top two rows of each of the heatmap visualizations were determined based on gene expression from matched CEL samples.

Radiophenotypes are correlated with immunologic and cellular proliferation networks in the NCEL.

We next investigated correlations between imaging features and enriched hallmark and gene ontology biological processes in the NCEL tumor samples, as we previously tested in the CEL samples. Primarily immunologic, mitotic, and cellular respiration networks were significantly correlated with rCBV, rADC, and CEL ADC mean (Table 3.7-3.8; Fig. 3.13, 3.14). Increasing rCBV was positively correlated with elevated immunological networks including aspects of both the innate and adaptive immune system, IFNγ signaling, regulation of interleukin signaling (IL-1, 2, 4, 6, 8, and 10), macrophage activation with decreased phagocytosis, and negative regulation of Il-1 and TNF production, while it negatively correlated with cell proliferation networks. Unlike in the CEL, rADC and NCEL ADC mean oppositely correlated with immunologic networks. While rADC was negatively correlated with immune networks, NCEL ADC was positively correlated with immune processes.

Table 3.7 Hallmark networks associated with radiophenotypes in NCEL.

	Positive correlation	Negative correlation
rCBV	**Immune response** (IL2/STAT5, IL6/JAK/STAT3, and TNFα via NFκB signaling, and IFNγ response), **KRAS** signaling	**Cell cycle/proliferation** (E2F targets and G2M checkpoint), **MYC targets expressed**
rADC	NA	**Immune response** (IFNα and IFNγ response, and IL6/JAK/STAT3 and TNFα via NFκB signaling)
NCEL ADC mean	**Mild immune response** (IL6/JAK/Stat3 signaling and INFγ response	**Oxidative phosphorylation**

Table 3.8 Biological process networks associated with radiophenotypes in NCEL.

	Positive correlation	Negative correlation
rCBV	**Immune response** (positive and negative regulation of defense & immune response, activation of innate & adaptive immunity, macrophage activation, positive regulation of T cell proliferation, B cell receptor signaling, cytokine secretion, regulation of IFNγ, IL6, IL4, IL8, & IL10, positive regulation of IFNγ, IL6 & IL10 production, negative regulation of Il1 & TFN superfamily cytokine production, phagocytosis, and mast cell immunity)	**Positive and negative regulation of mitosis** (DNA replication, chromatin remodeling, membrane disassembly, DNA repair, cell cycle checkpoints, negative regulation of the G1-S phase of cell cycle, and chromosome segregation) **RNA processing and transport, gene silencing**
rADC	Protein-protein interactions and nucleosome organization	**Immune response** (antigen processing and presentation via MHCI, response to type I and II IFN, activation of innate immune response, FC receptor signaling, and pattern recognition receptor signaling)
NCEL ADC mean	**Immune response** (innate and adaptive inflammatory response, pattern recognition receptor and toll like receptor signaling, Regulation of IL6, IL1, IL12, and TNF superfamily cytokine production, positive response to IL6 production, regulation of T cell activation and proliferation, myeloid leukocyte activation, necrotic cell death, leukocyte degranulation)	**Normal neuronal processes** (synapse structure and function, dendrite morphogenesis, synaptic plasticity, neurotransmitter transport, ion transport, cognition), **oxidative phosphorylation and cellular respiration**

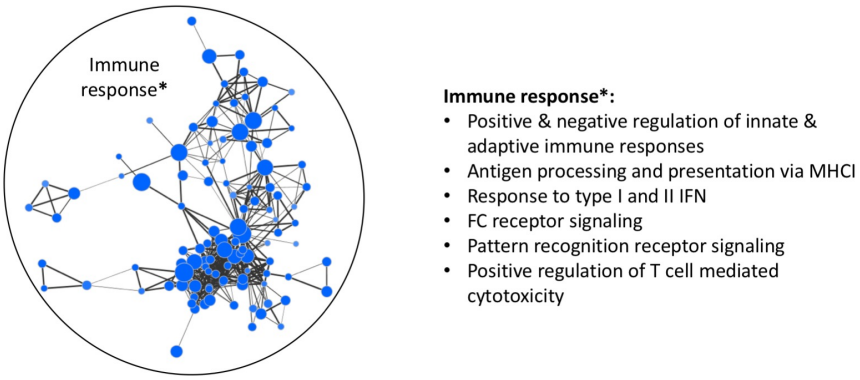

Figure 3.13. Biological networks correlated with ADC in NCEL. Gene Set Enrichment Analysis (GSEA) followed by enrichment map visualization shows gene ontology (GO) biological processes that are positively (red nodes) and negatively (blue nodes) correlated with increasing ADC in NCEL samples; no ADC positive correlations met the statistical threshold for NCEL samples. Nodes represent GO terms. Clusters of functionally related enriched GO terms were manually circled and labeled. Node color represents a positive (red) or negative (blue) correlation. Node size is proportional to the number of genes within each GO term. Edge thickness signifies the overlap between GO terms (number of genes shared between two gene sets); thicker edges depict connections between nodes that share more genes than thinner edges. P-value cutoff = 0.005, FDR q-value cutoff = 0.1.

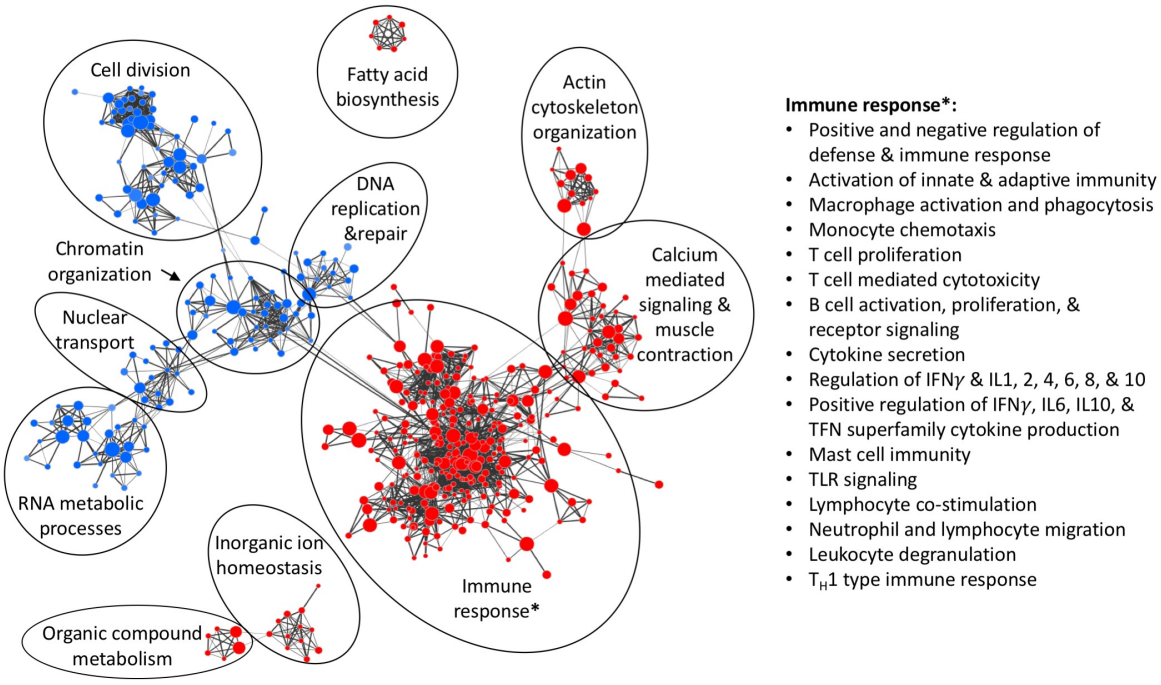

Figure 3.14. Biological networks correlated with rCBV in NCEL. Gene Set Enrichment Analysis (GSEA) followed by enrichment map visualization shows gene ontology (GO) biological processes that are positively (red nodes) and negatively (blue nodes) correlated with increasing rCBV in NCEL samples. Nodes represent GO terms. Clusters of functionally related enriched GO terms were manually circled and labeled. Node color represents a positive (red) or negative (blue) correlation. Node size is proportional to the number of genes within each GO term. Edge thickness signifies the overlap between GO terms (number of genes shared between two gene sets); thicker edges depict connections between nodes that share more genes than thinner edges. P-value cutoff = 0.005, FDR q-value cutoff = 0.1.

Histopathological phenotypes are correlated with immunologic, tumor proliferation, angiogenesis, cellular stress, and cellular metabolism networks in the NCEL.

We tested correlations between histopathological phenotypes with enriched hallmark/biological processes. Gene expression patterns matched their histopathological phenotypes, similar to results observed in the CEL samples (Table 3.9, 3.10). For instance, enrichment of cell division networks was significantly correlated with immunohistochemistry markers of cell proliferation and tumor cellularity. Two of the immunohistochemistry tissue features assessed in the CEL were not testable in the NCEL; Ca9 expression and expression of factor VIII showing complex morphology were not present in the non-enhancing tissue. The remaining vascular morphology patterns (total vascular expression, and factor VIII expression subdivided into delicate and simple vascular architecture) were positively correlated with cell proliferation networks and protein synthesis. Overall vascular expression was additionally positively correlated with immune features including response to interferons and antigen processing and presentation. Similar to networks patterns observed in the CEL, elevated MIB1L and cell counts were negatively correlated with immunological networks.

Table 3.9 Hallmark networks associated with histopathological phenotypes in NCEL.

	Positive correlation	Negative correlation
Ca9	NA	NA
Vascular Expression	**Cell cycle/proliferation** (E2F targets and G2M checkpoint), **immune response** (IFNα and IFNγ response), **epithelial-mesenchymal transition**, **MYC targets** expressed, and **cell stress** (unfolded protein response)	NA
FVIII Delicate	**Cell cycle/proliferation** (E2F targets and G2M checkpoint) and **MYC targets** expressed	NA
FVIII Simple	**Cell cycle/proliferation** (E2F targets and G2M checkpoint), **immune response** (IFNα and IFNγ response), **epithelial-mesenchymal transition**, and **MYC targets** expressed	NA
FVIII Complex	NA	NA
MIB1L	**Cell cycle/proliferation** (E2F targets and G2M checkpoint) and **MYC targets** expressed	**Protein secretion**
Cell Count	**Cell cycle/proliferation** (E2F targets and G2M checkpoint)	**Protein secretion**

Table 3.10 Biological processes associated with histopathological phenotypes in NCEL.

	Positive correlation	Negative correlation
Ca9	NA	NA
Vascular Expression	**Cell division** (DNA replication, repair, & packaging, sister chromatid separation, spindle assembly, and cell cycle phase transition), **RNA processing** (tRNA transport, gene silencing by RNA, ncRNA processing), **immune response** (response to IFNγ, antigen processing and presentation of peptide antigen), and **epigenetic regulation of gene expression**	Autophagosome organization and glutamate secretion
FVIII Delicate	**Gene organization and expression** (gene silencing by RNA, positive epigenetic regulation of gene expression, chromatin silencing, telomere organization, and DNA replication) and **protein synthesis and localization** (tRNA transport, protein localization to ER, ribosome biogenesis, and protein sumoylation)	**Normal neuronal processes** (modulation of synaptic transmission, neurotransmitter transport, glutamate secretion, synaptic signaling, amino acid transport, neuronal action potential, clathrin mediated endocytosis, calcium ion regulated exocytosis, and regulation of potassium ion transport)

FVIII Simple	**Cell division** (cell cycle phase transition, DNA packing, chromatin structural changes, sister chromatid segregation, histone methylation), **protein synthesis and localizatio**n (mRNA catabolic processes and protein localization to the ER), **response to IFNα**	**Catabolic processes** (fatty acid and monocarboxylic acid catabolic process, fatty acid β oxidation)
FVIII Complex	NA	NA
MIB1L	Positive and negative regulation of **cell division** (centromere complex assembly, DNA replication, repair, and packaging, Histone exchange, sister chromatid segregation, membrane disassembly, and cell cycle transition), **gene expression** (positive regulation of epigenetic gene expression, RNA splicing, and ribosome biogenesis)	**Immune response** (myeloid leukocyte activation, granulocyte activation, and positive regulation of macrophage derived from foam cell), **vascular regulation** (positive regulation of vasodilation & cell junction assembly), and cell structure modification (microvillus organization, membrane raft organization, and protein localization to cell surface)
Cell Count	**Normal neuronal processes** (synapse organization, synaptic signaling, synaptic transmission, dendrite development, glutamatergic synaptic transmission, modulation of excitatory action potential, exocytosis, GABA signaling pathway, glutamate secretion, neuron differentiation)	**Immune response** (regulation of macrophage derived from foam cell) and **cell structure modification** (microvillus organization and membrane raft organization)

The NCEL has a heterogeneous immune microenvironment, including variable expression of immune checkpoint genes, but different expression patterns than in the CEL.

Immunologic networks emerged as some of the most variable biological patterns in the NCEL samples. Thus, we probed further into the specifics of the immune response in the non-enhancing GBM tissue. Different patterns of immune presence and immune checkpoint expression in CEL and NCEL are critical to appreciate as they will likely contribute to treatment sensitivity and resistance mechanisms (*111, 352*). Immune checkpoint genes were most strongly expressed in NCEL samples that had matched CEL tissue classified as mesenchymal, but perhaps more interestingly has the most elevated NCEL ADC mean values (Figure 3.15 A,B).

Unexpectedly, NCEL samples with low expression of immune checkpoint genes appeared to have matched CEL samples of the classical subtype. Assessment of immune cell marking gene expression patterns in the NCEL suggest that T-cells may not be present in the same samples that have elevated expression of markers for phagocytic cells (Fig. 3.15 B). Furthermore, samples with elevated cell count and proliferation appear to have the lowest expression of immune cell genes. Probing expression gene panels associated with the M1 and M2 macrophage/microglia activation phenotypes showed mixed expression of the selected genes across samples (Fig. 3.15 C,D).

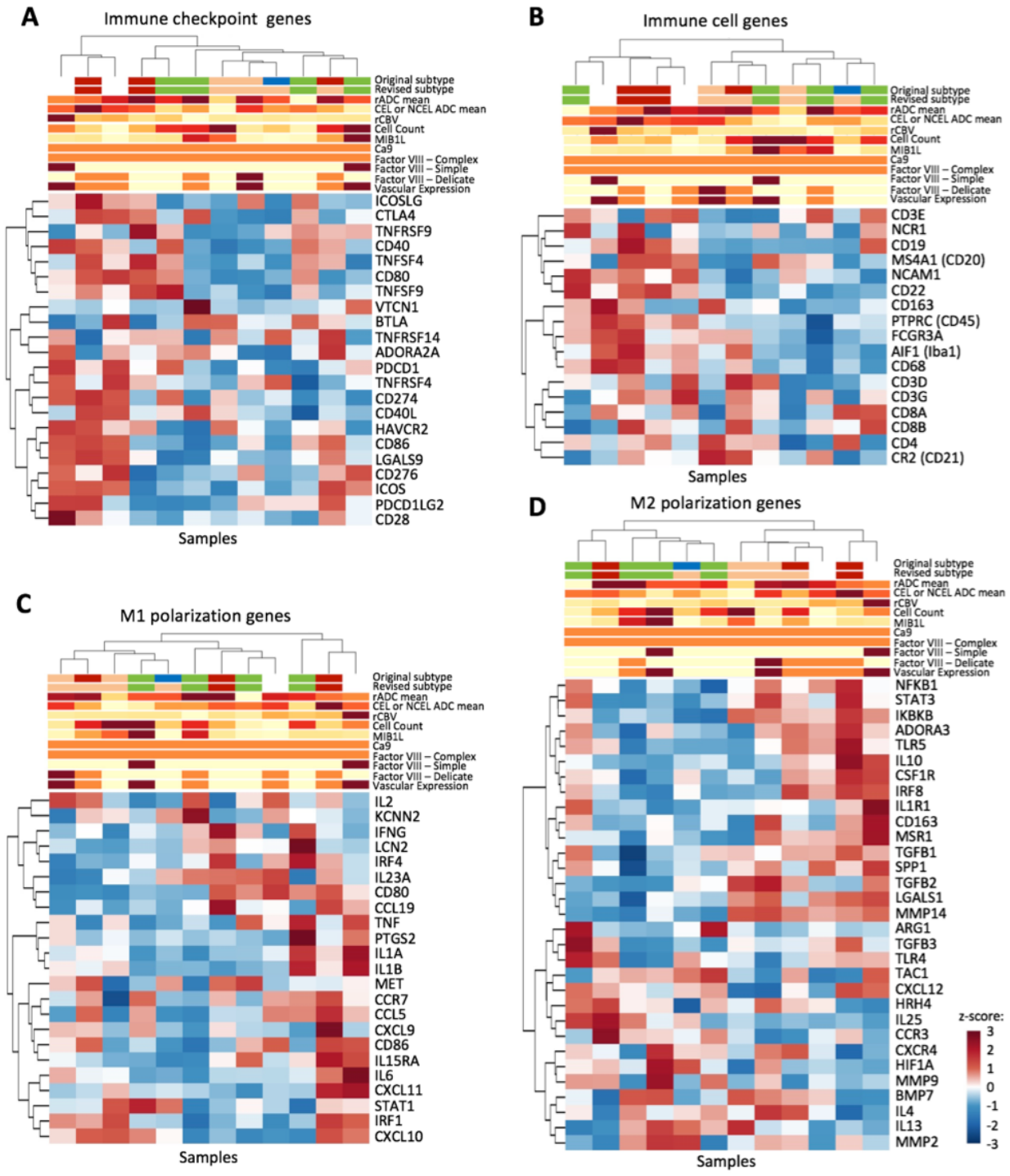

Figure 3.15. Immune gene expression in NCEL samples. Heatmaps showing unsupervised hierarchical clustering of **(A)** immune checkpoint genes, **(B)** immune cell marker genes, and **(C, D)** M1 and M2 polarization gene panels. Genes were z-score normalized across NCEL samples.

Radiophenotypes in the NCEL may provide biomarkers for specific immune network expression.

As we observed that immune networks were again some of the top enriched processes out of all hallmark and biological networks in the NCEL, we interrogated complex immune networks correlated with radiophenotypes in these samples. Our results demonstrated that rCBV, rADC, and NCEL ADC mean are all correlated with unique immune phenotypes in the NCEL (Table 3.11). Higher rCBV values were positively correlated with lowly activated macrophages, unstimulated and potentially pro-inflammatory lymphocyte populations, and possible low levels of NK cells, neutrophils, and eosinophils. Interestingly, rCBV was negatively correlated with effector CD8+ cytotoxic T cells. Increasing rADC was negatively correlated with immune networks including lowly stimulated, potentially M2 macrophages, anti-inflammatory T lymphocytes (both cytotoxic and helper T cells), naïve B cells, and possible small amounts of neutrophils and eosinophils. Unexpectedly, NCEL ADC mean was oppositely correlated with an immune reaction compared to rADC. However, this was similar to patterns we observed when testing for correlations with hallmark and biological processes in the NCEL. NCEL ADC mean was positively correlated with infiltrating monocytes/macrophages and activated microglia, mixed T cell phenotypes, and the presence of NK cells.

Table 3.11 Immunological networks associated with imaging phenotypes in NCEL.

		Positive correlation	Negative correlation
rCBV	Macrophage & Microglia	Possible unstimulated and pro-inflammatory monocytes; more macrophages/monocytes than T or NK cells	NA
	T cell	Th1>anergic Th1 CD4+, untreated>IL2 stimulated &IL4>control treated CD4+, Early memory>naïve CD8+	Effector CD8+ cell week 1 post activation
	B cell	Unstimulated>IgM stimulated B cells, less B than CD4 T cells	NA
	NK cell	Less NK cells than macrophages	NA
	Other	Possible neutrophils and eosinophils	NA
rADC	Macrophage & Microglia	NA	Lowly stimulated possibly anti-inflammatory microglia, macrophages and monocytes
	T cell	NA	BTLA+ CD8 cells, early memory CD8 cells, CXCR1- effector CD8 cells, Th2 CD4 cells, Tregs present
	B cell	NA	Naïve B cell > Plasmablast
	NK cell	NA	NA
	Other	NA	Possible neutrophils and eosinophils
NCEL ADC mean	Macrophage & Microglia	Possible monocytes, lowly activated microglia, and non-tumor suppressive macrophages	NA
	T cell	Mixed phenotypes, IL4>untreated and untreated>IL2 CD4, CD161 high CD8 cells	NA
	B cell	NA	NA
	NK cell	NK > NKT cells	NA
	Other	Macrophages > NK or T cells	NA

Several key immune genes are differential expressed between CEL, NCEL, and control samples.

To investigate potential differences in immune cells and immune checkpoint genes between tumor regions we compared the quantile normalized gene expression values across groups (CEL, NCEL, and controls) (Fig. 3.16). For most genes there were modest differences

between groups. Several genes did show differing expression levels and provide hypothesis-generating results for future work to assess protein levels for confirmation. FCGR3A, a gene expressed by NK cells (*353*), showed highest expression in CEL, medium expression in NCEL and lowest expression in gliotic non-tumor controls. CD68 and CD163 showed similar expression patterns to FCGR3A, and are expressed by macrophages, with CD163 frequently used to label M2 polarized cells, though this is controversial (*354*). CD8A, while not have a large spread in expression values did have a small cluster of 3 samples with elevated expression in the CEL. Follow-up analysis of these samples is warranted as CD8+ T cells are the main targets of many immune modulating therapies and understanding inter-tumoral differences in their presence is important to optimal therapeutic planning (*355*). Several of the immune checkpoint genes were differentially expressed in the groups. In particular, CD276 (which encodes B7-H3 protein) and CD40 (a member of the TNF-receptor superfamily) showed significant difference between CEL and controls (p-values = 0.015 and 0.042 respectively), and CD276 also showed a significant difference between CEL and NCEL samples (p-value = 0.001), after correcting for multiple comparisons. If these checkpoints are expressed and intact, this could provide a potential resistance mechanism to mono-therapies targeting other immune checkpoints, and requires further study. Other checkpoint genes showed trends in differences between tumor regions and controls, though were no longer significant once we accounted for multiple comparisons.

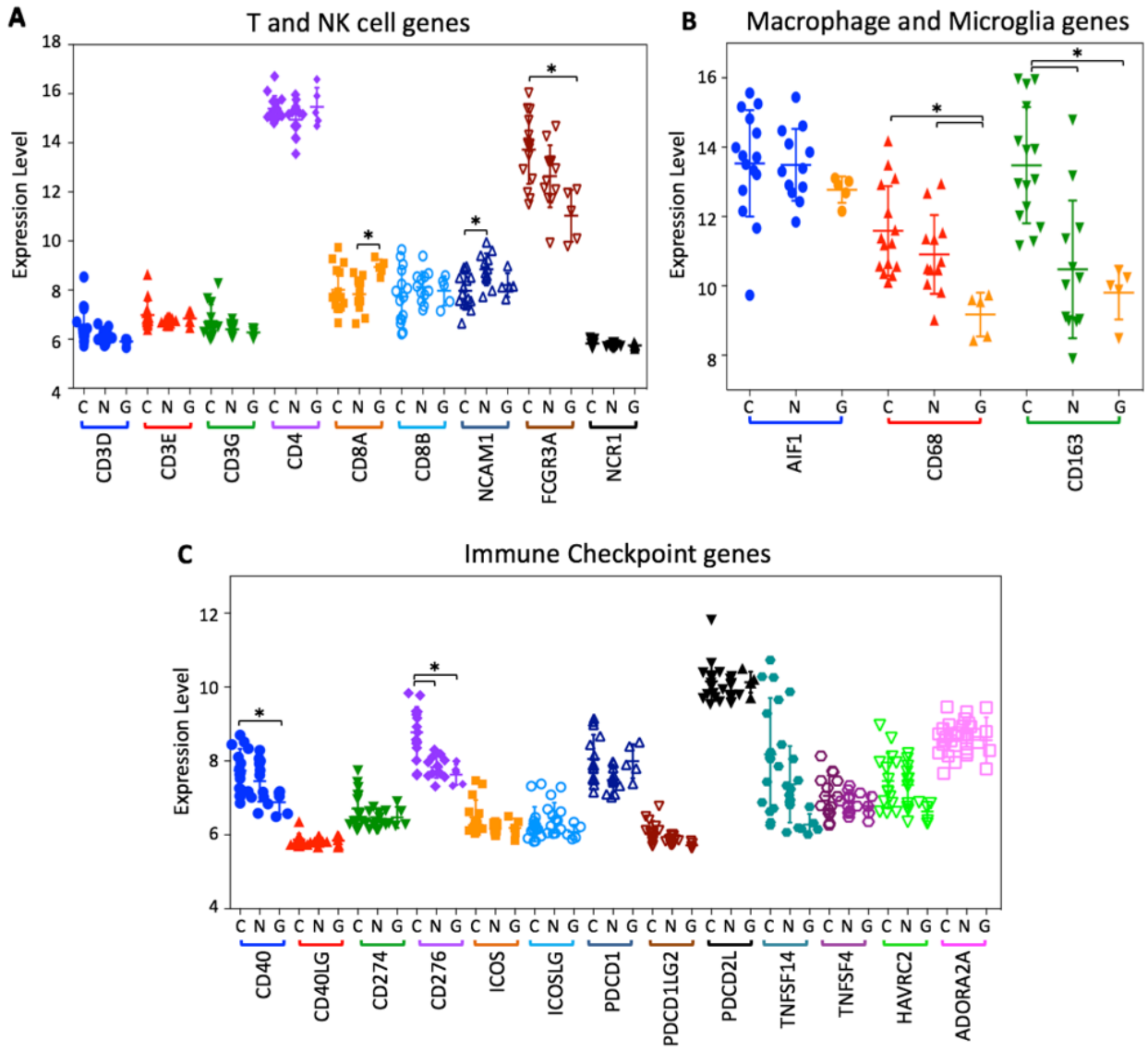

Figure 3.16. Immune cell and immune checkpoint gene expression in CEL, NCEL, and control sample groups. **(A)** Expression of T and NK cells markers genes clustered by group (CEL, NCEL, and gliotic non-tumor brain). **(B)** Expression of macrophage/microglia markers genes clustered by group. **(C)** Expression of immune checkpoint genes clustered by group. Each symbol represents an individual sample's expression value. C = CEL; N = NCEL; G = gliotic non-tumor control. Expression levels and quantile normalized gene expression values. * p-value < 0.05 after Bonferroni corrections.

3.5. Discussion

Improving outcomes for patients with GBM will require tailoring treatment regiments to the unique characteristics of each tumor and tumor microenvironment. Doing so necessitates gaining a better understanding of the extensive heterogeneity displayed by GBMs, and developing modalities to assess therapeutically-important tumor traits across a whole tumor, over time. We begin to address to the pressing issue of evaluating GBM heterogeneity, by investigating variable gene expression networks that correlate with tumor regions defined by MRI and histological features. We demonstrate that CEL and NCEL can be subdivided by physiologic imaging metrics (rCBV and rADC) and histological phenotypes to define tumor tissue with unique biological and immunological processes. Subdividing the CEL and NCEL was able to identify biological and immune niches within GBM tissue that on standard contrast imaging appear as a more homogenous tumor region. Differences in rCBV, rADC, and ADC mean all distinguished sub-regions of CEL and NCEL with differing immune composition. The CEL tissue in GBM displayed the strongest immune response and cellularity, compared to NCEL and control brain tissue. Relative CBV was correlated with inflammatory processes in both the CEL and NCEL, however it appeared to be polarized to an anti-inflammatory immune response in the CEL and a pro-inflammatory immune response in the NCEL. Interestingly, ADC, a marker of cellularity, was negatively correlated with inflammation in the NCEL. These results highlight that it may be feasible to develop imaging biomarkers of specific tumor-immune interaction niches. It is important to note that all biological and immunological patterns described herein are based solely on RNA expression and require confirmation at the protein level and validation in a prospective study to identify biomarkers.

Understanding the complexity of the immune response occurring within a tumor is crucial as the neuro-oncology field embarks on incorporating immune modulating therapies into treatments for GBM. The immune microenvironment of a GBM appears to be diverse across a tumor and between different tumors (*28, 32*). While GBMs are typically highly immunosuppressive compared to other tumor types (*356-358*), they have a tremendous number of macrophages and microglia throughout the bulk of the tumor, often accounting for 30-50% of the cells in the bulk tumor mass (*78, 138, 359, 360*). Our results support this finding, as upregulated gene expression signatures were indicative of elevated microglia and macrophages relative to other immune cells. Tumor associated macrophage (TAMs) play a significant role in tumor survival and growth, and helping orchestrate the overall immune response (*123*). Unexpectedly, we found that gene signatures for M1 and M2 macrophage polarization were upregulated in the same tumor samples, suggesting that TAMs in GBM are a mixed population and/or represent some intermediate phenotype on the M1/M2 spectrum. Future studies investigating protein expression patterns in tumor tissue from these regions is needed to differentiate these possibilities. Applying multiplexed immunohistochemistry methods to investigate the spatial co-distributions of M1 and M2 marker proteins in these samples would be highly valuable to better understand the distribution of TAM phenotypes in GBM (*361*).

Inter-tumoral variability in the immunologic state of GBM has been previously associated with GBM molecular subtypes (*26, 30-32*). Additionally, mesenchymal GBM subtype samples from TCGA have elevated PDL1 expression compared to other subtypes (*148*). Our results show that numerous immune checkpoints are upregulated in CEL samples of mesenchymal tumor, and that proneural tumors have very little expression of these genes. Early research studying immune checkpoints in cancer and the efficacy of immune checkpoint

blockade in murine models of various carcinomas suggest that more immunogenic tumors respond better to immunotherapies, while tumors with little pre-treatment immune infiltration require an immune stimulating vaccine prior to immunotherapy for anti-tumor effects (*140*). It is possible to speculate that mesenchymal GBMs, which consistently demonstrate a robust immune response, may be more responsive to immune modulating therapies, while tumors of the proneural subtype that have minimal immune features may require an immunogenic vaccine. As we observed a slight trend in mesenchymal tumors having elevated rCBV in their CEL and proneural tumors demonstrating lower rCBV in their CEL, exploring the potential use of rCBV threshold(s) in the CEL as a potential biomarker of GBM subtypes and response to immune checkpoint inhibition merits future investigation. Moreover, areas of CEL that had elevated rCBV were associated with possible immunosuppressive immune phenotypes, providing further evidence that the presence of this radiophenotype could identify patient cohorts that may benefit from checkpoint inhibition.

The immune microenvironment of GBM is not static, but can change over the course of treatment during both standard chemotherapy and immune modulating therapy (*26*). After chemoradiotherapy about 36% of GBMs show radiographic evidence of tumor growth (increased size of the gadolinium-enhancing lesion), that overtime resolves and the tumor volume decreases (*362, 363*). This imaging phenomenon is termed pseudoprogression and is nearly impossible to differentiate from tumor growth on standard MR imaging, greatly complicating clinical decision-making. Pseudoprogression is thought to be enhancement caused by an inflammatory response to the dying tumor cells (*364*). Ferumoxytol-enhanced MRI is one method that is being investigated and used to distinguish tumor progression from pseudoprogression, but additional modalities are needed. It is plausible that imaging biomarkers for variable immune phenotypes may provide

enhanced methods to different treatment-induced inflammation from tumor growth. Pseudoprogression is also observed following immunotherapies, and thus presents a significant problem in evaluating patients during clinical trials (*365*). Methods to resolve tumor inflammatory process by imaging would be highly applicable and clinically useful in this scenario (*139*).

Understanding the biology and immune microenvironment of the NCEL is import because this niche is implicated in treatment resistance and disease recurrence (*366-368*). GBM cells are highly infiltrative in nature. As such, the NCEL contains normal appearing brain with low numbers of dispersed tumor cells that may not be surgically resected and are then responsible for tumor regrowth. Developing imaging biomarkers for the underlying biology and unique immune response to this particular tumor microenvironment would help identify druggable targets unique to the non-resectable tumor edge, that could be inhibited in conjunction with resection of the bulk tumor to improve outcomes. In the current study we found that areas of NCEL with lower rADC values likely represent microenvironments with an anti-inflammatory immune response, which may benefit from immune checkpoint inhibitors.

In summary, the current study describes the biological differences in GBM tissue stratified into tumor microenvironments by MR imaging and simple histopathological features. We demonstrated that imaging and histologic differences in the tumor are associated with different molecular biology signatures, and the immune response plays a large role in the variance between tumor samples. Immune checkpoint genes are unevenly distributed across and between GBMs, and this may be identifiable in the future by molecular subtype and non-invasive imaging biomarkers. Future investigations are required to validate our findings in an independent cohort, and assess if these biological patterns are conserved at the protein level. Additionally,

evaluating associations between potential imaging biomarkers and responses to therapies in current and future clinical trials should be considered. We propose that imaging biomarkers may represent a feasible approach to non-invasively identify biologically and immunological unique tumor areas, which have the potential aid treatment planning and interpretation of therapeutic responses in GBM.

Acknowledgements. We sincerely thank Dr. Barajas's original research team including Dr. Soonmee Cha, MD and Joanna Philips at the University of California San Francisco for sharing this important data for further analysis. We also thank Cheryl Claunch, PhD and Rochelle Fu, PhD for meaningful discussions on R script development and statistical analysis methods, respectively.

Data and materials availability. All computer code used in this work will be made free and open-source software available at https://github.com/gbm-IGB upon manuscript publication. This text provides the code used for data analyses. These files are uploaded to GitHub and will be made public and freely available upon acceptance of the manuscript. The files include: (1) Identifying the top 1000 most variable genes in R; (2) Performing PCA in R; (3) Data normalization in R; (4) Creating the heatmaps in R; and (5) Performing spearman correlation analyses on genomic data.

CHAPTER 4: THE ROLE OF HER2, AVβ3-INTEGRIN, AND THE BRAIN MICROENVIRONMENT IN BREAST CANCER BRAIN METASTASIS

Authors: **Cymon N. Kersch[1],** Leslie L. Muldoon[1], DreeAnna Morris[1], Jessica Bills[1], Samantha Holland[1], Jeffery Wu[1], Sangeet Lal[2], Jing Wang[3], Xiaolin Nan[3,4], and Edward A. Neuwelt[1,5,6]

Affiliations:

[1]Department of Neurology, Blood-Brain Barrier Program, Oregon Health and Sciences University, Portland, OR 97239, USA.

[2] Department of Neurological Surgery, University of California San Francisco, San Francisco, CA 94117, USA.

[3] Department of Biomedical Engineering, Knight Cancer Institute, Oregon Health and Sciences University, Portland, OR 97239, USA.

[4] Program in Molecular and Cellular Biosciences, Oregon Health and Sciences University, Portland, OR 97239, USA.

[5] Department of Neurosurgery, Oregon Health and Sciences University, Portland, OR 97239, USA.

[6] Office of Research and Development, Department of Veterans Affairs Medical Center, Portland, OR 97239, USA.

Manuscript in preparation.

Important notes: Parts of text and data herein are published in:

Lal S, **Kersch C**, Beeson KA, Wu YJ, Muldoon LL, Neuwelt EA (2015) Interactions between αv-Integrin and HER2 and Their Role in the Invasive Phenotype of Breast Cancer Cells In Vitro and in Rat Brain. *PLoS ONE* 10(7): e0131842. https://doi.org/10.1371/journal.pone.0131842.

4.1. Abstract

Background**:** Several integrins and the human epidermal growth factor receptor 2 (HER2) are associated with breast cancer brain metastasis. We tested the hypotheses that αvβ3-integrin and HER2 influence the invasive phenotype of brain-trophic breast cancer cells through interactions with ligand(s) produced by reactive glia.

Methods**:** Clones of MDA-MB231-BR human breast cancer cells with stable knock down of αv- or β3-integrin in combination with high or low levels of HER2 were created. The interactions of these proteins and their combined effect on cell migration and invasion were investigated *in vitro* and *in vivo*. Expression of known ligands of these receptor families were evaluated for co-localization with reactive glia in rat models of breast cancer brain metastases and human breast cancer brain metastasis tissue by immunohistochemistry. Human breast cancer cells were stimulated with these ligands *in vitro* then assessed for changes in proliferation, morphology, and intracellular signaling. The effect of inhibiting one of these ligands, Galectin-3 (Gal3), on tumor growth was investigated in a xenograft model.

Results**:** HER2 co-precipitated with αv-integrin in three breast cancer cell lines *in vitro*, suggesting they complex in cells; immunofluorescent confocal and super resolution imaging demonstrate their localization in membrane nanodomains near cell protrusions. Knockdown and pharmacological inhibition of αv- and β3-integrin significantly reduced cell motility. After intracerebral inoculation, cells expressing high levels of αvβ3-integrins and HER2 showed a diffusely infiltrative tumor phenotype, while cells deficient in either integrin subunit with or without HER2 displayed a compact tumor growth phenotype. In the infiltrative tumors, the invading malignant cells were localized to the perivascular space where they were in close proximity to reactive glia. Reactive glia around these tumors expressed several known

tumorigenic ligands including Gal3. *In vitro*, Gal3 increased pro metastatic cellular phenotypes and was secreted by microglia when co-cultured with human breast cancer cells. Pharmacological inhibition of Gal3 in a xenograft model had minimal effect of tumor growth. Conclusions**:** αvβ3-integrin and HER2 influence the invasive phenotype of breast cancer cells, possibly in response to ligands, including Gal3, produced and secreted by reactive microglia in the tumor microenvironment. Targeting αvβ3-integrin in HER2-positive breast cancer cells or Gal3 in their microenvironment may slow growth and decrease infiltration in the brain.

4.2. Introduction

Breast cancer is the most common cancer in women, and ranks as the second most common malignancy to metastasize to the brain (*369*). Breast cancer brain metastases remain incurable. To improve outcome for patients with breast cancer brain metastases, a better understanding of how metastatic cells colonize and grow in the brain microenvironment are needed. Numerous reports identify differences between metastatic breast cancer cells and their primary tumor counterparts. Large genomic and proteomic studies have taken the mass data approach, while more focused reports have investigated individual or small numbers of specific proteins suspected to be altered or upregulated in metastatic cells and tumors based on *a priori* observations (*196, 267, 270, 274, 275, 289, 290*). Through these methods, two key families of cell surface receptors have been identified to be upregulated on metastatic breast cancer cells that could coordinate their interactions with the brain microenvironment: integrin adhesion receptors and growth factor receptors (GFR), including those of the epidermal growth factor receptor (EGFR) family (*11, 267, 270, 274, 284, 370, 371*).

The integrin family of transmembrane receptors mediate cell-ECM and cell-cell interactions, and are implicated in multiple steps of the metastatic cascade (*261, 271-273*). Integrins function as obligate αβ dimers, forming 24 known combinations of 18 α and 8 β subunits (*264*), The αv-integrin subunit is overexpressed in metastases, including brain metastases, and are important in the survival, proliferation, migration and invasion of cancer cells (*267-273*). Activation of the αvβ3-integrin heterodimer promotes tumor angiogenesis and metastatic growth in mouse brain (*274*), while transcriptional silencing of αvβ3-integrin with MYC decreases migration and invasion of cancer cells *in vitro* and *in vivo* (*275*). In preclinical models, targeting αv-integrin with the monoclonal antibody intetumumab or αvβ3- and αvβ5-integrins with the cyclic peptide cilengitide has shown anti-tumor effects as well as metastasis prevention activity (*282-284*). However, in clinical trials, intetumumab and cilengitide have demonstrated minimal therapeutic efficacy inducing tumor cell death in metastases (*285-287*).

The EGFR family of proteins is also associated with increased breast cancer brain metastasis (*11*). This family of includes EGFR and the human epidermal growth factors receptors 2, 3, and 4 (HER2, HER3, and HER4). Members of the EGFR family form homo- and hetero-dimers upon ligand binding, leading to trans-autophosphorylation of their intracellular tail, and triggering activation of downstream cellular signaling cascades that ultimately impacts cell survival, proliferation, migration, invasion, and drug resistance (*289*). Of this family, HER2, also known as ErbB2, is of particular interest in brain metastasis. HER2 is an orphan receptor tyrosine kinase that is implicated in enhanced cancer cell proliferation and aggressive tumorigenic behavior (*372*). Malignancies with HER2 overexpression show increased brain metastatic outgrowth in preclinical models and a high incidence of brain metastases clinically, with up to 30% of patients developing central nervous system lesions (*370, 371, 373*). However,

it is poorly understood how HER2-overexpressing cells gain an invasive metastatic phenotype that requires dynamic remodeling of cell adhesion, actin cytoskeletal assembly, and navigation of the ECM (*373, 374*). Similar to the failures of integrin-mediated therapies, HER2-target treatments have had modest results in decreasing breast cancer brain metastases (*158*). One of the main anti-HER2 therapies, trastuzumab, does not cross the blood-brain barrier, and thus has poor penetration into metastatic brain tumors (*306*). However, newer HER-2 targeted monoclonal antibodies, such as neratinib, have improved brain-brain barrier permeability and are being investigated for efficacy in HER2-positive brain metastases (*304*).

The failures of integrin- and HER2-targeted therapies emphasize the need to precisely understand the tumor-specific biology in the brain niche so that better use of current inhibitors or novel methods to inhibit these metastatic cellular behaviors can be achieved. Physical interactions between integrins and various growth factor receptors and crosstalk between these signaling systems have been reported in normal and pathological conditions, including cancer (*265, 375-378*). It is plausible that these interactions alter the effect of their functions in the tumor. Additionally, in the brain microenvironment these receptors can sense and respond to factors produced by non-neoplastic cells in the tumor microenvironment, including microglia and astrocytes (*224, 225*). Understanding tumorigenic interactions between malignant and resident brain cells could provide novel avenues for therapeutic intervention (*301*).

In this study, we evaluated the interaction of αvβ3-integrin and HER2 using a brain-trophic breast cancer cell line (MDA-MB231-BR-HER2) (*370*) and two non-transformed HER2-positive breast cancer cell lines, and assessed what factors produced by the brain microenvironment could act through these receptors to increase the metastatic potential of breast cancer. Our results suggested that αvβ3-integrin interacts with HER2, potentially through a

multi-protein complex on functional nanodomains of the cell membrane, and disrupting these proteins decreased the invasive behaviors of breast cancer cells. Further, we show that reactive glia in the tumor microenvironment produce several factors known to stimulate these receptors, and that Gal3 production by reactive microglia may contribute to a pro-tumorigenic signaling loop in brain metastasis outgrowth.

4.3. Methods

Human tumor tissue.

Human subjects. Archived human tissue specimens from confirmed breast cancer brain metastases that were previously collected at Oregon Health & Science University with informed consent by subjects and in accordance with the requirements of the local IRB remained de-identified throughout the course of present study and were used in accordance with the requirements of the local IRB. Immunohistochemical evaluation was performed on archival tissue from four subjects. Immunohistochemical staining was performed as described below.

Immunohistochemistry of paraffin-embedded tissue samples. Paraffin-embedded, 7-μm-thick tissue sections were cut and mounted onto charged microscope slides. Immunohistochemical stains were applied to sections after deparaffinization and antigen retrieval (5 min at room temperature in 95% formic acid followed by 30 min incubation in citrate buffer, pH 6.0, at 80°C). Tissue sections were blocked with 3% nonfat dry milk in phosphate buffered saline and stained with antibodies to HER2 (catalog #2242, Cell Signaling Technologies, Beverly MA) (1:200), αv-integrin (Q20-R, Santa Cruz Biotechnology, Dallas TX) (1:200), or Gal3 (sc-19283, Santa Cruz Biotechnology, Dallas TX) (1:200). Results were visualized after

application of appropriate secondary antibodies using 3, 3'-diaminobenzidine tetrahydrochloride hydrate (D5637, Sigma-Aldrich, St. Louis MO) or Vector Red (SK-5100, Vector Laboratories, Burlingame CA) as chromagens using an Olympus Bx50 microscope (Olympus Scientific Solutions, Waltham MA).

Cell lines and clonal line development.

Cell Lines. SKBR3, HCC1954, and MDA-MB-361 breast cancer cells, were obtained from ATCC (Manassas, VA), and cultured in McCoy's Medium (Corning Life Sciences—Mediatech, Manassas VA), RPMI1640 (Lonza BioWhittaker, Allendale NJ) and Leibovitz's L-15 Medium (ATCC, Manassas VA) respectively, supplemented with 10% fetal bovine serum. BV2 murine microglial cells were obtained from Dr. Randy Woltjer (Department of Pathology, Oregon Health and Science University, Portland OR) and cultured in RPMI1640 (Lonza BioWhittaker, Allendale NJ) supplemented with 10% fetal bovine serum. The brain-trophic human breast cancer cells transfected to express high HER2 (MDA-MB231BR-HER2, herein termed MM2BH cells) were obtained from Dr. Patricia Steeg (NCI, Rockville MD) and cultured in DMEM (Corning Life Sciences – Mediatech, Manassas VA) supplemented with 20% fetal bovine serum (IFBS-HU-24879, Innovative research, Novi MI), 20mM HEPES (BP310, Fischer Scientific, Waltham MA), 350mM Zeocin (#1621177A, Gibco Life Tech., Waltham MA) (*370*).

Clonal cell line generation. MM2BH cells were transduced with one of two distinct αv-integrin sequence-specific lentiviral shRNAi constructs (TRCN-768 and TRCN-769), two distinct β3-integrin sequence-specific lentiviral shRNAi constructs (TRCN-3236 and TRCN-3238) or a scrambled control shRNA (TRC1) derived from the MISSION library of Sigma-Aldrich (St Louis, MO). After 48 h, transduced cells were seeded in 96-well plate (catalog

#353072, Corning Life Sciences, Durham NC) with limited dilution per well and cultured in the presence of 1μg/ml puromycin (A11138-03, Gibco Life Technologies, Waltham MA). Stably transduced clones were selected and expanded from individual wells. The expression of αv-integrin, β3-integrin, and HER2 in selected clones was verified by western blotting of whole cell lysates and by flow cytometry. Five MM2BH clones with high or low expression of αv-integrin and high or low HER2 expression, as well as five MM2BH clones with high or low expression of β3-integrin and high or low HER2 expression were chosen for study: (a) αv+H2+, (b) αv+H2-, (c) αv-H2+sR1 (shRNA TRCN-769), (d) αv-H2+sR2 (shRNA TRCN-768), (e) αv-H2-, (f) β3+H2+, (g) β3+H2-, (h) β3-H2+sR1 (shRNA TRCN-3236), (i) β3H2+sR2 (shRNA TRCN-3236), (j) β3H2-. Knockdown clones were maintained in 0.5 μg/ml puromycin (A11138-03, Gibco Life Technologies, Waltham MA).

Flow cytometry.

Cells were harvested using TrypLE Express (12605-028, Gibco Life Technologies, Waltham MA) and suspended in blocking buffer (3% BSA in PBS pH 7.4) as a single-cell suspension. Cell surface protein expression was evaluated with the following antibodies: anti-HER2/neu-APC (BD340554, BD Biosciences, San Jose CA; 2.5uL per reaction), anti-αv-integrin (Q20-R, Santa Cruz Biotechnology; 1:200), anti-β3-integrin (ab75872, Abcam, Cambridge MA; 1:200), and Alexa Fluor 647 conjugated secondary antibody (Life Technologies, Waltham MA; 1:500) was used for αv- and β3-integrins. Cells (10^6 per antibody) were incubated with primary or direct conjugated antibodies for 45 min at 4°C, then with secondary antibodies for 30 min at 4°C. Cells were washed and resuspended in FACS buffer (PBS with 10% FBS and 0.1% NaN_3), and assessed within 1 h of antibody staining using the

FACSCanto II flow cytometer (BD Biosciences, San Jose CA) at the Oregon Health and Science University flow cytometry core. Analyses were completed using FlowJo software (http://www.flowjo.com/). For fixed permeabilized and not permeabilized cell analyses, the above methods were performed with fixation prior to incubation with the primary antibodies. Cells with either fixed with 4% paraformaldehyde and then immediately blocked and stained, or permeabilized with tritonX-100 (X-100, Sigma-Aldrich, St Louis MO) and then immunostained.

Protein interaction.

Co-immunoprecipitation. Modified lysis buffer (50mM Tris-Cl pH 7.5, 150mM NaCl, 1% NP-40, 0.5% Na-deoxycholate, 1mM EDTA and 1mM EGTA) supplemented with 1x Halt protease and phosphatase inhibitor cocktail (cat#78441, Thermo Scientific, Waltham MA), was used for lysate preparation from HCC1954, SKBR3, and MM2BH cells grown under normal culture conditions. After 30 min incubation in the lysis buffer on ice, cell suspensions were passed through a 21-gauge needle to disrupt genomic DNA and centrifuged to clarify unsolubilized proteins. 500μg cell lysate was incubated overnight with 5μg antibody against HER2, αv-integrin, β3-integrin, or EGFR. ProteinA-conjugated agarose beads (Thermo Scientific, Waltham MA) were added and incubation was continued for additional 2-3h. The immunocomplex was separated from unbound lysate by centrifugation and then pulled down proteins were eluted by boiling at 95°C for 5 min in Lamaelli buffer (catalog #161-0747, Bio-Rad, Hercules CA). Samples were assessed by western blotting (*274, 275, 376*).

Western blotting. Samples from co-immunoprecipitation assays and cell lysates were assessed by western blot. For general cell lysate preparation, cells were harvested using TrypLE Express (catalog #12605-028, Gibco Life Technologies, Waltham MA) and suspended in cold

RIPA buffer (50mM Tris-Cl, 150mM NaCl, 1% Triton X-100, 0.5% Na-deoxycholate, 0.1% SDS) supplemented with 1x Halt protease inhibitor cocktail (catalog #78430, Thermo Scientific, Waltham MA). After 15 min on ice, the suspension was centrifuged at 4°C to clear insoluble debris from supernatant lysate. Protein concentration was measured with the BCA assay kit (catalog #23225, Thermo Scientific, Waltham MA) and the western blotting was performed using SDS-PAGE loading equal amounts of protein per lane. The intensity of individual protein bands on immunoblots was quantified using UN-SCAN-IT gel software 6.1 (Silk Scientific, Orem UT) and normalized with that of β-actin (A1978, Sigma-Aldrich, St. Louis MO) loading control.

Proximity ligation assay. Duolink Proximity Ligation Assay (PLA) was performed on HCC1954 and SKBR3 cells, seeded onto #1.5 cover slips per company protocol (DUO92101, Sigma-Aldrich, St. Louis MO, USA). Cells were cultured in normal growth media prior to fixation with 4% paraformaldehyde. Cells were imaged on a Zeiss LSM-780 confocal microscope maintained by the OHSU Advanced Light Microscopy Core.

Protein localization.

Cell immunofluorescence. Cells were grown in 24 well-plates (catalog #353047, Corning Life Sciences, Durham NC) on #1.5 glass coverslips (catalog #12-545-81, Thermo Fisher Scientific, Waltham MA) for confocal imaging and in 8 chamber slides with #1.5 cover glass bottoms (C7182 , Thermo Fisher Scientific, Waltham MA) for super resolution imaging. Cells were fixed with 4% paraformaldehyde (Tousimis, Bethesda MD) at room temperature (RT), permeabilized with 0.25% TritonX-100 (X-100, Sigma Aldrich, St. Louis MO) and blocked in 5% bovine serum albumin (Sigma Aldrich, St. Louis MO). Fixed cells were incubated overnight

in primary antibodies (1:200) and fluorophore-conjugated species-specific secondary antibody was used at 1:600 dilution for 1-2h at RT. Antibodies used in this study are as follows; αv-integrin (sc-6617 Q20-R, Santa Cruz Biotechnology, Dallas TX), HER2 (catalog #2242, Cell Signaling Technology, Beverly MA), β3-integrin (ab75872, Abcam, Cambridge MA), αvβ3-integrin (MAB1976, Millipore, Temecula CA), CD9 (SC-13118 C4, Santa Cruz Biotechnology, Dallas TX), FAK (catalog #13009, Cell Signaling Technology, Beverly MA), pFAK (tyr925) (catalog #8556, Cell Signaling Technology, Beverly MA), Alexa Fluor-conjugated secondary antibodies were purchased from Life Technologies (Waltham, MA) or conjugated by the Nan laboratory as previously described (*379, 380*). F-Actin was stained with rhodamine phalloidine (R415; Life Technologies, Waltham MA) and Hoechst (H21486, Life Technologies, Waltham MA) was used to co-stain nuclei, and coverslips were mounted on microscope slides with Fluoromount-G (catalog #0100-01, Southern Biotech, Birmingham AL). Cells were post-fixed in 4% paraformaldehyde for 10 min at RT. Confocal cell imaging was performed using a laser scanning Zeiss LSM 780 confocal microscope (Carl Zeiss, Oberkochen, Germany) maintained by the OHSU Advanced Light Microscopy core facility. Post-acquisition processing was performed using FIJI:ImageJ software (NIH, Bethesda MD). Super resolution images were collected as previously described in collaboration with Dr. Xiaolin Nan (*379, 380*).

Tissue immunofluorescence. Cell membrane localization of αv-integrin and HER2 were probed in a human breast cancer brain metastasis specimen by super resolution microscopy using methods detailed in Creech et. al., 2017 (*379*)**.** 2μm-thick sections were immunostained. After sectioning, tissues were treated and incubated with the primary antibodies as detailed above in the *Immunohistochemistry of paraffin-embedded tissue samples* section. Antibodies used in this study are as follows; αv-integrin (sc-6617 Q20-R; Santa Cruz Biotechnology, Dallas TX), and

HER2 (catalog #2242, Cell Signaling Technology, Beverly MA). After overnight incubation with primary antibodies at 4ºC in a humidity chamber, tissues were washed 3 x 5 min in PBS and then incubated with secondary antibodies for 1h at RT in the dark. Tissues were washed 5 x 5 min in PBS, post fixed for 10 min at RT with 4% paraformaldehyde, and washed 3x5 min with PBS. #1.5 coverslips were mounted with Fluoromount-G (catalog #0100-01, Southern Biotech, Birmingham, AL). Images were acquired as detailed in (*379*)**.**

Assessing *in vitro* phenotypes in knockdown cell lines.

Western blotting. siRNA mediated protein knockdown was assessed by western blotting as described above.

Transwell migration and invasion assays. The migration and invasion of MM2BH clones were examined using transwell inserts (8μm pores; catalog #3422, Corning Life Sciences, Manassas VA). Uncoated inserts were used in migration; for invasion assays the upper chamber was coated with 30μg of Matrigel (BD Bioscience, San Jose CA). 50,000 cells, suspended in serum-free media, were added to the upper chamber and 10% serum was used as the chemoattractant in lower wells. Migration was continued for 8h and invasion for 64h after cell seeding. Cells were removed from the upper chamber with cotton swabs and cells that migrated on the bottom of the membrane were fixed with chilled methanol for 15 min. Subsequently, cells were stained in 1:5000 Hoechst solution (H21486, Life Technologies, Waltham MA) for 30min. The membranes were excised and mounted cell-side down on microscope slides using ProLong Gold antifade reagent (catalog #0100-01, Life Technologies, Waltham MA). Ten random fields were imaged at 5x objective magnification on the Zeiss Apotome microscope (Carl Zeiss,

Oberkochen, Germany) maintained by the OHSU advanced light microscopy core and the number of cells per field was quantified using the FIJI:ImageJ software (NIH, Bethesda MD).

Cell proliferation. Serial measurements of the number of viable cells after seeding of 2500 cells in opaque-walled 96-well plates (catalog #655098, Greiner Bio-One, Frickenhausen Germany) were collected using the Cell-Titer Glo luminescent viability assay kit (G7570, Promega, Madison WI). Luminescence intensity was quantified using a BioTek Flx800 plate reader (Winooski, VT).

***In vitro effect of* cilengitide on cell migration.**

MM2BH cells were seeded into 96-well plates (catalog #4379, Essen Bioscience, Ann Arbor MI), at a density of 30,000 cells/well and grown overnight in their normal growth media. Scratch wounds were made per the Essen Bioscience IncuCyte Scratch Wound Assay protocol, and then the αvβ3-integrin inhibitor cilengitide trifluoroacetate (catalog #S7077, Selleck Chemicals, Houston TX) was added immediately following wounding. Images were collected in the IncucyteZOOM every 2 hours for 50 hours. Images were processed using Incucyte ZOOM Essen Biosciences Scratch Wound Migration software module (Cat No 9600-0012, Essen BioScience, Ann Arbor MI). All experiments were done in triplicate.

Assessing *in vivo* phenotypes in knockdown cell lines.

Xenograft tumor model. The care and use of animals was approved by the Institutional Animal Care and Use Committee and supervised by the OHSU Department of Comparative Medicine. Female nude rats (rnu/rnu, 200-250g) were anesthetized with intraperitoneal injection of ketamine (60 mg/kg) and diazepam (7.5 mg/kg). Buprenorphine (0.1 mg/kg) was applied

subcutaneously for analgesia. The head was shaved and the rat placed in a stereotactic frame (David Kopf Instruments, Tejunga CA). A 2-mm diameter hole was drilled in the skull and a 27-gauge needle was lowered into the right caudate putamen using coordinates (bregma = 0; lateral = -0.31, vertical = -0.65). Animals were randomized and inoculated with 1.5x 10^6 of each MM2BH cell clone: (a) αv+H2+, (b) αv+H2-, (c) αv-H2+sR1, (d) αv-H2+sR2, and (e) αv-H2- (f) β3+H2+, (g) β3+H2-, (h) β3-H2+sR1 (shRNA TRCN-3236), (i) β3H2+sR2 (shRNA TRCN-3236), (j) β3H2- (n = 6-9 rats per group). Animals were monitored daily by Department of Comparative Medicine personnel and by research staff. The predetermined end point was 5 weeks after tumor implantation; one animal showed weight loss requiring early euthanasia. Euthanasia was performed with a lethal dose of IV euthasol (Virbac, Fort Worth TX). Whole brains were removed for processing, fixed in formalin for more than 3 days, and then vibratome-sectioned into 100μm-thick coronal slices (HM650V, Thermo Scientific, Waltham MA).

Tumor volumetrics. For tumor volumetrics, immunohistochemistry was performed on every sixth section, staining for human mitochondrial antigen (ab3298, Abcam, Cambridge, MA), as previously described (Wu et al 2012). The chromagen 3,3' Diaminobenzidine tetrahydrochloride hydrate (DAB) (D5637, Sigma-Aldrich, St.Louis MO) was used to visualize antibodies labeling, per manufacturers protocol. Total tumor area was manually outlined on scans of all stained sections by a blinded researcher and assessed using FIJI:ImageJ software (NIH, Bethesda MD). Tumor volume was determined by multiplying the sum of measured areas by the section thickness and section separation (sum [mm2] x0.1mm x6). The area of tumor visually judged to match the "infiltrative" phenotype was manually outlined in 2-6 central sections and the area occupied by infiltrating tumor cells was determined as a percentage of total tumor area. 1-2 rats in each group showed incorrect tumor placement (ventricle or base of brain)

or excessive post-mortem autolysis, and these tumors were not included in the analysis of the infiltrative phenotype.

Thick-section assessment using fluorescent immunohistochemistry. For immunofluorescent assessment of 100μm-thick, free floating sections, tissue was washed 3x10 min in PBS, incubated in 1% H_2O_2 x 30 min at RT, and incubated in permeabilization buffer (PBS + 0.2% Triton-X100) x 1 hr at RT. Samples were then blocked for 3 hr at RT in blocking buffer (10% sheep serum, 2% BSA, and 0.2% Triton-X100 in PBS). Primary antibodies diluted in blocking buffer were incubated with the tissue at 4°C on a rocking plate for 48 hours. Primary antibodies used in this study on thick tissue sections are as follows: AQP4 (ab9512, Abcam, Cambridge MA), GFAP (ab53554, Abcam, Cambridge MA), CD31 (AF-3628, R&D Systems, Minneapolis MN), Iba1 (GTX100042, GeneTex, Irvine CA), CD163 (catalog #MCA342R, Biorad ABDSerotec Inc., Raleigh, NC), NRG1 (H7660, Sigma Aldrich, St. Louis MO), Gal3 (sc-19283 D20, Santa Cruz Biotechnology, Dallas TX), HB-EGF (AF-259-NA, R&D Systems, Minneapolis MN), HMT (ab3298, Abcam, Cambridge MA), and PanCK (BP5069, Origene, Rockville MD). Tissues were washed 3 x 1 hr with PBST (0.05% Tween-20 in PBS) on a rocking plate at RT and then incubated with secondary antibodies diluted 1:400 in blocking buffer 24-48hr at 4°C on rocking plate. Alexa Fluor-conjugated secondary antibodies were purchased from Life Technologies (Waltham, MA). Sections were stained with Hoechst (1:800; H21486, Life Technologies, Waltham MA)) and in several cases tomato lectin (1:100; DL1177, Vector Laboratories, Burlingame CA) in PBST x 2 hr at RT on rocking plate. Tissues were washed 4 x 1 hr in PBST at RT on rocking plate and then mounted with CitiFluor CFMR2tissue clearing mounting media (catalog #17979-10, Electron Microscopy Sciences, Hatfield PA) using #1.5 cover slips (catalog #22266882, Thermo Fisher Scientific, Waltham MA). Slides were

stored at 4°C until imaging. Tissue imaging was performed using a laser scanning Zeiss LSM 780 confocal microscope (Carl Zeiss, Oberkochen, Germany) maintained the OHSU Advanced Light Microscopy core facility. Post-acquisition processing was performed using FIJI:ImageJ software (NIH, Bethesda MD).

Assessing *in vivo* microenvironment in non-transformed cell line xenograft and hematogenous metastasis.

Xenograft and hematogenous metastasis tumor models. Female nude rats (rnu/rnu, 200–250 g, from the OHSU Blood-Brain Barrier Program in-house colony) were anesthetized with isoflurane, and a catheter filled with heparinized saline was tied into the right external carotid artery. HCC1954 cells ($1x10^6$ cells) were infused into the right internal carotid artery as previously described; animals were euthanized after 40 days (Wu et. al. 2012). For immunohistochemistry analysis, brains were formalin fixed and sectioned at 100μm, as was done in the xenograft tumor model. Other tissues were not evaluated. Tissues sections underwent immunofluorescent assessment, as detailed above, followed by confocal microscopy imaging.

Molday ION macrophage labeling. Nude rats (n=3) were treated with molday ION rhodamine B MIRB (8 mg/kg i.v.; CL-50Q02-6A-50, BioPAL, Worcester MA) 1 hour prior to implantation of HCC1954 cells ($1.5x10^6$) into the right caudate putamen, as previously described. Control animal received tumor xenograft without MIRB. Seven days post tumor implantation animals underwent MR imaging using a horizontal bore 11.75 T (Bruker Scientific Instruments, Billerica MA) under IP dexmedetomidine (0.6 mg/kg) (Zoetis, Lincoln NE) and ketamine (15 mg/kg) sedation. Blood was drawn at this time point to assess MIRB in serum. Rats were euthanized and underwent perfusion fixation with formalin. Brains were fixed in formalin

for 3 days then vibratome sectioned (100μm-thick) for immunohistochemical analysis. Fluorescent immunohistochemistry and confocal imaging was performed as detailed above.

***In vivo* ligand stimulation assays.**

Incucyte cell proliferation assay. Influence of growth factors on cancer cell growth was evaluated using the IncuCyte Cell Confluence Proliferation Assay, per company protocol (Essen Biosciences, Ann Arbor, MI). HCC1954 cells were seeded at a density of 3,000 cells/well into a 96-well plate (catalog #353072, Corning Life Sciences, Durham NC). After adhering overnight in standard growth media, cells were washed 3x with sterile PBS then incubated overnight in serum free RPMI media. The following day, cells were washed 3x with pre-warmed serum-free RPMI then incubated in 0.1% FBS supplemented RPMI media with one of the following: no additional growth factors, 0.1, 1, or 10 μg/mL Gal3 (catalog #599706, Biolegend, San Diego CA), 0.1, 1, or 10 ng/mL HB-EGF (AF-259-NA, R&D Systems, Minneapolis MN), or 0.1, 1, or 10 ng/mL NRG1 (H7660, Sigma Aldrich, St. Louis MO). All treatments were plated in triplicate. 96-well plates were immediately placed in the IncucyteZOOM following addition of growth factors. Wells were imaged every 2 hours for a total of 3.5 days. Three images were collected per well at each time-point and averaged. Images were analyzed using the IncuCyte Software to calculate the cell confluence in each treatment group over time.

Cell morphology immunofluorescence imaging. HCC1954 cells were seeded onto #1.5 glass coverslips (catalog #12-545-81, Thermo Fisher Scientific, Waltham MA) in 24 well-plates (catalog #353047, Corning Life Sciences, Durham NC) at a density of 10,000 cells/well. Cells were allowed to adhere to coverglass for 24 hours then were cultured in serum-free RPMI media overnight. Cells were washed 3x with pre-warmed serum-free media and then incubated with 1

μg/mL Gal3 (catalog #599706, Biolegend, San Diego CA) for 5 min or 10 min. Control cells did not received Gal3. Cells were immediately fixed in 4% paraformaldehyde, and then immunostained as detailed above. Cells were stained with rhodamine-phalloidin (1:500, R415, Life Technologies, Waltham MA) to label f-actin and visualize structural changes. Fixed, stained cells were imaged using a laser scanning Zeiss LSM 780 confocal microscope (Carl Zeiss, Oberkochen, Germany) maintained the OHSU Advanced Light Microscopy core facility. 10 images were acquired per coverslip, and three coverslips per treatment group were collected for each replicate. Post-acquisition processing was performed using FIJI:ImageJ software (NIH, Bethesda MD). Images were manually assessed by a blinded researcher to count the number of cells positive for lamellipodia, which were defined as flattened, fan-like cell protrusions. If there was any question of the lamelipodia presence, the cell was counted as negative, i.e. not containing any lamellipodia, thus quantification erred on the side of under quantifying the presence of lamellipodia.

Phosphorylation assay. HCC1954 cells were seeded into 10cm tissue culture dished and grown to 80% confluency. Dishes were then washed 3x with pre-warmed serum-free media and incubated overnight in serum-free RPMI media. Dishes was then treated with one of the following: serum-free RPMI media, RPMI + 1ng/mL HB-EGF (AF-259-NA, R&D Systems, Minneapolis MN), 1ng/mL NRG1 (H7660, Sigma Aldrich, St. Louis MO), or 1 μg/mL Gal3 (catalog #599706, Biolegend, San Diego CA). Two dishes were treated with each of the ligands and were washed at fixed after either 20 min or 3 hours of incubation. Cell lysate collection and processing for each treatment was completed on ice following the steps outlined in *Western blotting* section above, with the addition of 1x Halt protease and phosphatase inhibitor cocktail (cat#78441, Thermo Scientific, Waltham MA) to the lysis buffer (50mM Tris-Cl pH 7.5, 150mM

NaCl, 1% NP-40, 0.5% Na-deoxycholate, 0.1% SDS). Phosphorylated protein levels were evaluated by western blot.

***In vivo* co-culture assays.**

Co-culture cell migration. For migration co-culture assays, 50,000 BV2 cells were seeded into the bottom chamber of a transwell insert (8μm pores; Corning Life Sciences, Manassas VA) onto a #1.5 coverslip (catalog #12-545-81, Thermo Fisher Scientific, Waltham MA) in the bottom of a 24-well plate (catalog #353047, Corning Life Sciences, Durham NC). Some wells were prestimulated with LPS (1 μg/mL; L3012, Sigma Aldrich, St.Louis MO). BV2 cells were allowed to adhere to the coverslip for 24 hr in normal growth conditions and media. The bottom well was then washed with serum-free media and replaced with RPMI media with 1%FBS. The upper chamber was then seeded with 60,000 HCC1954 cells suspended in RPMI media supplemented with 1%FBS. The upper chamber of several wells received cilengitide (catalog #S7077, Selleck Chemicals, Houston TX) diluted to produce a final concentration of 1ug/mL in the well. The transwell set-up was incubated in 5% CO2 at 37°C for 48 hours. At this time the inserts were removed and treated as described in the *Transwell migration and invasion assays* methods section to quantify the number of HCC1954 cells that migrated across the porous membrane. Media from each condition was collected, and after centrifugation to remove any cells, was used fresh or stored at -80°C for future soluble protein testing.

ELISA. A solid phase sandwich enzyme-linked immunosorbent assay (ELISA) was performed to test the level of Gal3 in the media of co-cultured BV2 and HCC1954 cells. The Human LGALS3 ELISA Pair Set (SEK10289, Sino Biological, Wayne, PA) was used for this

analysis, following the manufacturers protocol. Absorbance was quantified using a BioTek EL800 plate reader (Winooski, VT).

Cytokine array. BV2 cells were cultured alone or in transwell set-ups with BV2 in the lower chamber and HCC1954 cells in the upper chamber with RPMI media and 1% FBS for 24 hours. Supernatants (200 μl) from individual and co-cultures were characterized utilizing a multiplex Protein Profiler Array per company protocol (Mouse XL Cytokine Array, Cat # ARY028, RND Systems, Minneapolis MN). Media used in this assay was used fresh, immediately out of the co-culture set ups and was never frozen. Membranes were visualized using a 2:1 ratio of pico:femto chemiluminescent reagents (catalog #1859022 and 1856136, Thermo Scientific, Waltham MA). Pixel densities of protein spots were analyzed following the manufacturers protocol. Two replicates of each treatment group were used in this analysis.

***In vivo* assessment of GCS-100.**

Xenograft tumor growth with GSC-100 treatments. HCC1954 xenograft tumors were grown as described above. On days 4, 6, and 8 post tumor implantation rats were treated with 20mg/kg i.p. GCS-100 provided by La Jolla Pharmaceutical Company (San Diego, CA). Rats were euthanized on day 11, and whole brains fixed and sectioned for tumor volumetrics and immunohistochemical evaluations, as detailed prior.

Immunofluorescent assessment of Gal3. 100μm-thick sections were immunostained for pan-cytokeratin (BP5069, Origene, Rockville MD), Gal3 (SC19283, Santa Cruz Biotechnology, Santa Cruz CA), and Iba1 (GTX100042, GeneTex, Irvine CA). Tissue imaging was performed using a laser scanning Zeiss LSM 780 confocal microscope maintained the OHSU Advanced Light Microscopy core facility. Images of each tumor were collected using identical settings on

the microscope. Post-acquisition processing was performed using Zen Software (Carl Zeiss, Oberkochen, Germany) and FIJI:ImageJ software (NIH, Bethesda MD). The distance of Gal3 positivity from the Pan-Cytokeratin positive tumor edge was measured from three equidistant points along the Pan-Cytokeratin positive tumor mass (green) to the furthest Galectin-3 positive (red) point for each image. Three images were analyzed for each tumor for a total of nine measurements per tumor, which were averaged to collect a single value for each tumor.

Statistical analysis.

All *in vitro* studies were conducted in triplicate and with three biologic replicates, with the exception of the protein cytokine array assay, which included only two replicates due to supply limitations. Single time point data were compared by Student's *t*-test and multiple time points were assessed with repeated measures ANOVA. For the animal studies, numbers were based on previous studies for the MM2BH tumors and based on supply limitations for the GSC-100 treatment tumors; no power calculations were made *a priori* or *post hoc*. Tumor volume (total and infiltrative) was compared using ANOVA to determine overall significance and Student's *t*-test for comparison of individual groups. Analyses were performed with Microsoft Excel and Graphpad Prism software (version 8.0).

4.4. Results

αvβ3-integrin and HER2 are expressed in human breast cancer brain metastases and human breast cancer cell lines.

To confirm previous reports of αv-integrin and HER2 expression in human breast cancer brain metastases and test if they are expressed in the same tumor we immunostained four HER2-positive (HER2+) human breast cancer brain metastases. All HER2+ brain metastases also expressed αv-integrin (Fig. 4.1 A,B). We next tested if non-transfected HER2+ human breast cancer cell lines (HCC1954 and SKBR3), that are known to successfully form tumors upon engraftment into the rat brain, co-express αv- and β3-integrin. Immunofluorescent staining demonstrated that αv-integrin and HER2 were localized on or near the cell membrane (Fig. 4.1 C). Live cell flow cytometry confirmed the presence of HER2, αv- and β3-integrin on these cells (Fig. 4.1 D-I). As integrins are known to undergo rapid, carefully orchestrated intracellular recycling and we observed a subpopulation in both cell lines that appeared to be negative for β3-integrin, we investigated if there was an intracellular pool of 3-integrin by flow cytometry of fixed and permeabilized cells (Fig. 4.1 J,K). Both cell lines showed a double peak for β3-integrin in fixed not permeabilized cells that shifted to a single, positive peak in the fixed and permeabilized cells, suggesting the presence of an intracellular pool of β3-integrin.

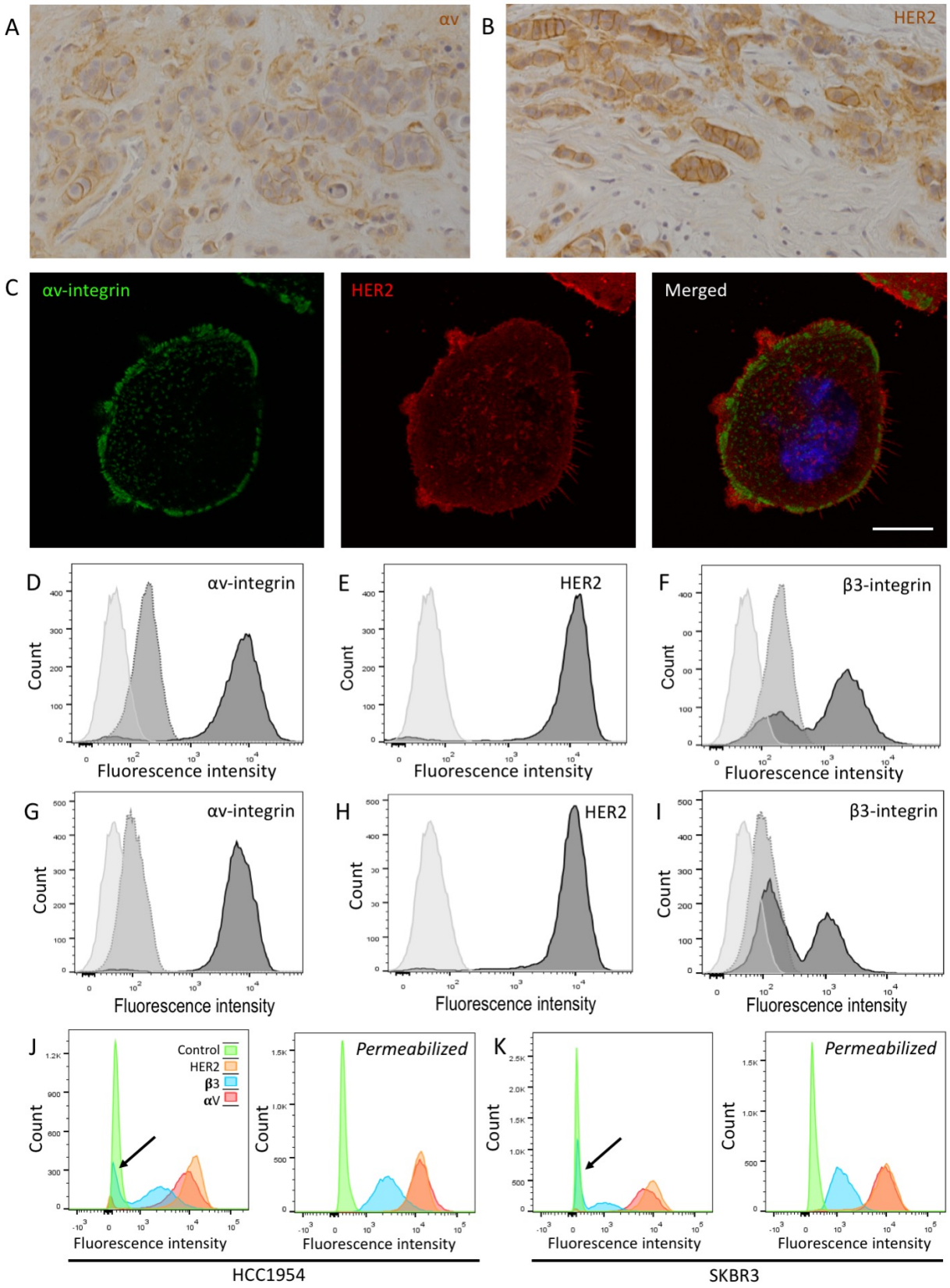
A
αv
B
HER2
C
αv-integrin
HER2
Merged
D
αv-integrin
E
HER2
F
β3-integrin
G
αv-integrin
H
HER2
I
β3-integrin
Count
Fluorescence intensity
J
Control
HER2
β3
αV
Permeabilized
K
Permeabilized
HCC1954
SKBR3

Figure 4.1. HER2, αv- and β3-integrin expression in human breast cancer brain metastasis and cell lines. Example image of αv-integrin **(A)** and HER2 **(B)** in breast cancer brain metastasis tissue. **(C)** Images from left to right depict typical patterns for αv-integrin, HER2, and their overlay in HCC1954 cells. **(D-I)** Representative flow cytometry fluorescence intensity plots demonstrating αv-, β3-integrin, and HER2 in live HCC1954 and SKBR3 cells. Dark grey: protein of interest; medium grey: secondary antibody only; light grey: unstained. **(J,K)** αv-integrin (red), β3-integrin (blue), and HER2 (orange) in fixed not permeabilized (left) and fixed and permeabilized (right) HCC1954 **(J)** and SKBR3 cells **(K)**.

αv-integrin and HER2 physically interact in human breast cancer cell lines.

Integrins and GFRs interact and influence one another's activation and function (*265, 294*). We tested if αv-integrin and HER2 physically interact in human breast cancer cell lines by co-immunoprecipitation (co-IP) and proximity ligation assays (PLA). Under non-denaturing conditions, αv-integrin and β3-integrin co-precipitated with HER2 in three HER2+ breast cancer cell lines, while β3-integrin and HER co-precipitated with αv-integrin (Fig. 4.2 A). As αv-integrin and β3-integrin failed to co-precipitate consistently we confirmed their association by immunofluorescent imaging using an anti-αvβ3-integrin antibody (Fig. 4.2 B). A second method, PLA, was used to further examination the interaction of αv-integrin and HER2 in HCC1954 and SKBR3 cells (Fig. 4.2 C,D). A red fluorescent signal, indicative of αv-integrin and HER2 within 40nm of each other, was observed in both cell lines. Representative images of a field of HCC1954 cells (Fig 4.2 C) and of optical sections of a single cell (Fig 4.2 D) are shown. The single cell images indicate that the protein interaction is restricted to on or near the cell membrane.

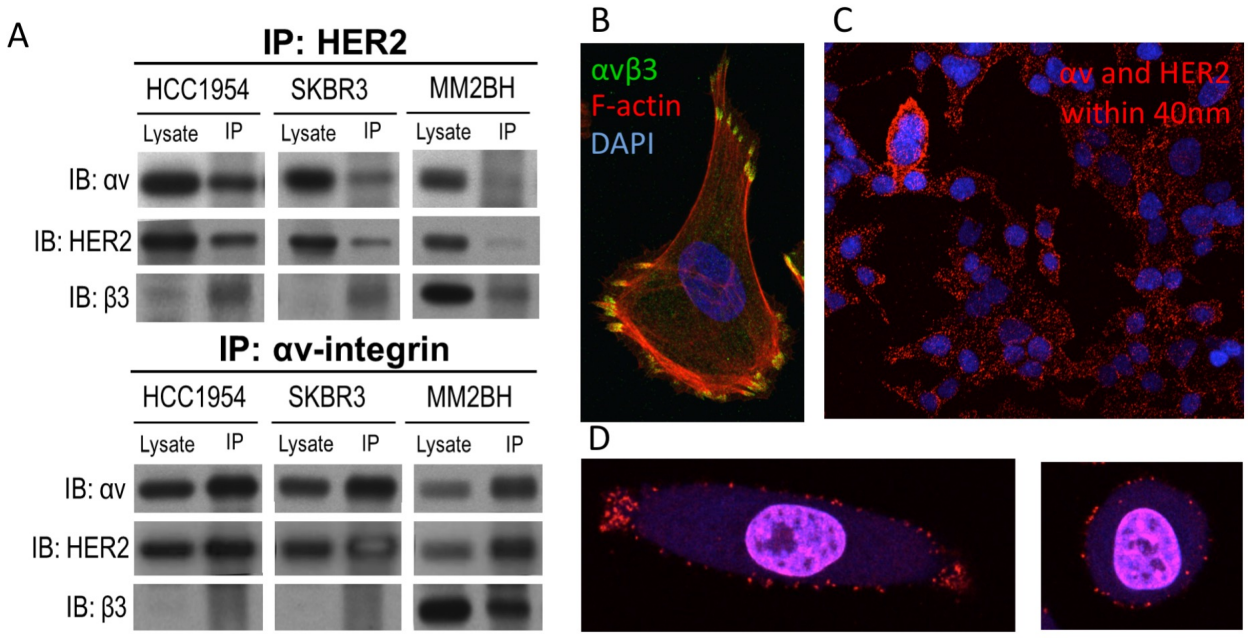

Figure 4.2. Physical interaction of αv-integrin and HER2 proteins in breast cancer cells. **(A)** Lysates from two non-transfected breast cancer cell lines (HCC1954 and SKBR3) and αv+, β3+, HER2+ MM2BH cells were incubated separately with antibodies against HER2 or αv-integrin. Components of the immunocomplex precipitate were analyzed by western blotting. Lysate: whole cell lysate, IP: the immunoprecipated protein complex, IB: immunoblot. **(B)** Cell immunofluorescence demonstrating expression of the αvβ3-integrin heterodimer in HCC1954 cells. **(C)** Proximity ligation assay (PLA) validating the close proximity of αv-integrin and HER2 in HCC1954 cells (red signal). **(D)** Close-up images of optical sections of HCC1954 cells demonstrating the peripherally localized red signal.

αv-integrin and HER2 are expressed on the leading edge and small membrane protrusions of human breast cancer cells.

Given the co-IP results and PLA signal localization, we investigated αv-integrin and HER2 localization by confocal and super resolution microscopy. In migrating cells, based on cell morphology (*381*), polarized αv-integrin and HER2 localization was observed (Fig. 4.3 A-D). At the leading edge (yellow asterisk), both proteins were present along the ruffled cell membrane. At the trailing edge (right side of image), αv-integrin clusters were present at the ends of actin bundles and on thin cell processes. HER2 expression was limited on the trailing edge. Super resolution microscopy showed αv-integrin on thin membrane processes and in clusters at the edge of thicker cell extensions (Fig. 4.3 E-H). HER2 was strongly expressed along the cell membrane and extending out on thin cell protrusions (Fig. 4.3 I-K). Multi-spectral super resolution microscopy demonstrated that while areas of co-localization occurred on the cell membrane and out along thin protrusions, distinct regions rich in each protein were present on or near the cell membrane, with αv-integrin clustered at/below the cell membrane and HER2 densely localized on membrane protrusions (Fig. 4.3 L,M). Super resolution imaging of a HER2+ human breast cancer brain metastasis identified expression of αv-integrin and HER2 localized on cell membranes (Fig. 4.3 N-Q). Evaluation of polarized cell membrane domains were not evaluated in the tissue sample as the areas of positive signal obtained were dense cell clusters.

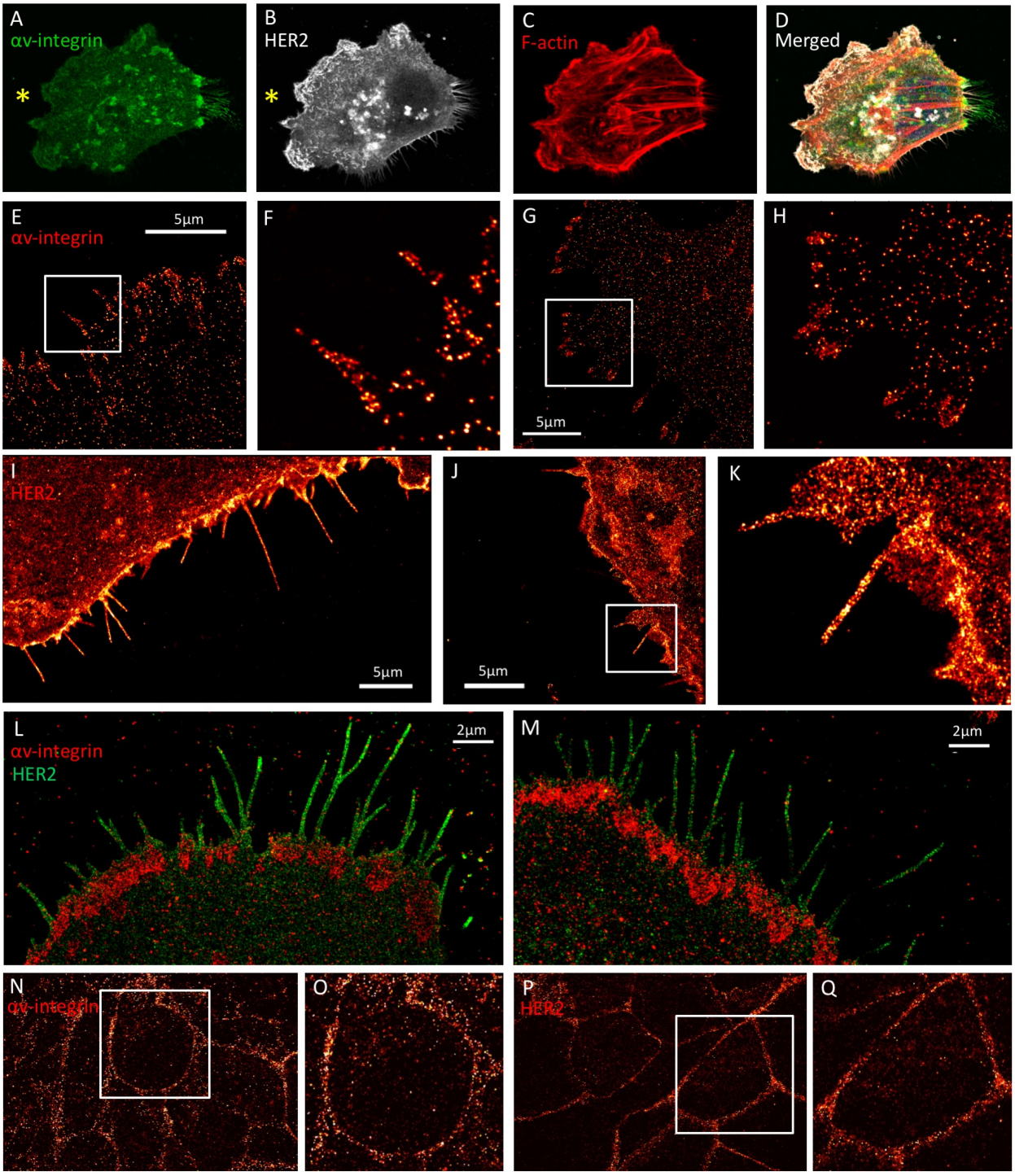

Figure 4.3. Localized expression of αv-integrin and HER2 in breast cancer cells and human brain metastasis tissue. (A-D) Representative confocal microscopy images of αv-integrin, HER2, and f-actin in a polarized HCC1954 cell *in vitro*. Yellow asterisk: leading edge. Super resolution microscopy of αv-integrin **(E)** on cell membrane protrusions, **(F)** close-up of outlined

region in (E), and in **(G)** clusters on thicker membrane extensions, **(H)** close-up of outlined region in (G). **(I,J)** Super resolution microscopy of HER2 on the cell membrane and thin membrane protrusions, **(K)** close-up of outlined region in (J). **(L,M)** Localization of αv-integrin and HER2 by multi-spectral super resolution imaging *in vitro*. **(N)** Expression of αv-integrin in human breast cancer brain metastasis tissue by super resolution microscopy; **(O)** close-up of outlined region in (N). **(P)** Expression of HER2 in human breast cancer brain metastasis tissue by super resolution microscopy; **(Q)** close-up of outlined region in (P).

Tetraspanin 29 (CD9) and focal adhesion kinase (FAK) may be involved in a multiprotein complex with αv-integrin and HER2 in breast cancer cells.

Cell motility is a complex behavior essential for metastasis that is orchestrated by multi-protein interactions on specialized membrane domains (*381-383*). Given the localization of αv-integrin and HER2 we hypothesized they may be functional in cell motility. We next investigated what additional proteins may be involved in their interaction and function. Co-immunoprecipitation experiments demonstrated that tetraspanin 29 (CD9) and focal adhesion kinase (FAK) precipitated with αv-integrin, β3-integrin and HER2 in HCC1954 and MM2BH cells (Fig. 4.4 A). CD9 can physical associated with integrins and with GFRs, while FAK is an intracellular signaling partner of integrins that induces cytoskeletal rearrangements for cell motility (*384-392*). CD9 localized to thin cell membrane protrusions, as demonstrated by super resolution microscopy (Fig. 4.2 B,C). Confocal imaging supported that CD9 is expressed on thin membrane protrusions, where its location overlapped in part with αv-integrin and HER2 (Fig. 4.4 D,E). FAK expression co-localized near perfectly with αv-integrin in dense clusters on thicker cell membrane extension and in clusters at/below areas of cell membrane with strong

HER2 presence (Fig. 4.4 F, left and right images, respectively). Taking these results together, we propose a potential multiprotein signaling complex involved in cell motility, wherein stimulation by either or both integrin and GFR ligands could potentially impact this pro-metastatic cell behavior (Fig. 4.4 G). In preliminary support of this hypothesis, we observed ring-like clustering of phosphorylated FAK around αvβ3-integrin when cells were stimulated with epidermal growth factor (EGF) (Fig. 4.4 H).

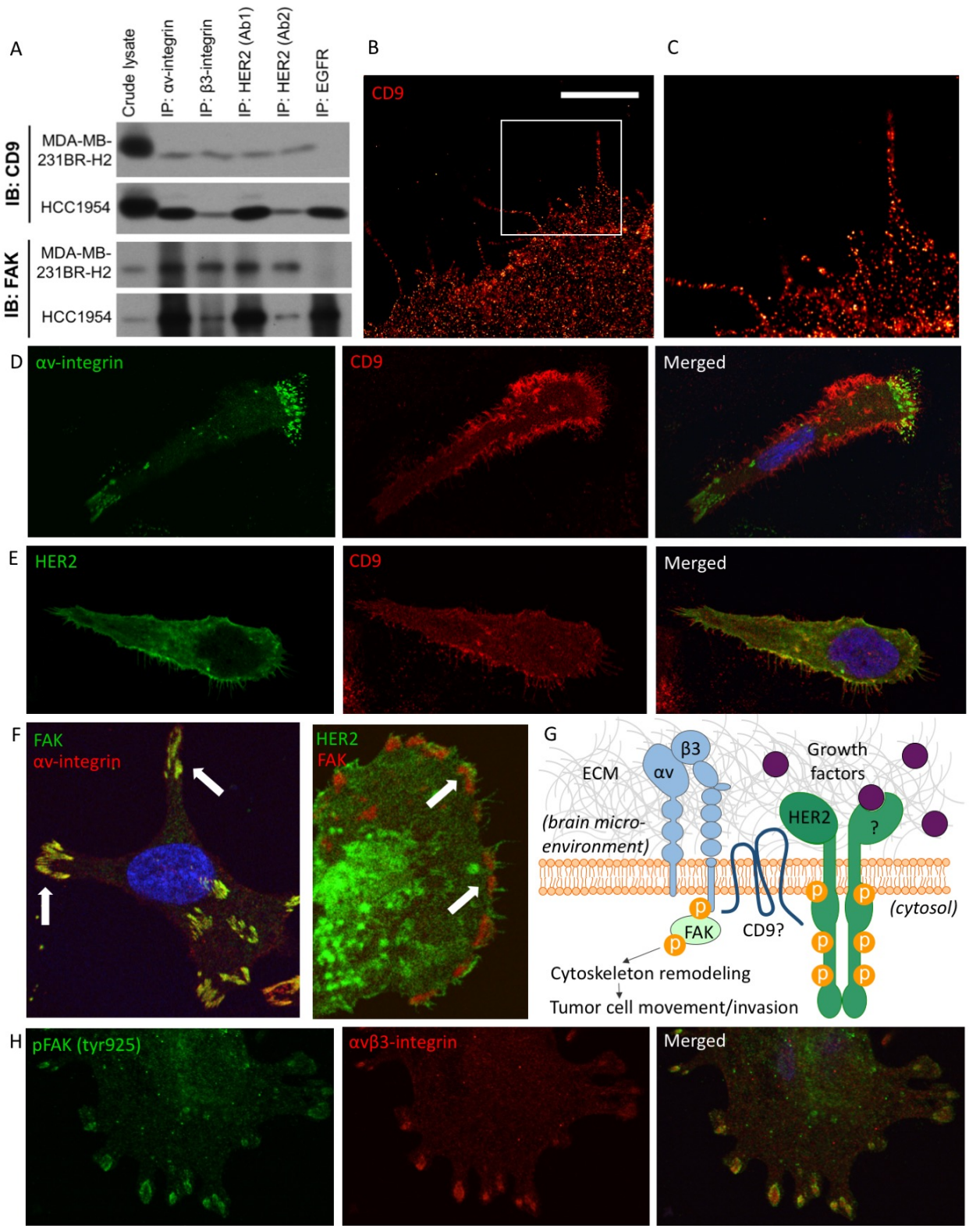

Figure 4.4. Potential interaction of CD9 and FAK with αv-integrin and HER2 in human breast cancer cells. (A) Lysates from HCC1954 and MM2BH cells were incubated separately

with antibodies against HER2, αv-integrin, β3-integrin, or EGFR. Presence of CD9 and FAK in the immunocomplex precipitate were analyzed by western blotting. Crude lysate: whole cell lysate; IP: the immunoprecipated protein complex; IB: immunoblot. **(B)** Super resolution microscopy showing CD9 on cell membrane protrusions; **(C)** close-up of outlined region in (B). Confocal microscopy images from left to right depict typical staining patterns for **(D)** αv-integrin, CD, and their overlay, and **(E)** HER2, CD, and their overlay in HCC1954 cells. **(F)** Representative confocal images of merged FAK (green) with αv-integrin (red) and merged FAK (red) with HER2 (green) in HCC1954 cells. White arrows: regions of overlap or close spatial association of FAK with αv-integrin and HER2. **(G)** Hypothesized multi-protein signaling complex. **(H)** HCC1954 cells were stimulated with EGF (1ng/mL) then fixed and immunostained. Images from left to right depict localized expression of phosphorylated FAK (tyr925), αvβ3-integrin, and their overlay.

αv-integrin, β3-integrin and HER2 influence pro-metastatic cellular behaviors in brain tropic breast cancer cells.

The human breast cancer cell line MDA-MB231BR, herein referred to as MM2BH cells, are brain tropic metastatic breast cancer cells transfected to overexpress HER2 (*370*). Utilizing this cell line, breast cancer cell clones with stable knockdown of αv-integrin or β3-integrin were created using shRNA vectors. As MM2BH cells heterogeneously express HER2 protein, each clone was examined for HER2 to identify clonal cell lines with different combinations of αv-integrin, β3-integrin, and HER2 protein levels. 106 clones were evaluated, and a set of clones with relatively high or low expression of each protein was selected: (a) αv+H2+ (high αv-

integrin, high HER2), (b) αv+H2- (high αv, low HER2), (c) αv-H2(a) (low αv, high HER2 clone 1), (d) αv-H2(b) (low αv, high HER2 clone 2), (e) αv-H2- (low αv, low HER2), (f) β3+H2+ (high β3, high HER2), (g) β3+H2-(high β3, low HER2), (h) β3-H2(a) (low β3, high HER2 clone 1), (i) β3H2(b) (low β3, high HER2 clone 2), and (j) β3-H2- (low β3, low HER2). Figures 4.5 A and B show representative immunoblots, while figures 4.5 C and D indicates protein levels quantified from three independent blots. Live cell flow cytometry confirmed a decrease in cell surface protein levels in the clonal cell lines (not pictured).

To assess the impact of αv-integrin, β3-integrin, and HER2 deficiency on *in vitro* migration and invasion of MM2BH cells, transwell migration and invasion assays were performed (Fig. 4.5 E-F). The αv-integrin and β3-integrin knockdown clones showed significant inhibition of motility compared to control cells (Fig 4.5 G,H). More than 82% and 77% lower migration and invasion was observed for αv-H2+(a) and for β3-H2+(a) cells, respectively (Fig. 4.5 G,H; $P<0.05$). The most pronounced decrease in migration and invasion, more than 88% lower than control cells, was recorded for αv-H2- and β3-H2- cells ($P<0.05$). To determine whether altered protein expression affected cell proliferation, the growth of each clone was measured by a luminescence-based assay. The knockdown of αv-integrin inhibited cell growth by 72 hours, while knockdown of β3-integrin had minimal effects on cell proliferation compared to control (Fig. 4.5 I,J).

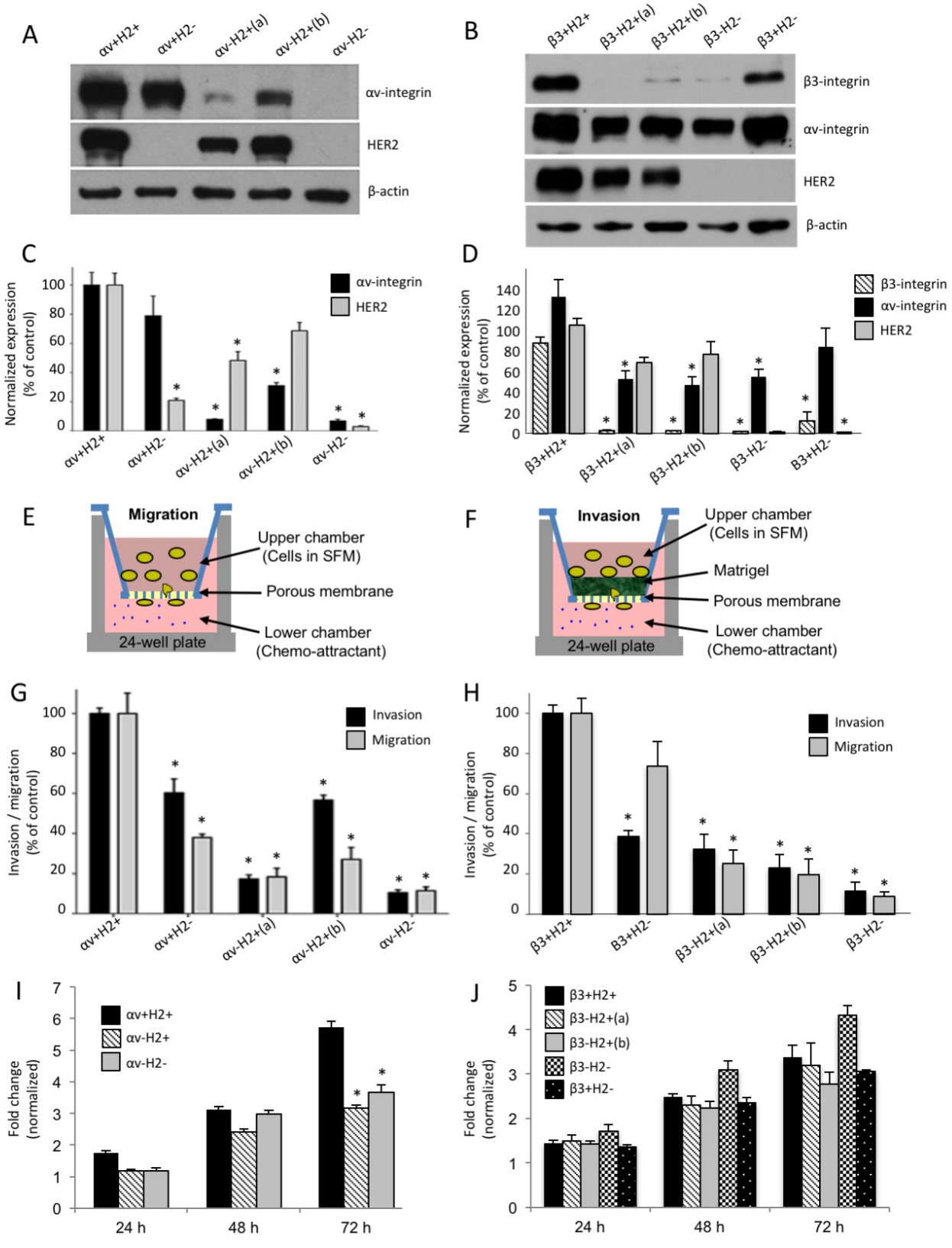
A
αv+H2+
αv+H2-
αv-H2+(a)
αv-H2+(b)
αv-H2-
αv-integrin
HER2
β-actin
B
β3+H2+
β3-H2+(a)
β3-H2+(b)
β3-H2-
β3+H2-
β3-integrin
αv-integrin
HER2
β-actin
C
Normalized expression (% of control)
αv-integrin
HER2
D
Normalized expression (% of control)
β3-integrin
αv-integrin
HER2
E
Migration
Upper chamber (Cells in SFM)
Porous membrane
Lower chamber (Chemo-attractant)
24-well plate
F
Invasion
Upper chamber (Cells in SFM)
Matrigel
Porous membrane
Lower chamber (Chemo-attractant)
24-well plate
G
Invasion / migration (% of control)
Invasion
Migration
H
Invasion / migration (% of control)
Invasion
Migration
I
Fold change (normalized)
αv+H2+
αv-H2+
αv-H2-
24 h
48 h
72 h
J
Fold change (normalized)
β3+H2+
β3-H2+(a)
β3-H2+(b)
β3-H2-
β3+H2-
24 h
48 h
72 h

Figure 4.5. Reduced levels of αv-, β3-integrin, and/or HER2 inhibit the migration and invasion of MM2BH cells. MM2BH breast cancer cells, previously transfected to overexpress HER2, were transduced with lentiviral shRNAs, scrambled or specific to αv-integrin or β3-integrin, to create stable knockdown cell lines in combination with high or low HER2 protein. **(A)** Immunoblotting of protein expression in MM2BH lines with αv-integrin knockdown in combination with high or low HER2 expression. **(B)** Immunoblotting of protein expression in MM2BH lines with β3-integrin knockdown in combination with high or low HER2 expression. **(C,D)** Relative expression of αv-integrin, β3-integrin, and HER2 in MM2BH clones quantified by densitometry of immunoblots from three total cell lysates prepared at different culture passages. The band intensity was normalized to β-actin as a loading control. Error bars show SEM and *$p<0.05$ in comparison to control cells. **(E,F)** Transwell migration and invasion assay experimental set ups. 10% FBS media was used as chemoattractant. Cell migration was evaluated after 7-8h and invasion through the Matrigel matrix was continued for 60h. Cells attached on the bottom surface of the insert membranes were counted using ImageJ. **(G,H)** Quantified migration and invasion of clonal cells lines. N=3 mean±SEM, *$p<0.05$. **(I,J)** Cell proliferation was measured every 24h with the Cell-Titer Glo luminescence assay. The graph shows average fold increase from eight replicate wells from separate experiments. Data are presented as mean ± SEM, *$p<0.05$ in comparison to control cells.

Pharmacological inhibition of αvβ3-integrin with cilengitide decreases cell migration of brain tropic breast cancer cells.

Results of protein knockdown studies suggested that αvβ3-integrin is involved in cell motility. To test if αvβ3-integrin-mediated cell migration could be blocked pharmacologically, we applied the small molecule αvβ3-integrin inhibitor cilengitide to MM2BH cells and quantified their motility over time in a scratch wound migration assay (Fig. 4.6) (*282, 393*). Increasing doses of cilengitide slowed and prevented wound closure over the course of 40 hours, while not having cytotoxic effects, as live cells were clearly visible at the experimental end point. A dose of 10 μg/mL cilengitide reduced cell migration more than 75% in multiple independent experiments. Melanomas are another cancer that frequently metastasize to the brain and display increased expression of αvβ3-integrin (*394*). A highly invasive melanoma cell line, A2058, was also treated with cilengitide and showed significantly decreased wound closure (not pictured).

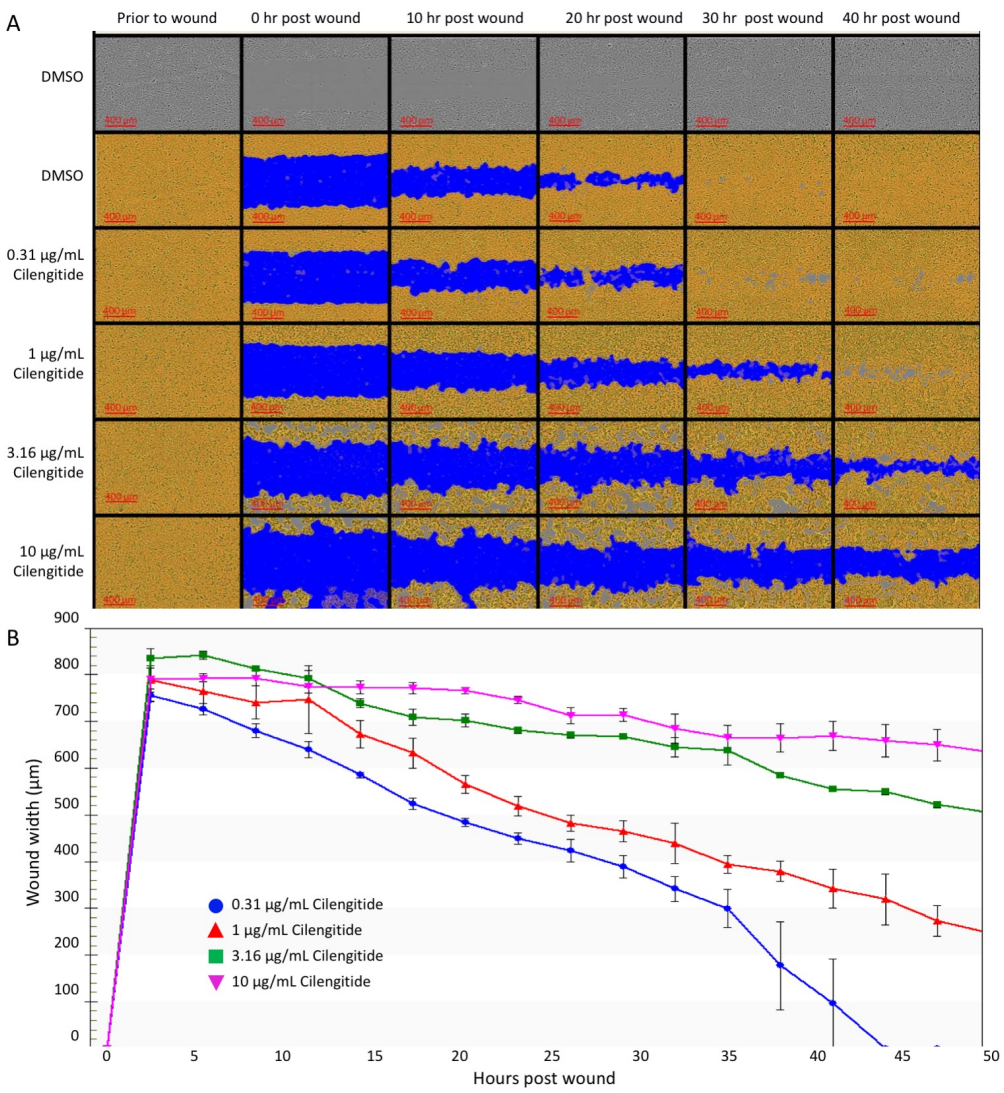

Figure 4.6. Pharmacologic inhibition of αvβ3-integrin decreases cell migration *in vitro*. (A) αv+β3+HER2+ MM2BH cells were seeded into 96 well plates and scratch wounds were made per the EssenBioscience Scratch Wound protocol. The αvβ3-integrin inhibitor cilengitide was added immediately following wounding. Images were collected in the IncucyteZOOM every 2 hours. Top row: raw images. Bottom 5 rows: A yellow cell mask and a blue wound mask were applied to example time-course images to demonstrate variable wound closure. **(B)** A representative graph of the average wound width across four wells is displayed; similar results were observed in three independent replicates and in a metastatic melanoma cell line.

Reduced expression αv- and β3-integrin alone and in combination with decreased HER2 reduced the infiltrative phenotype of breast cancer xenografts in the rat brain.

To evaluate the influence of αv-integrin, β3-integrin and HER2 protein expression on the proliferation and dispersal of breast cancer cells in the brain microenvironment we assessed the growth characteristics of MM2BH clones after intracerebral implantation in athymic nude rats. After 5 weeks of growth, xenograft tumor volumes were highly variable within each cell clone, with small and large tumors in each group. There was no difference in tumor volume between groups. Sections from αv+β3+H2+, αv-H2(a), αv-H2-, β3-H2(a), and β3-H2- brain tumors (Fig. 4.7 A,B) showed markedly different patterns of brain infiltration at the tumor edge (arrows in B). Xenografts expressing both αv-, β3-integrin and HER2 had a central solid tumor mass surrounded by an extensive region of loosely tumor-infiltrated brain (Figure 4.7 AB, left panel, and Fig. 4.7 C). In contrast, the cells deficient in αv and HER2 displayed a compact tumor mass without, or with minimal, peripheral brain infiltration (Fig. 4.7 D). The single deficient αv-knockdown clones and all β3-knockdown clones showed an intermediate phenotype. A blinded investigator quantified the percentage of tumor volume that was a solid mass versus the diffuse growth pattern (Fig. 4.7 E). In αv+β3+H2+ tumors, 57.2 ± 19.0% of the tumor was infiltrative, which was significantly different from the αv+H2- and αv-H2+(b) tumors. In the double deficient clone αv-H2-, infiltration was 5.8 ± 6.1% of the tumor mass, which was significantly less than all other groups ($p<0.05$). In the β3-H2+(a) clones a 8.1% ± 5.5% of the tumor was infiltrative.

The invasive edge of tumor lost with decreased integrin and HER2 expression appeared to follow a vascular pattern. To further investigate this observation we immunostained αv+β3+H2+ xenograft tumor sections for CD31, a vascular marker (Fig. 4.7 F). GFP-positive

MM2BH cells were observed extending out along cerebral vasculature away from the tumor mass. As this phenotype was lost or very minimal in knockdown clonal cell line xenografts it could not be evaluated. The GFP positive cells appeared to remain within close proximity to the CD31 positive endothelium, so we questioned if the malignant cells were invading through the perivascular space. Immunostaining for astrocytic endfeet (aquaporin 4: AQP4), which delineate this anatomic region, demonstrated that brain-infiltrating breast cancer cells did indeed spread through the perivascular space (Fig. 4.7 G). The GFP positivity had variable levels of intensity in the MM2BH cells, making some cells difficult to visualize, so we co-stained for pan-cytokeratin (PanCK), proteins expressed in breast but not brain tissue, to ensure cells outside of the perivascular space were not missed. High magnification confocal microscopy depicted PanCK expressing breast cancer cells situated between tomato-lectin stained cerebral vasculature and AQP4-positive astrocyte endfeet.

To further investigate the brain microenvironment of the invasive tumor edge, lost upon knockdown of integrins and HER2, we immunostained αv+β3+H2+ xenograft tumor sections for Iba1 and GFAP to label glial cells that are known to influence tumor progression in the CNS. Co-staining for Iba1, a marker for microglia and macrophages, revealed these phagocytic cells are abundant surrounding perivascular localized breast cancer cells (Fig. 4.7 H). Meanwhile, immunolabeling glial fibrillary acidic protein (GFAP), a protein present in astrocytes, demonstrated significant astrogliosis immediately around the tumor edge that tapers off into the brain around tumor (Fig. 4.8). Tumor cells could be visualized in a vascular pattern within the infiltrative tumor, surrounded by AQP4 positive astrocyte processes.

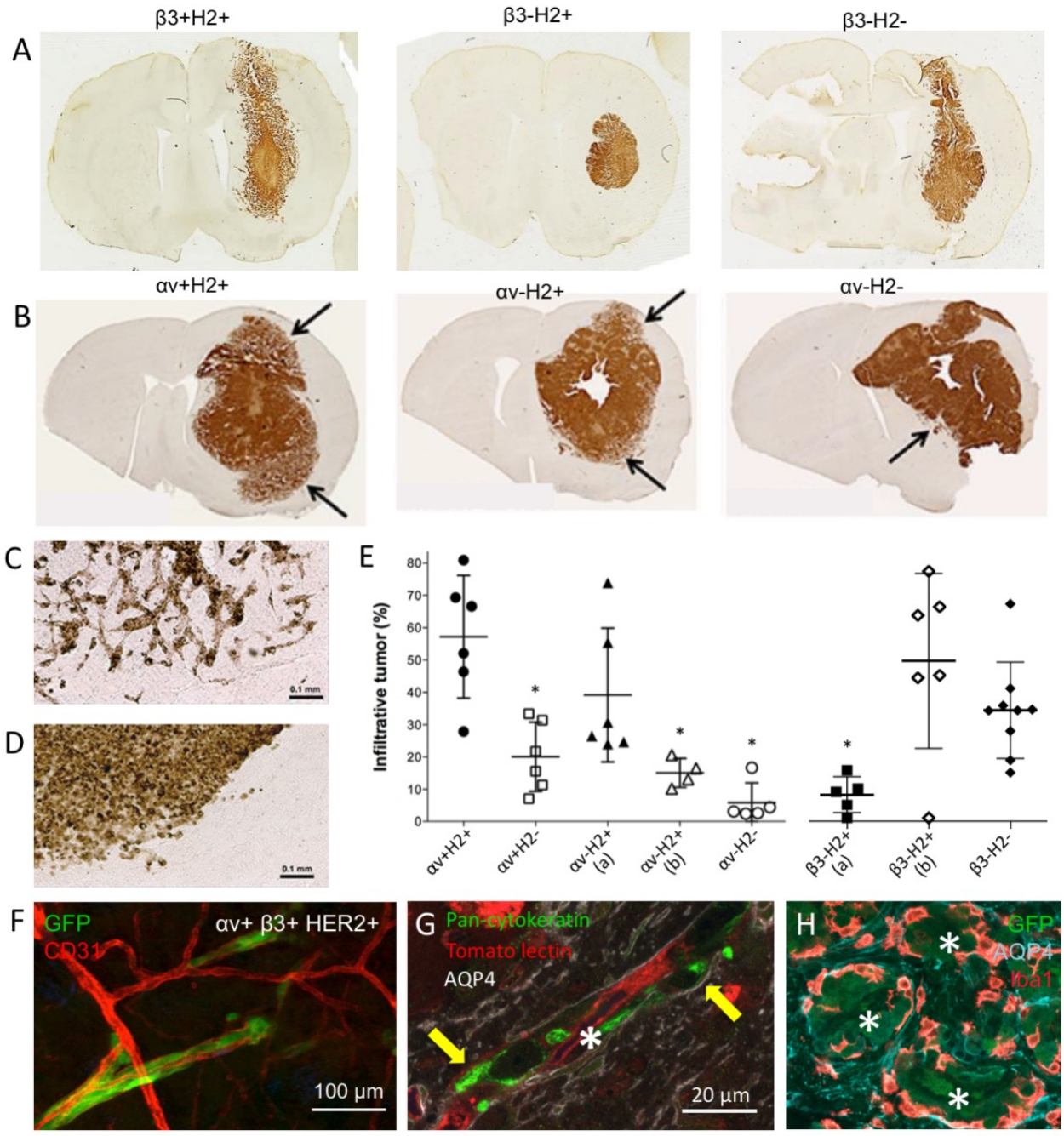

Figure 4.7. Reduced expression of αv- or β3- integrin with and without HER2 decreases infiltration of MM2BH cells through brain parenchyma *in vivo*. MM2BH clones were intracerebrally inoculated into the caudate putamen of athymic rats. Immunohistochemistry was completed with human mitochondrial antigen to mark tumor cells. **(A)** β3-integrin knockdown clone xenograft tumor phenotypes. **(B)** αv-integrin knockdown clone tumor xenograft

phenotypes. Arrows: infiltrative tumor. **(C)** Representative infiltrative edge of αv+β3+HER2+ tumors. **(D)** Representative dense edge of αv-HER2- tumors. **(E)** Quantification of infiltrative tumor in the clonal cell line xenografts; mean±SD , *$p<0.05$ compared to control. **(F)** Confocal image of the infiltrative edge of αv+β3+HER2+ tumors immunostained for CD31 to label vasculature. Tumor cells are GFP positive. **(G)** High magnification confocal image of the infiltrative edge of αv+β3+HER2+ tumors immunostained for AQP4 to delineate astrocyte endfeet, tomato lectin staining the endothelium, and PanCytokeratin (PanCK) to label breast cancer cells. Yellow arrows: tumor cells are within the perivascular space; asterisk: vascular lumen. **(H)** Confocal image of the infiltrative edge of αv+β3+HER2+ tumors immunostained for AQP4 and Iba1 to identify microglia and macrophages in relation to the tumor cells. Asterisk: vascular lumen.

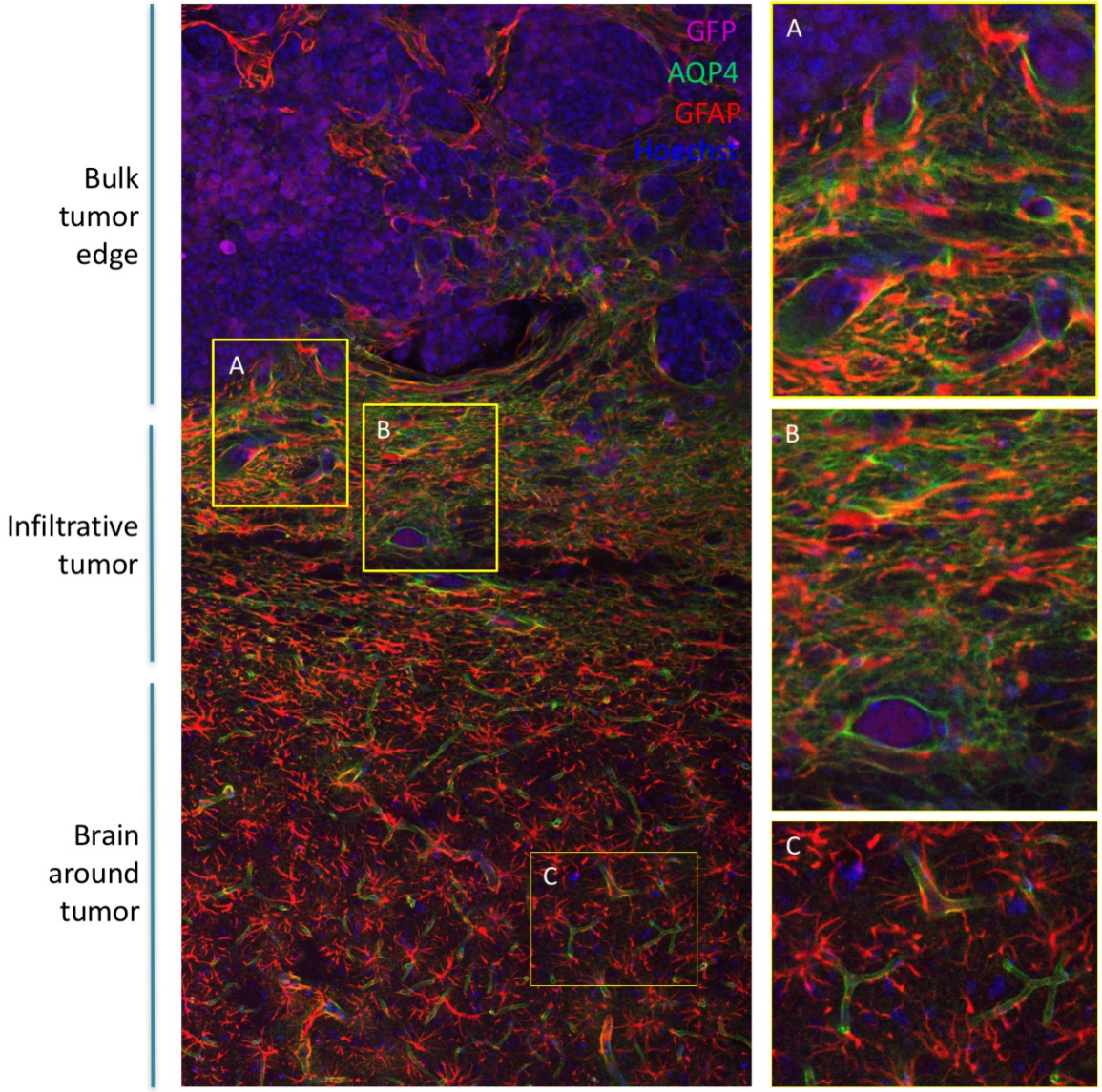

Figure 4.8. Reactive brain microenvironment at the infiltrative edge of MM2BH tumors in rat brain. αv+β3+HER2+ tumors were immunostained for AQP4 and GFAP to label astrocytes and imaged on laser-scanning confocal microscope under 10x magnification. A representative image is shown. Tumor cells are GFP+. Bulk tumor is depicted at the top of the image, infiltrative tumor in the middle, showing individual cells or small clusters of cells invading into the brain in a vascular pattern, and brain around tumor at the bottom. **(A-C)** Close-ups of outlined regions.

Reactive glia within and surrounding breast cancer brain metastasis lesions express ligands known to active αvβ3-integrin and HER2 heterodimers.

As receptors on the cancer cells appeared to be involved in mediating cell motility and infiltration at the leading edge of the tumor, we questioned is reactive glia in this particular tumor microenvironment could produce ligands that active these receptors. We immunostained HCC1954 xenograft tumor sections for the following ligands: Neuregulin 1 (NRG1; also termed heregulin, HRG), Gal3, and heparin binding EGF (HB-EGF) (Fig. 4.9 A-F). These proteins are known to bind and activate HER2:HER3 and HER2:HER4 heterodimers, αvβ3-integrin, and HER2:EGFR heterodimers, respectively (*276, 277, 279, 395-400*). NRG1 co-localized primarily with GFAP+ cells (Fig. 4.9 A,D), Gal3 with ionized calcium-binding adapter molecular 1 (Iba1) positive cells (Fig. 4.9 B,E), and HB-EGF with GFAP+ cells (Fig. 4.9 C,F). Gal3 expression was confirmed in human breast cancer biopsy sections by immunohistochemistry, where it showed localization with both macrophage/microglia and astrocytes, per cell morphology (Fig. 4.9 G). In both the human tumor tissue and the rat xenograft, Gal3 was only expressed in glial cells in and immediately surrounding the tumor and not in cells more distant from the tumor (Fig. 4.9 H,I).

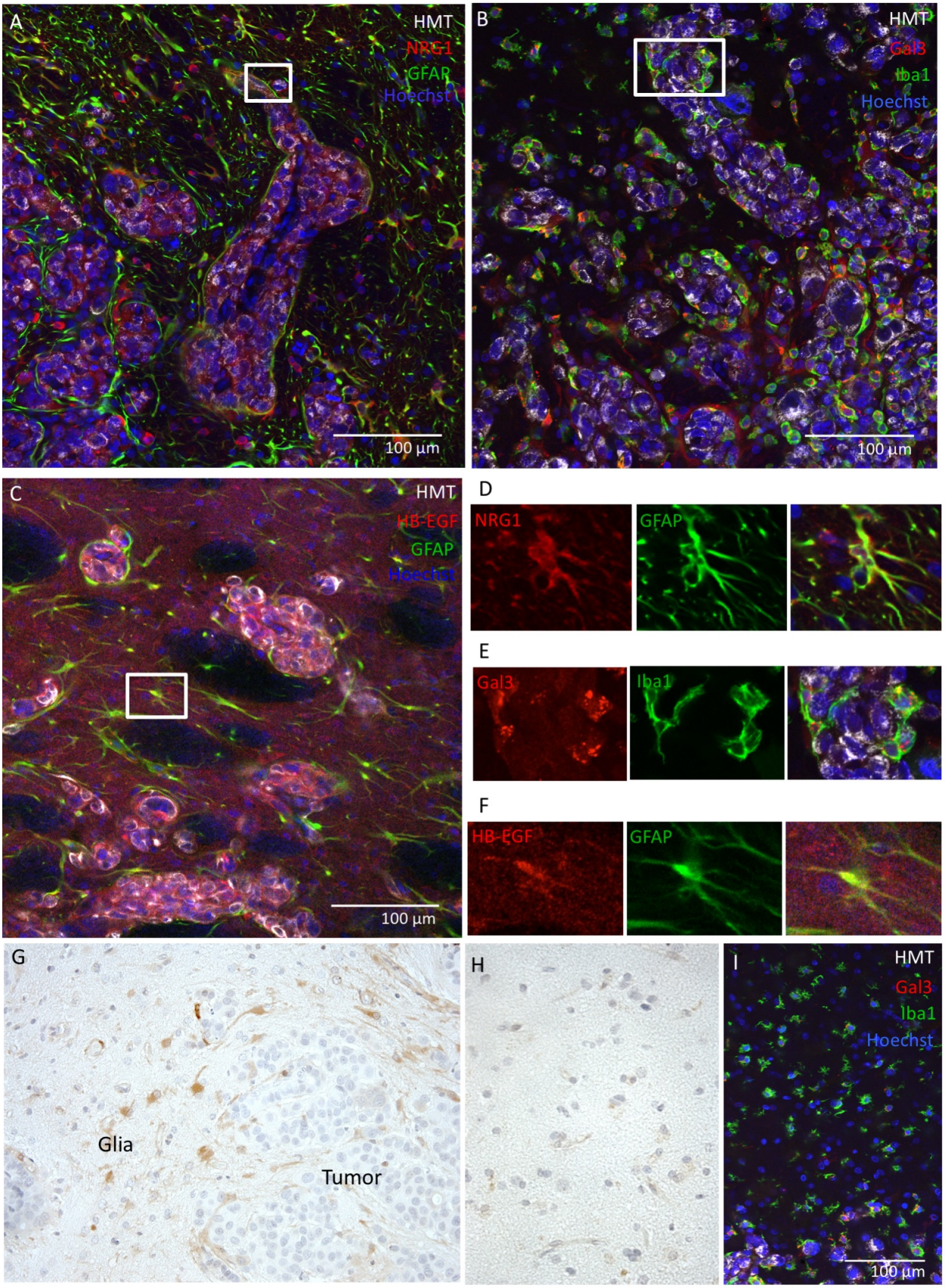
A
HMT
NRG1
GFAP
Hoechst
100 µm
B
HMT
Gal3
Iba1
Hoechst
100 µm
C
HMT
HB-EGF
GFAP
Hoechst
100 µm
D
NRG1
GFAP
E
Gal3
Iba1
F
HB-EGF
GFAP
G
Glia
Tumor
H
I
HMT
Gal3
Iba1
Hoechst
100 µm

Figure 4.9. Co-localization of NRG1, Gal3, and HB-EGF with reactive glia in rat xenograft tumors and human breast cancer brain metastasis tissue. **(A)** HCC1954 xenograft tumor sections were immunostained for **(A)** HMT, NRG1, and GFAP, **(B)** HMT, Gal3, and Iba1, or **(C)** HMT, HB-EGF, and GFAP; **(D-F)** Close-ups of outlined regions with split channels and merged images of (A-C) are shown. **(G)** Example image of Gal 3 positivity in human breast cancer brain metastasis reactive glial cells, and **(H)** negative immunostaining in brain around tumor. **(I)** HCC1954 xenograft tumor immunostained for HMT, Gal3, and Iba1. Sparse tumor cells from the infiltrative tumor are seen at the bottom on the image. Moving up in the image displays brain at further distance from the tumor's edge. Gal3 immunoreactivity was not observed in brain away from tumor.

αvβ3-integrin and HER2 heterodimer ligands that are expressed in the metastatic tumor microenvironment increase tumorigenic characteristics of breast cancer cells in vitro.

While NRG1, HB-EGF, and Gal3 have been reported in the literature to have numerous protumorigenic effects, we tested if some of these effects were maintained in breast cancer cell lines able to form tumors in the brain (*276, 277, 279, 395-402*). Stimulation of HCC1954 with Gal3, HB-EGF, and NRG1 all increased cell proliferation, as evidenced by increased cell confluence (Fig. 4.10 A-C). Similar effects were seen in SKBR3 cells (not pictured). We next aimed to test if stimulation with these factors caused a change in protein localization in the cancer cells, evaluated by cell immunofluorescence experiments. While no consistent or clear differences were observed in protein localization, a substantial change in cell morphology was seen in cells treated with Gal3 (Fig. 4.10 D). At 5 and 10 min post stimulation with Gal3, cells formed numerous lamellipodia (Fig.4.10 D, yellow arrows), which are cellular structures formed

at the initiation of migration (*381, 403-405*). Quantification of the number of cells per field of view that contained lamellipodia demonstrated that the vast majority of cells extended lamellipodia (Fig.4.10 E). Lastly, we explored if these ligands influenced the phosphorylation of proteins involved in cell motility. A representative western blot demonstrating minor increases in phosphorylation of FAK, extracellular-signal-related kinase (ERK), and glycogen synthase kinase (GSK)-3β is shown (Fig. 4.10 F).

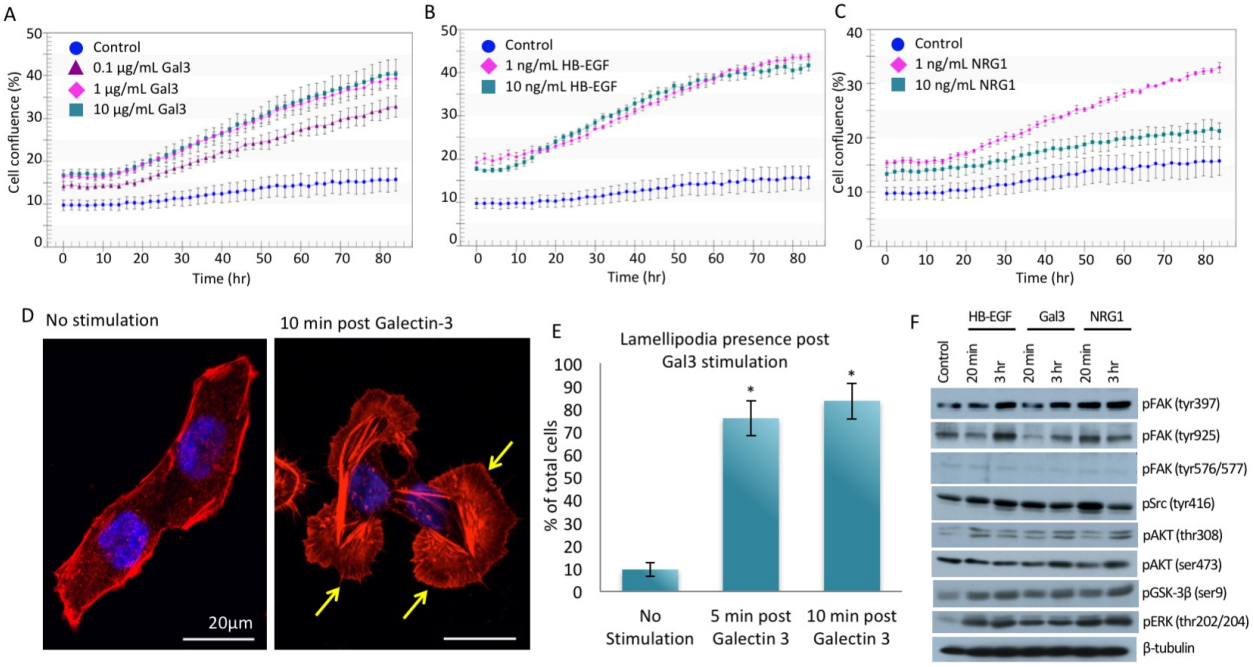

Figure 4.10. NRG1, HB-EGF, and Gal3 influence pro-tumorigenic cell behaviors *in vitro*. **(A-C)** Cell confluence assays tested in the IncuCyte. HCC1954 cells were seeded into 96-well plate at low density, treated with increasing concentrations of **(A)** Gal3, **(B)** HB-EGF, or **(C)** NRG1. Images were taken every 2 hours over the course of 3.5 days. **(D)** Example images of HCC1954 cells with no stimulation or 10 min post treatment with Gal-3. Yellow arrows: lamellipodia. **(E)** Quantification of the number of cells in each treatment group that had lamellipodia present. *p<0.001. **(F)** Western blot of phosphorylated proteins post HB-EGF, Gal3, or NRG1 stimulation.

Microglia produce and secrete pro-tumorigenic factors in vitro.

Our data thus far suggested that reactive glia in infiltrative tumor microenvironment express ligands that, when applied to breast cancer cells *in vitro,* increased cellular characteristics important for metastatic tumor growth. We next questioned if microglia cells, which co-localized with Gal3, secreted tumorigenic ligands in the presence of breast cancer cells. Using a modified boyden chamber migration assay, we tested if HCC1954 cell migration increased when BV2 microglial cells were present in the lower chamber. As both cell lines are adherent cells, any increase in migration would be due to soluble factors. Breast cancer cell migration significantly increased in the presence or BV2 cells, with or without pre-stimulation of the BV2 cells by lipopolysaccharide (LPS) (Fig. 4.11 A). Conditioned media from BV2 cells showed a trend toward increasing HCC1954 cell migration, but it was not statistically significant. Addition of cilengitide abolished the migratory stimulus of the BV2 cells. We next investigated what soluble factors could be present in the media that caused the increase in cell migration. Using an ELISA, we demonstrated that Gal3 was increased in media of BV2 cells co-cultured with HCC1954 cells, compared to BV2 cells alone (Fig. 4.11 B). As HB-EGF and NRG1 co-localized with astrocytes, we did not assess their concentrations in this assay.

Beyond NRG1, HB-EGF, and Gal3, numerous cytokines have been implicated in increased the migratory behaviors of metastatic cancer cells (*7*). In the tumor microenvironment it is likely that multi-factorial cellular behaviors such as cell migration and invasion will be dictated by a combination of factors. Thus, we performed a cytokine protein profiler on BV2 media and media from BV2 cells co-cultured with HCC1954 cells, demonstrating increased levels of multiple cytokines in the co-culture condition compared to the BV2 cells alone (Fig.11 C,D).

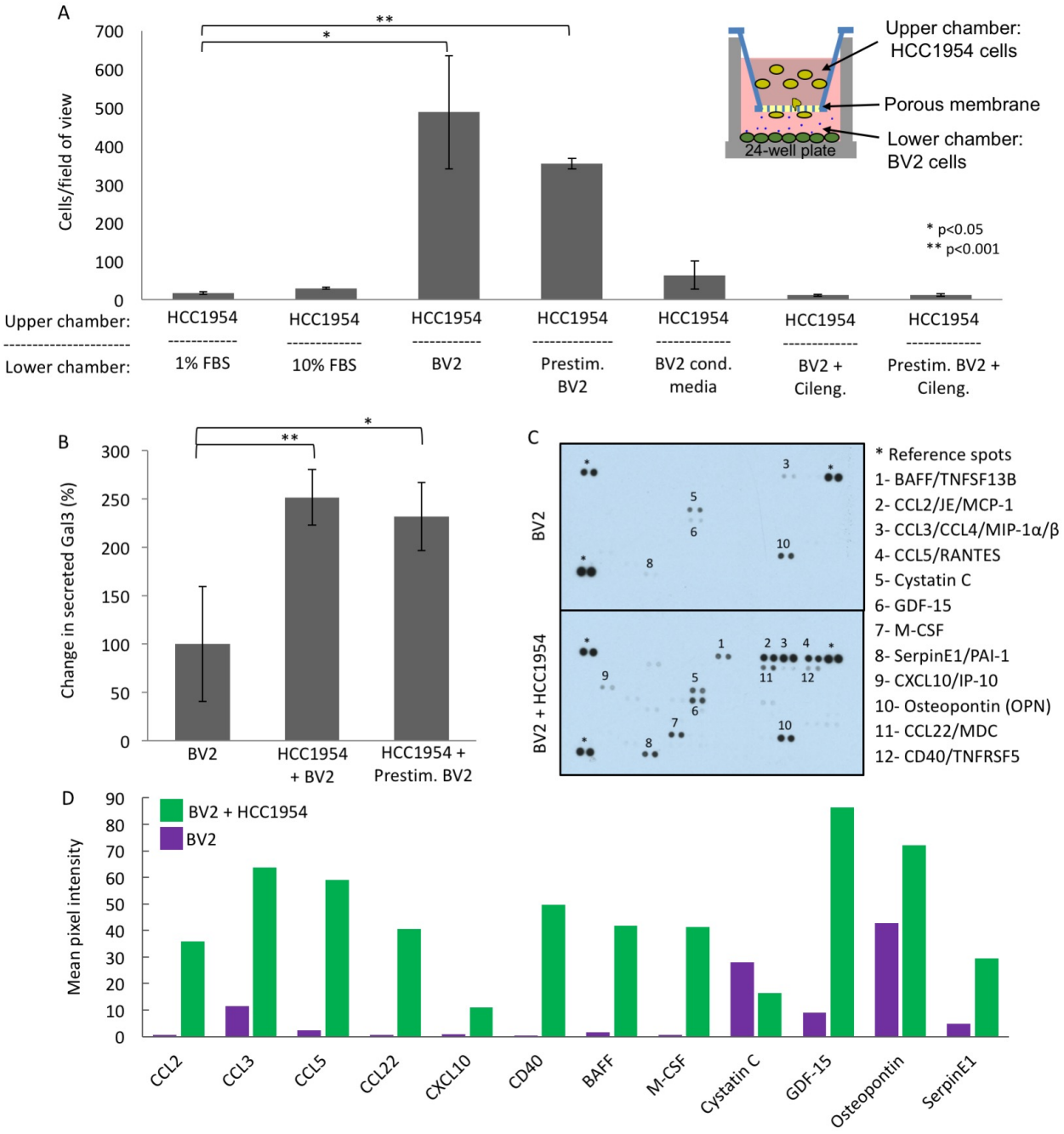

Figure 4.11. *In vitro* microglia increase the migration of human breast cancer cells, secreting Gal3 and multiple cytokines. (A) BV2 microglia cells were seeded into the bottom well of a modified boyden chamber assay. BV2 cells were allowed to adhere overnight, and several wells were treated with LPS to pre-stimulate the cells. HCC1954 breast cancer cells were seeded into the upper chamber alone, or with the integrin inhibitor cilengitide. After 48 hours the

number of cells that migrated through the porous membrane towards the BV2 cells were quantified. Replicates from 3 independent experiments were averaged. Insert: diagram of assay set-up. *p<0.05, **p<0.001. **(B)** Gal3 concentration was quantified in the media of BV2 cells culture alone or in combination with HCC1954 cells, as tested by ELISA. *p<0.05, **p<0.001. **(C)** Spot blots of a mouse cytokine protein array, incubated with media from BV2 cells or BV2 cells co-cultured with HCC1954 cells. Numbers on the blot identify two replicate spots that indicate specific cytokines, listed to the left of the blot. **(D)** Quantification of blot intensity from two independent replicates of the example data depicted in (C). While no statistical differences were calculated as only two replicates were performed, blots from each replicate showed similar results.

Galectin-3 expression is reproduced in hematogenous metastases, and co-localized with both microglia and infiltrating macrophages.

We next aimed to test if the localization of Gal3 with Iba1+ cells could be replicated in a hematogenous metastasis model, which better mimics the biological growth of metastatic tumors. HCC1954 cells were infused in the right external carotid artery to seed the brain, rather than directly inoculated into brain tissue. Gal3 co-localized with Iba1+ cells in a rat hematogenous metastasis model tissue (Fig. 4.12 A).

Iba1+ cells represent a mixed cell population that can include resident brain microglia and infiltrating bone marrow derived macrophages. We next investigated if Gal3 was expressed solely in one or both of these cell population utilizing a cell tracking technique. Molday IONs (MIRBs) are ironoxide nanoparticles coating in a highly cross-linked dextran coating conjugated to Texas red fluorophores. MIRBs were engineered specifically for their high propensity to be take-up by circulating monocytes. Intravenous injection of MIRB has been demonstrated to differentiate infiltrating macrophages from brain resident microglia in previous studies investigating CNS inflammatory lesions (*406*). We injected MIRB i.v. one day prior to HCC1954 tumor implantation, and after one week assessed the co-localization of MIRB, Gal3, and Iba1. Immunofluorescent imaging demonstrated the co-localization of all three signals around tumor lesions, indicating that Gal3 can be expressed by infiltrating macrophages (Fig. 4.12 B, yellow arrows). Not all Iba1+Gal3+ cells co-stained for MIRB, suggesting that both macrophages and microglia likely produce Gal3 around breast cancer brain metastases, however technical limitations hindered our ability to decisively conclude the cell of origin.

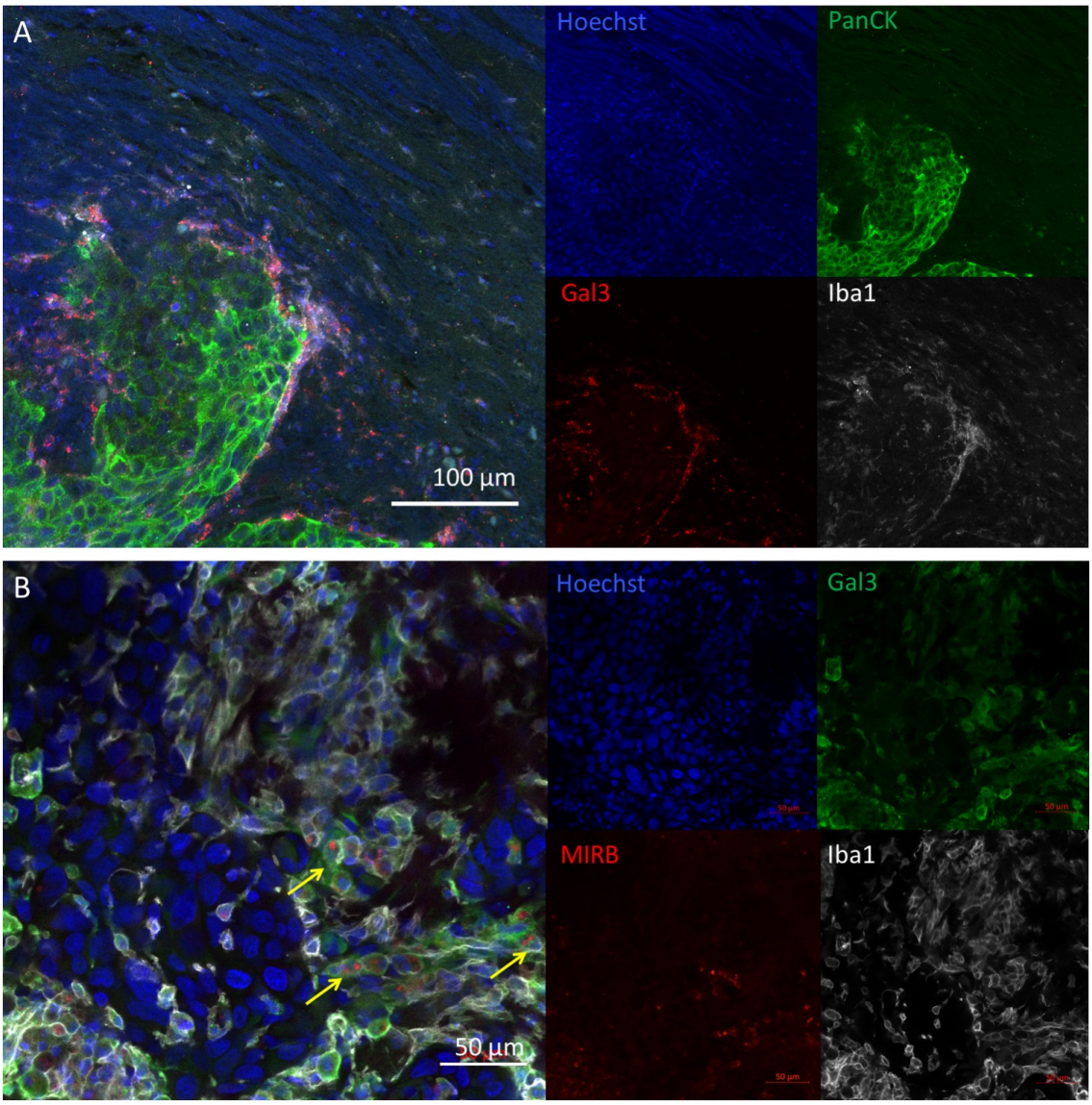

Figure 4.12. Gal3 is expressed in brain around hematogenous metastases and co-localized with MIRB, suggesting expression in microglia and infiltrating macrophages. HCC1954 hematogenous metastasis brain tissue sections were immunostained for pan-cytokeratin (PanCK), Gal3, and Iba1, demonstrating the phenotype of Gal3 expression is conserved across rodent tumor models. **(B)** Following i.v. injection of MIRB, HCC1954 cells were inoculated into the caudate putamen per standard xenograft model methods. After 7 days the brains were fixed, sectioned, and immunostained for Gal3 and Iba1 to assess co-localization with intracellular MIRB. Yellow arrows: clusters of cells positive for Gal3, Iba1, and MIRB.

Pharmacologically inhibiting Gal-3 had minimal effects on tumor growth and Gal-3 presence around breast cancer intracerebral xenografts.

Lastly, we questioned if inhibition of Gal-3 could decrease breast cancer xenograft brain tumor volume. A small pilot cohort of rats (n=10 total, 5 per group) received HCC1954 tumor inoculation into the caudate putamen and then were treated with intra peritoneal (i.p.) GCS-100, a Gal-3 inhibitor, on days 4, 6, and 8 (Fig. 4.13 A). Rats were euthanized on day 11, and brains were fixed, sectioned, and subject to immunohistochemical analysis for tumor volume and Gal3 expression. No difference was seen in tumor volumes between the treatment groups (Fig. 4.13 B). Example images of the tumors are displayed (Fig. 4.13 C). In both the control and treatment groups, tumors with large potentially necrotic cores were observed. No statistically significant difference was seen in the mean or max distance that Gal3 was expressed away from the tumor edge (Fig. 13 D,E). Representative immunofluorescent images of control and treatment tumors and their surrounding microenvironment are displayed (Fig. 13 F-I). Gal-3 signal is clearly visible in the brain immediately surrounding the PanCK+ tumor cells, where there is a high density of Iba1+ cells, in both control and treatment brains.

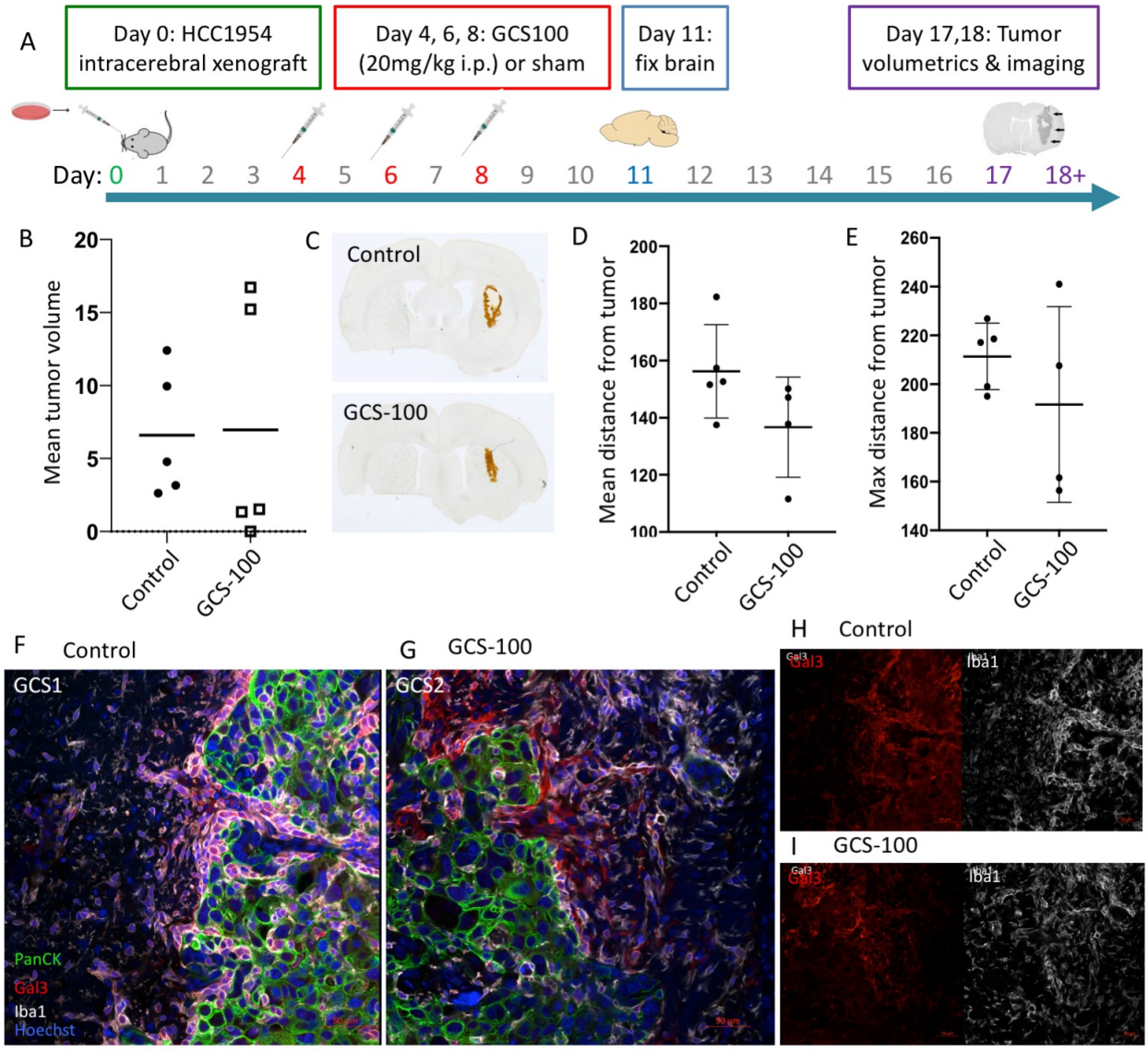

Figure 4.13. Inhibition of Gal3 with GCS-100 has minimal effect on intracerebral xenograft growth and their microenvironment. **(A)** Experimental design. **(B)** Tumor volumetrics from control and treatment arms. **(C)** Example images of tumors in the control and GCS-treated animals. **(D,E)** Distance of Gal3 expression away from the leading edge of the tumor quantified as the mean **(D)** and maximum **(E)** distances. **(F,G)** Representative immunofluorescent images of control **(F)** and GCS-100 treated **(G)** tumors immunolabeled for PanCK, Gal3, and Iba1. **(H,I)**. Single channel images displaying only Gal3 and Iba1 staining in the merged images (F,G).

4.5. Discussion

The diagnosis of brain metastasis is associated with extremely poor prognosis, yet current therapies are limited to radiation and surgical interventions and prevention strategies are restricted to whole brain radiation (*407*). Improving pharmacologic therapies would be extremely beneficial, but requires a better understanding of the unique biomolecular properties of brain-trophic tumor cells and how they aid the metastatic cells in outgrowth in the unique brain microenvironment. A complete picture of how cancer cells thrive in the brain microenvironment remains unclear (*373, 374, 408*).

Role of αvbeta3-integrin and HER2 breast cancer brain metastasis.

Individually, HER2 and integrins are known factors in cancer metastasis. HER2 accentuates the metastatic phenotype and brain organotropism in breast cancers, increasing brain metastasis in preclinical models (*370*) and in patients (*371, 373*). However, despite the prevalence of HER2 in brain metastases, anti-HER2 agents such as lapatinib and trastuzumab have not yet found a role in prevention or treatment of this disease (*373*). Similarly, αv-integrin and αvβ3-integrin have emerged as a negative diagnostic biomarkers (*267-270*). Targeting αvβ3-integrin has both therapeutic and preventive activity in preclinical models (*282-284*), but these benefits have not transferred to the clinical setting (*285-287*).

In the current study we investigated the role of αvβ3-integrin and HER2 in breast cancer brain metastases, and how they may mediate microenvironment interactions in a pro-tumorigenic fashion. We demonstrated that αvβ3-integrin and HER2 can physically interact in human breast cancer cells, and that they are spatially associated with membrane protrusions, a potential linker protein CD9, and a functional kinase, FAK. Knockdown or pharmacological inhibition of these

proteins reduced cell motility *in vitro*. *In vivo,* cells with reduced αvβ3-integrin with or without HER2 had decreased infiltration into the brain through the perivascular space where they were in close proximity to reactive glia.

Multiple reports document the presence of direct interactions between various integrins and members of the EGFR family, and suggest that interactions between these proteins may be important in metastatic cancers (*271, 376*). In breast cancer cells, α3β1 integrin regulates dimerization of HER2 to the active form (*375*), and β4-integrin enhances HER2 activity and stimulates mammary cell tumorigenesis (*409*). Additionally, α6β4 integrin interactions with HER2 resulting in increased cell motility and survival (*378*), and inhibition of this heterodimer blocks HER2 signaling and growth of orthotopic xenografts (*410*). We have now demonstrated that αvβ3-integrin and HER2 can also physically interact, and propose that their interaction may be involved in regulating cell motility. HER2 and integrins are both known to influence cell motility individually (*271, 378, 411*).

When the invasive phenotype of these clonal populations was assessed *in vivo*, a gross morphological change was observed. It is important to assess cell motility in the brain microenvironment as it plays a crucial and multifactorial role in the progression and metastatic dispersal of tumor cells (*408*). In the xenograft breast cancer brain metastasis model, the tumor infiltrative growth phenotype was dependent on both integrin and HER2 expression. A more infiltrative phenotype would increase the difficulty of achieving full tumor resection in patients, increasing the likelihood of tumor recurrence. It is possible that dual inhibition of integrins and HER2 could alter tumor morphology to make them more resectable. Furthermore, the enhanced infiltrative nature of breast cancer cells with high integrin and HER2 expression placed them in close proximity to glia where they could potentially activate the glial cells to a tumor-supportive

phenotype. Modifying this phenotype could alter how metastatic tumor cells engage elements of the brain microenvironment to support tumor growth. These possibilities warrant further investigation.

Role of the brain microenvironment in HER2-positive breast cancer brain metastatic outgrowth.

Components of the brain microenvironment play an essential role in the seeding and outgrowth of metastatic tumors in the brain, as was extensively reviewed in Chapter 1. However, out of the resident brain cells, microglia have been minimally studied in the context of breast cancer brain metastases. In other CNS tumors, such as glioblastoma, microglia are known to play critical functions in tumor development, growth, and treatment resistance (*78, 130*). One mechanism by which glial cells impact tumor growth is through the production and secretion of soluble factors able to activate oncogenic pathways in malignant cells. In the present study we investigated if reactive glia could produce and secrete factors able to influence metastatic breast cancer cells through integrins and HER2 heterodimers.

Here we report that several factors, Gal-3, NRG1, and HB-EGF are expressed in microglia and astrocytes in tumor xenografts, and *in vitro* increase metastatic phenotypes of culture human breast cancer cells. We focus in on one specific factor, Gal3. We identified Gal3 expression in a hematogenous metastasis model and in human breast cancer brain metastasis tissue, to confirm this observation was unlikely to be an artifact of the xenograft tumor model. Furthermore, Gal-3 appeared to be expressed in both microglia and infiltrating macrophages from systemic circulation. Our co-culture experiments support that microglia can increase pro-metastatic phenotypes in breast cancer cells, by stimulating an increase in their migration. This increased migration was abrogated in the presence of cilengitide, suggesting the soluble factor

released by the culture microglial cells the impacts breast cancer cell migration likely functioned through activating αvβ3-integrin. In accordance with this observation, we identified increased levels of Gal3 in the media of co-cultures compared to BV2 cells alone. Interestingly, BV2 cells appeared to have increased release of Gal-3 and cytokines only when co-cultures with the breast cancer cells, suggesting that the cancer cells first have to stimulate the microglia.

When we pharmacologically inhibited Gal-3 with GCS-100 in a xenograft tumor model, we observed little to no effect on tumor growth patterns. In this experiment GCS-100 was delivered i.p., and the permeability of GCS-100 across the blood-brain barrier (BBB) is unknown. It is likely that given the inconsistent permeability of tumor vasculature, that the BBB inhibited drug delivery to the tumor. It is plausible that delivering GCS-100 with BBB disruption could enhance delivery and result in anti-tumor effects. As a significant body of scientific literature is now reporting Gal-3 as a druggable target in several metastatic cancers and GCS-100 has a favorable side-effect profile in clinical trials, future investigations into the permeability of GCS-100 across the BBB and its efficacy when delivery is enhanced are merited (*279, 412*).

Limitations and future directions.

A limitation of this study is the use of a single brain-trophic cell line for many of the experiments, albeit multiple knockdown clones were used, and we evaluated both *in vitro* and *in vivo* growth characteristics. Additional studies are required to replicate the experiments in cell lines of different origin to confirm the findings. Additionally, many of the findings in this report are observational and hypothesis generating.

Taken together, our findings highlight the complex interaction of integrin and HER2 signaling on the plasma membrane of neoplastic breast cancer cells and the potential role of the

brain tumor microenvironment in promoting metastatic behaviors of invading breast cancer cells. Future studies are needed to further investigating the tumor-microenvironment cross talk. Specifically, follow-up work assessing the permeability of GCS-100 across the BBB and its effects after sufficient delivery into the tumor bed, which could be achieve with osmotic BBB disruption of focus ultrasound mediated BBB disruption, are warranted. The results of the cytokine protein array herein merit follow-up to assess effects of modulating individual cytokines that were upregulated when the BV2 cells were co-cultured with breast cancer cells. Several of the cytokines that were upregulated have known pro-tumorigenic effects in other CNS malignancies. Lastly, future work should address how the breast cancer cells stimulated the BV2 cells to increase secretion of pro-metastatic factors. This information would provide a full mechanistic loop describing how invading breast cancer cells alter the brain microenvironment to become a niche where resident cells produce and secrete tumor promoting factors, and disrupting any point in this pro-metastatic cycle would present potential therapeutic targets.

Acknowledgements

We sincerely thank Dr. Rochelle Fu for meaningful discussion on statistic and Dr. Randy Woltjer for the opportunity to confirm our observation in archival human tumor tissue. We also thank the staff at the OHSU Advanced Light Microscopy Core and Flow Cytometry Core for their assistance and equipment throughout this project.

CHAPTER 5: IMPROVING OUTCOMES FOR PATIENTS WITH FOR MALIGNANT BRAIN TUMORS – WHERE ARE WE NOW AND HOW DO WE PROGRESS?

Current challenges hindering therapeutic improves for brain tumors.

Despite exciting preclinical therapeutic results, novel treatment strategies for malignant tumors in the CNS have largely failed to improve survival in the clinic. These failures include treatments that have shown clinical efficacy in systemic neoplasms, such as targeted therapeutics and immunotherapies. Why have these not worked in the CNS? Multiple factors contribute to these disappointing results including imperfect model systems for primary and metastatic brain tumors, extensive and multi-layered tumor heterogeneity, hindered drug delivery across the BBB/BTB, CNS toxicities, limited longitudinal tumor evaluation modalities, and an incomplete understanding of the unique brain tumor microenvironment.

In this dissertation I explored several of these limitations including tumor heterogeneity, modalities to improve CNS tumor evaluation, and tumor-microenvironment crosstalk. An improved appreciation for the impact that intra-tumoral heterogeneity has on assessing prognostic and predictive gene expression panels can advance methods to robustly compare tumors, identify clinically-meaningful cohorts, and potentially predict treatment sensitivity on an individual basis. Meanwhile, developing modalities to assess biological tumor properties in a non-invasive manner through imaging biomarkers will permit the evaluation of biological signatures across a whole tumor and over the course of treatment in each patient. Lastly, improving our basic knowledge of how tumors interact with their unique microenvironment to promote tumor growth will identify novel pathways that could provide therapeutic benefit in

CNS malignancies. Together, these studies deliver important information for the field, generate new hypotheses, and highlight the remaining gaps in our knowledge and research tools.

Remaining problems and future directions.

1. Brain tumor models – A major limitation in brain tumor research, and thus in producing clinically-translatable findings, lies in the currently available model systems. Until recently nearly all murine models of CNS tumors have been developed in immunocompromised hosts (*301, 413*). While these models do provide essential tools in the study of brain tumors, they do not recapitulate the entire tumor microenvironment and prevent studies investigating the role of the systemic immune system in tumors. Syngeneic models for brain tumors are still highly limited, and advancements in this area are needed (*414*). Developing models that incorporate a fully intact immune system would permit more detailed investigations of immunotherapies, and perhaps help uncover why these therapies have shown limited efficacy in CNS tumors.

Additionally, neither GBM nor metastatic tumors models perfectly mimic the biological properties of their human tumor counterparts. Many common GBM models that have been highly utilized in preclinical work do not display the characteristic infiltrative nature of human GBM, and thus, their microenvironment interactions may be dissimilar preventing research investigating the complex cellular cross-talk that dictates GBM growth. Recent developments of patient derived xenograft models of GBM, whereby tumor cells are transferred directly from animal to animal without culture outside of the brain, have generated tumors that display histologic features more similar to human GBM (*415*). Though, these tumors are grown in immunocompromised rodents. Models of breast cancer brain metastases present an even greater challenge, as a perfect model would include all elements of the metastatic cascade to most

accurately recapitulate the tumor microenvironment (*301, 416*). Unfortunately, spontaneous breast cancer tumor models are limited and even within these models the development of brain metastases is rare (*417*). Furthermore, as brain metastasis is often a late stage complication in cancer, metastatic lesions in other tissues prior to the brain cause the animal to deteriorate before biological modulation and treatment studies can be completed on brain lesions. Improved models that mimic human tumors as closely as possible are needed to permit studies on the biology of tumor-microenvironment interactions, understand the contribution of the systemic immune system to these tumors, and better assess the efficacy of novel therapeutics.

2. Diagnostic tests and biomarkers – a major clinical limitation in care for patients with brain tumors is a lack of optimal methods to evaluate and follow tumor progression over the course of treatment. As discussed in depth, current tumor evaluation methods include assessment of a small panel of prognostic genes/proteins in a random biopsy sample at the time of diagnosis and in some cases repeated at the time of tumor relapse. Meanwhile, MR imaging is the principal non-invasive modality used to assess tumors over time. Individually, these techniques provide a small window of information about the tumor. Improving larger prognostic and predictive signatures, and developing robust methods to evaluate these features over the whole tumor and across the time-span of treatment will be hugely beneficial.

Imaging genomics presents a new research area with the potential to have a substantial impact on patient care by permitting non-invasive investigation of complex molecular features of tumors (*61, 62, 418*). Importantly, it will be necessary to confirm all potential biological patterns identified at the transcriptional level in protein panels and in prospective studies to develop validated, robust biomarkers. Developing imaging biomarkers could allow clinicians to follow

oncogenic pathways and immune reactions in tumors over time, which would help tailor individual treatments to address how each tumor is behaving at a specific point in time. Improved imaging metrics are also needed that clearly delineate tumor growth from treatment-induced inflammation (e.g. differentiate between true tumor growth and radiographic pseudoprogression) (*363*); imaging biomarkers of specific inflammatory processes could provide a tool for this delineation. Ferumoxytol contrast enhanced imaging is currently being used to evaluate pseudoprogression in patients with GBM (*419, 420*). Performing imaging genomics studies of Ferumoxytol verses gadolinium contrast enhanced tumor regions could provide increased resolution of molecular tumor characteristics and merits future investigation.

3. Drug delivery to tumors behind the BBB/BTB – Drug delivery to brain tumors remains a considerable problem despite decades of research on the BBB/BTB and our ability to transiently open the barrier using multiple modalities in animals and humans. Unfortunately, in rodent tumor models the physical size of the vasculature and surgical ligations required to catheterize the external carotid artery for intra-arterial mannitol infusion limit experimental models to only one osmotic BBB disruption (BBBD) per animal, making this method not feasible for studies testing multiple dose regiments. In human trials, osmotic BBBD followed by intra-arterial infusions of chemotherapies has shown benefit in numerous patient cohorts (*421-423*). Developing model systems that allow for multiple BBBD treatments would permit studies of drug efficacy in CNS tumors without the limitation of restricted passage across the BBB.

While decades of research and clinical use of osmotic BBBD have shown its safety in humans, recent work is demonstrating that BBBD elicits a sterile pro-inflammatory response in the brain that could be harnessed for anti-tumor effects. Similar to results from focused

ultrasound mediated BBBD (*406*), osmotic BBBD causes increased expression of inflammatory cytokines and activation of microglia and astrocytes in the brain (unpublished data). Transcriptomic profiling of brain tissue following osmotic BBBD suggests that the inflammatory response may polarize microglia/macrophages towards an M1 phenotype, and as such could serve as a novel technique to activate an anti-tumor immune microenvironment. The role of BBBD in not only increasing drug delivery to the brain, but also in altering the brain microenvironment to become a hostile niche for tumor growth warrants further research.

Is attempting to improve outcome for brain tumors a futile effort?

Malignant brain tumors present an exceptionally challenging scientific and clinical problem as they are a highly complex, heterogeneous, multi-factorial set of diseases that will likely require personalized treatment for optimal patient outcomes. Developing a thorough understanding of the intricate biological, pathological, and physiological processes that promote tumor formation, growth, and treatment sensitivity will be paramount in moving the field forward, and will likely require a collaborative interdisciplinary approach. Optimistically, recent advances in numerous fields critical for studying brain tumors, including large scale data production, bioinformatics, data processing/analysis, neurobiology, immunology, oncology, radiology, and new rodent models, will make these remaining obstacles surmountable.

REFERENCES

1. R. Stupp *et al.*, Effects of radiotherapy with concomitant and adjuvant temozolomide versus radiotherapy alone on survival in glioblastoma in a randomised phase III study: 5-year analysis of the EORTC-NCIC trial. *Lancet Oncol* **10**, 459-466 (2009).
2. R. Stupp *et al.*, Radiotherapy plus concomitant and adjuvant temozolomide for glioblastoma. *N Engl J Med* **352**, 987-996 (2005).
3. R. Stupp *et al.*, Effect of Tumor-Treating Fields Plus Maintenance Temozolomide vs Maintenance Temozolomide Alone on Survival in Patients With Glioblastoma: A Randomized Clinical Trial. *JAMA* **318**, 2306-2316 (2017).
4. Q. T. Ostrom *et al.*, CBTRUS Statistical Report: Primary brain and other central nervous system tumors diagnosed in the United States in 2010-2014. *Neuro Oncol* **19**, v1-v88 (2017).
5. D. N. Louis *et al.*, The 2016 World Health Organization Classification of Tumors of the Central Nervous System: a summary. *Acta Neuropathol* **131**, 803-820 (2016).
6. X. Lin, L. M. DeAngelis, Treatment of Brain Metastases. *J Clin Oncol* **33**, 3475-3484 (2015).
7. A. S. Achrol *et al.*, Brain metastases. *Nat Rev Dis Primers* **5**, 5 (2019).
8. H. A. Tawbi, C. Chung, K. Margolin, Nivolumab and Ipilimumab in Melanoma Metastatic to the Brain. *N Engl J Med* **379**, 2178 (2018).
9. H. A. Tawbi *et al.*, Combined Nivolumab and Ipilimumab in Melanoma Metastatic to the Brain. *N Engl J Med* **379**, 722-730 (2018).
10. P. W. Sperduto *et al.*, Effect of tumor subtype on survival and the graded prognostic assessment for patients with breast cancer and brain metastases. *Int J Radiat Oncol Biol Phys* **82**, 2111-2117 (2012).
11. H. Kennecke *et al.*, Metastatic behavior of breast cancer subtypes. *J Clin Oncol* **28**, 3271-3277 (2010).
12. S. Lapointe, A. Perry, N. A. Butowski, Primary brain tumours in adults. *Lancet* **392**, 432-446 (2018).
13. D. W. Parsons *et al.*, An integrated genomic analysis of human glioblastoma multiforme. *Science* **321**, 1807-1812 (2008).
14. H. Ohgaki, P. Kleihues, The definition of primary and secondary glioblastoma. *Clin Cancer Res* **19**, 764-772 (2013).
15. S. R. Alcantara Llaguno, L. F. Parada, Cell of origin of glioma: biological and clinical implications. *Br J Cancer* **115**, 1445-1450 (2016).
16. F. H. Gage, Mammalian neural stem cells. *Science* **287**, 1433-1438 (2000).
17. C. Liu, H. Zong, Developmental origins of brain tumors. *Curr Opin Neurobiol* **22**, 844-849 (2012).
18. D. Friedmann-Morvinski *et al.*, Dedifferentiation of neurons and astrocytes by oncogenes can induce gliomas in mice. *Science* **338**, 1080-1084 (2012).
19. S. R. Alcantara Llaguno *et al.*, Adult Lineage-Restricted CNS Progenitors Specify Distinct Glioblastoma Subtypes. *Cancer Cell* **28**, 429-440 (2015).
20. S. Alcantara Llaguno *et al.*, Malignant astrocytomas originate from neural stem/progenitor cells in a somatic tumor suppressor mouse model. *Cancer Cell* **15**, 45-56 (2009).

21. C. W. Brennan *et al.*, The somatic genomic landscape of glioblastoma. *Cell* **155**, 462-477 (2013).
22. Cancer Genome Atlas Research Network, Comprehensive genomic characterization defines human glioblastoma genes and core pathways. *Nature* **455**, 1061-1068 (2008).
23. M. M. Inda, R. Bonavia, J. Seoane, Glioblastoma multiforme: a look inside its heterogeneous nature. *Cancers (Basel)* **6**, 226-239 (2014).
24. H. S. Phillips *et al.*, Molecular subclasses of high-grade glioma predict prognosis, delineate a pattern of disease progression, and resemble stages in neurogenesis. *Cancer Cell* **9**, 157-173 (2006).
25. R. G. Verhaak *et al.*, Integrated genomic analysis identifies clinically relevant subtypes of glioblastoma characterized by abnormalities in PDGFRA, IDH1, EGFR, and NF1. *Cancer Cell* **17**, 98-110 (2010).
26. Q. Wang *et al.*, Tumor Evolution of Glioma-Intrinsic Gene Expression Subtypes Associates with Immunological Changes in the Microenvironment. *Cancer Cell* **32**, 42-56 e46 (2017).
27. K. P. L. Bhat *et al.*, Mesenchymal differentiation mediated by NF-kappaB promotes radiation resistance in glioblastoma. *Cancer Cell* **24**, 331-346 (2013).
28. M. Abedalthagafi, D. Barakeh, K. M. Foshay, Immunogenetics of glioblastoma: the future of personalized patient management. *NPJ Precis Oncol* **2**, 27 (2018).
29. W. Cheng *et al.*, Bioinformatic analyses reveal a distinct Notch activation induced by STAT3 phosphorylation in the mesenchymal subtype of glioblastoma. *J Neurosurg* **126**, 249-259 (2017).
30. T. Doucette *et al.*, Immune heterogeneity of glioblastoma subtypes: extrapolation from the cancer genome atlas. *Cancer Immunol Res* **1**, 112-122 (2013).
31. W. C. Rutledge *et al.*, Tumor-infiltrating lymphocytes in glioblastoma are associated with specific genomic alterations and related to transcriptional class. *Clin Cancer Res* **19**, 4951-4960 (2013).
32. Z. Chen, D. Hambardzumyan, Immune Microenvironment in Glioblastoma Subtypes. *Front Immunol* **9**, 1004 (2018).
33. A. P. Patel *et al.*, Single-cell RNA-seq highlights intratumoral heterogeneity in primary glioblastoma. *Science* **344**, 1396-1401 (2014).
34. K. D. Aldape *et al.*, Immunohistochemical detection of EGFRvIII in high malignancy grade astrocytomas and evaluation of prognostic significance. *J Neuropathol Exp Neurol* **63**, 700-707 (2004).
35. T. E. Taylor, F. B. Furnari, W. K. Cavenee, Targeting EGFR for treatment of glioblastoma: molecular basis to overcome resistance. *Curr Cancer Drug Targets* **12**, 197-209 (2012).
36. J. Yang, J. Yan, B. Liu, Targeting EGFRvIII for glioblastoma multiforme. *Cancer Lett* **403**, 224-230 (2017).
37. Y. Tohma *et al.*, PTEN (MMAC1) mutations are frequent in primary glioblastomas (de novo) but not in secondary glioblastomas. *J Neuropathol Exp Neurol* **57**, 684-689 (1998).
38. F. Han *et al.*, PTEN gene mutations correlate to poor prognosis in glioma patients: a meta-analysis. *Onco Targets Ther* **9**, 3485-3492 (2016).

39. M. E. Hegi *et al.*, MGMT gene silencing and benefit from temozolomide in glioblastoma. *N Engl J Med* **352**, 997-1003 (2005).
40. M. Weller *et al.*, MGMT promoter methylation in malignant gliomas: ready for personalized medicine? *Nat Rev Neurol* **6**, 39-51 (2010).
41. M. Sanson *et al.*, Isocitrate dehydrogenase 1 codon 132 mutation is an important prognostic biomarker in gliomas. *J Clin Oncol* **27**, 4150-4154 (2009).
42. A. L. Cohen, S. L. Holmen, H. Colman, IDH1 and IDH2 mutations in gliomas. *Curr Neurol Neurosci Rep* **13**, 345 (2013).
43. K. Aldape, P. C. Burger, A. Perry, Clinicopathologic aspects of 1p/19q loss and the diagnosis of oligodendroglioma. *Arch Pathol Lab Med* **131**, 242-251 (2007).
44. J. Zhao, W. Ma, H. Zhao, Loss of heterozygosity 1p/19q and survival in glioma: a meta-analysis. *Neuro Oncol* **16**, 103-112 (2014).
45. J. Schwartzentruber *et al.*, Driver mutations in histone H3.3 and chromatin remodelling genes in paediatric glioblastoma. *Nature* **482**, 226-231 (2012).
46. C. Koschmann, P. R. Lowenstein, M. G. Castro, ATRX mutations and glioblastoma: Impaired DNA damage repair, alternative lengthening of telomeres, and genetic instability. *Mol Cell Oncol* **3**, e1167158 (2016).
47. P. Nandakumar, A. Mansouri, S. Das, The Role of ATRX in Glioma Biology. *Front Oncol* **7**, 236 (2017).
48. X. Wang *et al.*, Gain of function of mutant TP53 in glioblastoma: prognosis and response to temozolomide. *Ann Surg Oncol* **21**, 1337-1344 (2014).
49. B. England, T. Huang, M. Karsy, Current understanding of the role and targeting of tumor suppressor p53 in glioblastoma multiforme. *Tumour Biol* **34**, 2063-2074 (2013).
50. A. Chaurasia, S. H. Park, J. W. Seo, C. K. Park, Immunohistochemical Analysis of ATRX, IDH1 and p53 in Glioblastoma and Their Correlations with Patient Survival. *J Korean Med Sci* **31**, 1208-1214 (2016).
51. A. Sottoriva *et al.*, Intratumor heterogeneity in human glioblastoma reflects cancer evolutionary dynamics. *Proc Natl Acad Sci U S A* **110**, 4009-4014 (2013).
52. K. Strommer, M. F. Hamou, H. Diggelmann, N. de Tribolet, Cellular and tumoural heterogeneity of EGFR gene amplification in human malignant gliomas. *Acta Neurochir (Wien)* **107**, 82-87 (1990).
53. E. Padfield, H. P. Ellis, K. M. Kurian, Current Therapeutic Advances Targeting EGFR and EGFRvIII in Glioblastoma. *Front Oncol* **5**, 5 (2015).
54. J. Kim *et al.*, Spatiotemporal Evolution of the Primary Glioblastoma Genome. *Cancer Cell* **28**, 318-328 (2015).
55. J. K. Lee *et al.*, Spatiotemporal genomic architecture informs precision oncology in glioblastoma. *Nat Genet* **49**, 594-599 (2017).
56. Allen Institute for Brain Science. (2015), vol. 2017.
57. N. J. Szerlip *et al.*, Intratumoral heterogeneity of receptor tyrosine kinases EGFR and PDGFRA amplification in glioblastoma defines subpopulations with distinct growth factor response. *Proc Natl Acad Sci U S A* **109**, 3041-3046 (2012).
58. M. Meyer *et al.*, Single cell-derived clonal analysis of human glioblastoma links functional and genomic heterogeneity. *Proc Natl Acad Sci U S A* **112**, 851-856 (2015).

59. M. A. Qazi *et al.*, Intratumoral heterogeneity: pathways to treatment resistance and relapse in human glioblastoma. *Ann Oncol* **28**, 1448-1456 (2017).
60. R. Reinartz *et al.*, Functional Subclone Profiling for Prediction of Treatment-Induced Intratumor Population Shifts and Discovery of Rational Drug Combinations in Human Glioblastoma. *Clin Cancer Res* **23**, 562-574 (2017).
61. H. X. Bai *et al.*, Imaging genomics in cancer research: limitations and promises. *Br J Radiol* **89**, 20151030 (2016).
62. M. G. ElBanan, A. M. Amer, P. O. Zinn, R. R. Colen, Imaging genomics of Glioblastoma: state of the art bridge between genomics and neuroradiology. *Neuroimaging Clin N Am* **25**, 141-153 (2015).
63. C. C. Jaffe, Imaging and genomics: is there a synergy? *Radiology* **264**, 329-331 (2012).
64. W. B. Pope, Genomics of brain tumor imaging. *Neuroimaging Clin N Am* **25**, 105-119 (2015).
65. A. M. Rutman, M. D. Kuo, Radiogenomics: creating a link between molecular diagnostics and diagnostic imaging. *Eur J Radiol* **70**, 232-241 (2009).
66. P. M. Thompson, N. G. Martin, M. J. Wright, Imaging genomics. *Curr Opin Neurol* **23**, 368-373 (2010).
67. M. A. Mazurowski, Radiogenomics: what it is and why it is important. *J Am Coll Radiol* **12**, 862-866 (2015).
68. D. H. Heiland *et al.*, Integrative Diffusion-Weighted Imaging and Radiogenomic Network Analysis of Glioblastoma multiforme. *Sci Rep* **7**, 43523 (2017).
69. Z. C. Li *et al.*, Multiregional radiomics features from multiparametric MRI for prediction of MGMT methylation status in glioblastoma multiforme: A multicentre study. *Eur Radiol* **28**, 3640-3650 (2018).
70. M. C. Mabray, R. F. Barajas, Jr., S. Cha, Modern brain tumor imaging. *Brain Tumor Res Treat* **3**, 8-23 (2015).
71. S. Moton, M. Elbanan, P. O. Zinn, R. R. Colen, Imaging Genomics of Glioblastoma: Biology, Biomarkers, and Breakthroughs. *Top Magn Reson Imaging* **24**, 155-163 (2015).
72. M. Aghi *et al.*, Magnetic resonance imaging characteristics predict epidermal growth factor receptor amplification status in glioblastoma. *Clin Cancer Res* **11**, 8600-8605 (2005).
73. S. Drabycz *et al.*, An analysis of image texture, tumor location, and MGMT promoter methylation in glioblastoma using magnetic resonance imaging. *Neuroimage* **49**, 1398-1405 (2010).
74. J. A. Carrillo *et al.*, Relationship between tumor enhancement, edema, IDH1 mutational status, MGMT promoter methylation, and survival in glioblastoma. *AJNR Am J Neuroradiol* **33**, 1349-1355 (2012).
75. D. A. Gutman *et al.*, MR imaging predictors of molecular profile and survival: multi-institutional study of the TCGA glioblastoma data set. *Radiology* **267**, 560-569 (2013).
76. S. Narang *et al.*, Tumor image-derived texture features are associated with CD3 T-cell infiltration status in glioblastoma. *Oncotarget* **8**, 101244-101254 (2017).

77. R. F. Barajas, Jr. *et al.*, Glioblastoma multiforme regional genetic and cellular expression patterns: influence on anatomic and physiologic MR imaging. *Radiology* **254**, 564-576 (2010).
78. N. A. Charles, E. C. Holland, R. Gilbertson, R. Glass, H. Kettenmann, The brain tumor microenvironment. *Glia* **60**, 502-514 (2012).
79. D. F. Quail, J. A. Joyce, The Microenvironmental Landscape of Brain Tumors. *Cancer Cell* **31**, 326-341 (2017).
80. W. T. Farmer, K. Murai, Resolving Astrocyte Heterogeneity in the CNS. *Front Cell Neurosci* **11**, 300 (2017).
81. H. L. McConnell, C. N. Kersch, R. L. Woltjer, E. A. Neuwelt, The Translational Significance of the Neurovascular Unit. *J Biol Chem* **292**, 762-770 (2017).
82. A. L. Betz, J. A. Firth, G. W. Goldstein, Polarity of the blood-brain barrier: distribution of enzymes between the luminal and antiluminal membranes of brain capillary endothelial cells. *Brain Res* **192**, 17-28 (1980).
83. A. Badhwar, D. B. Stanimirovic, E. Hamel, A. S. Haqqani, The proteome of mouse cerebral arteries. *J Cereb Blood Flow Metab* **34**, 1033-1046 (2014).
84. A. M. Katz *et al.*, Astrocyte-specific expression patterns associated with the PDGF-induced glioma microenvironment. *PLoS One* **7**, e32453 (2012).
85. C. C. John Lin *et al.*, Identification of diverse astrocyte populations and their malignant analogs. *Nat Neurosci* **20**, 396-405 (2017).
86. M. Brandao, T. Simon, G. Critchley, G. Giamas, Astrocytes, the rising stars of the glioblastoma microenvironment. *Glia* **67**, 779-790 (2019).
87. B. H. Rath, J. M. Fair, M. Jamal, K. Camphausen, P. J. Tofilon, Astrocytes enhance the invasion potential of glioblastoma stem-like cells. *PLoS One* **8**, e54752 (2013).
88. W. Chen *et al.*, Human astrocytes secrete IL-6 to promote glioma migration and invasion through upregulation of cytomembrane MMP14. *Oncotarget* **7**, 62425-62438 (2016).
89. D. Biasoli *et al.*, Glioblastoma cells inhibit astrocytic p53-expression favoring cancer malignancy. *Oncogenesis* **3**, e123 (2014).
90. A. I. Oliveira *et al.*, Crosstalk between glial and glioblastoma cells triggers the "go-or-grow" phenotype of tumor cells. *Cell Commun Signal* **15**, 37 (2017).
91. P. Jin *et al.*, Astrocyte-derived CCL20 reinforces HIF-1-mediated hypoxic responses in glioblastoma by stimulating the CCR6-NF-kappaB signaling pathway. *Oncogene* **37**, 3070-3087 (2018).
92. W. Chen *et al.*, Glioma cells escaped from cytotoxicity of temozolomide and vincristine by communicating with human astrocytes. *Med Oncol* **32**, 43 (2015).
93. S. Oushy *et al.*, Glioblastoma multiforme-derived extracellular vesicles drive normal astrocytes towards a tumour-enhancing phenotype. *Philos Trans R Soc Lond B Biol Sci* **373**, (2018).
94. J. Chen *et al.*, The pathological structure of the perivascular niche in different microvascular patterns of glioblastoma. *PLoS One* **12**, e0182183 (2017).
95. A. Sharma, A. Shiras, Cancer stem cell-vascular endothelial cell interactions in glioblastoma. *Biochem Biophys Res Commun* **473**, 688-692 (2016).
96. A. Pietras *et al.*, Osteopontin-CD44 signaling in the glioma perivascular niche enhances cancer stem cell phenotypes and promotes aggressive tumor growth. *Cell Stem Cell* **14**, 357-369 (2014).

97. D. W. Infanger *et al.*, Glioblastoma stem cells are regulated by interleukin-8 signaling in a tumoral perivascular niche. *Cancer Res* **73**, 7079-7089 (2013).
98. O. van Tellingen *et al.*, Overcoming the blood-brain tumor barrier for effective glioblastoma treatment. *Drug Resist Updat* **19**, 1-12 (2015).
99. N. Charles, E. C. Holland, The perivascular niche microenvironment in brain tumor progression. *Cell Cycle* **9**, 3012-3021 (2010).
100. J. Anido *et al.*, TGF-beta Receptor Inhibitors Target the CD44(high)/Id1(high) Glioma-Initiating Cell Population in Human Glioblastoma. *Cancer Cell* **18**, 655-668 (2010).
101. E. Fessler, T. Borovski, J. P. Medema, Endothelial cells induce cancer stem cell features in differentiated glioblastoma cells via bFGF. *Mol Cancer* **14**, 157 (2015).
102. A. Schulte *et al.*, Glioblastoma stem-like cell lines with either maintenance or loss of high-level EGFR amplification, generated via modulation of ligand concentration. *Clin Cancer Res* **18**, 1901-1913 (2012).
103. R. Wang *et al.*, Glioblastoma stem-like cells give rise to tumour endothelium. *Nature* **468**, 829-833 (2010).
104. S. Das, P. A. Marsden, Angiogenesis in glioblastoma. *N Engl J Med* **369**, 1561-1563 (2013).
105. R. K. Jain *et al.*, Angiogenesis in brain tumours. *Nat Rev Neurosci* **8**, 610-622 (2007).
106. K. Angara, T. F. Borin, A. S. Arbab, Vascular Mimicry: A Novel Neovascularization Mechanism Driving Anti-Angiogenic Therapy (AAT) Resistance in Glioblastoma. *Transl Oncol* **10**, 650-660 (2017).
107. C. A. Shaifer, J. Huang, P. C. Lin, Glioblastoma cells incorporate into tumor vasculature and contribute to vascular radioresistance. *Int J Cancer* **127**, 2063-2075 (2010).
108. S. Watkins *et al.*, Disruption of astrocyte-vascular coupling and the blood-brain barrier by invading glioma cells. *Nat Commun* **5**, 4196 (2014).
109. P. R. Lockman *et al.*, Heterogeneous blood-tumor barrier permeability determines drug efficacy in experimental brain metastases of breast cancer. *Clin Cancer Res* **16**, 5664-5678 (2010).
110. J. N. Sarkaria *et al.*, Is the blood-brain barrier really disrupted in all glioblastomas? A critical assessment of existing clinical data. *Neuro Oncol* **20**, 184-191 (2018).
111. N. F. Brown, T. J. Carter, D. Ottaviani, P. Mulholland, Harnessing the immune system in glioblastoma. *Br J Cancer* **119**, 1171-1181 (2018).
112. A. Louveau *et al.*, Structural and functional features of central nervous system lymphatic vessels. *Nature* **523**, 337-341 (2015).
113. A. Aspelund *et al.*, A dural lymphatic vascular system that drains brain interstitial fluid and macromolecules. *J Exp Med* **212**, 991-999 (2015).
114. D. Hambardzumyan, D. H. Gutmann, H. Kettenmann, The role of microglia and macrophages in glioma maintenance and progression. *Nat Neurosci* **19**, 20-27 (2016).
115. F. Ginhoux *et al.*, Fate mapping analysis reveals that adult microglia derive from primitive macrophages. *Science* **330**, 841-845 (2010).
116. Z. Chen *et al.*, Cellular and Molecular Identity of Tumor-Associated Macrophages in Glioblastoma. *Cancer Res* **77**, 2266-2278 (2017).

117. G. Genard *et al.,* Reprogramming of Tumor-Associated Macrophages with Anticancer Therapies: Radiotherapy versus Chemo- and Immunotherapies. *Front Immunol* **8**, 828 (2017).
118. J. Xue *et al.*, Transcriptome-based network analysis reveals a spectrum model of human macrophage activation. *Immunity* **40**, 274-288 (2014).
119. A. Mantovani, F. Marchesi, A. Malesci, L. Laghi, P. Allavena, Tumour-associated macrophages as treatment targets in oncology. *Nat Rev Clin Oncol* **14**, 399-416 (2017).
120. D. G. DeNardo, B. Ruffell, Macrophages as regulators of tumour immunity and immunotherapy. *Nat Rev Immunol*, (2019).
121. V. Bronte, P. J. Murray, Understanding local macrophage phenotypes in disease: modulating macrophage function to treat cancer. *Nat Med* **21**, 117-119 (2015).
122. A. Mantovani, S. Sozzani, M. Locati, P. Allavena, A. Sica, Macrophage polarization: tumor-associated macrophages as a paradigm for polarized M2 mononuclear phagocytes. *Trends Immunol* **23**, 549-555 (2002).
123. S. Aras, M. R. Zaidi, TAMeless traitors: macrophages in cancer progression and metastasis. *Br J Cancer* **117**, 1583-1591 (2017).
124. W. Li, M. B. Graeber, The molecular profile of microglia under the influence of glioma. *Neuro Oncol* **14**, 958-978 (2012).
125. K. Gabrusiewicz *et al.*, Characteristics of the alternative phenotype of microglia/macrophages and its modulation in experimental gliomas. *PLoS One* **6**, e23902 (2011).
126. F. Szulzewsky *et al.*, Glioma-associated microglia/macrophages display an expression profile different from M1 and M2 polarization and highly express Gpnmb and Spp1. *PLoS One* **10**, e0116644 (2015).
127. Y. Sakai *et al.*, Common transcriptional signature of tumor-infiltrating mononuclear inflammatory cells and peripheral blood mononuclear cells in hepatocellular carcinoma patients. *Cancer Res* **68**, 10267-10279 (2008).
128. S. J. Coniglio *et al.*, Microglial stimulation of glioblastoma invasion involves epidermal growth factor receptor (EGFR) and colony stimulating factor 1 receptor (CSF-1R) signaling. *Mol Med* **18**, 519-527 (2012).
129. S. M. Pyonteck *et al.*, CSF-1R inhibition alters macrophage polarization and blocks glioma progression. *Nat Med* **19**, 1264-1272 (2013).
130. I. Bettinger, S. Thanos, W. Paulus, Microglia promote glioma migration. *Acta Neuropathol* **103**, 351-355 (2002).
131. A. Gieryng, D. Pszczolkowska, K. A. Walentynowicz, W. D. Rajan, B. Kaminska, Immune microenvironment of gliomas. *Lab Invest* **97**, 498-518 (2017).
132. G. A. Alexiou *et al.*, Circulating progenitor cells: a comparison of patients with glioblastoma or meningioma. *Acta Neurol Belg* **113**, 7-11 (2013).
133. S. F. Hussain *et al.*, The role of human glioma-infiltrating microglia/macrophages in mediating antitumor immune responses. *Neuro Oncol* **8**, 261-279 (2006).
134. A. B. Heimberger *et al.*, Incidence and prognostic impact of FoxP3+ regulatory T cells in human gliomas. *Clin Cancer Res* **14**, 5166-5172 (2008).
135. J. F. Jacobs *et al.*, Prognostic significance and mechanism of Treg infiltration in human brain tumors. *J Neuroimmunol* **225**, 195-199 (2010).

136. D. A. Wainwright, M. Dey, A. Chang, M. S. Lesniak, Targeting Tregs in Malignant Brain Cancer: Overcoming IDO. *Front Immunol* **4**, 116 (2013).
137. J. Lohr *et al.*, Effector T-cell infiltration positively impacts survival of glioblastoma patients and is impaired by tumor-derived TGF-beta. *Clin Cancer Res* **17**, 4296-4308 (2011).
138. M. L. Rossi, J. T. Hughes, M. M. Esiri, H. B. Coakham, D. B. Brownell, Immunohistological study of mononuclear cell infiltrate in malignant gliomas. *Acta Neuropathol* **74**, 269-277 (1987).
139. J. Huang *et al.*, Immune Checkpoint in Glioblastoma: Promising and Challenging. *Front Pharmacol* **8**, 242 (2017).
140. D. M. Pardoll, The blockade of immune checkpoints in cancer immunotherapy. *Nat Rev Cancer* **12**, 252-264 (2012).
141. M. Preusser, M. Lim, D. A. Hafler, D. A. Reardon, J. H. Sampson, Prospects of immune checkpoint modulators in the treatment of glioblastoma. *Nat Rev Neurol* **11**, 504-514 (2015).
142. C. Guillerey, N. D. Huntington, M. J. Smyth, Targeting natural killer cells in cancer immunotherapy. *Nat Immunol* **17**, 1025-1036 (2016).
143. J. Hsu *et al.*, Contribution of NK cells to immunotherapy mediated by PD-1/PD-L1 blockade. *J Clin Invest* **128**, 4654-4668 (2018).
144. X. L. Iraolagoitia *et al.*, NK Cells Restrain Spontaneous Antitumor CD8+ T Cell Priming through PD-1/PD-L1 Interactions with Dendritic Cells. *J Immunol* **197**, 953-961 (2016).
145. A. Beldi-Ferchiou *et al.*, PD-1 mediates functional exhaustion of activated NK cells in patients with Kaposi sarcoma. *Oncotarget* **7**, 72961-72977 (2016).
146. S. R. Gordon *et al.*, PD-1 expression by tumour-associated macrophages inhibits phagocytosis and tumour immunity. *Nature* **545**, 495-499 (2017).
147. A. S. Berghoff *et al.*, PD1 (CD279) and PD-L1 (CD274, B7H1) expression in primary central nervous system lymphomas (PCNSL). *Clin Neuropathol* **33**, 42-49 (2014).
148. A. S. Berghoff *et al.*, Programmed death ligand 1 expression and tumor-infiltrating lymphocytes in glioblastoma. *Neuro Oncol* **17**, 1064-1075 (2015).
149. O. Bloch *et al.*, Gliomas promote immunosuppression through induction of B7-H1 expression in tumor-associated macrophages. *Clin Cancer Res* **19**, 3165-3175 (2013).
150. T. Avril *et al.*, Distinct effects of human glioblastoma immunoregulatory molecules programmed cell death ligand-1 (PDL-1) and indoleamine 2,3-dioxygenase (IDO) on tumour-specific T cell functions. *J Neuroimmunol* **225**, 22-33 (2010).
151. S. Wintterle *et al.*, Expression of the B7-related molecule B7-H1 by glioma cells: a potential mechanism of immune paralysis. *Cancer Res* **63**, 7462-7467 (2003).
152. T. Magnus *et al.*, Microglial expression of the B7 family member B7 homolog 1 confers strong immune inhibition: implications for immune responses and autoimmunity in the CNS. *J Neurosci* **25**, 2537-2546 (2005).
153. R. Duchnowska *et al.*, Immune response in breast cancer brain metastases and their microenvironment: the role of the PD-1/PD-L axis. *Breast Cancer Res* **18**, 43 (2016).
154. A. S. Berghoff *et al.*, Tumour-infiltrating lymphocytes and expression of programmed death ligand 1 (PD-L1) in melanoma brain metastases. *Histopathology* **66**, 289-299 (2015).

155. J. R. D. Pearson, T. Regad, Targeting cellular pathways in glioblastoma multiforme. *Signal Transduct Target Ther* **2**, 17040 (2017).
156. K. E. Warren *et al.*, A phase II study of O6-benzylguanine and temozolomide in pediatric patients with recurrent or progressive high-grade gliomas and brainstem gliomas: a Pediatric Brain Tumor Consortium study. *J Neurooncol* **106**, 643-649 (2012).
157. P. Ambady *et al.*, Enhancing the cytotoxicity of chemoradiation with radiation-guided delivery of anti-MGMT morpholino oligonucleotides in non-methylated solid tumors. *Cancer Gene Ther* **24**, 348-357 (2017).
158. A. F. Eichler *et al.*, The biology of brain metastases-translation to new therapies. *Nat Rev Clin Oncol* **8**, 344-356 (2011).
159. N. Wang, R. K. Jain, T. T. Batchelor, New Directions in Anti-Angiogenic Therapy for Glioblastoma. *Neurotherapeutics* **14**, 321-332 (2017).
160. O. L. Chinot *et al.*, Bevacizumab plus radiotherapy-temozolomide for newly diagnosed glioblastoma. *N Engl J Med* **370**, 709-722 (2014).
161. M. R. Gilbert *et al.*, A randomized trial of bevacizumab for newly diagnosed glioblastoma. *N Engl J Med* **370**, 699-708 (2014).
162. W. Wick *et al.*, Phase III study of enzastaurin compared with lomustine in the treatment of recurrent intracranial glioblastoma. *J Clin Oncol* **28**, 1168-1174 (2010).
163. T. T. Batchelor *et al.*, Phase III randomized trial comparing the efficacy of cediranib as monotherapy, and in combination with lomustine, versus lomustine alone in patients with recurrent glioblastoma. *J Clin Oncol* **31**, 3212-3218 (2013).
164. W. P. Mason, End of the road: confounding results of the CORE trial terminate the arduous journey of cilengitide for glioblastoma. *Neuro Oncol* **17**, 634-635 (2015).
165. A. C. Filley, M. Henriquez, M. Dey, Recurrent glioma clinical trial, CheckMate-143: the game is not over yet. *Oncotarget* **8**, 91779-91794 (2017).
166. A. Omuro *et al.*, Nivolumab with or without ipilimumab in patients with recurrent glioblastoma: results from exploratory phase I cohorts of CheckMate 143. *Neuro Oncol* **20**, 674-686 (2018).
167. D. A. Reardon *et al.*, OS10.3 Randomized Phase 3 Study Evaluating the Efficacy and Safety of Nivolumab vs Bevacizumab in Patients With Recurrent Glioblastoma: CheckMate 143. *Neuro-Oncology* **19**, iii21 (2017).
168. A. Mantovani, P. Allavena, A. Sica, F. Balkwill, Cancer-related inflammation. *Nature* **454**, 436-444 (2008).
169. D. F. Quail *et al.*, The tumor microenvironment underlies acquired resistance to CSF-1R inhibition in gliomas. *Science* **352**, aad3018 (2016).
170. J. M. Cavaleri, E. A. Monaco, 3rd, Periostin: a potential target for glioblastoma multiforme treatment. *Neurosurgery* **76**, N17-19 (2015).
171. W. Zhou *et al.*, Periostin secreted by glioblastoma stem cells recruits M2 tumour-associated macrophages and promotes malignant growth. *Nat Cell Biol* **17**, 170-182 (2015).
172. S. Sarkar *et al.*, Therapeutic activation of macrophages and microglia to suppress brain tumor-initiating cells. *Ann Neurosci* **20**, 154 (2013).
173. J. L. Frazier *et al.*, Local delivery of minocycline and systemic BCNU have synergistic activity in the treatment of intracranial glioma. *J Neurooncol* **64**, 203-209 (2003).

174. L. Nayak, E. Q. Lee, P. Y. Wen, Epidemiology of brain metastases. *Curr Oncol Rep* **14**, 48-54 (2012).
175. A. M. Martin *et al.*, Brain Metastases in Newly Diagnosed Breast Cancer: A Population-Based Study. *JAMA Oncol* **3**, 1069-1077 (2017).
176. C. M. Sperduto *et al.*, A validation study of a new prognostic index for patients with brain metastases: the Graded Prognostic Assessment. *J Neurosurg* **109 Suppl**, 87-89 (2008).
177. P. W. Sperduto, B. Berkey, L. E. Gaspar, M. Mehta, W. Curran, A new prognostic index and comparison to three other indices for patients with brain metastases: an analysis of 1,960 patients in the RTOG database. *Int J Radiat Oncol Biol Phys* **70**, 510-514 (2008).
178. P. W. Sperduto *et al.*, Summary report on the graded prognostic assessment: an accurate and facile diagnosis-specific tool to estimate survival for patients with brain metastases. *J Clin Oncol* **30**, 419-425 (2012).
179. W. Chen, A. D. Hoffmann, H. Liu, X. Liu, Organotropism: new insights into molecular mechanisms of breast cancer metastasis. *NPJ Precis Oncol* **2**, 4 (2018).
180. I. J. Fidler, G. Poste, The "seed and soil" hypothesis revisited. *Lancet Oncol* **9**, 808 (2008).
181. N. A. Howlader N, Krapcho M, Miller D, Brest A, Yu M, Ruhl J, Tatalovich Z, Mariotto A, Lewis DR, Chen HS, Feuer EJ, Cronin KA SEER Cancer Statistics Review, 1975-2016. *National Cancer Institute. Bethesda, MD,* , (2018).
182. B. Weigelt, J. S. Reis-Filho, Histological and molecular types of breast cancer: is there a unifying taxonomy? *Nat Rev Clin Oncol* **6**, 718-730 (2009).
183. H. G. Russnes, O. C. Lingjaerde, A. L. Borresen-Dale, C. Caldas, Breast Cancer Molecular Stratification: From Intrinsic Subtypes to Integrative Clusters. *Am J Pathol* **187**, 2152-2162 (2017).
184. B. Haupt, J. Y. Ro, M. R. Schwartz, Basal-like breast carcinoma: a phenotypically distinct entity. *Arch Pathol Lab Med* **134**, 130-133 (2010).
185. H. P. Sinn, H. Kreipe, A Brief Overview of the WHO Classification of Breast Tumors, 4th Edition, Focusing on Issues and Updates from the 3rd Edition. *Breast Care (Basel)* **8**, 149-154 (2013).
186. T. Sorlie *et al.*, Gene expression patterns of breast carcinomas distinguish tumor subclasses with clinical implications. *Proc Natl Acad Sci U S A* **98**, 10869-10874 (2001).
187. C. M. Perou *et al.*, Molecular portraits of human breast tumours. *Nature* **406**, 747-752 (2000).
188. M. Laakso *et al.*, Basoluminal carcinoma: a new biologically and prognostically distinct entity between basal and luminal breast cancer. *Clin Cancer Res* **12**, 4185-4191 (2006).
189. N. Cancer Genome Atlas Research *et al.*, The Cancer Genome Atlas Pan-Cancer analysis project. *Nat Genet* **45**, 1113-1120 (2013).
190. S. Nik-Zainal *et al.*, Landscape of somatic mutations in 560 breast cancer whole-genome sequences. *Nature* **534**, 47-54 (2016).
191. C. Stirzaker, E. Zotenko, S. J. Clark, Genome-wide DNA methylation profiling in triple-negative breast cancer reveals epigenetic signatures with important clinical value. *Mol Cell Oncol* **3**, e1038424 (2016).

192. Z. I. Mitri *et al.*, Implementing a comprehensive translational oncology platform: from molecular testing to actionability. *J Transl Med* **16**, 358 (2018).
193. E. S. Bergen *et al.*, Prognostic impact of breast cancer subtypes in elderly patients. *Breast Cancer Res Treat* **157**, 91-99 (2016).
194. F. Heitz *et al.*, Triple-negative and HER2-overexpressing breast cancers exhibit an elevated risk and an earlier occurrence of cerebral metastases. *Eur J Cancer* **45**, 2792-2798 (2009).
195. N. U. Lin *et al.*, Clinicopathologic features, patterns of recurrence, and survival among women with triple-negative breast cancer in the National Comprehensive Cancer Network. *Cancer* **118**, 5463-5472 (2012).
196. P. D. Bos *et al.*, Genes that mediate breast cancer metastasis to the brain. *Nature* **459**, 1005-1009 (2009).
197. J. Y. Lee *et al.*, Gene Expression Profiling of Breast Cancer Brain Metastasis. *Sci Rep* **6**, 28623 (2016).
198. J. Massague, A. C. Obenauf, Metastatic colonization by circulating tumour cells. *Nature* **529**, 298-306 (2016).
199. A. W. Lambert, D. R. Pattabiraman, R. A. Weinberg, Emerging Biological Principles of Metastasis. *Cell* **168**, 670-691 (2017).
200. Y. Wu, M. Sarkissyan, J. V. Vadgama, Epithelial-Mesenchymal Transition and Breast Cancer. *J Clin Med* **5**, (2016).
201. A. S. Ribeiro, J. Paredes, P-Cadherin Linking Breast Cancer Stem Cells and Invasion: A Promising Marker to Identify an "Intermediate/Metastable" EMT State. *Front Oncol* **4**, 371 (2014).
202. R. M. Hoffman, Stromal-cell and cancer-cell exosomes leading the metastatic exodus for the promised niche. *Breast Cancer Res* **15**, 310 (2013).
203. J. Ursini-Siegel, P. M. Siegel, The influence of the pre-metastatic niche on breast cancer metastasis. *Cancer Lett* **380**, 281-288 (2016).
204. Y. Liu *et al.*, Premetastatic soil and prevention of breast cancer brain metastasis. *Neuro Oncol* **15**, 891-903 (2013).
205. H. K. Avraham *et al.*, Angiopoietin-2 mediates blood-brain barrier impairment and colonization of triple-negative breast cancer cells in brain. *J Pathol* **232**, 369-381 (2014).
206. A. R. Chin, S. E. Wang, Cancer Tills the Premetastatic Field: Mechanistic Basis and Clinical Implications. *Clin Cancer Res* **22**, 3725-3733 (2016).
207. N. Tominaga *et al.*, Brain metastatic cancer cells release microRNA-181c-containing extracellular vesicles capable of destructing blood-brain barrier. *Nat Commun* **6**, 6716 (2015).
208. S. P. Chiang, R. M. Cabrera, J. E. Segall, Tumor cell intravasation. *Am J Physiol Cell Physiol* **311**, C1-C14 (2016).
209. M. Labelle, S. Begum, R. O. Hynes, Direct signaling between platelets and cancer cells induces an epithelial-mesenchymal-like transition and promotes metastasis. *Cancer Cell* **20**, 576-590 (2011).
210. M. Labelle, S. Begum, R. O. Hynes, Platelets guide the formation of early metastatic niches. *Proc Natl Acad Sci U S A* **111**, E3053-3061 (2014).

211. M. Labelle, R. O. Hynes, The initial hours of metastasis: the importance of cooperative host-tumor cell interactions during hematogenous dissemination. *Cancer Discov* **2**, 1091-1099 (2012).
212. N. Reymond, B. B. d'Agua, A. J. Ridley, Crossing the endothelial barrier during metastasis. *Nat Rev Cancer* **13**, 858-870 (2013).
213. L. Sevenich *et al.*, Analysis of tumour- and stroma-supplied proteolytic networks reveals a brain-metastasis-promoting role for cathepsin S. *Nat Cell Biol* **16**, 876-888 (2014).
214. W. Zhou *et al.*, Cancer-secreted miR-105 destroys vascular endothelial barriers to promote metastasis. *Cancer Cell* **25**, 501-515 (2014).
215. J. Fan *et al.*, Integrin beta4 signaling promotes mammary tumor cell adhesion to brain microvascular endothelium by inducing ErbB2-mediated secretion of VEGF. *Ann Biomed Eng* **39**, 2223-2241 (2011).
216. B. Kusters *et al.*, Vascular endothelial growth factor-A(165) induces progression of melanoma brain metastases without induction of sprouting angiogenesis. *Cancer Res* **62**, 341-345 (2002).
217. S. Izraely *et al.*, The metastatic microenvironment: brain-residing melanoma metastasis and dormant micrometastasis. *Int J Cancer* **131**, 1071-1082 (2012).
218. Y. Kienast *et al.*, Real-time imaging reveals the single steps of brain metastasis formation. *Nat Med* **16**, 116-122 (2010).
219. C. M. Ghajar *et al.*, The perivascular niche regulates breast tumour dormancy. *Nat Cell Biol* **15**, 807-817 (2013).
220. M. Valiente *et al.*, Serpins promote cancer cell survival and vascular co-option in brain metastasis. *Cell* **156**, 1002-1016 (2014).
221. M. Lorger, B. Felding-Habermann, Capturing changes in the brain microenvironment during initial steps of breast cancer brain metastasis. *Am J Pathol* **176**, 2958-2971 (2010).
222. C. M. Ghajar, Metastasis prevention by targeting the dormant niche. *Nat Rev Cancer* **15**, 238-247 (2015).
223. P. Carlson *et al.*, Targeting the perivascular niche sensitizes disseminated tumour cells to chemotherapy. *Nat Cell Biol* **21**, 238-250 (2019).
224. J. Termini, J. Neman, R. Jandial, Role of the neural niche in brain metastatic cancer. *Cancer Res* **74**, 4011-4015 (2014).
225. D. P. Fitzgerald *et al.*, Reactive glia are recruited by highly proliferative brain metastases of breast cancer and promote tumor cell colonization. *Clin Exp Metastasis* **25**, 799-810 (2008).
226. A. Sierra *et al.*, Astrocyte-derived cytokines contribute to the metastatic brain specificity of breast cancer cells. *Lab Invest* **77**, 357-368 (1997).
227. H. N. Chuang *et al.*, Carcinoma cells misuse the host tissue damage response to invade the brain. *Glia* **61**, 1331-1346 (2013).
228. L. Wang *et al.*, Astrocytes directly influence tumor cell invasion and metastasis in vivo. *PLoS One* **8**, e80933 (2013).
229. Q. Chen *et al.*, Carcinoma-astrocyte gap junctions promote brain metastasis by cGAMP transfer. *Nature* **533**, 493-498 (2016).

230. B. Gril *et al.*, Pazopanib inhibits the activation of PDGFRbeta-expressing astrocytes in the brain metastatic microenvironment of breast cancer cells. *Am J Pathol* **182**, 2368-2379 (2013).
231. M. Noda *et al.*, IL-6 receptor is a possible target against growth of metastasized lung tumor cells in the brain. *Int J Mol Sci* **14**, 515-526 (2012).
232. F. Xing *et al.*, Reactive astrocytes promote the metastatic growth of breast cancer stem-like cells by activating Notch signalling in brain. *EMBO Mol Med* **5**, 384-396 (2013).
233. S. J. Kim *et al.*, Astrocytes upregulate survival genes in tumor cells and induce protection from chemotherapy. *Neoplasia* **13**, 286-298 (2011).
234. C. A. Sartorius *et al.*, Estrogen promotes the brain metastatic colonization of triple negative breast cancer cells via an astrocyte-mediated paracrine mechanism. *Oncogene* **35**, 2881-2892 (2016).
235. L. Zhang *et al.*, Microenvironment-induced PTEN loss by exosomal microRNA primes brain metastasis outgrowth. *Nature* **527**, 100-104 (2015).
236. A. S. Berghoff, H. Lassmann, M. Preusser, R. Hoftberger, Characterization of the inflammatory response to solid cancer metastases in the human brain. *Clin Exp Metastasis* **30**, 69-81 (2013).
237. E. R. O'Brien *et al.*, Glial activation in the early stages of brain metastasis: TSPO as a diagnostic biomarker. *J Nucl Med* **55**, 275-280 (2014).
238. R. L. Bowman *et al.*, Macrophage Ontogeny Underlies Differences in Tumor-Specific Education in Brain Malignancies. *Cell Rep* **17**, 2445-2459 (2016).
239. C. Binder *et al.*, Relaxins enhance growth of spontaneous murine breast cancers as well as metastatic colonization of the brain. *Clin Exp Metastasis* **31**, 57-65 (2014).
240. D. J. Silver *et al.*, Chondroitin sulfate proteoglycans potently inhibit invasion and serve as a central organizer of the brain tumor microenvironment. *J Neurosci* **33**, 15603-15617 (2013).
241. E. Louie *et al.*, Neurotrophin-3 modulates breast cancer cells and the microenvironment to promote the growth of breast cancer brain metastasis. *Oncogene* **32**, 4064-4077 (2013).
242. T. Pukrop *et al.*, Microglia promote colonization of brain tissue by breast cancer cells in a Wnt-dependent way. *Glia* **58**, 1477-1489 (2010).
243. S. Roesch, C. Rapp, S. Dettling, C. Herold-Mende, When Immune Cells Turn Bad-Tumor-Associated Microglia/Macrophages in Glioma. *Int J Mol Sci* **19**, (2018).
244. A. Sica, T. Schioppa, A. Mantovani, P. Allavena, Tumour-associated macrophages are a distinct M2 polarised population promoting tumour progression: potential targets of anti-cancer therapy. *Eur J Cancer* **42**, 717-727 (2006).
245. N. B. Hao *et al.*, Macrophages in tumor microenvironments and the progression of tumors. *Clin Dev Immunol* **2012**, 948098 (2012).
246. K. E. Andreou *et al.*, Anti-inflammatory Microglia/Macrophages As a Potential Therapeutic Target in Brain Metastasis. *Front Oncol* **7**, 251 (2017).
247. Z. Dong, J. Yoneda, R. Kumar, I. J. Fidler, Angiostatin-mediated suppression of cancer metastases by primary neoplasms engineered to produce granulocyte/macrophage colony-stimulating factor. *J Exp Med* **188**, 755-763 (1998).
248. A. C. da Fonseca *et al.*, The impact of microglial activation on blood-brain barrier in brain diseases. *Front Cell Neurosci* **8**, 362 (2014).

249. N. Lou *et al.*, Purinergic receptor P2RY12-dependent microglial closure of the injured blood-brain barrier. *Proc Natl Acad Sci U S A* **113**, 1074-1079 (2016).
250. J. Neman *et al.*, Human breast cancer metastases to the brain display GABAergic properties in the neural niche. *Proc Natl Acad Sci U S A* **111**, 984-989 (2014).
251. D. P. Fitzgerald *et al.*, Opposing effects of pigment epithelium-derived factor on breast cancer cell versus neuronal survival: implication for brain metastasis and metastasis-induced brain damage. *Cancer Res* **72**, 144-153 (2012).
252. W. S. Carbonell, O. Ansorge, N. Sibson, R. Muschel, The vascular basement membrane as "soil" in brain metastasis. *PLoS One* **4**, e5857 (2009).
253. M. S. Soto, S. Serres, D. C. Anthony, N. R. Sibson, Functional role of endothelial adhesion molecules in the early stages of brain metastasis. *Neuro Oncol* **16**, 540-551 (2014).
254. L. T. Lyle *et al.*, Alterations in Pericyte Subpopulations Are Associated with Elevated Blood-Tumor Barrier Permeability in Experimental Brain Metastasis of Breast Cancer. *Clin Cancer Res* **22**, 5287-5299 (2016).
255. E. K. Nduom, C. Yang, M. J. Merrill, Z. Zhuang, R. R. Lonser, Characterization of the blood-brain barrier of metastatic and primary malignant neoplasms. *J Neurosurg* **119**, 427-433 (2013).
256. D. H. Murrell *et al.*, Understanding Heterogeneity and Permeability of Brain Metastases in Murine Models of HER2-Positive Breast Cancer Through Magnetic Resonance Imaging: Implications for Detection and Therapy. *Transl Oncol* **8**, 176-184 (2015).
257. M. N. Henry, Y. Chen, C. D. McFadden, F. C. Simedrea, P. J. Foster, In-vivo longitudinal MRI study: an assessment of melanoma brain metastases in a clinically relevant mouse model. *Melanoma Res* **25**, 127-137 (2015).
258. K. Yonemori *et al.*, Disruption of the blood brain barrier by brain metastases of triple-negative and basal-type breast cancer but not HER2/neu-positive breast cancer. *Cancer* **116**, 302-308 (2010).
259. A. Morikawa *et al.*, Capecitabine and lapatinib uptake in surgically resected brain metastases from metastatic breast cancer patients: a prospective study. *Neuro Oncol* **17**, 289-295 (2015).
260. R. Ogiya *et al.*, Comparison of immune microenvironments between primary tumors and brain metastases in patients with breast cancer. *Oncotarget* **8**, 103671-103681 (2017).
261. H. Hamidi, J. Ivaska, Every step of the way: integrins in cancer progression and metastasis. *Nat Rev Cancer* **18**, 533-548 (2018).
262. H. Hamidi, M. Pietila, J. Ivaska, The complexity of integrins in cancer and new scopes for therapeutic targeting. *Br J Cancer* **115**, 1017-1023 (2016).
263. L. Seguin, J. S. Desgrosellier, S. M. Weis, D. A. Cheresh, Integrins and cancer: regulators of cancer stemness, metastasis, and drug resistance. *Trends Cell Biol* **25**, 234-240 (2015).
264. J. D. Humphries, A. Byron, M. J. Humphries, Integrin ligands at a glance. *J Cell Sci* **119**, 3901-3903 (2006).
265. J. Ivaska, J. Heino, Interplay between cell adhesion and growth factor receptors: from the plasma membrane to the endosomes. *Cell Tissue Res* **339**, 111-120 (2010).

266. D. P. White, P. T. Caswell, J. C. Norman, alpha v beta3 and alpha5beta1 integrin recycling pathways dictate downstream Rho kinase signaling to regulate persistent cell migration. *J Cell Biol* **177**, 515-525 (2007).
267. B. Felding-Habermann *et al.*, Integrin activation controls metastasis in human breast cancer. *PNAS* **98**, 1853-1858 (2001).
268. T. Sato, K. Konishi, K. Maeda, K. Yabushita, A. Miwa, Integrin alpha v, c-erbB2 and DNA ploidy in lung metastases from colorectal cancer. *Hepato-gastroenterol* **50**, 27-30 (2003).
269. C. van den Hoogen *et al.*, Integrin alphav expression is required for the acquisition of a metastatic stem/progenitor cell phenotype in human prostate cancer. *Am J Pathol* **179**, 2559-2568 (2011).
270. A. Vogetseder *et al.*, α v-Integrin isoform expression in primary human tumors and brain metastases. *Int J Cancer* **133**, 2362-2371 (2013).
271. J. S. Desgrosellier, D. A. Cheresh, Integrins in cancer: biological implications and therapeutic opportunities. *Nat Rev Cancer* **10**, 9-22 (2010).
272. L. Seguin, J. S. Desgrosellier, S. M. Weis, D. A. Cheresh, Integrins and cancer: regulators of cancer stemness, metastasis, and drug resistance. *Trends Cell Biol* **25**, 234-240 (2015).
273. C. Margadant, H. N. Monsuur, J. C. Norman, A. Sonnenberg, Mechanisms of integrin activation and trafficking. *Curr Opin Cell Biol.* **23**, 607-614 (2011).
274. M. Lorger, J. S. Krueger, M. O'Neal, K. Staflin, B. Felding-Habermann, Activation of tumor cell integrin alphavbeta3 controls angiogenesis and metastatic growth in the brain. *Proc Natl Acad Sci U S A* **106**, 10666-10671 (2009).
275. H. Liu *et al.*, MYC suppresses cancer metastasis by direct transcriptional silencing of v and 3 integrin subunits. *Nature Cell Biology* **14**, 567-574 (2012).
276. H. Ahmed, D. M. AlSadek, Galectin-3 as a Potential Target to Prevent Cancer Metastasis. *Clin Med Insights Oncol* **9**, 113-121 (2015).
277. A. Fortuna-Costa, A. M. Gomes, E. O. Kozlowski, M. P. Stelling, M. S. Pavao, Extracellular galectin-3 in tumor progression and metastasis. *Front Oncol* **4**, 138 (2014).
278. Y. Hayashi *et al.*, Galectin-3 Inhibits Cancer Metastasis by Negatively Regulating Integrin beta3 Expression. *Am J Pathol* **189**, 900-910 (2019).
279. L. Seguin *et al.*, Galectin-3, a Druggable Vulnerability for KRAS-Addicted Cancers. *Cancer Discov* **7**, 1464-1479 (2017).
280. U. V. Wesley, R. Vemuganti, E. R. Ayvaci, R. J. Dempsey, Galectin-3 enhances angiogenic and migratory potential of microglial cells via modulation of integrin linked kinase signaling. *Brain Res* **1496**, 1-9 (2013).
281. M. Xin, X. W. Dong, X. L. Guo, Role of the interaction between galectin-3 and cell adhesion molecules in cancer metastasis. *Biomed Pharmacother* **69**, 179-185 (2015).
282. G. C. Alghisi, L. Ponsonnet, C. Ruegg, The integrin antagonist cilengitide activates alphaVbeta3, disrupts VE-cadherin localization at cell junctions and enhances permeability in endothelial cells. *PLoS One* **4**, e4449 (2009).
283. S. Ning, J. Tian, D. J. Marshall, S. J. Knox, Anti-{alpha}v integrin monoclonal antibody intetumumab enhances the efficacy of radiation therapy and reduces metastasis of human cancer xenografts in nude rats. *Cancer Res* **70**, 7591-7509 (2010).

284. Y. J. Wu *et al.*, Targeting α v integrins decreased metastasis and increased survival in a nude rat breast cancer brain metastasis model. *J Neuro-Oncol* **110**, 27-36 (2012).
285. A. Heidenreich *et al.*, A randomized, double-blind, multicenter, phase 2 study of a human monoclonal antibody to human alpha v integrins (intetumumab) in combination with docetaxel and prednisone for the first-line treatment of patients with metastatic castration-resistant prostate cancer. *Annals Oncol* **24**, 329-336 (2013).
286. S. O'Day *et al.*, A randomised, phase II study of intetumumab, an anti-v-integrin mAb, alone and with dacarbazine in stage IV melanoma. *Br J Cancer* **105**, 346-352 (2011).
287. K. B. Kim *et al.*, A randomized phase II study of cilengitide (EMD 121974) in patients with metastatic melanoma. *Melanoma Res* **22**, 294-301 (2012).
288. H. Linardou, I. J. Dahabreh, D. Bafaloukos, P. Kosmidis, S. Murray, Somatic EGFR mutations and efficacy of tyrosine kinase inhibitors in NSCLC. *Nat Rev Clin Oncol* **6**, 352-366 (2009).
289. S. R. Sirkisoon *et al.*, EGFR and HER2 signaling in breast cancer brain metastasis. *Front Biosci (Elite Ed)* **8**, 245-263 (2016).
290. H. Wikman *et al.*, Relevance of PTEN loss in brain metastasis formation in breast cancer patients. *Breast Cancer Res* **14**, R49 (2012).
291. N. L. Grupka, K. C. Lear-Kaul, B. K. Kleinschmidt-DeMasters, M. Singh, Epidermal growth factor receptor status in breast cancer metastases to the central nervous system. Comparison with HER-2/neu status. *Arch Pathol Lab Med* **128**, 974-979 (2004).
292. J. Gaedcke *et al.*, Predominance of the basal type and HER-2/neu type in brain metastasis from breast cancer. *Mod Pathol* **20**, 864-870 (2007).
293. L. Da Silva *et al.*, HER3 and downstream pathways are involved in colonization of brain metastases from breast cancer. *Breast Cancer Res* **12**, R46 (2010).
294. K. M. Yamada, S. Even-Ram, Integrin regulation of growth factor receptors. *Nat Cell Biol* **4**, E75-76 (2002).
295. C. Sundberg, K. Rubin, Stimulation of beta1 integrins on fibroblasts induces PDGF independent tyrosine phosphorylation of PDGF beta-receptors. *J Cell Biol* **132**, 741-752 (1996).
296. J. F. Wang, X. F. Zhang, J. E. Groopman, Stimulation of beta 1 integrin induces tyrosine phosphorylation of vascular endothelial growth factor receptor-3 and modulates cell migration. *J Biol Chem* **276**, 41950-41957 (2001).
297. W. Guo *et al.*, Beta 4 integrin amplifies ErbB2 signaling to promote mammary tumorigenesis. *Cell* **126**, 489-502 (2006).
298. H. Liu *et al.*, MYC suppresses cancer metastasis by direct transcriptional silencing of alphav and beta3 integrin subunits. *Nat Cell Biol* **14**, 567-574 (2012).
299. N. Kotecki, F. Lefranc, D. Devriendt, A. Awada, Therapy of breast cancer brain metastases: challenges, emerging treatments and perspectives. *Ther Adv Med Oncol* **10**, 1758835918780312 (2018).
300. N. Niikura *et al.*, Treatment outcomes and prognostic factors for patients with brain metastases from breast cancer of each subtype: a multicenter retrospective analysis. *Breast Cancer Res Treat* **147**, 103-112 (2014).

301. P. S. Steeg, Targeting metastasis. *Nat Rev Cancer* **16**, 201-218 (2016).
302. P. K. Brastianos *et al.*, Genomic Characterization of Brain Metastases Reveals Branched Evolution and Potential Therapeutic Targets. *Cancer Discov* **5**, 1164-1177 (2015).
303. A. M. Brufsky *et al.*, Central nervous system metastases in patients with HER2-positive metastatic breast cancer: incidence, treatment, and survival in patients from registHER. *Clin Cancer Res* **17**, 4834-4843 (2011).
304. R. Duchnowska, S. Loibl, J. Jassem, Tyrosine kinase inhibitors for brain metastases in HER2-positive breast cancer. *Cancer Treat Rev* **67**, 71-77 (2018).
305. H. J. Stemmler *et al.*, Ratio of trastuzumab levels in serum and cerebrospinal fluid is altered in HER2-positive breast cancer patients with brain metastases and impairment of blood-brain barrier. *Anticancer Drugs* **18**, 23-28 (2007).
306. V. A. Venur, J. P. Leone, Targeted Therapies for Brain Metastases from Breast Cancer. *Int J Mol Sci* **17**, (2016).
307. S. Loibl, L. Gianni, HER2-positive breast cancer. *Lancet* **389**, 2415-2429 (2017).
308. C. H. Han, P. K. Brastianos, Genetic Characterization of Brain Metastases in the Era of Targeted Therapy. *Front Oncol* **7**, 230 (2017).
309. P. A. Burke *et al.*, Cilengitide targeting of alpha(v)beta(3) integrin receptor synergizes with radioimmunotherapy to increase efficacy and apoptosis in breast cancer xenografts. *Cancer Res* **62**, 4263-4272 (2002).
310. N. R. Parker, P. Khong, J. F. Parkinson, V. M. Howell, H. R. Wheeler, Molecular heterogeneity in glioblastoma: potential clinical implications. *Front Oncol* **5**, 55 (2015).
311. K. Urbanska, J. Sokolowska, M. Szmidt, P. Sysa, Glioblastoma multiforme - an overview. *Contemp Oncol (Pozn)* **18**, 307-312 (2014).
312. J. C. Buckner, Factors influencing survival in high-grade gliomas. *Semin Oncol* **30**, 10-14 (2003).
313. M. Weller *et al.*, Molecular predictors of progression-free and overall survival in patients with newly diagnosed glioblastoma: a prospective translational study of the German Glioma Network. *J Clin Oncol* **27**, 5743-5750 (2009).
314. M. Esteller *et al.*, Inactivation of the DNA-repair gene MGMT and the clinical response of gliomas to alkylating agents. *N Engl J Med* **343**, 1350-1354 (2000).
315. S. Le, J. Josse, F. Husson, FactoMineR: An R Package for Multivariate Analysis. *Journal of Statistical Software* **25**, 1-18 (2008).
316. F. Pedregosa *et al.*, Scikit-learn: Machine Learning in Python. *Journal of Machine Learning Research* **12**, 2825-2830 (2011).
317. A. Subramanian *et al.*, Gene set enrichment analysis: a knowledge-based approach for interpreting genome-wide expression profiles. *Proc Natl Acad Sci U S A* **102**, 15545-15550 (2005).
318. D. Merico, R. Isserlin, O. Stueker, A. Emili, G. D. Bader, Enrichment map: a network-based method for gene-set enrichment visualization and interpretation. *PLoS One* **5**, e13984 (2010).
319. H. Colman *et al.*, A multigene predictor of outcome in glioblastoma. *Neuro Oncol* **12**, 49-57 (2010).

320. A. Theocharidis, S. van Dongen, A. J. Enright, T. C. Freeman, Network visualization and analysis of gene expression data using BioLayout Express(3D). *Nat Protoc* **4**, 1535-1550 (2009).
321. T. C. Freeman *et al.*, Construction, visualisation, and clustering of transcription networks from microarray expression data. *PLoS Comput Biol* **3**, 2032-2042 (2007).
322. V. K. Mootha *et al.*, PGC-1alpha-responsive genes involved in oxidative phosphorylation are coordinately downregulated in human diabetes. *Nat Genet* **34**, 267-273 (2003).
323. M. Ashburner *et al.*, Gene ontology: tool for the unification of biology. The Gene Ontology Consortium. *Nat Genet* **25**, 25-29 (2000).
324. The Gene Ontology Consortium, Expansion of the Gene Ontology knowledgebase and resources. *Nucleic Acids Res* **45**, D331-D338 (2017).
325. A. S. Morrissy *et al.*, Spatial heterogeneity in medulloblastoma. *Nat Genet* **49**, 780-788 (2017).
326. A. Liberzon *et al.*, The Molecular Signatures Database (MSigDB) hallmark gene set collection. *Cell Syst* **1**, 417-425 (2015).
327. A. van Elsas, A. A. Hurwitz, J. P. Allison, Combination immunotherapy of B16 melanoma using anti-cytotoxic T lymphocyte-associated antigen 4 (CTLA-4) and granulocyte/macrophage colony-stimulating factor (GM-CSF)-producing vaccines induces rejection of subcutaneous and metastatic tumors accompanied by autoimmune depigmentation. *J Exp Med* **190**, 355-366 (1999).
328. B. Li *et al.*, Anti-programmed death-1 synergizes with granulocyte macrophage colony-stimulating factor--secreting tumor cell immunotherapy providing therapeutic benefit to mice with established tumors. *Clin Cancer Res* **15**, 1623-1634 (2009).
329. A. Minajeva *et al.*, Impact of Blood Vessel Quantity and Vascular Expression of CD133 and ICAM-1 on Survival of Glioblastoma Patients. *Neurosci J* **2017**, 5629563 (2017).
330. T. Homma *et al.*, Correlation among pathology, genotype, and patient outcomes in glioblastoma. *J Neuropathol Exp Neurol* **65**, 846-854 (2006).
331. G. B. Toth *et al.*, Current and potential imaging applications of ferumoxytol for magnetic resonance imaging. *Kidney Int* **92**, 47-66 (2017).
332. M. Martinez-Garcia *et al.*, SEOM clinical guidelines for diagnosis and treatment of glioblastoma (2017). *Clin Transl Oncol* **20**, 22-28 (2018).
333. D. Annibali *et al.*, Myc inhibition is effective against glioma and reveals a role for Myc in proficient mitosis. *Nat Commun* **5**, 4632 (2014).
334. J. Wang *et al.*, c-Myc is required for maintenance of glioma cancer stem cells. *PLoS One* **3**, e3769 (2008).
335. J. R. Whitfield, M. E. Beaulieu, L. Soucek, Strategies to Inhibit Myc and Their Clinical Applicability. *Front Cell Dev Biol* **5**, 10 (2017).
336. G. Marziali *et al.*, Metabolic/Proteomic Signature Defines Two Glioblastoma Subtypes With Different Clinical Outcome. *Sci Rep* **6**, 21557 (2016).
337. X. Yang, F. Lay, H. Han, P. A. Jones, Targeting DNA methylation for epigenetic therapy. *Trends Pharmacol Sci* **31**, 536-546 (2010).
338. R. K. Lai *et al.*, Genome-wide methylation analyses in glioblastoma multiforme. *PLoS One* **9**, e89376 (2014).

339. J. W. Jeong *et al.*, Multi-modal imaging of tumor cellularity and Tryptophan metabolism in human Gliomas. *Cancer Imaging* **15**, 10 (2015).
340. R. F. Barajas, Jr. *et al.*, Regional variation in histopathologic features of tumor specimens from treatment-naive glioblastoma correlates with anatomic and physiologic MR Imaging. *Neuro Oncol* **14**, 942-954 (2012).
341. J. H. Sherman *et al.*, Neurosurgery for brain tumors: update on recent technical advances. *Curr Neurol Neurosci Rep* **11**, 313-319 (2011).
342. B. Rybinski, K. Yun, Addressing intra-tumoral heterogeneity and therapy resistance. *Oncotarget* **7**, 72322-72342 (2016).
343. K. Veretennikoff, D. Walker, V. Biggs, G. Robinson, Changes in Cognition and Decision Making Capacity Following Brain Tumour Resection: Illustrated with Two Cases. *Brain Sci* **7**, (2017).
344. T. Van Meter *et al.*, Microarray analysis of MRI-defined tissue samples in glioblastoma reveals differences in regional expression of therapeutic targets. *Diagn Mol Pathol* **15**, 195-205 (2006).
345. U. S. M. C. Facility. (2008), vol. 2008.
346. A. Technologies. (2008), vol. 2008.
347. A. Liberzon *et al.*, Molecular signatures database (MSigDB) 3.0. *Bioinformatics* **27**, 1739-1740 (2011).
348. J. Godec *et al.*, Compendium of Immune Signatures Identifies Conserved and Species-Specific Biology in Response to Inflammation. *Immunity* **44**, 194-206 (2016).
349. E. Lee, R. L. Yong, P. Paddison, J. Zhu, Comparison of glioblastoma (GBM) molecular classification methods. *Semin Cancer Biol* **53**, 201-211 (2018).
350. X. Guan *et al.*, Molecular subtypes of glioblastoma are relevant to lower grade glioma. *PLoS One* **9**, e91216 (2014).
351. M. Felices *et al.*, Continuous treatment with IL-15 exhausts human NK cells via a metabolic defect. *JCI Insight* **3**, (2018).
352. S. Osuka, E. G. Van Meir, Overcoming therapeutic resistance in glioblastoma: the way forward. *J Clin Invest* **127**, 415-426 (2017).
353. N. M. Mahaweni *et al.*, A comprehensive overview of FCGR3A gene variability by full-length gene sequencing including the identification of V158F polymorphism. *Sci Rep* **8**, 15983 (2018).
354. M. H. Barros, F. Hauck, J. H. Dreyer, B. Kempkes, G. Niedobitek, Macrophage polarisation: an immunohistochemical approach for identifying M1 and M2 macrophages. *PLoS One* **8**, e80908 (2013).
355. B. Farhood, M. Najafi, K. Mortezaee, CD8(+) cytotoxic T lymphocytes in cancer immunotherapy: A review. *J Cell Physiol* **234**, 8509-8521 (2019).
356. A. Waziri, Glioblastoma-derived mechanisms of systemic immunosuppression. *Neurosurg Clin N Am* **21**, 31-42 (2010).
357. C. Hao *et al.*, Cytokine and cytokine receptor mRNA expression in human glioblastomas: evidence of Th1, Th2 and Th3 cytokine dysregulation. *Acta Neuropathol* **103**, 171-178 (2002).
358. E. K. Nduom, M. Weller, A. B. Heimberger, Immunosuppressive mechanisms in glioblastoma. *Neuro Oncol* **17 Suppl 7**, vii9-vii14 (2015).

359. W. Roggendorf, S. Strupp, W. Paulus, Distribution and characterization of microglia/macrophages in human brain tumors. *Acta Neuropathol* **92**, 288-293 (1996).
360. C. S. Morris, M. M. Esiri, Immunocytochemical study of macrophages and microglial cells and extracellular matrix components in human CNS disease. 1. Gliomas. *J Neurol Sci* **101**, 47-58 (1991).
361. T. Tsujikawa *et al.*, Quantitative Multiplex Immunohistochemistry Reveals Myeloid-Inflamed Tumor-Immune Complexity Associated with Poor Prognosis. *Cell Rep* **19**, 203-217 (2017).
362. A. W. Abbasi *et al.*, Incidence of Tumour Progression and Pseudoprogression in High-Grade Gliomas: a Systematic Review and Meta-Analysis. *Clin Neuroradiol* **28**, 401-411 (2018).
363. S. C. Thust, M. J. van den Bent, M. Smits, Pseudoprogression of brain tumors. *J Magn Reson Imaging*, (2018).
364. D. Brandsma, L. Stalpers, W. Taal, P. Sminia, M. J. van den Bent, Clinical features, mechanisms, and management of pseudoprogression in malignant gliomas. *Lancet Oncol* **9**, 453-461 (2008).
365. S. Ranjan *et al.*, Clinical decision making in the era of immunotherapy for high grade-glioma: report of four cases. *BMC Cancer* **18**, 239 (2018).
366. C. Angelucci *et al.*, Cancer stem cells from peritumoral tissue of glioblastoma multiforme: the possible missing link between tumor development and progression. *Oncotarget* **9**, 28116-28130 (2018).
367. P. Ruiz-Ontanon *et al.*, Cellular plasticity confers migratory and invasive advantages to a population of glioblastoma-initiating cells that infiltrate peritumoral tissue. *Stem Cells* **31**, 1075-1085 (2013).
368. J. M. Lemee, A. Clavreul, P. Menei, Intratumoral heterogeneity in glioblastoma: don't forget the peritumoral brain zone. *Neuro Oncol* **17**, 1322-1332 (2015).
369. A. Patil, G. V. Sherbet, Therapeutic approach to the management of HER2-positive breast cancer metastatic to the brain. *Cancer Letters* **358**, 93-99 (2015).
370. D. Palmieri *et al.*, Her-2 overexpression increases the metastatic outgrowth of breast cancer cells in the brain. *Cancer Res* **67**, 4190-4198 (2007).
371. A. M. Brufsky *et al.*, Central nervous system metastases in patients with HER2-positive metastatic breast cancer: Incidence, treatment, and survival in patients from registHER. *Clin Cancer Res* **17**, 4834-4843 (2011).
372. A. Dittrich, H. Gautrey, D. Browell, A. Tyson-Capper, The HER2 Signaling Network in Breast Cancer—Like a Spider in its Web. *J Mammary Gland Biol Neoplasia*, 1-18 (2014).
373. S. Puhalla *et al.*, Unsanctifying the sanctuary: challenges and opportunities with brain metastases. *Neuro Oncol* **17**, 639-651 (2015).
374. K. D. Beasley, S. A. Toms, The molecular pathobiology of metastasis to the brain: a review. *Neurosurgery clinics North America* **22**, 7-14 (2011).
375. V. Novitskaya *et al.*, Integrin alpha3beta1-CD151 complex regulates dimerization of ErbB2 via RhoA. *Oncogene* **33**, 2779-2789 (2014).
376. Y. H. Soung, J. L. Clifford, J. Chung, Crosstalk between integrin and receptor tyrosine kinase signaling in breast carcinoma progression. *BMB Rep* **43**, 311-318 (2010).

377. S. E. Wang *et al.*, Transforming growth factor beta induces clustering of HER2 and integrins by activating Src-focal adhesion kinase and receptor association to the cytoskeleton. *Cancer Res* **69**, 475-482 (2009).
378. H. Wang, H. Jin, D. M. Beauvais, A. C. Rapraeger, Cytoplasmic domain interactions of syndecan-1 and syndecan-4 with $\alpha 6 \beta 4$ integrin mediate human epidermal growth factor receptor (HER1 and HER2)-dependent motility and survival. *J Biol Chem* **289**, 30318-30332 (2014).
379. M. K. Creech, J. Wang, X. Nan, S. L. Gibbs, Superresolution Imaging of Clinical Formalin Fixed Paraffin Embedded Breast Cancer with Single Molecule Localization Microscopy. *Sci Rep* **7**, 40766 (2017).
380. T. Huang *et al.*, Simultaneous Multicolor Single-Molecule Tracking with Single-Laser Excitation via Spectral Imaging. *Biophys J* **114**, 301-310 (2018).
381. M. Vicente-Manzanares, D. J. Webb, A. R. Horwitz, Cell migration at a glance. *J Cell Sci* **118**, 4917-4919 (2005).
382. M. Yilmaz, G. Christofori, Mechanisms of motility in metastasizing cells. *Mol Cancer Res* **8**, 629-642 (2010).
383. G. Jacquemet, H. Hamidi, J. Ivaska, Filopodia in cell adhesion, 3D migration and cancer cell invasion. *Curr Opin Cell Biol* **36**, 23-31 (2015).
384. F. Berditchevski, E. Odintsova, Characterization of integrin-tetraspanin adhesion complexes: role of tetraspanins in integrin signaling. *J Cell Biol* **146**, 477-492 (1999).
385. V. Novitskaya *et al.*, Integrin alpha3beta1-CD151 complex regulates dimerization of ErbB2 via RhoA. *Oncogene* **33**, 2779-2789 (2014).
386. C. S. Stipp, Laminin-binding integrins and their tetraspanin partners as potential antimetastatic targets. *Expert Rev Mol Med* **12**, e3 (2010).
387. J. L. Guan, Focal adhesion kinase in integrin signaling. *Matrix Biol* **16**, 195-200 (1997).
388. S. Huveneers, E. H. Danen, Adhesion signaling - crosstalk between integrins, Src and Rho. *J Cell Sci* **122**, 1059-1069 (2009).
389. P. Nankivell *et al.*, Tetraspanins CD9 and CD151, epidermal growth factor receptor and cyclooxygenase-2 expression predict malignant progression in oral epithelial dysplasia. *Br J Cancer* **109**, 2864-2874 (2013).
390. S. S. Peddibhotla *et al.*, Tetraspanin CD9 links junctional adhesion molecule-A to alphavbeta3 integrin to mediate basic fibroblast growth factor-specific angiogenic signaling. *Mol Biol Cell* **24**, 933-944 (2013).
391. G. Rappa, T. M. Green, J. Karbanova, D. Corbeil, A. Lorico, Tetraspanin CD9 determines invasiveness and tumorigenicity of human breast cancer cells. *Oncotarget* **6**, 7970-7991 (2015).
392. S. K. Mitra, D. A. Hanson, D. D. Schlaepfer, Focal adhesion kinase: in command and control of cell motility. *Nat Rev Mol Cell Biol* **6**, 56-68 (2005).
393. J. S. Desgrosellier, D. A. Cheresh, Integrins in cancer: biological implications and therapeutic opportunities. *Nat Rev Cancer* **10**, 9-22 (2010).
394. R. Huang, E. K. Rofstad, Integrins as therapeutic targets in the organ-specific metastasis of human malignant melanoma. *J Exp Clin Cancer Res* **37**, 92 (2018).
395. H. Jeong *et al.*, Neuregulin-1 induces cancer stem cell characteristics in breast cancer cell lines. *Oncol Rep* **32**, 1218-1224 (2014).

396. J. Newbern, C. Birchmeier, Nrg1/ErbB signaling networks in Schwann cell development and myelination. *Semin Cell Dev Biol* **21**, 922-928 (2010).
397. W. J. Zhao, M. Schachner, Neuregulin 1 enhances cell adhesion molecule l1 expression in human glioma cells and promotes their migration as a function of malignancy. *J Neuropathol Exp Neurol* **72**, 244-255 (2013).
398. P. P. Ongusaha *et al.*, HB-EGF is a potent inducer of tumor growth and angiogenesis. *Cancer Res* **64**, 5283-5290 (2004).
399. Y. Su, G. E. Besner, Heparin-binding EGF-like growth factor (HB-EGF) promotes cell migration and adhesion via focal adhesion kinase. *J Surg Res* **189**, 222-231 (2014).
400. H. Y. Kuo *et al.*, Galectin-3 modulates the EGFR signalling-mediated regulation of Sox2 expression via c-Myc in lung cancer. *Glycobiology* **26**, 155-165 (2016).
401. T. Funasaka, A. Raz, P. Nangia-Makker, Galectin-3 in angiogenesis and metastasis. *Glycobiology* **24**, 886-891 (2014).
402. W. Jia, H. Kidoya, D. Yamakawa, H. Naito, N. Takakura, Galectin-3 accelerates M2 macrophage infiltration and angiogenesis in tumors. *Am J Pathol* **182**, 1821-1831 (2013).
403. K. L. Wu *et al.*, Overexpression of galectin-3 enhances migration of colon cancer cells related to activation of the K-Ras-Raf-Erk1/2 pathway. *J Gastroenterol* **48**, 350-359 (2013).
404. A. Arjonen, R. Kaukonen, J. Ivaska, Filopodia and adhesion in cancer cell motility. *Cell Adh Migr* **5**, 421-430 (2011).
405. C. E. Chan, D. J. Odde, Traction dynamics of filopodia on compliant substrates. *Science* **322**, 1687-1691 (2008).
406. Z. I. Kovacs *et al.*, Disrupting the blood-brain barrier by focused ultrasound induces sterile inflammation. *Proc Natl Acad Sci U S A* **114**, E75-E84 (2017).
407. T. K. Owonikoko *et al.*, Current approaches to the treatment of metastatic brain tumours. *Nature Reviews: Clin Oncol* **11**, 203-223 (2014).
408. P. Friedel, S. Alexander, Cancer invasion and the microenvironment: Plasticity and reciprocity. *Cell* **147**, 992-1009 (2011).
409. W. Guo *et al.*, Beta 4 integrin amplifies ErbB2 signaling to promote mammary tumorigenesis. *Cell* **126**, 489-502 (2006).
410. P. Gupta, S. K. Srivastava, Inhibition of HER2-integrin signaling by Cucurbitacin B leads to in vitro and in vivo breast tumor growth suppression. *Oncotarget* **5**, 1812-1828 (2014).
411. D. P. White, P. T. Caswell, J. C. Norman, α v β 3 and α 5 β 1 integrin recycling pathways dictate downstream Rho kinase signaling to regulate persistent cell migration. *J Cell Biol* **177**, 515-525 (2007).
412. L. Seguin *et al.*, An integrin beta(3)-KRAS-RalB complex drives tumour stemness and resistance to EGFR inhibition. *Nat Cell Biol* **16**, 457-468 (2014).
413. P. C. Huszthy *et al.*, In vivo models of primary brain tumors: pitfalls and perspectives. *Neuro Oncol* **14**, 979-993 (2012).
414. T. Oh *et al.*, Immunocompetent murine models for the study of glioblastoma immunotherapy. *J Transl Med* **12**, 107 (2014).

415. M. Patrizii, M. Bartucci, S. R. Pine, H. E. Sabaawy, Utility of Glioblastoma Patient-Derived Orthotopic Xenografts in Drug Discovery and Personalized Therapy. *Front Oncol* **8**, 23 (2018).
416. M. S. Soto, N. R. Sibson, Mouse Models of Brain Metastasis for Unravelling Tumour Progression. *Adv Exp Med Biol* **899**, 231-244 (2016).
417. M. Kijewska *et al.*, Using an in-vivo syngeneic spontaneous metastasis model identifies ID2 as a promoter of breast cancer colonisation in the brain. *Breast Cancer Res* **21**, 4 (2019).
418. R. Anil, R. R. Colen, Imaging Genomics in Glioblastoma Multiforme: A Predictive Tool for Patients Prognosis, Survival, and Outcome. *Magn Reson Imaging Clin N Am* **24**, 731-740 (2016).
419. S. Gahramanov *et al.*, Diagnosis of pseudoprogression using MRI perfusion in patients with glioblastoma multiforme may predict improved survival. *CNS Oncol* **3**, 389-400 (2014).
420. M. Nasseri *et al.*, Evaluation of pseudoprogression in patients with glioblastoma multiforme using dynamic magnetic resonance imaging with ferumoxytol calls RANO criteria into question. *Neuro Oncol* **16**, 1146-1154 (2014).
421. L. Angelov *et al.*, Blood-brain barrier disruption and intra-arterial methotrexate-based therapy for newly diagnosed primary CNS lymphoma: a multi-institutional experience. *J Clin Oncol* **27**, 3503-3509 (2009).
422. N. D. Doolittle *et al.*, Safety and efficacy of a multicenter study using intraarterial chemotherapy in conjunction with osmotic opening of the blood-brain barrier for the treatment of patients with malignant brain tumors. *Cancer* **88**, 637-647 (2000).
423. K. Jahnke *et al.*, Intraarterial chemotherapy and osmotic blood-brain barrier disruption for patients with embryonal and germ cell tumors of the central nervous system. *Cancer* **112**, 581-588 (2008).